Enhancing Terahertz Photoconductive Switches Using Nanotechnology

by

Barmak Heshmat Dehkordi
B.Sc., Isfahan University of Technology, 2006
M.Sc., Isfahan University of Technology, 2008

A Dissertation Submitted in Partial Fulfillment
of the Requirements for the Degree of

DOCTOR OF PHILOSOPHY

in the Department of Electrical and Computer Engineering

© Barmak Heshmat Dehkordi, 2012
University of Victoria

All rights reserved. This dissertation may not be reproduced in whole or in part, by
photocopy or other means, without the permission of the author.

Supervisory Committee

Enhancing Terahertz Photoconductive Switches by Nanotechnology

by

Barmak Heshmat Dehkordi
B.Sc., Isfahan University of Technology, 2006
M.Sc., Isfahan University of Technology, 2008

Supervisory Committee

Dr. Thomas Edward Darcie, (Department of Electrical and Computer Engineering)
Supervisor

Dr. Reuven Gordon, (Department of Electrical and Computer Engineering)
Departmental Member

Dr. Alex Brolo (Department of Chemistry)
Outside Member

Abstract

Supervisory Committee

Dr. Thomas Edward Darcie, (Department of Electrical and Computer Engineering)
Supervisor

Dr. Reuven Gordon, (Department of Electrical and Computer Engineering)
Departmental Member

Dr. Alex Brolo, (Department of Chemistry)
Outside Member

In this thesis we use three main approaches to enhance the performance of terahertz photoconductive switches (THz PC switches). We first propose two novel materials (GaBiAs and carbon nanotubes) for the substrate. The resulting enhancement in THz emission and reception are significant for GaBiAs. As thoroughly analyzed and addressed in Chapter 2, both the emission bandwidth and the emission amplitude of the device are improved by these materials. A systematic study of CNTs predicts 2 orders of magnitude enhancement in THz emission and one order of magnitude enhancement in THz reception. Experimental results for GaBiAs indicate 0.5 THz increase in bandwidth and 68% increase in the emitted THz wave amplitude. The bandwidth enhancement is in comparison to premium commercial devices. The optical excitation of the PC switch is studied and optimized next as the second enhancement approach (Chapter 3). The study presented in Chapter 3 provides an insight on the subwavelength dynamics of the optical excitation E-field at the edge of the electrodes. The study reveals that majority of the fast photocarriers are collected at the edge of the electrode in a subwavelength scale area. This insight leads to optimization of illumination profile and also the third enhancement approach, namely, the enhancement of electrode structure (Chapter 4). In Chapter 4 we have engineered the electrodes down to nanometer scale. This significantly enhances the optical excitation of the substrate and also overcomes the undesired properties of some substrate materials such as long carrier lifetime. Fabricated devices and fabrication processes are assessed in Chapter 5. Results (Chapter 6) highlight more than two orders of magnitude enhancement for nanostructures on GaAs.

Table of Contents

Supervisory Committee ..... **ii**

Abstract ..... **iii**

Table of Contents ..... **iv**

Acknowledgments ..... **ix**

Chapter 1 Introduction **1**
1.1 Significance of THz waves 1
1.2 THz generation and detection with PC switches 2
1.3 Enhancement in THz PC switches 8
1.4 Scope and outline of this thesis 10
1.5 Contributions 10
1.5.1 GaBiAs THz PC switches: Substrate Optimization and Nanoplasmonic gap design 11
1.5.2 Single wall carbon nanotubes as base material for THz photomixing: A Theoretical study from input power to output THz emission 11
1.5.3 THz detection with carbon nanotube based photoconductive switches: An assessment of capabilities and limitations 11
1.5.4 Optical efficiency enhancement methods for terahertz receiving photoconductive switches 11
1.5.5 Tuning plasmonic resonances of an annular aperture in metal plate 12
1.5.6 THz photoconductive switching with plasmonic interlaced nanostructures on GaAs 12

Chapter 2 Material Enhancement **13**
2.1 GaAs and LT-GaAs 13
2.2 GaBiAs potential 17
2.3 Fabrication of PC switches with GaBiAs substrate 18
2.4 CNT Potential and properties 23
2.4.1 Thermal conductance 25
2.4.2. Band gap structure and work Function 26
2.4.3. Electrical conductance 27
2.4.4. Breakdown voltage and optical illumination limit 28
2.4.5. Optical absorption in CNTs 29

Chapter 3 Optical Excitation Enhancement **32**
3.1 Microscopic study of optical excitation in THz PC switches 32
3.2 Polarization effect 35
3.3 Subwavelength edge effect 35

Chapter 4 Structure Enhancement 36
4.1 Enhanced optical coupling through EOT 37
4.2 Nanostructures for THz PC switches 39
4.2 Nanostructures simulation guide..40

Chapter 5 Assessment of Enhanced THz PC switches 45
5.1 GaBiAs as THz transmitting PC switch (Appendix A).................................45
5.2 GaBiAs as THz receiving PC switch 45
5.3 CNTs as a material for THz transmitting PC switch (Appendix B) 47
5.4 CNTs as a material THz receiving PC switch (Appendix C) 48
5.5 Fabrication of CNT-based PC switches 48
5.6 Nanostructured THz receiving PC switches on GaAs (Appendix F)..............50

Chapter 6 Conclusions...52

Chapter 7 Main Contributions and Future Concepts 53
7.1 Future works 55

Bibliography 58

Appendix A: GaBiAs THz PC switches: substrate optimization and nanoplasmonic gap design...66

ppendix B: Single-walled carbon nanotubes as base material for THz photoconductive switching 79

Appendix C: Carbon nanotube based photoconductive switches for THz detection: An assessment of capabilities and limitations...100

Appendix D: Optical efficiency enhancement methods for terahertz receiving photoconductive switches 128

Optical efficiency enhancement methods for terahertz receiving photoconductive switches 129

Appendix E: Tuning plasmonic resonances of an annular aperture in metal plate 141

Appendix F: Nanoplasmonic Terahertz Photoconductive Switch on GaAs............159

List of Figures

Figure 1.1 Terahertz waves within the electromagnetic spectrum. The range starts from 300GHz (100µm or 1.2meV) and ends at 10 THz (30 µm or 41.4 meV). 1

Figure 1.2 Output power from different THz sources. The areas that are shaded are for sources that have very narrow bandwidth. The sources can be categorized into four groups: vacuum tube oscillators, semiconducting and gas lasers, photoconductive antennas, high frequency circuits and diodes. 3

Figure 1.3 (a) THz Time domain spectroscopy setup (b) THz photomixing heterodyne setup for FDTS. “L1” stands for optical lens and “SL1” stands for silicon lens. 5

We have used both aspherical silicon lenses that focus the THz beam (f=5.5cm) and hemispherical Si lenses that collimate the THz beam. In case of hemispherical lens, further Teflon lenses or hyperbolic gold mirrors are necessary to focus the THz beam. The receiver is connected to a lock-in amplifier. The reference signal is provided from the chopped bias of the THz transmitting PC switch. ..5

Figure 1.4 (a) Detected current at THz receiver, the inset shows the schematic of a typical THz PC switch with a dipole antenna structure and a LT-GaAs/GaAs substrate. (b) The Fourier spectrum of the power of the detected signal (20log |FFT(x)|). 7

Figure 1.5 Illustration of different types of loss that are included in THz transmission efficiency. Aspherical focusing silicon lens is abbreviated as SL. Teflon lenses and parabolic mirrors are among the common THz optics. Also THz waveguides can substitute the THz optics and silicon lenses. 9

Figure 2.1 (a) Common pump and probe configurations for carrier lifetime measurement through reflection modulation detection...15

Figure 2.2 Reflection variations vs time delay for (a) SI-GaAs and (b) SI-GaAs and annealed LT-GaAs. 15

Figure 2.3 Carrier lifetime measurement results for different GaAs samples. LT-GaAs is grown on SI-GaAs wafer. 16

Figure 2.4 SEM image of phase separated Ga-Bi metallic droplet on top of the GaAsBi surface. The inset picture shows an EDX spectra map of 800 nm diameter Ga-Bi droplet (Magnification 25K, HV= 6K, working distance 15.6 mm) 20

Figure 2.5 (a) High resolution X-ray (004) θ-2θ scans for $GaAs_{1-x}Bi_x$ epilayers with Bi content of 1.4%, 5%, and 10%. The corresponding sample thicknesses are 152, 56, and 30 nm, respectively. All samples show weak interference fringes. (b) Photoluminescence intensity comparison of thin film GaBiAs epilayer with p+ GaAs wafer (P+ GaAs wafer is around 300 times thicker than GaAsBi layer) [45]. 21

Figure 2.6 Graphite, graphene, and the illustration of chiral and translational vectors [49-51]....24

Figure 2.7 (a) Armchair wrapping. (b) Zigzag wrapping. (C) Arbitrary chiral wrapping [50]. 25

Figure 2.8 (a) 3D bandgap structure of graphene. (b) to (e) shows two different chiral angles that has resulted in two different band gap structures. (b) The folding angle has resulted in a semiconducting behavior shown in (c). (c) The conduction and valence band does not meet. (d) A folding angle that results in a metallic behavior shown in (e). (e) The conductance and valence band are touching each other. [51] 26

Figure 2.9 Mean free path of different scattering mechanisms. As the length increases more scattering effects are added. 27

Figure 2.10 Measured increase in break down voltage with increase in length of CNT [52]. 28

Figure 2.11 (a) DOS for 1D material. (b) Absorption spectrum of CNT bundle. S_{11} and S_{22} are the most noticeable HV singularities [49]. 29

Figure 2.12 (a) Absorption spectrum of CNT for two different diameters differs slightly. (b) Density of states for CNTs with different diameters and (n,m) also differ slightly (c). The peaks are broadened for CNT bundle absorption spectrum [60]. 30

Figure 2.13 Kataura plots for CNT absorption [60]. 31

Figure 3.1 (a) Schematic of an autocorrelation measurement setup. The pulse beam is first split into two path one which can be varied. The two paths then reunite on a photodetector to detect the autocorrelation. (b) First order autocorrelation signal detected with an InGaAs detector. 33

Figure 3.2 (a). Graph of the spectral width at −10 dB as a function of the pump pulse width (circles) at a bias voltage of 30 V. The power of the signal emitted is also plotted with triangles as a function of the pump pulse duration, the dotted curve shows the power calculated taking into account the number of photogenerated carriers and their effective mass, the dashed line includes additionally the effective bias electric field. [67]....34

Figure 3.3 Measured THz signal as a function of illumination position for an electrode bias of 67 V (regenerated from [66])..34

Figure 4.1 Three different microantenna designs for PCAs. (a) a center-fed dipole. (b) a center-fed bowtie antenna. (c) A log-periodic antenna. Reproduced from [69]. 36

Figure 4.2 Different gap designs. (a) Interlaced structure. (b) Parallel metallic strips in the gap. (c) Ordinary micrometer sized gap. (d) Gap with tip to tip electrodes. (e) Another tip to tip design generated by overlapping circles. 37

Figure 4.3 surface plasmon waves propagating along the surfacec boundary of a metal and dielectric medium. The wave can be exited wither by electrons or by photons...38

Figure 5.1 Temporal profile of a THz pulse detected with different devices. The substrate used for the red and orange curve are grown separately but are aimed to be similar. 46

Figure 5.2 (a) Schematic view of a THz photomixer; (b) Fabrication challenges for deposition of SWNTs in the gap of adipole..49

Figure 5.3 (a) Schematic view of a THz PC switch with stripline structure. (b) The CNT bundles are seen in the SEM image of the device. (c) Slip-stick deposition method. The sample is dipped into the CNT solution....................................49

Figure 7.1 (a) Concept sketch of an all in one THz PC switch. (b) Concept sketch of a THz microscopy setup. The probe uses enhanced resonant transmission........56

Figure 7.2 (a) Concept sketch of a THz flexible slotline-probe. The gold lines are printed with cheap silver printing technology. (b) A metal mesh that is resonant in THz is used for gas sensing. 57

Acknowledgments

I would like to thank my family for their unlimited kind support. Specifically, I would like to thank my mother, Prof. Kermanshahi, for encouraging me in every step of my education, and my father, Dr. Heshmat, for his inspirational attitude toward publicizing science.

I dearly appreciate my supervisor, Prof. T. E. Darcie, for his full support and trust. Prof. Darcie's unique perspective on Ph.D. students offered me a vast scientific space that I could fully and freely explore. Because of such constructive attitude and enabling support, I was able to communicate and collaborate with multiple different disciplines. And therefore, I would like to take this opportunity to thank Dr. C. Papadopoulos and Dr. M. C. Beard for their guidance in handling carbon nanotubes, Dr. R. Gordon, for his collaboration on plasmonic nanostructures, and Prof. T. Tiedje for significantly supporting this work with his MBE group.

I also want to thank my special friends in OSTL Lab at the University of Victoria, James Zhang, Hamid Pahlevaninezhad, and Levi Smith.

Chapter 1

Introduction

Terahertz (THz) waves are electromagnetic waves ranging in frequency from 300 gigahertz to 10 terahertz. This range of frequencies is considered too high from the electronics perspective and too low from the optics point of view (Fig. 1.1). Exploration of this range of frequencies started 30 to 40 years ago and the challenges for adequate generation and detection of THz radiation remain significant [1, 2].

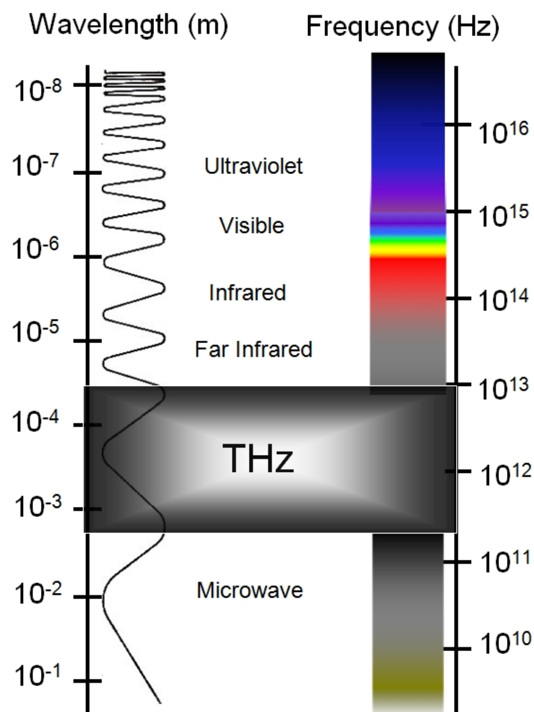

Figure 1.1 Terahertz waves within the electromagnetic spectrum. The range starts from 300GHz (100μm or 1.2meV) and ends at 10 THz (30 μm or 41.4 meV).

1.1 Significance of THz waves

THz frequencies are important from two different perspectives. From the electronics and communications side, THz switching capability is the natural progression due to ever growing bandwidth demand. From the optics perspective, the THz frequency region is rather unexplored. There are many conventional applications and techniques that can be

implemented in THz region, including spectroscopy, imaging, microscopy, telescopy, and remote sensing. Additionally, there are newly emerging applications that are specific to this range of frequencies. These include noninvasive analysis of biological and chemical samples. Unlike X-ray, THz radiation is too low in frequency to damage cells (damage can only happen due to an extreme optical fluence); however, it significantly interacts with many biological compounds. That is because many biological compounds and molecules have intra- and inter-molecular low-band rotational and vibrational state frequencies in the THz region, especially frequently in the 1-3 THz range [3]. THz waves have been used to identify and distinguish many key materials such as, water, CO, HCN, Glycine, Glycerol (amino acid basis), Thymine, Deoxycytidine (nucleosides), Adenosine, D-glucose (sugar basis), Tryptophan, and L-alanine [3]. The detection capabilities of THz radiation have been further stretched to living samples such as Bacillus subtilis and other microorganisms. [4, 5].

Studying the THz dynamics of physical phenomena in different materials and especially newly emerging nanomaterials such as carbon nanotubes and semiconducting nanowires [6, 7] is also done with THz waves.

1.2 THz generation and detection with PC switches

There are many methods for generation of THz waves [8]. Gunn diodes, Schottky diodes, impact ionization avalanche transit-time diodes (IMPATT diodes), InGaAs resonant tunnelling diodes (RTDs), free electron lasers, gas lasers, quantum cascade lasers (QCLs), klystrons, backward wave oscillators (BWOs), InP microwave monolithic integrated circuits (MMICs), optical rectifiers (OPRs), THz photomixers and photoconductive switches are all different types of THz emitters. The attainable frequencies of each of these sources are shown in Fig. 1.2. Unlike THz photoconductive switches (PC switches), the power level of most THz sources decreases significantly at 1-3 THz frequency range. From the GHz-frequency electronics side, capacitive effects reduce power and from the far infrared optical side, it is difficult to engineer a room-temperature operated band gap that matches the low energy level of THz photons (4meV). Gas lasers are bulky and very expensive. QCLs are compact solid state THz

sources but the complex fabrication process and necessity of a cryogenic cooling system set serious practical limitations.

In between the high-frequency optical and the low-frequency electrical ends of the THz device spectrum there is an optoelectronic approach that covers the 0.1-5 THz frequency gap. PC switches or photoconductive antennas (PCA) are optoelectronic devices that can be used both as THz transmitters and THz detectors. These devices are made of a microantenna fabricated on an ultra-fast material (material with sub-picosecond carrier lifetime). The substrate material is usually a GaAs-based material [9-12].

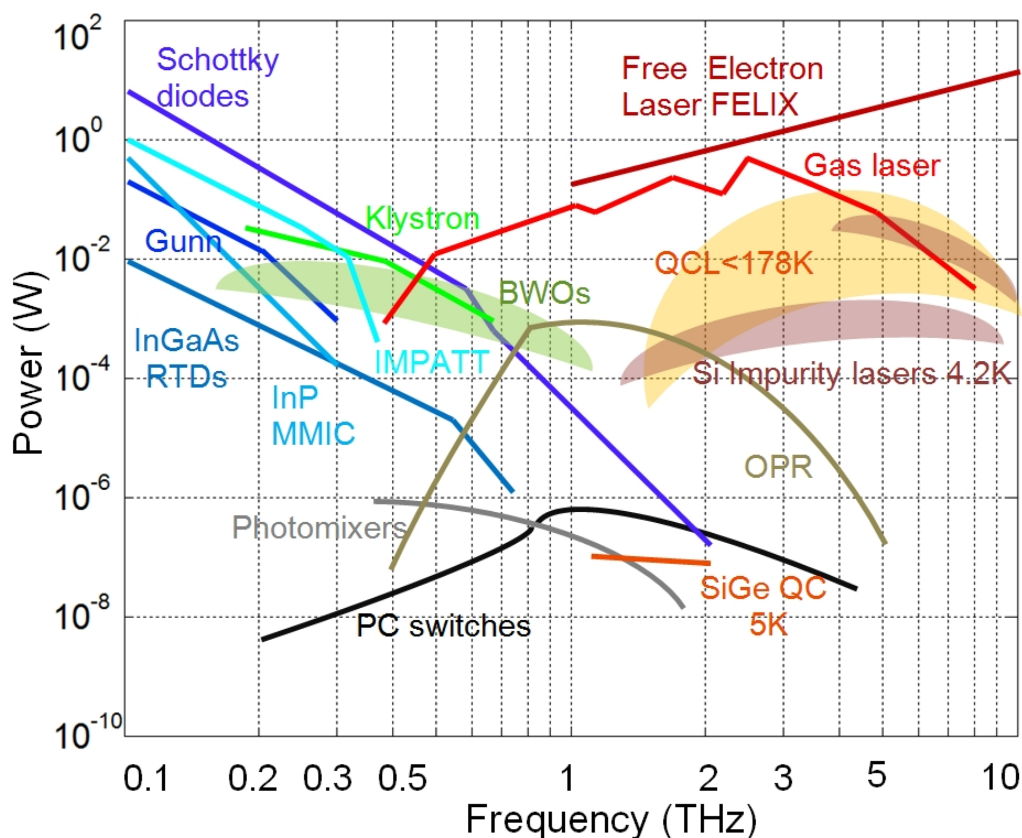

Figure 1.2 Output power from different THz sources. The areas that are shaded are for sources that have very narrow bandwidth. The sources can be categorized into four groups: vacuum tube oscillators, semiconducting and gas lasers, photoconductive antennas, high frequency circuits and diodes.

Another THz generation method that covers the 0.5-5 THz frequency range is optical rectification. Optical rectifiers (OPRs) are nonlinear crystals that are excited with high power fs laser pulses. These crystals (ZnTe, $LiNbO_3$, CdTe, GaSe, etc.) provide a second-order nonlinear medium in which the optical pulse is rectified. Due to nonlinearity (large second-order electrical susceptibility terms) different frequency components of the pulse

are mixed into the THz range. Recently, the efficiency of OPRs has been significantly improved with resonant nanostructures and semiconductors with periodically-inverted (periodically poled) crystalline orientation [13, 14]. The recent generation of OPRs has out performed PC switches in maximum output power, since the nonlinear crystals can operate with higher input optical powers. However, large size, costly pump lasers, limited fractional bandwidth from phase matching, complex detection, and pulsed operation are among the disadvantages of these devices.

Major advantages of PCAs include room temperature operation, compatibility with conventional femtosecond pulse lasers, broadband and narrowband operation capability, dual THz transmission/detection capability, and lower cost compared to some of the other optical approaches. These advantages are followed with several drawbacks. Low sensitivity and output power level (low efficiency) and necessity for optical excitation are two major draw backs for these devices.

For broadband THz emission, the antenna is first biased with a DC voltage and then an optical excitation pulse excites the carriers in the gap of the antenna (Fig 1.3 (a)). The photocarriers accelerate due to the existing field between the antenna electrodes and this feeds the antenna with a sub-picosecond surge of current. The radiation due to this current pulse is detected at the receiver side by another PCA (Fig. 1.3). The pulse temporal phase or delay in the heterodyne setup (Fig. 1.3(a)) is varied finely via a moving retro reflector or an optical delay line. The temporal profile of the generated THz pulse is recorded as the relative phase between THz pulse and the incident optical pulse in the receiver is scanned. Such a setup is typically used for time domain THz Time Domain Spectroscopy (TDTS) of chemical and biological samples [3, 15].

For narrow band operation the pulsed optical excitation is replaced with a continuous optical excitation. In this continuous wave mode (CW mode) a mixture of two continuous wave lasers with slightly different frequencies excites the antenna gap (Fig. 1.3(b)). The difference between two laser frequencies is in the THz range and thus the conductivity of the ultrafast material in the gap of the antenna is modulated with these THz components. Only a fraction of the antenna feed current possesses the THz components and thus THz photomixing (or CW mode) operation is more inefficient than wideband pulsed mode

operation [1, 16]. Additionally, when illuminated, the peak photoconductivity of the gap is increased much more significantly than the average photoconductivity in CW mode. This realizes a much more efficient radiation impedance value and consequently a higher average power for pulsed mode compared to that of CW.

The setup shown in Fig 1.3 (b) is usually used for frequency domain THz spectroscopy (FDTS). The incident beating optical excitation and the CW THz wave can be either in phase or out of phase in the receiver. The phase depends on the delay line position

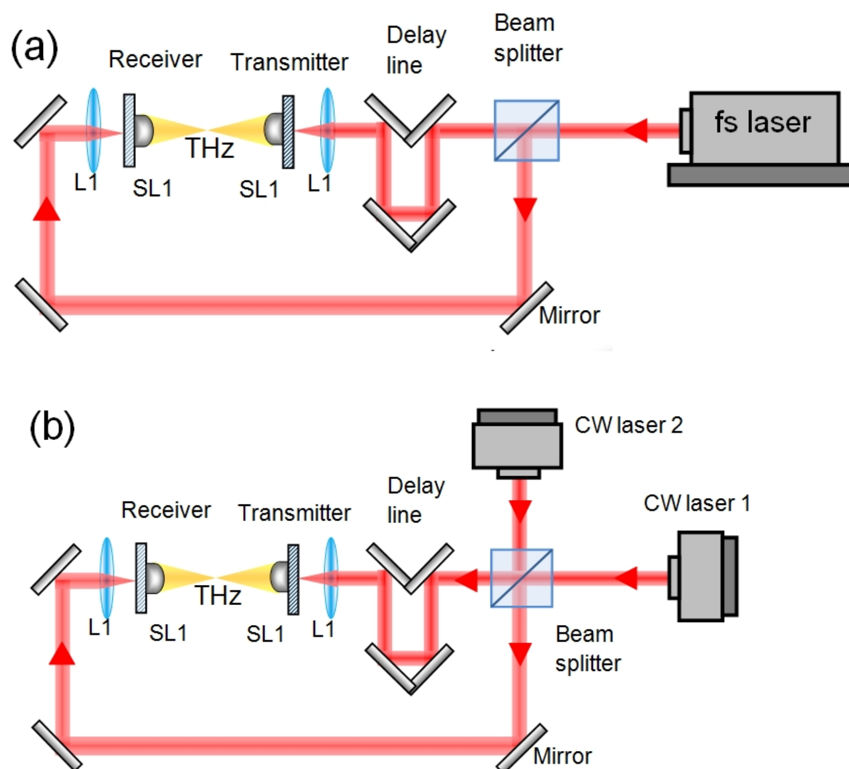

Figure 1.3 (a) THz Time domain spectroscopy setup (b) THz photomixing heterodyne setup for FDTS. “L1” stands for optical lens and “SL1” stands for silicon lens. We have used both aspherical silicon lenses that focus the THz beam (f=5.5cm) and hemispherical Si lenses that collimate the THz beam. In case of hemispherical lens, further Teflon lenses or hyperbolic gold mirrors are necessary to focus the THz beam. The receiver is connected to a lock-in amplifier. The reference signal is provided from the chopped bias of the THz transmitting PC switch.

As with THz emission, there are numerous approaches for detection of THz waves. Bolometric, electronic, and optoelectronic approaches are among the main trends for THz detection (Table 1.1) [17-19].

As mentioned previously, PCAs can also function as THz receivers. In reception mode, PCAs generate a DC current in nA range. This current is measured using a lock-in amplifier that is connected to the PC switch. There is no DC bias involved in the process of THz reception and the receiver photoconductive antenna is biased only with the impinging THz waves. The excited photocarriers are collected due to this THz bias and this results in the detected DC current. In heterodyne setups (Fig. 1.3(a)) the transmitted THz pulse is chopped either by optically chopping the excitation beam or by electronically modulating the transmitter DC bias. This low frequency modulation signal also functions as a reference signal for the lock-in amplifier. The modulation parameters are given in Table 1.1.

Table 1.1 List of THz detectors and their parameters [17].

Detector type	Modulation frequency (Hz)	Operation frequency (THz)	Noise equivalent power ($W/Hz^{1/2}$)
Golay cell	≤ 20	≤ 30	10^{-9}-10^{-10}
Pyroelectric	≤ 300	≤ 3	$\approx(0.4\text{-}1.25)\times10^{-9}$
PC switches	$\leq 10^4$	≤ 5	10^{-8}-10^{-9}
VO_x microbolometer	$\leq 10^2$	≤ 30	$>3\times10^{-10}$
Bi microbolometer	$\leq 10^6$	≤ 3	1.6×10^{-10}
Nb microbolometer	-	≤ 30	5×10^{-11}
Schottky diodes	$\leq 10^{10}$	≤ 10	$\geq10^{-10}$
Si MOSFET	3×10^4	0.645	$\approx3\times10^{-10}$
Si FET	-	≤ 30	$>10^{-10}$
HgCdTe HEB	$< 10^8$	$\approx0.03\text{-}2$	$\approx4\times10^{-10}$
Low-temperature bolometer	-	≤ 30	$\approx(0.4\text{-}3)\times10^{-19}$

A typical temporal profile of the measured current is given in Fig. 1.4 (a). The inset picture shows the schematic of a typical THz PC switch with a dipole antenna structure. The center gap is where the excitation pulse is focused. The Fourier spectrum shows that the signal has components higher than 1THz (Fig. 1.4 (b)). As we will see in following chapters, this current has a direct relation with the incident THz field.

The polarization of the emitted THz is linear and in parallel to the dipole microantenna. Therefore, the receiver dipole must be aligned in the same direction to pick up the highest signal. The polarization of the optical excitation beam is independent of the polarization of the generated THz waves since the process is an absorption-emission process. Polarization effects will be further discussed in chapter 3.

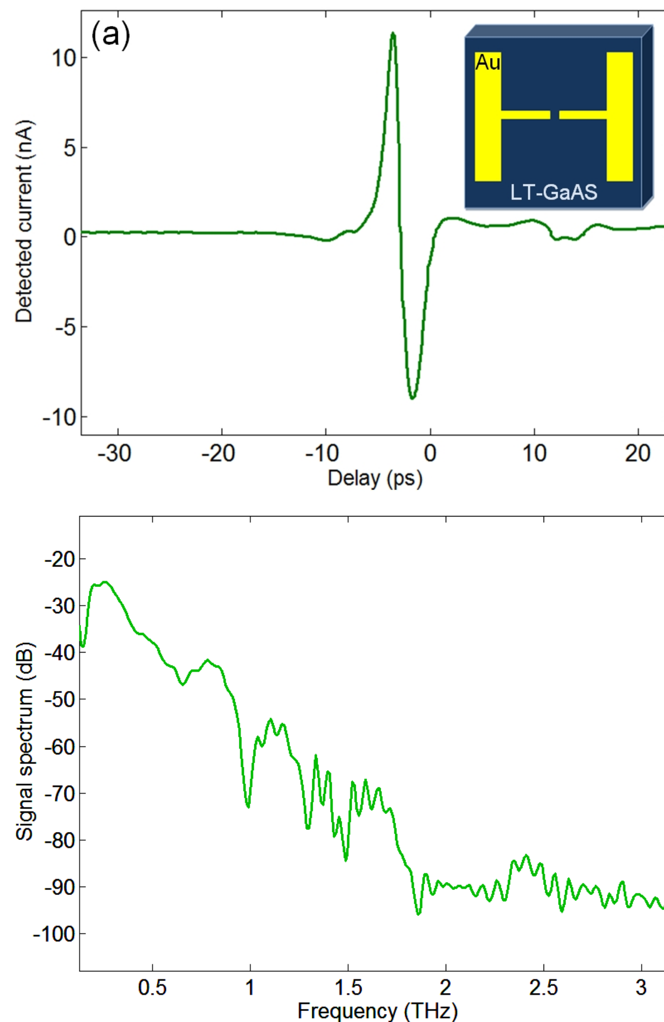

Figure 1.4 (a) Detected current at THz receiver, the inset shows the schematic of a typical THz PC switch with a dipole antenna structure and a LT-GaAs/GaAs substrate. (b) The Fourier spectrum of the power of the detected signal (20log |FFT(x)|).

1.3 Enhancement in THz PC switches

Since THz PCAs are among the least costly and easiest to use THz sources that can operate from 0.1-5 THz at room temperature, there has been a significant effort toward enhancing the efficiency of these devices [9-12]. Although in theory PCAs can surpass the Manley-Rowe limit as accelerated electrons in the dipole can emit several THz photons, unfortunately in practice, the optical conversion efficiency of PCAs (less than 10^{-4}) is one to two orders of magnitude lower than Manley-Rowe conversion efficiency limit ($\sim 10^{-3}$) for passive nonlinear crystals [1]. Manely-Rowe relations are based on conversion of energy. These relations state that the rate of created and annihilated photons should be kept equal at all the frequencies involved in the optical nonlinear process in a lossless medium. For example this can be expressed as below for a nonlinear loss less medium with 2 input frequencies ω_1 and ω_2 the relation is given as:

$$\Sigma\Sigma\frac{iP_{i,j}}{i\omega_1 + j\omega_2} = 0 \; and \; \Sigma\Sigma\frac{iP_{i,j}}{i\omega_1 + j\omega_2} = 0 \quad (1.1)$$

where i and j are integers. The relations also predict the energy for each generated frequency in a lossy medium. The Manley-Rowe limit may be overcome by recycling photons in a cascaded process [13. 14] but it sets an upper limit for the optical-to-THz conversion efficiency in bulk nonlinear crystals. Such poor performance of PCAs reduces the functionality of these devices for wide band (0.1-5 THz) THz spectroscopy and many other applications [2, 16, 19]. The output maximum power is limited by the electrical and thermal breakdown of the PCA, and therefore, pushing these limits can also be considered as a technique to obtain higher output power along with increasing the efficiency. Some researchers have tried to push the maximum power throughput by growing LT-GaAs on a Si wafer which has higher thermal conduction [20, 21]. However, there are two major factors that further highlight the importance of increasing efficiency rather than merely increasing optical illumination. The first factor is the current industrial trend toward modest-power (30-50 mW), compact fs pulse lasers. These lasers provide more desirable form factors and also have lower prices that are very appealing for commercial applications and products. The second factor is the fundamental limitation of the substrate material for absorbing the excitation light. Excessive increase in input

power can push the substrate to the saturated absorption region [22]. In this nonlinear regime further increase in input power will not increase the number of photo-excited carriers and the consequent THz output power. The same saturation effect can limit the sensitivity of the THz receiving PCA.

Based on the process of THz generation and detection in the TDTS configuration (Fig. 1.3 (a)), there are several major bottle necks that can be further engineered. Optical excitation efficiency, THz transmission efficiency and electrical efficiency are three main areas that require improvement. Optical coupling efficiency refers to the conversion of excitation photons to excited photocarriers. This is important both in transmitter and receiver. The number of photocarriers defines the depth of photoconductivity modulation in the gap of a PCA. Deeper modulation will result in higher THz power and THz sensitivity. THz transmission efficiency is the efficiency of coupling the generated THz waves to the detector micro antenna. There are several losses involved in THz transmission (Fig. 1.5). Finally, electrical efficiency refers to efficiency of collecting the photo-excited carriers and the electrical contribution of the photocurrent to the detected signal. The electrical efficiency can be enhanced both by optimizing the field profile in the gap and by engineering the THz frequency response of the antenna circuitry.

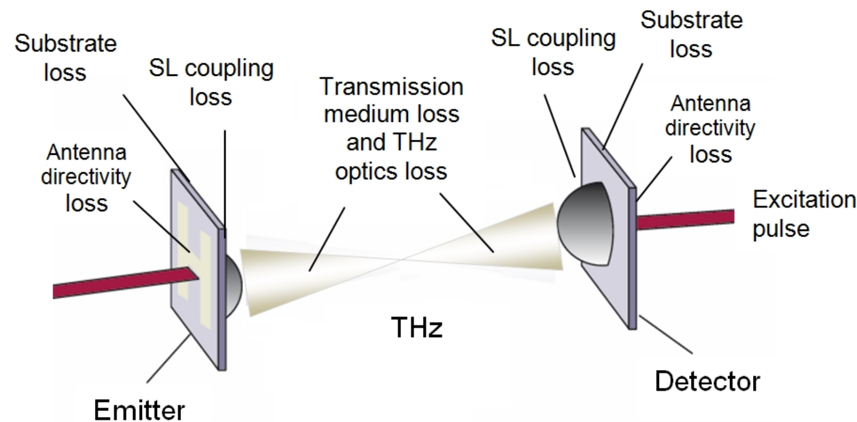

Figure 1.5 Illustration of different types of loss that are included in THz transmission efficiency. Aspherical focusing silicon lens is abbreviated as SL. Teflon lenses and parabolic mirrors are among the common THz optics. Also THz waveguides can substitute the THz optics and silicon lenses.

A notable amount of research has been done on improving the performance of PCAs through all three mentioned approaches [9-12, 23-25]. The optical efficiency is usually enhanced with antireflection coatings and engineering the substrate material [23, 26]. The

transmission efficiency has been improved both by antenna design and implementing more efficient THz optics and THz waveguides [23-26]. Finally, the electrical efficiency has also been improved through optimized microantenna design [27]. Micrometer-sized interlaced structures [25] and impedance-tuned antennas are used to enhance the electrical efficiency [24]. Complexity of design and moderate enhancement has prevented many of these approaches from spreading into commercial applications. Therefore, considerable effort continues toward defining a simple, inexpensive approach that can significantly enhance performance.

1.4 Scope and outline of this thesis

Aside from THz transmission efficiency, other efficiencies require engineering three main components, namely, substrate material, antenna structure, and optical excitation coupling. The objective of this thesis is to enhance the performance of THz PCAs through all of these three factors. This thesis is written in the article-style dissertation format in which the main text provides only a general overview and the appendices (published or submitted scientific journal papers) provide the details of the work. The rest of the thesis is organized as follows: Chapter 2 presents a short study on two new materials (GaBiAs and carbon nanotubes) for THz PC switching. Chapter 3 briefly addresses the potential for optical excitation enhancement for PCAs. Chapter 4 focuses on the electrode structure enhancement and Chapter 5 summarizes the assessment of fabricated devices and the fabrication process itself. It must be emphasized that based on the article-style format the three enhancement approaches are outlined in detail in the article manuscripts presented in the Appendices.

1.5 Contributions

Considering the publication-based article-style format of this thesis, each chapter is based on one or more of our journal publications. Each part of the work has been either published or submitted to a peer-reviewed scientific journal. The contributions of authors are given in details in the following subsections.

1.5.1 GaBiAs THz PC switches: Substrate Optimization and Nanoplasmonic gap design

The manuscript was written by B. Heshmat and Prof. Darcie. Pump and probe, THz reception, and THz emission results were measured by B. Heshmat. The fabrication process was mostly done by B. Heshmat and M. Masnadi. The project was funded and supported by Prof. T. Darcie, Dr. R. Gordon, and Prof. T. Tiedje. M. Masnadi and R. Lewis provided their knowledge of material science to the project which helped with interpreting the measured data. The manuscript was reviewed and edited by all the authors.

1.5.2 Single wall carbon nanotubes as base material for THz photomixing: A Theoretical study from input power to output THz emission

The manuscript was written by B. Heshmat. Mr. Heshmat performed the Monte Carlo simulations, developed the circuit theory and evaluated the theory. The experimental results for LT-GaAs were also measured by B. Heshmat. Dr. C. Papadopoulos helped with DS model interpretation for CNT materials. Also, the rate equations were suggested with Dr. M. C. Beard and explicitly solved by B. Heshmat. Prof. Darcie supervised and funded the project. Dr. H. Pahlevaninezhad helped with conceptualizing the problem. He additionally reviewed and edited the text along with other authors.

1.5.3 THz detection with carbon nanotube based photoconductive switches: An assessment of capabilities and limitations

B. Heshmat wrote the manuscript, performed the analysis of DS model and circuit model. Dr. H. Pahlevaninezhad reviewed and edited the text. He also helped with numerical evaluation of the circuit equations. Prof. Darcie, funded and supervised the project in addition to reviewing and editing the manuscript. Dr. C. Papadopoulos helped with CNT deposition and fabrication.

1.5.4 Optical efficiency enhancement methods for terahertz receiving photoconductive switches

B. Heshmat wrote the text, measured the results and also performed the theoretical part of the work. The theoretical part included the ray optics calculations and near field finite-difference time-domain (FDTD) simulations of the electrode edges. Dr. H.

Pahlevaninezhad, helped with the experimental part. Prof. Darcie funded and supervised the project -- his suggestions and guidance were critical to the project. And finally the manuscript was reviewed and edited by all the authors.

1.5.5 Tuning plasmonic resonances of an annular aperture in metal plate

This work consisted of three major parts: coupled mode theory (CMT) formulation, CMT numerical evaluation, and FDTD simulations. B. Heshmat developed the CMT formulations and evaluated it. D. Li did the FDTD simulations of the annular aperture. The manuscript was written by B. Heshmat. Dr. Gordon significantly helped the conceptualization of the paper and text quality. Prof. Darcie reviewed and edited the text in addition to supervising the project.

1.5.6 THz photoconductive switching with plasmonic interlaced nanostructures on GaAs

B. Heshmat and Dr. Gordon conceptualized the idea and the work was performed with significant guidance from Prof. Darcie. The manuscript preparation was carried out by B. Heshmat and further perfected by Dr. Gordon and Prof. Darcie. Devices were made and tested by B. Heshmat and Dr. H. Pahlevaninezhad. The FDTD simulation part was also preformed by B. Heshmat with help of Dr. Pang. Dr. Tiedje, M. Masnadi, and R. Lewis provided substrate material for one of the figures in the paper.

Chapter 2

Material Enhancement

Substrate material defines many key parameters such as carrier mobility, breakdown voltage, thermal break down, absorption efficiency, and bandwidth of the generated THz pulse. In this chapter we will first introduce and investigate the prior conventional material and then we will propose and evaluate two new materials for THz PC switching.

2.1 GaAs and LT-GaAs

There are different figures of merit for the THz transmitting PCAs. Some studies use maximum output power as a figure of merit while others use the ratio of THz power to pump power (P_{THz}/ P_{pump}) or conversion efficiency. For the THz receiving PCA, the sensitivity (A/W) per unit of optical illumination ($I_{detected}/P_{THz}.P_{pump}$) can be considered as a criterion for performance. The substrate material plays a definitive role in the performance. The ideal scenario for a THz transmitting PCA the substrate material should have high breakdown voltage, high thermal breakdown limit, high optical density, high mobility, high saturation velocity, low carrier lifetime (sub-picosecond), and low dark conductance. As previously shown [25, 28, 29] and also calculated in case of carbon nanotubes (Appendices B and C), these parameters dictate the performance of the material (the output power or sensitivity) for THz photoconductive switches.

The aim is to have the deepest modulation in the conductivity of the substrate material. Hypothetically, an ideal PCA substrate material would become short circuited when illuminated and it would act as an open circuit when in dark. Based on such a scheme, high optical absorption should be followed by high mobility and high saturation velocity to allow efficient collection of the photocarriers. In practice, the absorption and mobility are limited. Therefore, in order to increase photocurrent either the optical intensity of the excitation pulse or the applied voltage should be increased. This explains the desire for

higher breakdown voltage and breakdown temperature in the substrate material. Another aspect of an optical switch is its switching speed. This is dictated directly by the time that photo-excited carriers are present in the material; a parameter known as carrier lifetime. For THz operation the carrier lifetime should be in sub-picosecond range. While fast photocarrier rise time can partially generate higher THz frequency components, short carrier lifetime is necessary for higher detection resolution in the receiver and sharper high bandwidth emission peaks in the transmitter. As it will be shown in table 2.2 the carrier lifetime of LT-GaAs is over 3 orders of magnitude lower than that of SI-GaAs. However, this short carrier lifetime comes at the price of a lower mobility (about an order of magnitude lower). As the numbers imply the mobility is a nonlinear function of the carrier lifetime. While the lower mobility directly (quadratically [25]) reduces the emitted THz power, it is yet preferred to use a material with shorter carrier lifetime. Lower carrier lifetime is necessary to modulate the photoconduction in the continuous wave (CW) photomixers, it is also necessary to detect the higher frequency components of the received THz both in CW and pulsed mode. Therefore, it is not possible to setup a low noise high bandwidth THz time domain spectroscopy setup without conventional dipoles in a long carrier lifetime substrate. Another drawback of longer carrier lifetime is detection and emission of low frequency noise. Presence of photocarriers in the GaAs for over 200 ps renders the low frequency noise into the detection. This can be undesired in some spectroscopy applications.

Among bulk materials, LT-GaAs has been the dominant material for THz PC switching [21-25]. Short carrier lifetime of LT-GaAs enables THz-frequency switching. Depending on growth condition and annealing temperature the carrier lifetime of LT-GaAs can be reduced to 0.3 ps [30]. The lifetime is usually measured with pump and probe technique [31]. Fig. 2.1 shows the schematic of our optical pump - optical probe setup.

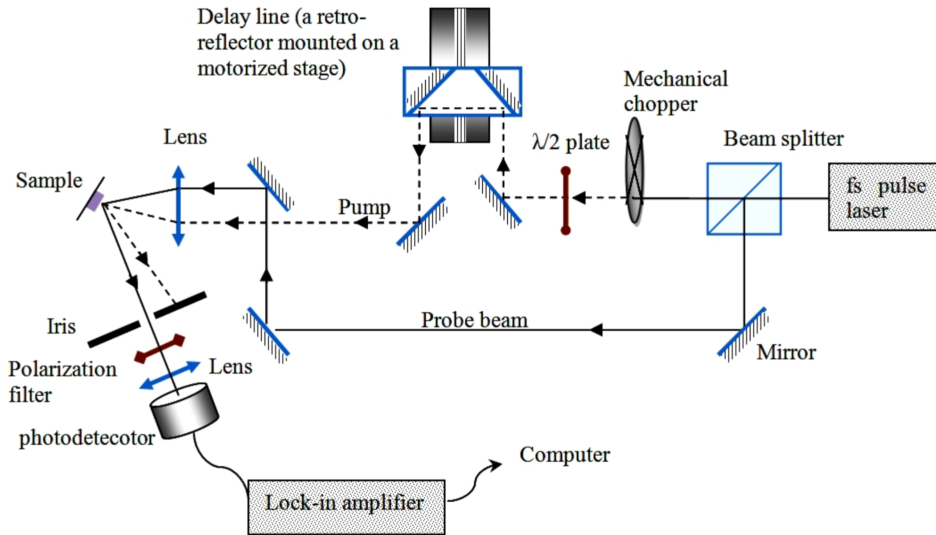

Figure 2.1 (a) Common pump and probe configurations for carrier lifetime measurement through reflection modulation detection.

In this scheme the Ti-Sapphire fs pulse beam is split into two beams; one is used as a pump (~40 mW average power) to excite the carriers in the sample and thus change its reflectivity. The other is used as a probe (10 mW; cross polarized) to measure the changes in reflectivity. The phase difference between pump and probe pulses is controlled with a retro-reflector mounted on an automated stage. Carrier lifetime of semi-insulating GaAs (SI-GaAs) is known to be over 200 ps. As confirmed in Fig 2.2 (a), the reflection from SI-GaAs does not return to its original value even 100 ps after the pump incidence. This value is reduced to less than 1 ps for LT-GaAs (Fig. 2.2 (b), Fig. 2.3). The carrier lifetime for three different samples is compared in Fig. 2.3; The details of growth parameters for these samples will be discussed in the next section.

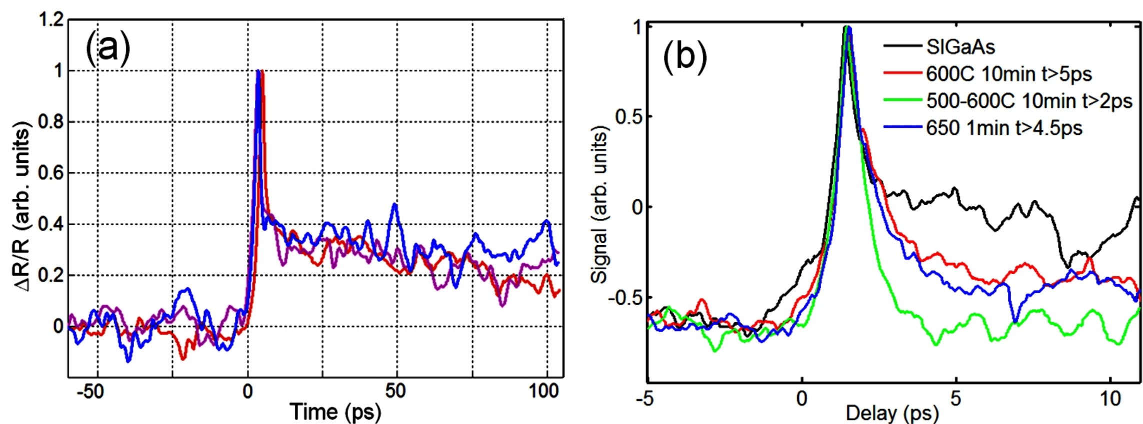

Figure 2.2 Reflection variations vs time delay for (a) SI-GaAs and (b) SI-GaAs and annealed LT-GaAs.

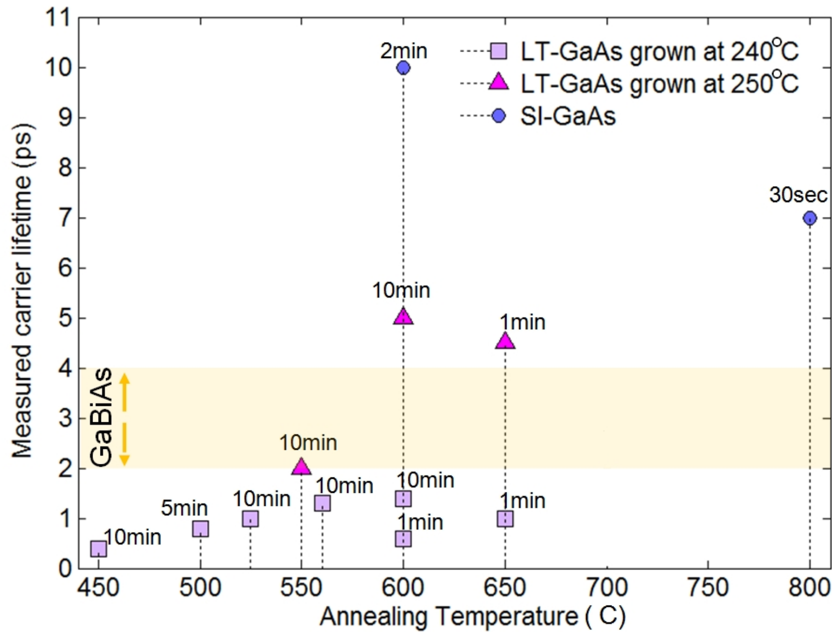

Figure 2.3 Carrier lifetime measurement results for different GaAs samples. LT-GaAs is grown on SI-GaAs wafer.

As seen in Fig. 2.2 (b) and 2.3 the lifetime is a nonlinear function of annealing time and temperature. Full understanding of the carrier recombination process in GaAs and LT-GaAs is yet a topic of research. However, there are several major processes that are known to contribute to carrier lifetime: carrier trapping, trap emptying, exciton-exciton annihilation, and recombination in ionic cores (dopings, As antisites, and impurities) are usually combined with a more rigorous continuity equations to match the measured data. Several scattering rates such as carrier collision rate, impurity scattering rate and lattice (acoustic-phonon) scattering rate can enter the Drude-like equations to predict the THz photoconductivity [30-32]. These scattering time constants are different in average length (carrier-carrier ~100 fs < carrier-phonon~ps <interband ~ns). The measured reflectivity variations is directly sensitive to interband transition and deeper defect level transitions, therefore, the other scattering rates are not directly visible in the measured signal. In fact, multiple intraband scatterings can occur before an interband transition occurs, therefore, the detected signal is the integration of all that time. Some studies suggest that the initial overshoot can be due to carrier trapping and the relaxing tail is dominated by trap emptying process [40, 46]. The recombination time also depends on the depth of defect level, spatial spacing of the defect clusters, and many other parameters. The rates are also usually different for surface and bulk. This may further explain the higher sharp peak

shown in 2.2 (a). The sharp overshoot followed by a slowly relaxing tail (after 4 ps) in case of SI-GaAs is also partly due to subtle scattering of the pump beam (from the sample surface) into the probe beam path that results in a very weak interference in the receiver right at the beginning of the pulse. This interference noise is in the range of <200 fs. The setup is highly alignment sensitive. Unfortunately shorter carrier lifetime of LT-GaAs comes at the price of lower mobility – a parameter that directly affects the performance of the device. Low mobility reduces the efficiency of the PC switch [1, 24-27], and therefore, although LT-GaAs is the dominant commercial substrate material [26, 32-34], there is a need to find a better substitute for LT-GaAs.

2.2 GaBiAs potential

Bismuth (Bi) is a poor metal (a soft metal with a low boiling point) that can be used along with Arsenic (As) to grow GaBiAs material. GaBiAs has been shown to have promising performance for THz PC switching. This material is yet under research as incorporation of Bi into GaAs is challenging. Increase in Bi concentration in GaBiAs is known to shrink the band gap. Other parameters of the material are found to have complex dependencies on Bi percentage. GaBiAs has several advantages over conventional GaAs for PCA applications [35, 36]. Table 2.1 compares the relative parameters of Si, GaAs, LT-GaAs, and GaBiAs [35-42]. As seen in this Table, there are several attractive factors for using GaBiAs. Those are shown with green arrows. The undesired factors that are expected to reduce the performance are shown with red arrows from GaBiAs column to LT-GaAs column. The size of each arrow is chosen relative to the significance of the variation. As seen in Table 2.1 the main advantage of LT-GaAs over GaAs is carrier lifetime. The mobility is however reduced by an order of magnitude. This is due to induced defects during low temperature growth. The defects clustering condition is further affected by annealing temperature and duration (Fig. 2.4). GaBiAs can be grown in higher temperatures (300-350°C) and thus exhibits a higher mobility. The quantitative assessment of GaBiAs for THz PC switching is found in chapter 5 and Appendix A.

The carrier lifetime of GaBiAs samples cannot be accurately measured with our 810 nm pump-probe setup. The band gap shrinkage that is induced due to presence of Bi causes

the 810 nm pulses to excite the carriers to higher states in the conduction band. Therefore, in GaBiAs the photocarriers that are excited with 810 nm laser relax thermally to the bottom of the conduction band. This distorts the original signal that is to be measured from the changes in the reflection of the sample due to recombination of the photocarriers. The mentioned behavior along with surface roughness in GaBiAs samples reduces the accuracy of the 810 nm pump-probe measurement results for GaBiAs. Different pump and probe frequencies should be used for GaBiAs and this requires a more sophisticated setup. It is reported that the carrier lifetime of GaBiAs can be reduced to a few picoseconds with proper annealing [42].

Table 2.1 Relevant parameters of different materials for THz PC switching. Si is included as a common semiconducting material [35-42]. Moving from left column to right column, the green arrows show an advantage and the red arrows show a disadvantage.

Name of the parameter	Si	GaAs	LT-GaAs	GaBiAs
Break down field (V/cm)	3×10^5	4×10^5	→ (green) 5×10^5	$\geq5\times10^4$
Mobility of electrons ($cm^2\ V^{-1}s^{-1}$)	≤1400	≤8500	← (red) ≈200-800	→ (green) ≤2300
Mobility of holes ($cm^2\ V^{-1}s^{-1}$)	≤450	≤400	← (red) ≤150	≤150
Saturation velocity (cm/s) at 300K	1×10^7	1.2×10^7	0.2×10^7	?
Thermal cond. W/(m·K) at 300K	149	55	← (red) 12.6	← (red) ~10
Refractive index (1.5ev)	3.8	3.3	3.55	3.3
Band gap (ev)	1.12	1.424	1.43	-70 meV/%
Absorption coef. (1/cm) at 830nm	10^3	10^4	→ (green) 1.5×10^4	→ (green) 2×10^4
Carrier lifetime (ps)	1000	≥300	→ (green) 0.3	← (red) 2-4 ?

2.3 Fabrication of PC switches with GaBiAs substrate

For the substrate material LT-GaAs and bismuth containing samples were grown on semi-insulating GaAs (001) substrates in a VG-V80H molecular beam epitaxy machine. The system has standard Ga-type effusion cells for Ga and Bi, together with a valved two-zone cracker for As_2. Substrate temperature was measured using optical band gap thermometry with an accuracy of +/- 5 °C. Reflection high energy electron diffraction

(RHEED) was used during the growth to monitor the surface reconstructions and roughness.

The details of annealing and growth condition for each GaBiAs sample is given in Table 2.2. As seen in Table 2.2 there are two methods of annealing, Three-zone-furnace and Rapid-thermal annealing abbreviated as TZF and RTA respectively. For RTA the chamber is evacuated down to 10^{-6} torr and a thermocouple measures the sample surface. TZF has three heating coils which accurately control the temperature distribution in the annealing chamber. The chamber pressure in three-zone furnace (TZF) is similar to that of an RTA. The highest annealing temperature for our RTA is 670 °C. The TZF can surpass that by 1100°C maximum temperature. TZF does not have the N_2 pressure cooling mechanism as in RTA and thus its cooling process is slower than RTA.

Table 2.2 Growth and annealing parameters of different GaBiAs substrates. (NA stands for Not Applicable)

Code	Bi%	Growth Temp. (°C)	Annealing condition	X-ray quality	PL quality-Peak(nm)-FWHM(nm)	Thick. (nm)	As_2:Ga BEP
r2303	1.8	328	RTA	Normal	Good-1106-242	500	As_2/Ga BEP: 3.01 Bi/Ga BEP: 0.032
r2202	2.2	365	RTA	Normal	Good-1015-90	350	As_2/Ga BEP= 2.21
r2275	2.25	245	TZF	Good	Good-1046-220	117	N/A
r2198	3.0	360	RTA	Normal	Good-1151-82	90	As_2/Ga BEP= 1.14
r2304	4.25	215	RTA	Normal	Weak-1187-180	292	As_2/Ga BEP: 2.26 Bi/Ga BEP: 0.113
r2147	4.4	295	TZF	Good	Good-1128-140	75	N/A
r2299	9.6	225	RTA	Normal	NA	140	As_2/Ga BEP: 2.36
r2345	13.8	250	NA	Normal	NA	~ 60	As_2/Ga BEP: 1.48 Bi/Ga BEP: 0.31
r2341	19	225	NA	Normal	NA	~ 60	As_2/Ga BEP: 1.72 Bi/Ga BEP: 0.55

The last column in Table 2.2 shows either the value for Beam Equivalent Pressure (BEP) or the Flux Ration (FR). BEP is the molecular pressure of each source and FR is number

of atoms per centimetre squared per second on the sample surface. BEP and FR can be converted to each other if necessary [43, 44].

The surface for GaBiAs samples plays an important role in THz properties of a PC switch. With increase in Bi concentration the surface becomes rougher due to appearance of Ga-Bi droplets. Without the smoothing process the surface can have large droplets (Fig. 2.4) (up to 1 micron in some cases).

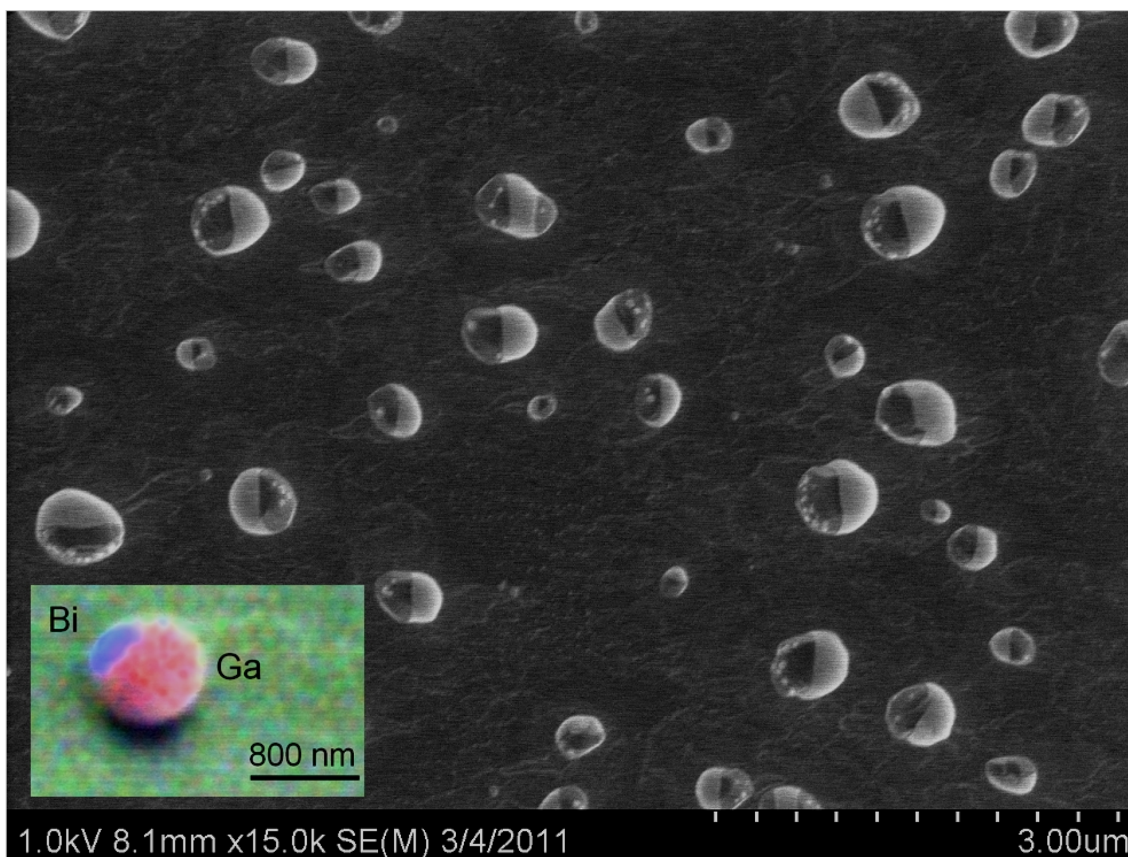

Figure 2.4 SEM image of phase separated Ga-Bi metallic droplet on top of the GaAsBi surface. The inset picture shows an EDX spectra map of 800 nm diameter Ga-Bi droplet (Magnification 25K, HV= 6K, working distance 15.6 mm)

These droplets can be partially etched off by HCL aquatic solution. The surface can become fairly smooth after this process. For instance, for 2.2% Bi samples the RMS roughness was measured to be less than 1 nm after the etching process. The roughness is measured by atomic force microscopy (AFM). Energy dispersive X-ray spectroscopy can be used in the scanning electron microscope to identify the composition of the droplets (inset Figure in Fig. 2.4).

A high resolution X-ray diffraction (HR-XRD) machine (Bruker D8 Advance) was used to measure the X-ray diffraction patterns for the samples (Fig. 2.5 (a)). X-ray measurements reveal the thickness of the GaBiAs layer, the quality of the GaAs buffer layer beneath the GaBiAs layer, and the Bi concentration. The machine uses the best Vegard's fit to fit the measured signal (dotted curves in Fig. 2.5 (a)).

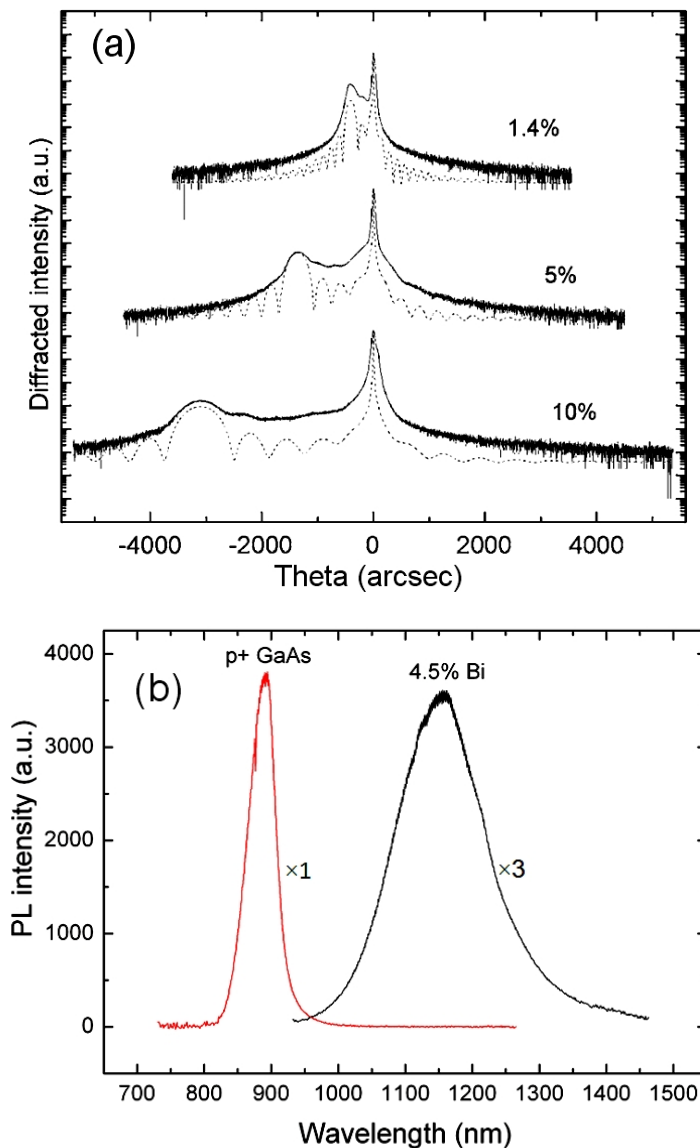

Figure 2.5 (a) High resolution X-ray (004) θ-2θ scans for $GaAs_{1-x}Bi_x$ epilayers with Bi content of 1.4%, 5%, and 10%. The corresponding sample thicknesses are 152, 56, and 30 nm, respectively. All samples show weak interference fringes. (b) Photoluminescence intensity comparison of thin film GaBiAs epilayer with p+ GaAs wafer (P+ GaAs wafer is around 300 times thicker than GaAsBi layer) [45].

The fit data can be used to infer the Bi concentration in the GaBiAs layers. In the fifth column of Table 2.2, the X-ray results are summarized into two category of “Good” and “Normal”. Good X-ray quality refers to a strong peak with clear thickness fringes that indicate an abrupt change from GaAs to GaBiAs in the crystal structure. Such an abrupt transition requires a high quality GaAs buffer layer beneath the GaBiAs layer. “Normal” refers to a clear X-ray peak with weak thickness fringes; this is the dominant measurement result for our GaBiAs samples.

Another method to study the structure of the sample is the photoluminescence (PL) measurement. The PL measurement also verifies the Bi concentration, dislocations in the crystal structure, and impurity. PL can further reveal if the recombination of photocarriers is radiative or non-radiative. This depends on defect levels in the material. The incorporation of Bi shifts the PL peak to higher frequencies. This is the direct result of band gap shrinkage caused by Bi incorporation (~80 meV/1% [46]). Impurities and defects broaden and weaken the peak (Fig. 2.5 (b)). The sixth column in Table 2.2, indicates the PL quality for each sample, the results are categorized into “Good” and “Weak” categories which are chosen based on the relative amplitude of the measured peak. A 532 nm 20 ns pulsed diode-pumped solid-state laser at room temperature excites the samples for the photoluminescence (PL) measurements. The diode-pumped laser has 1.5 mW average power and repetition rate of 2 kHz. The peak power density is 105 W/cm^2. The PL signal is dispersed using a SpectraPro-300i spectrograph and then detected by a liquid nitrogen-cooled InGaAs array detector [47]. The detector has a cut-off of 1600 nm and therefore the PL signal for samples with higher Bi percentage cannot be measured (Table 2.2) with our system.

Table 2.3 shows the same parameters for LT-GaAs samples. Low growth temperature for these samples results in incorporation of a lot of defects. These defects cause the photocarriers to recombine non-radiatively which weakens the PL signal down to noise level. However, X-ray technique can be still used to investigate the quality of the layers. Table 2.3 gives the details of growth condition for LT-GaAs samples. These parameters should be well tuned to obtain the desired THz emission. As seen in Table 2.3 the typical As_2/Ga BEP is much higher compared to GaBiAs while the growth temperature is generally lower. This suggests that the carrier recombination hubs of LT-GaAs are

different from that of GaBiAs surface. In LT-GaAs the recombination hubs are defects induced by excess arsenic (a group V metalloid). In GaBiAs the recombination hubs are likely to be GaBi defects as well as similar deep donor levels of the As_{Ga} antisite defect in LT-GaAs (Appendix A).

Table 2.3 Growth and annealing parameters of different LT-GaAs substrates.

Code	Excess As %	Growth Temp. (°C)	Annealing condition	X-ray quality	Thick. (nm)	As_2:Ga BEP
r2328	0.5	250	RTA and MBE	Good	1000 nm	As_2/Ga BEP: 12
r2340	0.7	240	RTA	Good	900 nm	As_2/Ga BEP: 17.64

In MBE annealing, the samples were annealed in the MBE machine under As_2 background pressure of 10^{-8} torr. The mentioned background As_2 pressure favorably prevents the As evaporation from the sample surface while annealing. For MBE the temperature is measured through band gap thermometry that is more accurate than a thermocouple in RTA. However, RTA can quickly (less than 1 min) cool the sample down to room temperature under N_2 pressure. This is not possible with MBE annealing; there is no N_2 pressure in MBE chamber, and therefore, cooling the sample is much slower (4 times slower).

2.4 CNT potential and properties

With a range of interesting properties, such as high absorption, ballistic transportation, and high thermal conductance, carbon nanotubes (CNTs) are potential candidates for THz device fabrication [48-51].

Graphite is a carbon-based material found in nature and used in everyday life. For example, we still use graphite-based compounds in pencil tips. This material is made up of thin layers of carbon atom sheets, or “graphene.” Graphene is comprised of a sheet of monolayer carbon atoms connected in a hexagonal honey comb structure, as shown in Fig. 2.6. By using different processes, these sheets of carbon can be wrapped into thin tubes named carbon nanotubes. The angle of wrapping the graphene sheet dramatically affects the properties of CNT [50, 51]. In order to determine the type of CNT being used,

two basic vectors specify the angle, axial period, and circumferential period. “Chiral vector” identifies the angle of wrapping, while “translation vector” specifies the axial period. In order to establish a common basis for all chiral and translational vectors, there are two basic vectors a_1 and a_2 from whose linear combinations all chiral and translational vectors can be written.

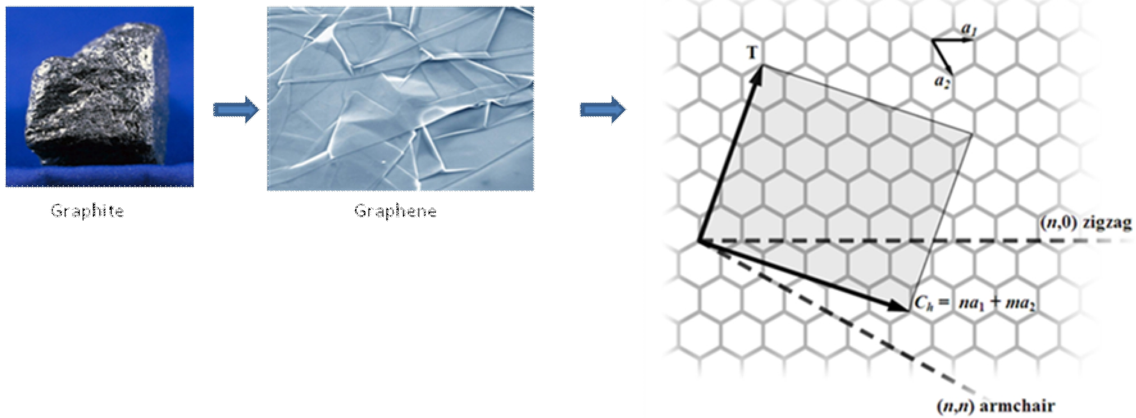

Figure 2.6 Graphite, graphene, and the illustration of chiral and translational vectors [49-51].

The multiples of each fundamental vector that create a chiral vector are shown by (n, m), or in other notations by (n_1, n_2). This index indicates the properties expected from that type of CNT. Based on n and m the CNT can be metallic, quasi-metallic, or semiconducting (Fig. 2.7). The CNT is metallic or quasi-metallic if n-m=3q where q=0,1,2…; otherwise it is semiconducting. The diameter of the CNT is calculated with relation to n and m based on Eq. 2.1.

$$d = \frac{\sqrt{3}}{\pi} a_{c-c} \sqrt{n^2 + m^2 + nm}\,,$$
$$a_{c-c} = 0.14nm \qquad (2.1)$$

In this equation, a_{c-c} is carbon to carbon atom distance. There are many other properties and parameters that can be expressed using (n, m), but we will focus on related properties and topics in the following sub-sections. For more detail on other properties, refer to [49-51]. The following sub-sections focus on CNT properties that might be useful for THz applications, including thermal conductance, band gap structure, electrical conductance, and breakdown voltage and optical illumination limit. Since CNT is a 1D

material its properties cannot be conveniently (accurately) compared to that of a bulk material such as GaBiAs or LT-GaAs. Therefore, we preferred to briefly explain each property instead of simply adding another column for CNTs in Table 2.1.

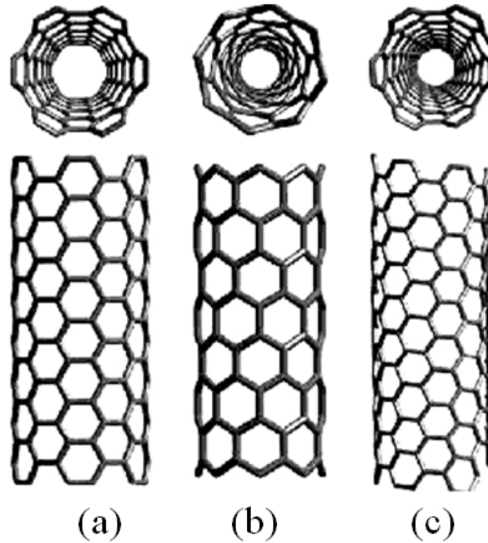

Figure 2.7 (a) Armchair wrapping. (b) Zigzag wrapping. (C) Arbitrary chiral wrapping [49].

2.4.1 Thermal conductance

Thermal conductance is the quantity of heat, ΔQ, transmitted during time Δt through a thickness x, in a direction normal to a surface of area A, due to a temperature difference ΔT, under steady state conditions and when the heat transfer is dependent only on the temperature gradient. Eq. 2.2 shows this quantity.

$$k = \frac{\Delta Q.x}{A\Delta tT} \tag{2.2}$$

Thermal conductance has the dimension of [W/mK]. This property is significant in THz applications as it affects the breakdown voltage, which will be explained shortly. Note that CNTs usually have a high thermal conductance (up to 6000 W/m.K), which even exceeds thermal conductivity of diamond (900–2,320 W/mK), copper (385W/m.K), and gold (318 W/m.K). Also, the phonons can be transported ballistically in CNTs for small distances. It should be noted that CNTs are not isotropic in thermal conduction; their

behaviors are like thermal insulators perpendicular to the CNT axis. Additionally, CNTs are flexible and extremely strong.

2.4.2. Band gap structure and work function

Semiconducting carbon nanotubes are generally considered to be direct band gap semiconductors.

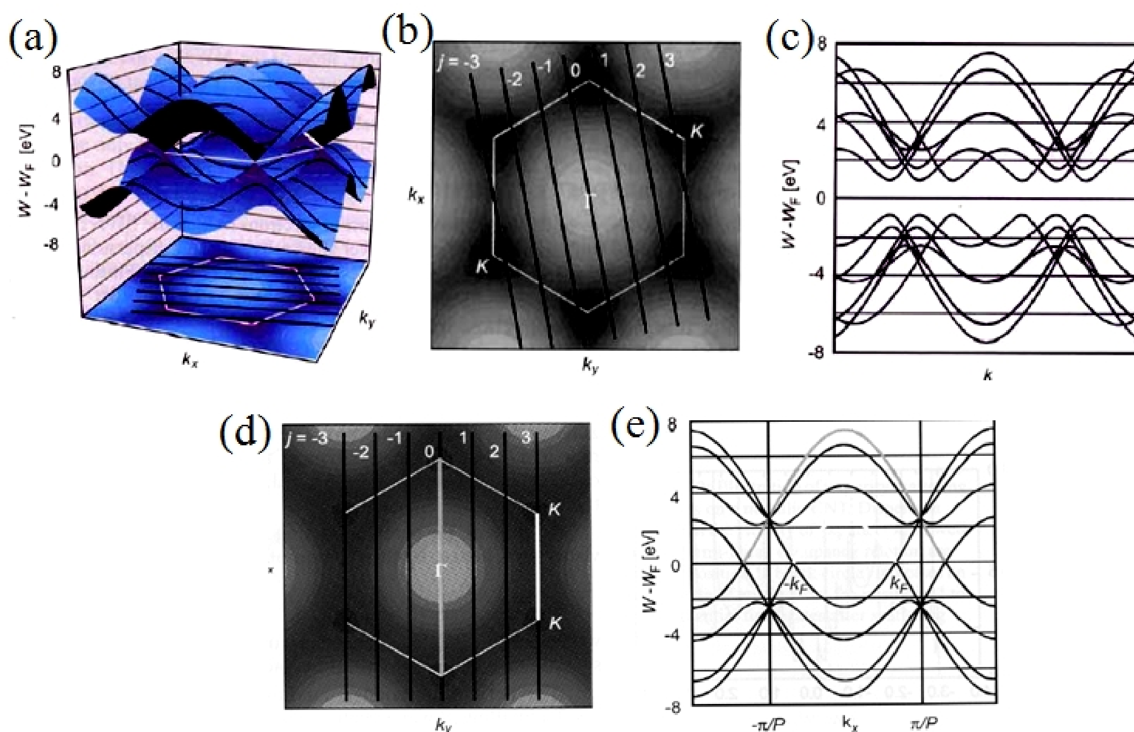

Figure 2.8 (a) 3D bandgap structure of graphene. (b) to (e) shows two different chiral angles that has resulted in two different band gap structures. (b) The folding angle has resulted in a semiconducting behavior shown in (c). (c) The conduction and valence band does not meet. (d) A folding angle that results in a metallic behavior shown in (e). (e) The conductance and valence band are touching each other. [51] Copyright (2013) by Wiley-VCH

CNTs band gap structure actually comes from cross-sectioning the 2D band gap structure of graphene. This can be estimated by zone folding schemes or other methods. For each chiral angle the cross-section will be different, which is why different chiral angles demonstrate different electronic properties. Fig. 2.8 shows two different chiralities and the associated band gap structures created. For semiconducting CNTs, the band gap energy usually ranges from Eg=0.5 to Eg=1.5 eV, and a rough estimation of the work function is 4.5eV+0.5×Eg. In practice the band gap structure is not as easily obtained as mentioned in this estimation [49-51].

2.4.3. Electrical conductance

In theory, metallic carbon nanotubes carry an electrical current density of 4×10^9 A/cm^2, which is more than 1,000 times greater than metals such as copper. This is due to high intrinsic mobility level followed by ballistic transportation in CNTs. Electrical conductance has a direct relation with mobility:

$$\mu = Gl / ne \tag{2.3}$$

where l is mean free path (MFP) and n is the linear carrier density. Mobility in CNT is typically around10^5 cm^2/vs. MFP is related to scattering mechanism along the CNT axis. There are different scattering mechanisms and each has its own cause and MFP. Conductance is reduced with the addition of each scattering mechanism [52-54]. Fig. 2.9 shows MFP of different scattering effects that occur as the length of the carbon nanotube increases.

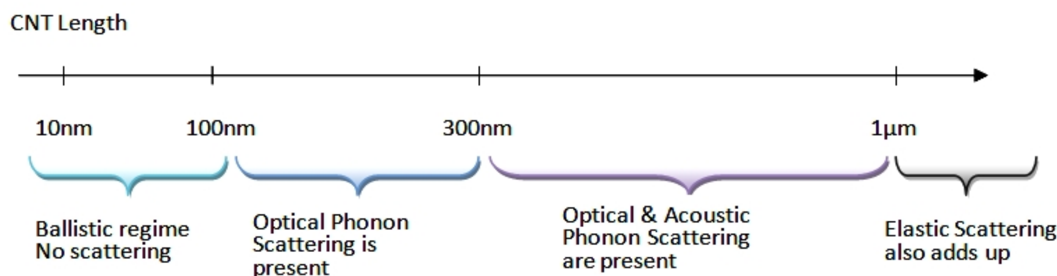

Figure 2.9 Mean free path of different scattering mechanisms. As the length increases more scattering effects are added.

Since researchers tend to work with many CNTs bundled together, the electrical conductance of CNT bundles are important. A CNT bundle usually consists of many types of CNTs with different chirality. In order to calculate conductance of a CNT bundle, the conductance should first be calculated for all types of CNTs present in the bundle. If there are multi-wall CNTs (MWCNT) present in the bundle, the conductance should first be calculated for each shell. Each shell can have some number of conductance channels depending on the diameter of the tube. Since MWCNTs can have several coaxial shells, they are highly conductive. The total conductance is obtained by integrating the conductance of all CNTs present in the bundle. Considering the large mobility in CNTs the resistance of a CNT bundle is usually small (<1kΩ).

2.4.4. Breakdown voltage and optical illumination limit

The definition of breakdown voltage for a single CNT is the voltage at which the connection area, or any other point along the CNT, starts to decompose or malfunction electrically. For CNT bundles, the V_{BD} is defined as the minimum of all V_{BD} for all CNTs present in the bundle. There are different results for breakdown voltage of CNTs and CNT bundles. V_{BD} grows with length, and for typical 1 μm CNT bundles a voltage less than 3.6V should be safe. Eq. 2.4 expresses breakdown voltage, current, and power for CNT bundles.

$$\left.\begin{aligned} I_{BD} &= \left[G_{shell}\left(2\pi d^2 k_{th} + \frac{\pi l k_{ox}}{\ln(8t_{ox}/\pi d)}\right)(T_{BD} - T_{ENV})\right]^{1/2} \\ P_{BD} &= \left(2\pi d^2 k_{th} + \frac{\pi l k_{ox}}{\ln(8t_{ox}/\pi d)}\right)(T_{BD} - T_{ENV}) \end{aligned}\right\} \Rightarrow V_{BD,Bundle} = Min\left(\frac{P_{BD,i}}{I_{BD,i}}\right) \tag{2.4}$$

Where G_{shell} is the conductance of each shell in a MWCNT, d is the diameter of CNT T_{BD} is the breakdown temperature (approximately 800K), T_{ENV} is the environment temperature, k_{th} is the thermal conductivity constant of the CNT, l is the CNT length, t_{ox} is the thickness of the oxide layer beneath the bundle, and k_{ox} is the thermal constant of the substrate. Fig. 2.10 shows the increase in V_{BD} with increase in length [53-55].

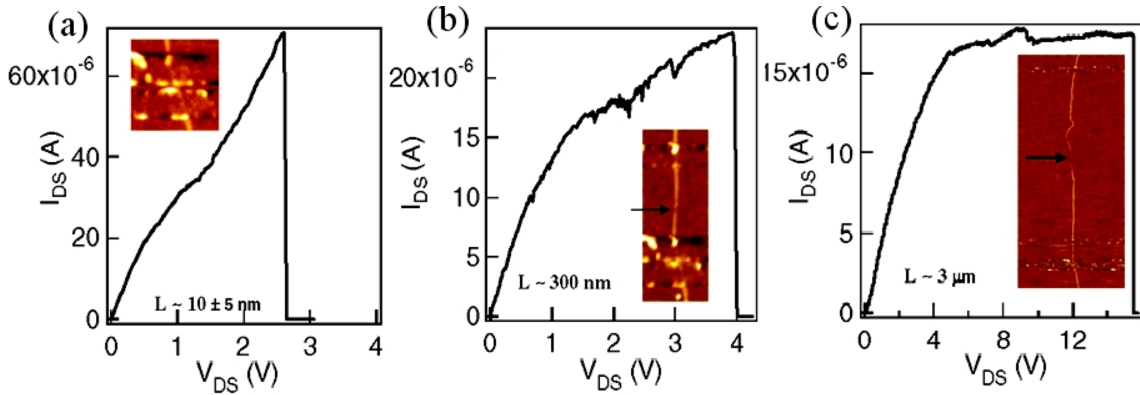

Figure 2.10 Measured increase in break down voltage with increase in length of CNT [52]. Copyright (2013) by The American Physical Society

The other factor to be noticed when illuminating a CNT bundle is the maximum optical power throughput, which varies depending on the structure under illumination. There is no predefined breakdown optical power for a CNT bundle because the

absorption spectrum varies for different chiralities [56, 57]. But as an optimistic limit, one can assume an average intensity of 1mW/μm^2 for continuous mode or 0.4J/cm^2 for pulsed mode [57, 58].

2.4.5. Optical absorption in CNTs

For the purpose of this study, absorption is important in determining the required thickness, diameter, and (n, m) parameter of the CNT. Absorption for simple conventional 3D bulk materials is defined via a coefficient known as the absorption coefficient. However, since CNTs are 1D materials their absorption behavior is rather different because the density of states in 1D material differs from that of 3D bulk materials. For 1D systems, density of states (DOS) tends to be as illustrated as in Fig. 2.11. The spikes in DOS cause singularities in absorption spectrum. These are called Van Hove singularities. These result when energy levels in a 1D system are quantized and only photons with energies equal to the quantization levels are absorbed. The singularity is named S_{ij} if it refers to the difference between “i”th energy level in valence band and “j”th energy level in conduction band in semiconducting CNT; the singularity is termed M_{ij} if it refers to the energy difference between “i”th valence and “j”th conductance energy levels in a metallic CNT. There is also some plasma background absorption, which is added in the spectroscopy of the absorption.

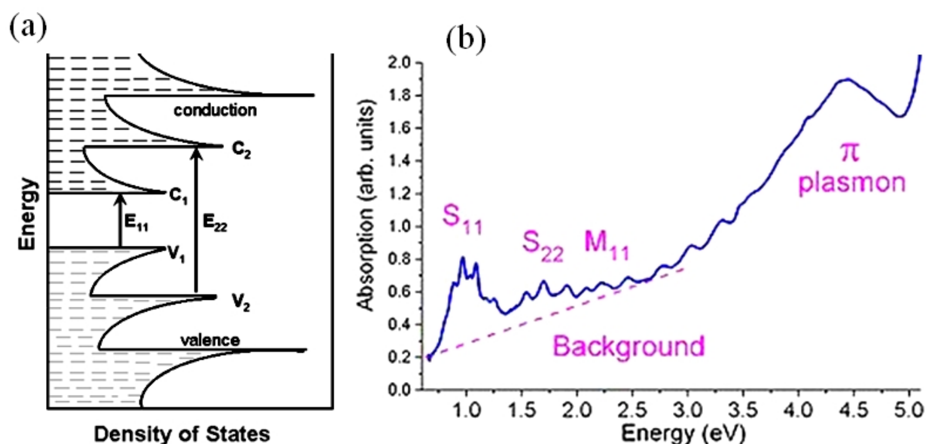

Figure 2.11 (a) DOS for 1D material. (b) Absorption spectrum of CNT bundle. S_{11} and S_{22} are the most noticeable HV singularities

Due to the high aspect ratio (1 nm diameter to 1-10 μm length) in CNTs, the absorption is usually highly anisotropic. Also, CNTs are highly absorbent in IR range

(24×10^4 cm^{-1}) and are even used as IR absorptive coating [59]. However, it's hard to find absolute values for absorption coefficient in CNTs since optical absorption spectrum is rather variant and is thus directly used for characterization. Employing optical absorption enables researchers to find dielectric function and reflectance.

As mentioned previously, many devices require CNT bundles or CNT film instead of a single CNT. Typically, it is difficult to achieve high purities of one type of CNT in the bundle; therefore, there are usually different types of CNTs available in the bundle, which will cause the absorption spectrum singularities to smear or widen. The level of this spreading depends on the level of purification.

Fig. 2.12 shows how this spreading can happen [60]. As shown by the arrow, the spectrum of perpendicular polarization radically differs from that of parallel polarization due to anisotropy of CNT absorption. In order to more conveniently recognize the CNT type or deal with different CNTs absorption spectrum, Kataura plots are used. Kataura plots show the location of Van Hove (VH) singularities for a specific type of CNT.

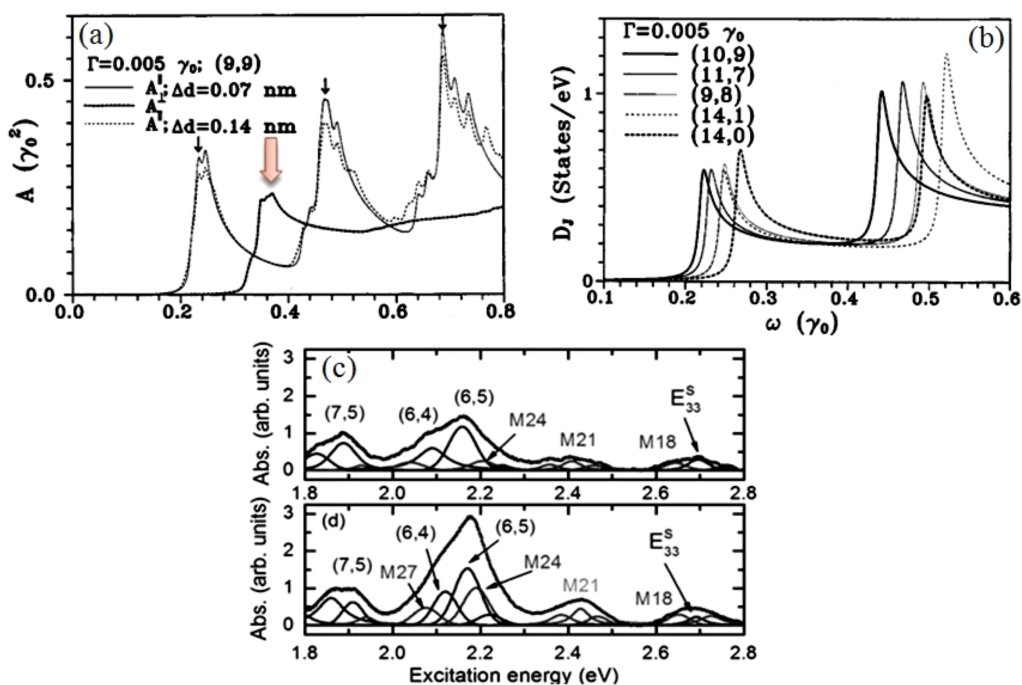

Figure 2.12 (a) Absorption spectrum of CNT for two different diameters differs slightly. (b) Density of states for CNTs with different diameters and (n,m) also differ slightly (c). The peaks are broadened for CNT bundle absorption spectrum [60]. Copyright (2013) by The American Physical Society

Based on this plot, even the type of catalyzer needed to synthesize the CNT can be predicted. The plot demonstrates that CNTs with close diameters tend to have closer

energy band gaps in comparison to CNTs with close indices (n, m); see Fig. 2.13. [61, 62].

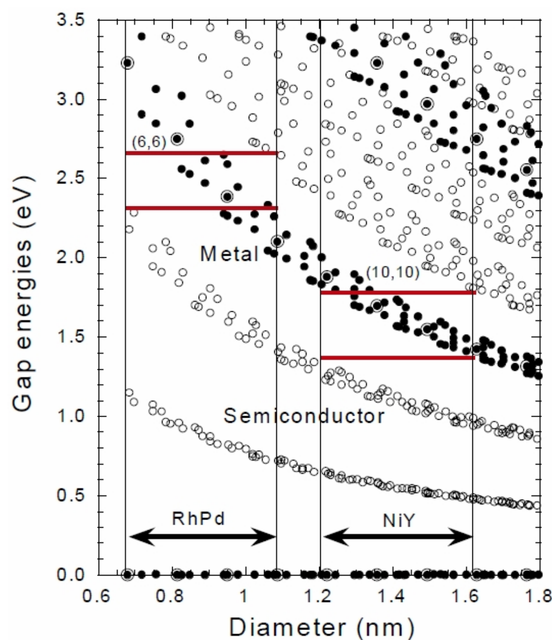

Figure 2.13 Kataura plots for CNT absorption [61]. Copyright (2013) by Elsevier

By extrapolating from these graphs, it can be seen that for wavelength 1550 nm, which will provide photons with 0.8 eV energy, the diameter for S_{11} absorption is approximately 1.05 nm. These indices of CNT fall within the mentioned diameter range: {(8,7), (10,5),(13,0), (12,2), (11,4)}. For S_{22} absorption, the following indices fall within 2.15 nm diameter range, which is the diameter range for S_{22} to be 0.8 eV, {(21,8), (20,9),(17,3), (16,4) ,(26,1), (20,12), (25,3) , (19,12), (19,11) ,(24,4) ,(23,6), (16,15), (23,7) ,(18,13), (22,8)}. By selecting the desired wavelength, the CNT type and diameter is extrapolated from Kataura plots. Finally, the effect of each of the mentioned material parameters is thoroughly studied in chapter 5 (Appendix B and C).

Chapter 3

Optical Excitation Enhancement

The carriers in the valence band of the substrate material are excited to conduction band due to absorption of the incident optical femtosecond pulses. These photocarriers are then collected with the electrode to generate or detect the THz pulses. The optical excitation of the substrate material in THz PCAs is important from two different aspects. The first aspect is its effect on performance of the device and the second is the definitive role of optical excitation on the price of the system. There have been several studies on the effects of the pulse parameters such as pulse width and pulse fluence on PC switch performance [63-68]. We have also addressed some of these effects in Appendix B and C for CNT-based PCAs. This chapter investigates the dynamics of optical excitation at submicron scale. Such investigation is necessary to enhance the efficiency of optical excitation and thus THz PCAs.

On the other hand, due to the high price of Ti-Sapphire femtosecond pulse lasers (~80,000$) and low power of emerging 830 nm Er-doped fs fiber lasers (~30,000$) there is a demand for a more cost effective replacement of the optical excitation source. This has led the researchers to look for materials that can be excited with 1550 nm laser pulses. 1550 nm wavelength is widely used in optical communications, and therefore, many components and sources can be found at a lower price. More specifically, in case of THz photomixing, where two continuous wave lasers can be used, the cost of tunable optical excitation source can be reduced significantly.

3.1 Microscopic study of optical excitation in THz PC switches

Starting with the optical pulse itself, for the most of our experiments we used 810 nm, 30 fs Ti-sapphire pulse laser (from KMLAbs; Kapteyn-Murnane Laboratories). This is one of the common laser pulse sources used for ultra-fast studies [27, 38]. It can provide roughly 140 mw of optical power. The pulse width is also roughly adjustable with

external cavity alignments. We have measured the pulse width with an autocorrelation setup as shown in Fig. 3.1 (a). The detector is connected to an oscilloscope. The two femtosecond pulses come in and out of phase multiple times per second depending on the delay line sweeping time. This will result in first order autocorrelation of the two beams as shown in Fig. 3.1 (b). The full width at half maximum (FWHM) of these autocorrelation signal pulses are 66 fs which corresponds to less than 33 fs optical pulse width [68].

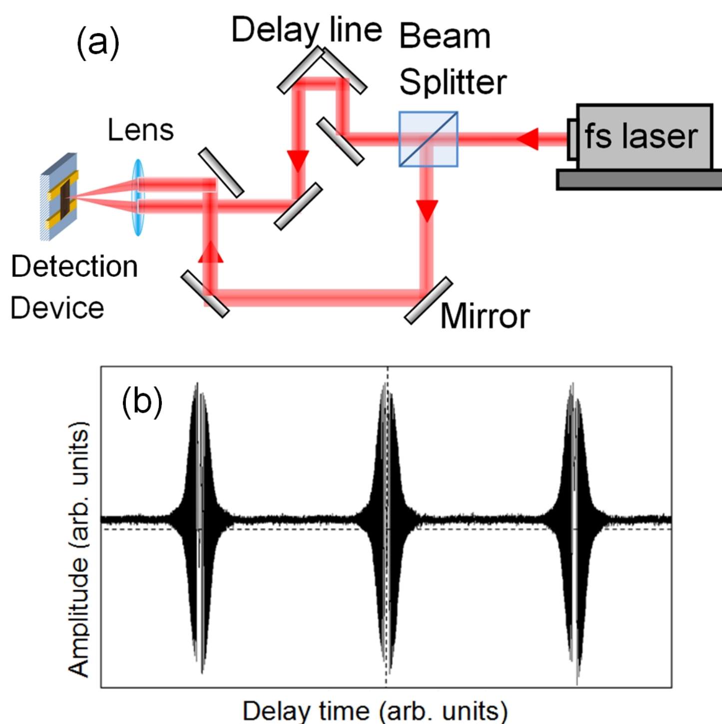

Figure 3.1 (a) Schematic of an autocorrelation measurement setup. The pulse beam is first split into two path one which can be varied. The two paths then reunite on a photodetector to detect the autocorrelation. (b) First order autocorrelation signal detected with an InGaAs detector.

The effects of the width of the femtosecond optical excitation pulse on the performance of PCAs have been investigated [67]. It might be thought that a shorter pulse width would generate a higher bandwidth THz pulse. However, it is found that the optical excitation pulse length has a nonlinear effect in the amplitude and the bandwidth of the generated THz pulse (Fig. 3.2). This is because the time of the photocurrent surge into the dipole is defined by the maxima of the carrier lifetime and optical excitation time. Several studies have reported a significant variation in the THz signal level relative

to the location of the excitation spot in the gap of the antenna. The reason for this peak close to the anode is the larger electron mobility of the LT-GaAs substrate compared to hole mobility. Another factor that causes the peak is short carrier lifetime of the substrate. When the illumination spot is brought closer to the electrode, more carriers will make it to the dipole antenna and thus a larger signal is detected (Fig. 3.3).

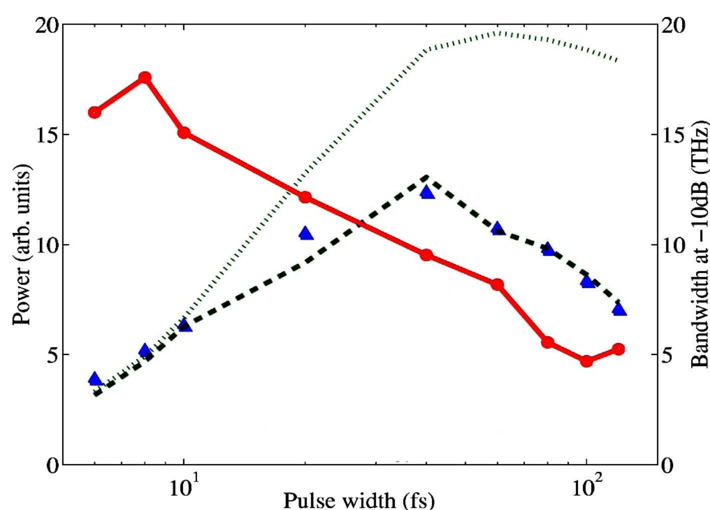

Figure 3.2 (a). Graph of the spectral width at −10 dB as a function of the pump pulse width (circles) at a bias voltage of 30 V. The power of the signal emitted is also plotted with triangles as a function of the pump pulse duration, the dotted curve shows the power calculated taking into account the number of photogenerated carriers and their effective mass, the dashed line includes additionally the effective bias electric field. [67] Copyright (2013) by The American Physical Society

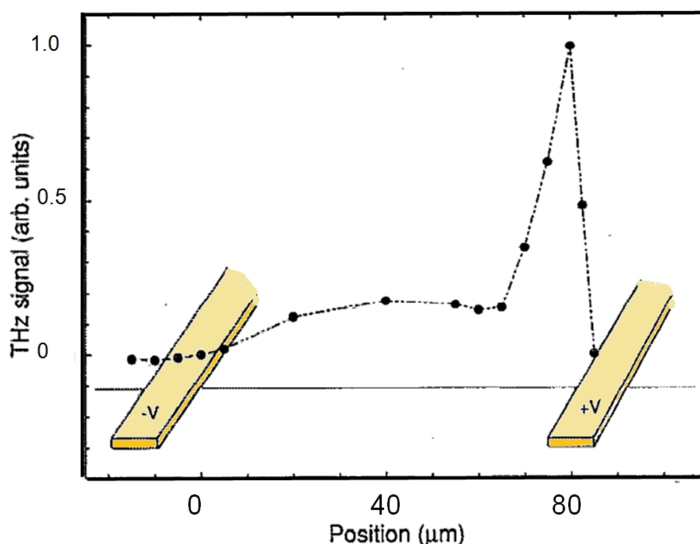

Figure 3.3 Measured THz signal as a function of illumination position for an electrode bias of 67 V (regenerated from [66]) Copyright (2013) by The American Institute of Physics

The so mentioned peak (Fig. 3.3) has not been studied at the microscopic scale. In this chapter we fully investigate this edge effect. The result is a better understanding of the polarization dependence and the optimum spatial illumination profile.

3.2 Polarization effect

The polarization of the excitation pulse has an effect on the efficiency of the optical coupling [65]. As is thoroughly studied in Appendix D, there are two factors that lead to polarization dependent performance. The first factor is the polarization dependent absorption in the substrate material, and the second is the structure of the electrodes. As seen in Appendix D, the optical field distribution at the edges of the electrodes is very sensitive to the polarization. Because of the boundary conditions at the edge of the gold electrodes the polarization variation can significantly affect the concentration of the E-field close to the electrode. Majority of the fast photocarriers are collected right at the vicinity of the electrode. We have measured the effect of the polarization in sensitivity of a THz receiving PCA in the form of a polar plot (Appendix D). The results show 30% improvement in the performance of a THz receiving PCA with merely optimizing the polarization of the excitation pulse.

3.3 Subwavelength edge effect

The strong sensitivity of the signal to edge illumination can be further harvested by shaping the illumination profile right next to the electrode (Appendix D). We have elongated the illumination profile along the edge of one of the electrodes in a stripline THz receiving PCA. Based on our theory and also measurements, more photocarriers are collected with such an elongated profile. The results show up to 100% improvement compared to a conventional circular excitation profile. Such improvement is of significance, since the polarization and illumination profile can be conveniently adjusted with a conventional cylindrical lens and a half-wave plate. In general we did not see any significant change in the detection bandwidth of the device after elongation of the excitation profile or optimization of the polarization. This is expected since the improvement is obtained with sole increase in collected photocarriers right at the edge of the electrodes.

Chapter 4

Structure Enhancement

The gold structure on the substrate is the third key component that defines the performance of a THz PC switch. Different antenna designs are shown in Fig. 4.1. These structures are usually made of gold. There are three main roles that an ideal structure should fulfill; the gold structure (antenna and its gap) should provide a proper bias field to the gap of the antenna; it should allow an efficient optical excitation of the substrate material at the gap, and finally it must efficiently guide and radiate the THz waves. The antenna designs can be similar to other microwave antennas [69], however, the dimensions should be reduced to match the sub-millimetre wavelength of the THz waves. Due to optical excitation, the gap of these antennas can be rather different from that of an ordinary antenna.

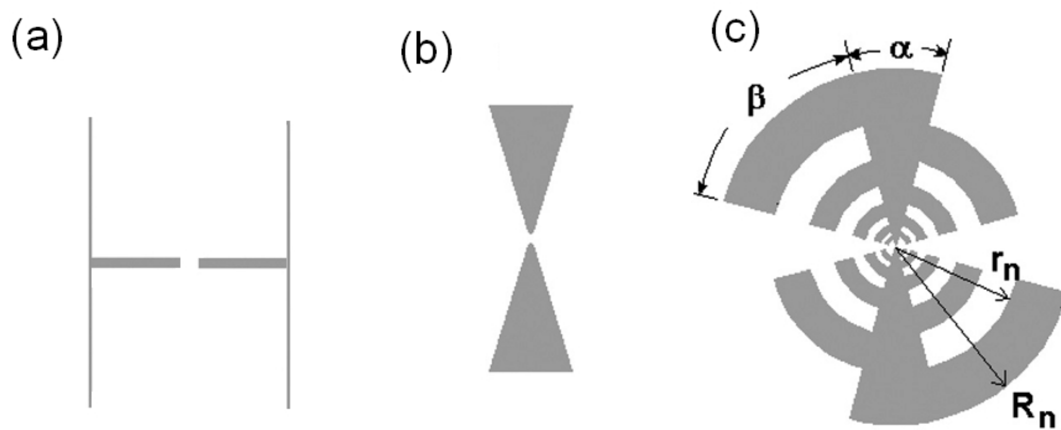

Figure 4.1 Three different microantenna designs for PCAs. (a) a center-fed dipole. (b) a center-fed bowtie antenna. (c) A log-periodic antenna.

The gap of the antenna can play a significant role in the overall performance. There are many studies on THz antennas and waveguides since these are conveniently fabricated with photolithographic techniques. However, for the gap of these antennas the fabrication

challenges are relatively more pronounced due to submicron dimensions. Fig. 4.2 shows five different gap designs. As it will be mentioned in section 4.2 each of these designs has its own advantage and disadvantages.

It is also noteworthy that the optimal designs of transmitter and receiver can be rather different. Although the dipole antenna is the dominant commercial design, there are few studies that have emphasized the differences in the design of a PC switch as a THz receiver and as a THz transmitter [70-72]. We will also address these differences in chapter 5.

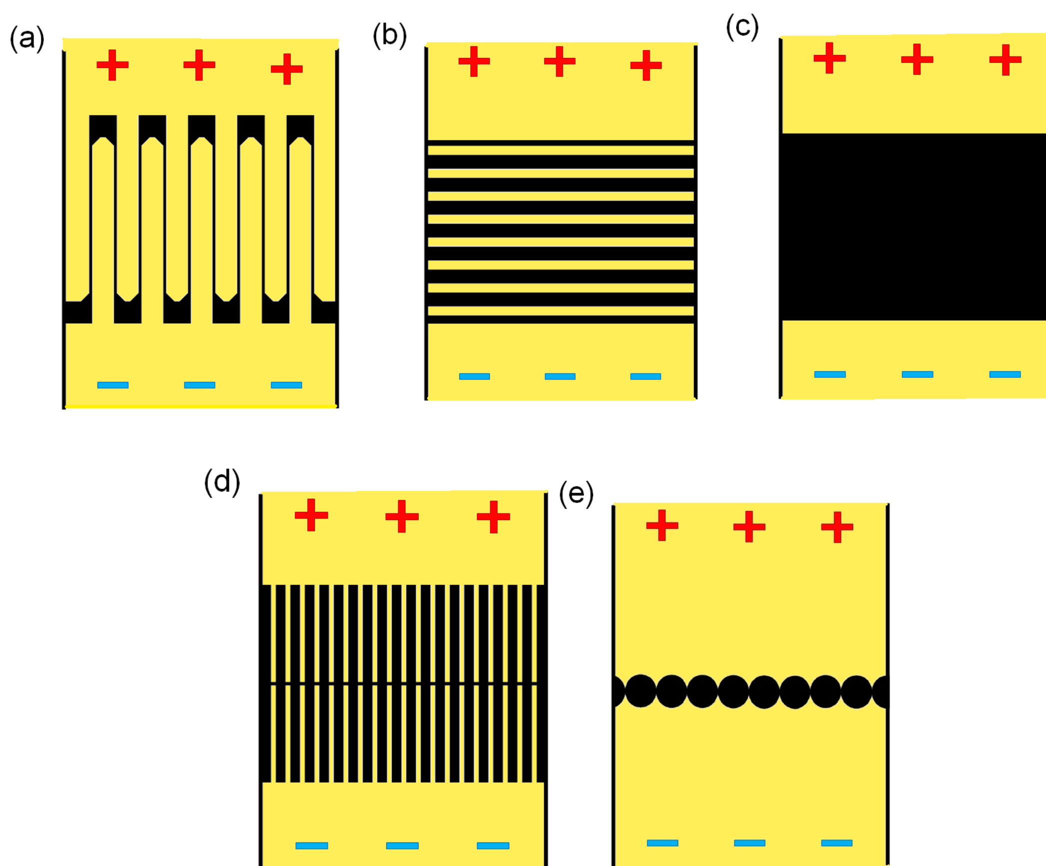

Figure 4.2 Different gap designs. (a) Interlaced structure. (b) Parallel metallic strips in the gap. (c) Ordinary micrometer sized gap. (d) Gap with tip to tip electrodes. (e) Another tip to tip design generated by overlapping circles.

4.1 Enhanced optical coupling through EOT

The continuity equations along with Maxwell equations indicate that there should be an evanescent electromagnetic wave along the surface of the metal-dielectric boundary.

These waves that propagate through the coherent resonances of the surface electrons of the metal (Fig. 4.3) are known as surface plasmon waves or surface plasmon polaritons.

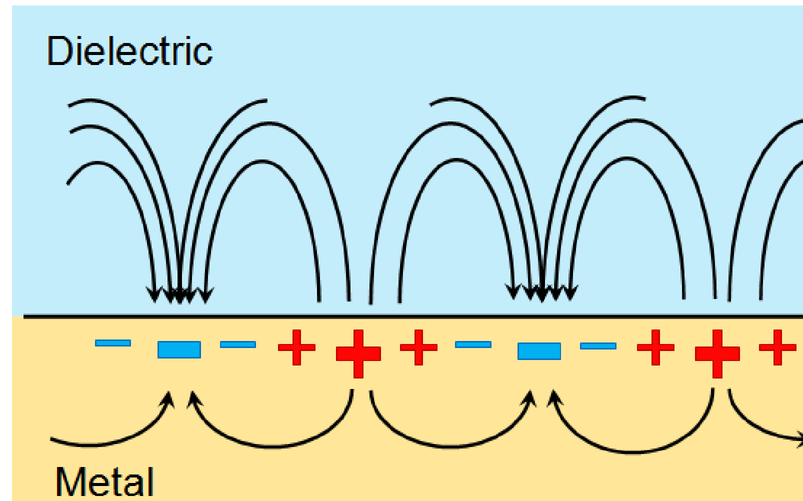

Figure 4.3 surface plasmon waves propagating along the surfacec boundary of a metal and dielectric medium. The wave can be exited either by electrons or photons.

Surface plasmon waves have been engineered to enhance the optical performance of different devices [73-76]. For example, the optical transmission through subwavelength metallic structures was first enhanced by plasmonic resonances at 1998 [73]. Since then the extraordinary optical transmission or EOT along with resonant transmission have been used to improve the performance of many different structures such as subwavelength optical probes [74], Raman spectroscopy, [75, 76] etc. The transmission is enhanced due to plasmonic resonances in the metal surface. These subwavelength structures are usually designed using finite-difference time-domain (FDTD) software. FDTD software applies a grid (with a few nanometer resolution in our studies) and applies a discretized time dependent Maxwell equations to obtain the EM field at given location for a given instance. This numerical method is widely used for field analysis of nonlinear material and subwavelength geometries. Depending on the geometry of the structure, the calculations can be intense and thus resource consuming. A faster method is mode-matching. This analytical method can be used to broadly investigate the transmission and the reflection of a structure. For example we have used both FDTD and mode-matching analysis for an annular aperture (Appendix E). As seen in Appendix E, the results reveal the reflection and transmission peaks of an annular aperture made of

gold. Since the reflection and transmission are studied with variation of geometry, the geometrical parameters can be used to fabricate an aperture with desired transmission peaks. Similar to the same EOT concept, resonant transmissions can be used to enhance the optical coupling of the excitation pulse in the gap of a THz PC switch. Unlike EOT in apertures the resonant transmission between parallel fingers does not have a cut off frequency.

4.2 Nanostructures for THz PC switches

As seen in Fig. 4.2, different structures can be used in the gap to enhance the performance of a PCA. Each structure enhances the performance of the device differently. For example, the interlaced resonant electrodes (Fig. 4.2 (a)) with submicron gap size are very good candidates for THz reception (Appendix F). The periodicity of the parallel electrodes is chosen so that the whole structure is resonant with the incident light. The incident optical excitation pulses excite the surface plasmon of the metallic structure. In the next step the Bragg resonance of the surface plasmon in the periodic structure with the incident light induce a resonant transmission (constructive interference through the gaps). The Bragg condition is found when the surface plasmon waves have constructive interference, that is:

$$\left|\vec{k}_S\right| = \frac{2\pi}{\Lambda} \tag{4.1}$$

where k_s is the wave-vector of the surface plasmon wave in the grating and Λ is the periodicity of the structure. In order to find the wave-vector of the SPP waves of the structure rigorous calculations should be carried out to find the solutions of the Maxwell equations. Therefore, numerical approaches such as FDTD appear more appealing than analytical approaches. This resonant transmission enhances the optical coupling to the substrate. The small gap between the electrodes also intensifies the received field on the gap. And finally, since the electrodes are electrically parallel the current from each one of the fingers is added and this boosts the total detected current level. Unlike the DC dark current (the current detected from the structure when biased in the absence of an optical illumination), a high photocurrent current level is favorably desired in both the receiver and the transmitter. In the other structure with metallic strips in the middle of the gap the voltage is divided across the gap via the metallic strips (Fig. 4.2 (b)) this allows higher

bias voltage with lower dark current which tends to be a more proper design for transmitters (Appendix F). Tip to tip structures (Fig. 4.2 (d), (e)) enhance the performance of the device by boosting the field in the tip of the electrodes [5]. Such structures have only been successfully used as transmitters and it is not known if they equally outperform the ordinary plane gap (Fig. 4.2 (c)) when used as THz receivers. In addition to field intensification and enhancement in optical coupling, it is found that for some of the nanostructures the performance of the device is enhanced by the reduced carrier sweep-out time in the small electrode gaps (Appendix F). This shows that the small gap structure can compensate for some of the undesired properties of the substrate material in the PC switch.

On the other hand the small gaps form meal-insulator-metal structures (MIM) that induce a high capacitance in the gap. Therefore, as in photodetectors with interlaced electrodes there is a trade-off between the efficiency enhancement obtained by using interlaced structure and loss of bandwidth. Based on our results in the case of nanoplasmonic structure on SI-GaAs (Appendix F). the higher bandwidth is comparable to LT-GaAs commercial device while the lower frequency components (<500GHz) are significantly enhanced. Consequently, the overall effect of using nanoplasmonic structure in SI-GaAs is beneficial to the performance of the material that possesses carrier lifetime of over 200 picosecond.

Nanoplasmonic interlaced structures are polarization dependent, in some applications such as integration of the PC switch into small silicon photonic-based optical circuits there might be necessity for polarization independent operation. In such scenario plasmonic nanoislands or circular patterns might be used as a resonant grid to fabricate a polarization independent resonant structure.

4.3 Nanostructures simulation guide

As mentioned earlier in the thesis, we chose Lumerical FDTD software (Lumerical Solution Inc.) among other software (such as Computer Simulation Technology Studio or High Frequency Structural Simulator- HFSS from Ansys). This software is run on Linux on our networked high performance computers and it is well known for its accuracy for simulation of surface plasmon effects in optical frequencies. Since the computer

machines are networked the communication terminal should be used to access the main processing machine. Also more computational resources are available through cloud shared resources.

Since our structure was assumed to be very long in length compared to the dimensions of the gap, we used 2D simulation mode in the software. This significantly shortens the simulation time compared to 3D case of the same structure. The boundary conditions and material library that were used for gold and semiconductors are mentioned in the Appendix F.

After entering the geometry of the structure and assigning the materials in the software, the simulation mesh size is set. We used 1 nm for our structure. This is a fair resolution for a device with >50 nm features. Surely there is a trade-off between the mesh resolution and the simulation time. The operator can always check if the mesh size is proper by checking a higher resolution and comparing the results with prior lower resolution.

Next to structure geometry and simulation mesh, the probes should be inserted into the simulation space. Probes should be placed inside the simulation mesh and their location is very important. We used three E-field probes to measure, transmission, reflection and loss. The reflection probe was placed almost 500 nm above the structure, another probe was placed flush at the surface of the SI-GaAs, and the third one was placed 200 nm deep inside the substrate. As we have discussed in Appendix F, this is necessary to capture the dynamics of the subsurface photocarrier with shorter sweep-out time.

The final step to confirm the simulation settings is to run the simulation once and investigate the generated results. As any other FDTD simulation software, the Lumerical software can provide both the spatial and temporal profile of the E-field. Simulations may not converge if correct parameters are not chosen. The field distribution should be fair to the trained eye of an electrical engineer.

A single run of the simulation is very useful to initially debug the simulation. However, usually it is not enough for designing a nanoplasmonic structure. Geometrical sweeping is necessary to come closer to an optimized design. This requires a code to be loaded into the script feed of the software. We used three different loops to change the periodicity, the gap size, and the thickness of the structure. The results were then stored as a

MATLAB file with the command (lum2mat). These would be data files readable in MATLAB software. The transmission spectrum, subsurface loss spectrum, and reflection spectrum, were plotted along with Field profile as shown in Appendix F. A sample script of the code is given bellow:

```
  P = 300:100:1000;            #Periodicity
TG = 50:50:200;               #Thickness of gold
WG = 50:50:200;               #Width of grooves

for (Pn=1:length(P)) {
for (TGn=1:length(TG)) {
for (WGn=1:length(WG)) {

      Samplename = "Sample_Groove";
      load(Samplename + ".fsp");
      switchtolayout;

      structures;
      select("Ti");
      set("x span", (P(Pn)-WG(WGn))*1e-9);

      select("Au");
      set("x span", (P(Pn)-WG(WGn))*1e-9);
      set("y max", (TG(TGn)+2)*1e-9);

      simulation;
      select("FDTD");
      set("x span", P(Pn)*1e-9);
      # set("background index", Ind(Indn));

      select("mesh");
      set("x span", (P(Pn))*1e-9);
```

```
        # set("y max", (TG(TGn)+20)*1e-9);

        monitors;
        select("Field");
        set("x span", (P(Pn))*1e-9);

        run;
   #    save(Samplename+".fsp");
        name =
"P"+num2str(P(Pn))+"_TG"+num2str(TG(TGn))+"_WG"+num2str(WG(WGn));

        R = transmission("Refl");
        T = -transmission("Trans");
        Loss = 1-(R+T);
        f = getdata("Refl","f");

        mname="Field";
        x_f = getdata(mname,"x");
        y_f = getdata(mname,"y");
        f_f = getdata(mname,"f");
        Ex_f = getdata(mname,"Ex");
        Ey_f = getdata(mname,"Ey");

        savedata(name, R, T, Loss, f,  x_f,y_f,f_f,Ex_f,Ey_f);
        lum2mat(name+".ldf");
        del(name+".ldf");
        #save(name+".fsp");
   }
   }
   }
```

As seen in the code, the three loops sweep the periodicity (in 100 nm steps from 300 nm to 1000 nm), the gap width and thickness (in 50 nm steps from 50 nm to 200 nm).

After running the code and plotting the results with MATLAB the design with best results (highest transmission peak and subsurface loss peak at optical excitation wavelength) is chosen and fabricated.

Chapter 5

Assessment of Enhanced THz PC switches

Potentially advantageous materials and structures were discussed in previous chapters. In this chapter we assess the proposed devices in theory and practice. We address the fabrication process and challenges for each device. The performance of each device is presented in a quantitative comparative fashion.

5.1 GaBiAs as THz transmitting PC switch (Appendix A)

THz transmitting PCAs can significantly benefit from the higher mobility of GaBiAs. Here (Appendix A) we have investigated and demonstrated the superb performance of GaBiAs material for transmitting THz pulses. We have fabricated similar dipole antennas on GaBiAs substrate with different Bi percentage and different annealing conditions. Experimental results suggest that the Bi droplets and surface defect clusters act as carrier recombination hubs. These clusters significantly shorten the lifetime at the surface and thus increase the emission frequency. It is revealed that the annealing time has a significant effect on the generated photocurrent and emitted THz amplitude. On the other hand the photocarriers at the depth of the substrate (less than 1μm below the surface) accelerate for a longer time. These photocarriers also generate a significant secondary peak with sub-THz (< 600 GHz) frequency components. Finally, after substrate optimization, the transmission amplitude is further increased by means of plasmonic strips (Appendix A). The results provide a new insight to the dynamics of GaBiAs for THz PC switching and also shows 68% improvement in efficiency and 0.5 THz increase in bandwidth relative to a commercial LT-GaAs based PCA with similar structure.

5.2 GaBiAs as THz receiving PC switch

Unlike the case of THz transmission, the dual carrier lifetime behaviour in GaBiAs substrates can be considered as a disadvantage in the receiver. Duality in carrier lifetime

distorts the detected pulses. Fig. 5.1 shows such distortions. As seen in this Figure, regardless of its amplitude, the detected signal for GaBiAs doesn't exactly follow the original green curve. The amplitude is higher relative to similar structures we fabricated on LT-GaAs and SI-GaAs substrates. A commercial PC switch was used as the emitter and the experimental setup is a heterodyne TDTS setup as explained in Appendix F. The green curve shows the original profile of the THz pulse detected with an identical commercial device (BATOP PCA-800 nm) at the receiver. The commercial device has a 10 µm dipole with 5 µm gap and our devices have 20 µm dipole with 5 µm center gap on 1.8% GaBiAs substrate. The commercial device has increased amplitude because of AR coating and optimization of growth and fabrication conditions.

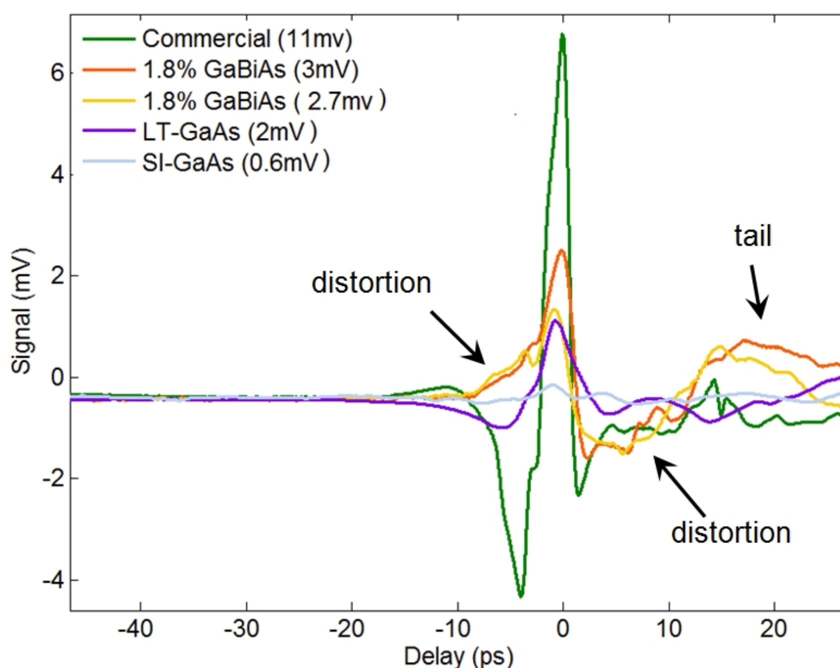

Figure 5.1 Temporal profile of a THz pulse detected with different devices. The substrate used for the red and orange curve are grown separately but are aimed to be similar.

The distortion might be improved by further etching the surface of the GaBiAs sample with HCL solution. Also a thicker layer of crystalline GaBiAs (~1 µm) on top of the GaAs wafer might help to unify the carrier lifetime. Unfortunately it is very challenging to grow a uniform thick crystalline GaBiAs layer. Bi has a tendency to generate droplets and this tendency increases with increase in Bi percentage and layer thickness [44-46]. The induced distortion may be less of an issue for a continuous wave application where the temporal profile of the THz signal is not required. This result exemplifies the

differences between the role of the substrate material in THz transmitting PCA and THz receiving PCA.

5.3 CNTs as a material for THz transmitting PC switch (Appendix B)

As mentioned previously, carbon nanotubes (CNT) have many appealing parameters for THz PC switching. In a systematic assessment of CNT parameters for THz PC switching a two order of magnitude improvement in output THz power is predicted compared to an LT-GaAs PCA (Appendix B). The assessment approach starts with the input optical power; it calculates the photocarrier density, photoconductivity modulation, and the resulted output THz emission considering the equivalent circuit model of the PCA. As it appears, the number of free photocarriers is the key parameter for engineering the SWNT film, and this number is affected by many parameters such as incident power, carrier lifetime, film optical density, filling factor, etc. These are dependent on SWNT chirality, purity, and fabrication method (Appendix B). Estimation of number of free photocarriers in the SWNT film can then be followed by using the proper model to derive the conductivity of the film. We used Drude-Smith model along with Monte Carlo simulations to estimate the conductivity of partially aligned CNTs. The modified Drude-Smith model that is used in our study is a form of Drude-based model that assumes that electrons are bouncing randomly in between the heavier stationary ion cores in the crystal structure of the material. While it is yet controversial whether Drude-Smith can accurately predict the photoconductivity of nanomaterials [78]. Previous studies indicate a reasonable agreement between the measured results and theoretical predictions of the modified DS model for carbon nanotubes [48]. Competing theories are effective medium based theories (EMT) that are generally used to explain the macroscopic conductivity of a composite material through homogenization formulas. In our study the conductivity of the CNT film (CNTs are spanning in the PC switch gap) is modulated by the optical pump. These modulations are fed into a circuit model that predicts the THz output power (Appendix B). The key results of this analysis are the extensive dynamics that are revealed with the so told systematic approach. The approach is also extendable to other emerging nanomaterials such as GaAs nanowires. The dynamics further explains the

effect of fabrication quality – parameters like CNT alignment and contact resistance – in the output THz power.

5.4 CNTs as a material THz receiving PC switch (Appendix C)

CNTs have been already used for detecting THz with bolometric approaches. However, CNTs can also be used in the context of THz receiving PCAs. Theoretical assessment of the dynamics of a THz receiving PC switch shows relative improvement compared to LT-GaAs (Appendix C). The enhancement in THz detection is, however, less notable compared to a THz emitting CNT-based PC switch due to notable imaginary part of THz conductivity in CNT bundles. While it is thought that the mobility is a linear function of carrier scattering time ($\mu = e\tau_S / m^*$) it should be emphasized that that is not indeed the case since the effective mass itself is a nonlinear function of the carrier scattering time, temperature, conduction band shifts and chirality. Therefore, although counter intuitive, it is possible to have a material with higher mobility and shorter carrier lifetime. The effective mass of the electron is found to play an important role in the CNT-based receiver PC switch (Appendix C).

We have extended the systematic approach used in the case of the transmitter to the case of the receiver. The main results of this study are the discovery of significant differences in the performance and dynamics of the CNTs as a material for THz receiving PCA. Compared to a THz transmitting PCA, there are two key differences in the receiver: first, the gap bias is provided by the received THz pulse, and second, the outcome of the device is a current. As seen in Appendix C, this sets new restrictions on the desired properties of the gap material (in this case CNTs) which requires a more sophisticated analysis of the high frequency photoconductance.

5.5 Fabrication of CNT-based PC switches

As addressed in Appendix B and C, fabrication of a CNT-based PCA is significantly challenging. CNTs of the appropriate chirality must be aligned; the tubes must be spanning the gap with sufficient density to absorb the optical excitation. This must be realized with good electrical contact to the electrode (gold) structure. Since these are common challenges with CNTs, many fabrication remedies exist to overcome these

challenges [79-80]. Fig.5.2 (a) shows a schematic view of a THz PC switch. An example of CNTs deposited across a 5 μm gap at the feed point of a 20 μm dipole antenna on SiO_2/Si wafer is shown in Fig. 5.2 (b). Fabrication challenges include: CNT alignment and precise deposition location, CNT film thickness control, CNT purity and quality, and CNT to electrode contact. All these challenges should be properly over come for the device to operate. The micrometer sized dipole structure makes the CNT deposition even more challenging (Fig. 5.2 (a)). Therefore, in another fabrication attempt we used striplines that required less deposition precision (Fig. 5.3 (a)).

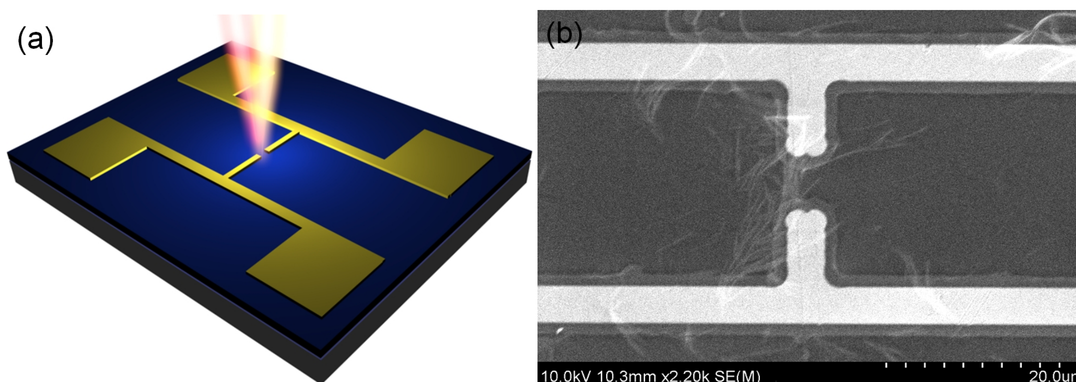

Figure 5.2 (a) Schematic view of a THz photomixer; (b) Fabrication challenges for deposition of SWNTs in the gap of adipole.

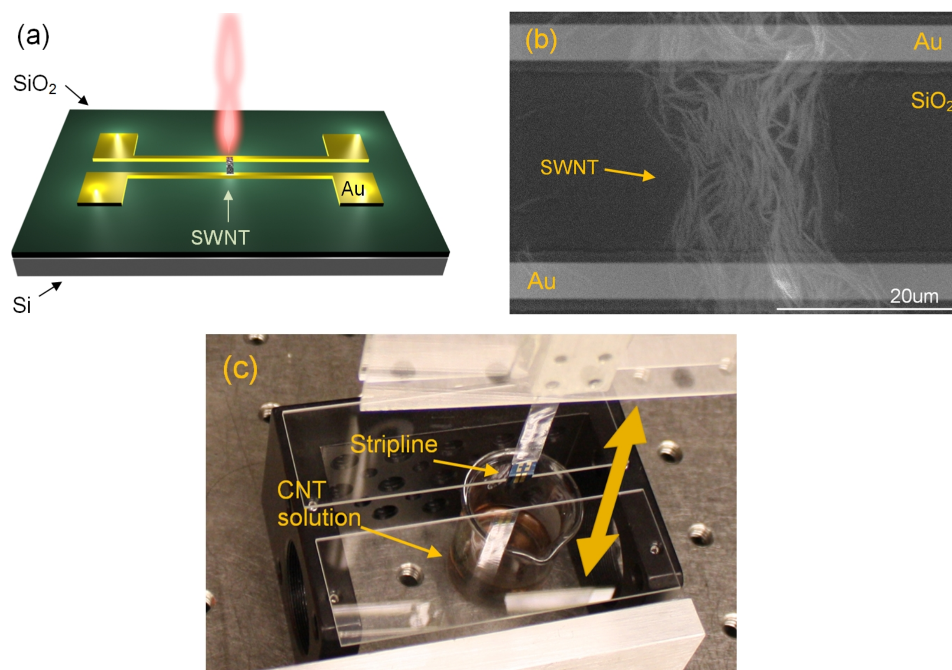

Figure 5.3 (a) Schematic view of a THz PC switch with stripline structure. (b) The CNT bundles are seen in the SEM image of the device. (c) Slip-stick deposition method. The sample is dipped into the CNT solution.

The slip-stick method was used for deposition (Appendix B). In this deposition method the PC switch that is made on SiO_2/Si wafer (float zone intrinsic Si, resistivity> 20000 ohm-cm, 4" diameter and 525 μm thickness,100 nm oxide layer on the top, <111> orientation) is vertically submerged halfway into a CNT solution (Fig. 5.3 (b)). The sample is either moved out very slowly or is left in the solution for a long time to allow the CNTs to sit in the gap along to the solution surface. We realized more photosensitive devices with this approach. However, we could not easily repeat the process and we were unable to measure THz output for our devices.

In our last attempt we used electrophoresis method on glass substrates. The electrophoresis method provides thicker CNT films in the gap, however due to presence of metallic CNTs in the solution; we noticed that there is a significant increase in dark current for samples made through electrophoresis. The PC switch gap should be filled with uniformly distributed semiconducting CNTs. This level of sophistication in synthesis may be realized with more complex approaches such as on wire lithography technique and assembly inside anodized aluminum oxide pores [81].

5.6 Nanostructured THz receiving PC switches on GaAs (Appendix F)

As seen in previous chapters replacement of substrate material is possible yet expensive. For instance, the growth of GaBiAs requires an MBE machine and takes time. CNT deposition also appeared to be very challenging. In the case of optical excitation the procedure was very straight forward (also almost free of cost) but the achieved enhancement was relatively minor (30%) and limited to specific designs. Engineering the gap structure can provide a significant (orders of magnitude) enhancement for lower cost.

Previous studies have used such periodic gap designs on GaAs and LT-GaAs. Interlaced structures with micron scale dimensions were conventionally used [25, 70]. While interlaced structures can provide a larger optical absorption area, the reflection from the gold fingers themselves decreases the external quantum efficiency of the device. Using resonant nanoantennas to compensate for such reduction in external quantum efficiency on SI-GaAs was recently proposed by Park et al on SI-GaAs at 2012 and then followed by Jarrahi et al. on LT-GaAs in the same year [89, 90]. The first work used resonant nanoantenna to reduce the reflection even below the reflection level of plain SI-

GaAs and the second study uses nanoplasmonic contacts to spread the active region. We fabricated nanointerlaced structures on semi-insulating GaAs wafers that both efficiently couple the light into the structure and collect the photocarriers within ps time scale. The structure consists of a 600 nm interlaced fingers with separation gaps of 100 nm and thickness of 100nm. The gaps are made with focused ion beam that sputter the gold with Ga ions. This can damage the surface of the SI-GaAs beneath. To sputter just the gold and not the GaAs beneath several tests are performed on redundant corners of the same sample to choose the right parameters for the machine. At our settings (mentioned in Appendix F) 10-15 nm of excess sputtering can be expected. The effects of such surface damages are investigated with reflection extinction ratio measurements (Appendix F). The chip is used in a TDTS set up and the results are compared to commercial THz receiving PCA and conventional dipoles on GaAs and LT-GaAs substrates. It is found that such short gap width can cover for long carrier lifetime in GaAs and provide up to 40 fold increase relative to a dipole on GaAs (Appendix F). The structure is designed in such a way to trigger the resonant transmission via Bragg interferences. This significantly enhances the optical coupling through such small gaps. Although the capacitive effect of closely packed electrodes limits the bandwidth of the device, the amplitude magnification is significant enough to outperform the current dipoles on LT-GaAs material. FDTD simulations and reflection measurements are performed to prove the presence of resonant transmission.

Chapter 6

Conclusions

In this dissertation we studied and enhanced the performance of THz PCAs. The enhancement was achieved experimentally through three different approaches.

We studied new substrate materials such as GaBiAs and carbon nanotubes. GaBiAs is a novel bulk material that is shown to outperform conventional LT-GaAs. We thoroughly experimented with GaBiAs for THz PC switching. We found a significant increase in efficiency by tuning the annealing temperature (0.5 THz increase in bandwidth and 68% increase in amplitude compared to commercial devices). Optimal annealing and growth conditions were discussed. In the case of CNTs, our theoretical study shows that a CNT-based PC switch can potentially outperform the LT-GaAs THz transmitting PCAs by more than an order of magnitude. It was found that such level of enhancement is not achievable in case of THz receiving PC switch due to large imaginary part of THz conductivity in CNT films. Fabrication challenges remain significant for CNT-based THz PCAs.

In chapter 3 the dynamics of PC switch response to optical excitation polarization and illumination profile were studied down to the submicron level. It was found (both experimentally and theoretically) that an electrode edge effect plays an important role in the efficiency of the substrate absorption. This insight to subwavelength illumination dynamics was further used to engineer a nanostructure that can repeatedly use the mentioned subwavelength edge effect. The result was a novel PC switch with resonant interlaced electrodes. In this PC switch, the surface plasmon of the nanostructured gold electrodes resonates with the incident light. This triggers a phenomenon known as resonant transmission which renders the gold electrodes as semi-transparent to the optical excitation pulse. Therefore, high optical transmission along with submicron gap width significantly enhances (over 2 orders of magnitude enhancement was measured in case of GaAs) the performance of the system.

Chapter 7

Main Contributions and Future Concepts

The main contributions of this work are as follows:

- Investigation and fabrication of GaBiAs-based PCAs. We found that GaBiAs can outperform conventional LT-GaAs both in terms of amplitude and bandwidth.
- Extensive study of carbon nanotubes as THz transmitting photomixers. The systematic approach used in this study can be applied to other nanomaterials.
- Systematic analysis of CNTs for THz reception. This study covers an extensive theoretical approach which predicts the performance of SWNTs for THz reception with variation in each of the parameters.
- Optimization of optical excitation for THz PCAs in terms of illumination profile and polarization state. The submicron field analysis presented in this work sets guideline for electrode design.
- Engineering of nanoapertures such as an annular aperture for extra ordinary optical transmission (EOT). FDTD simulations along with mode-matching technique are used to engineer the geometry of a nanoaperture in a gold film. This provided an insight for designing plasmonic electrodes with nanostructures.
- Presentation of plasmonic resonant electrodes on ordinary GaAs and GaBiAs substrate which out performs the conventional commercial designs by two fold and 68% repectively.

This work was done in parallel with other projects in THz applications and waveguides. On these parallel projects which were led by Dr. Hamid Pahlevaninezhad we had following contributions [82-85]:

- Exploring the two-wire waveguide as a low-loss, non-dispersive waveguide for THz frequencies,

- introducing and evaluating two novel slot-line structures for THz waves,
- presenting experimental verification for the two-wire waveguide and the slot-line,
- applying two-wire waveguides in spectroscopic analysis of cosmetic products.

The research work presented in this dissertation resulted in the following publications and patent:

1. **B. Heshmat**, M. Masnadi, R. B. Lewis, T. Tiedje, R. Gordon and T. E. Darcie "Nanoplasmonic GaBiAs-based Terahertz Photoconductive Switch" submitted.
2. **B. Heshmat,** H. Pahlevaninezhad, T.E. Darcie "Optical efficiency enhancement methods for terahertz receiving photoconductive switches", submitted.
3. **B. Heshmat**, H. Pahlevaninezhad,Y. Pang, M. Masnadi, R. Lewis, T. Tiedje, R. Gordon and T. E. Darcie "Nanoplasmonic Terahertz Photoconductive switch on GaAs" **Nano Letters**, accepted.
4. **B. Heshmat**, H. Pahlevaninezhad, and T. E. Darcie, "THz detection with carbon nanotube-based photoconductive switches: An assessment of capabilities and limitations", **IEEE Photonics Journal**, Vol. 4, Iss. 3, pp.970 (2012).
5. **B. Heshmat**, H. Pahlevaninezhad, M. C. Beard, C. Papadopoulos and T.E. Darcie, "Single wall carbon nanotubes as base material for THz photomixing: A Theoretical study from input power to output THz emssion", **Optics Express,** Vol. 19 Issue 16, pp.15077-15089 (2011).
6. **B. Heshmat**, D. Li, T. E. Darcie, R. Gordon, " Tuning plasmonic resonances of an annular aperture in metal plate " **Optics Express**, Vol. 19, Iss. 7, pp. 5912–5923 (2011).
7. **B. Heshmat**, H. Pahlevaninezhad, T.E. Darcie, "Efficient low-power autocorrelation measurement with carbon nanotube photoconductors", CLEO, pp. JW2A.3, 2012.
8. **B. Heshmat**, H. Pahlevaninezhad, T.E. Darcie and C. Papadopoulos, "Evaluation of carbon nanotubes for THz photomixing", IEEE Int. Conference, 2010.

9. H. Pahlevaninezhad, **B. Heshmat,** L. Smith, T.E. Darcie "Highly-sensitive THz spectroscopy using two-wire waveguides", submitted.
10. H. Pahlevaninezhad, **B. Heshamt**, and T. E. Darcie, “Efficient terahertz slot-line waveguides,” **Optics Express** 19, 26, B47-B55, 2011.
11. T. E. Darcie, H. Pahlevaninezhad, and **B. Heshmat**, “Efficient terahertz waveguides,” 37th ECOC, OSA, 2011 (Invited paper).
12. H. Pahlevaninezhad, T. E. Darcie, and **B. Heshmat**, “Advances in terahertz waveguides and transmission lines,” SPIE Proceeding 8007, 80070S, 2011 (Invited paper).
13. H. Pahlevaninezhad, **B. Heshmat**, and T. E. Darcie, “Advances in terahertz waveguides and sources,” **IEEE Photonic Journal**, Breakthrough in Photonics 2010, 2011 (Invited paper).
14. **B. Heshmat**, H. Pahlevaninezhad, J. Zhang, and T. E. Darcie, “Dynamics of noise in THz photomixers as a receiver sensor,” Optical Sensors, OSA, 2011.
15. H. Pahlevaninezhad, T. E. Darcie, and **B. Heshmat**, “Two-wire waveguide for terahertz,” Optics Express 18, 7, 7415-7420, 2010.
16. H. Pahlevaninezhad, **B. Heshmat**, and T. E. Darcie, “Modeling terahertz heterodyne detection based on photomixing,” IEEE Int. Conference, 113-116, 2010.
17. T. E. Darcie, H. Pahlevaninezhad, **B. Heshmat**, and J. Zhang, “Advances in terahertz technology,” 23rd Annual Meeting of IEEE Photonics Society, 435-436, 2010 (Invited paper).

- B. Hehmat, T. E. Darcie, R. Gordon, “Nanointerlaced plasmonic PC switch on GaAs,” US Provisional Patent, Oct. 2012.

7.1 Future works

THz technology has the potential to revolutionize the way we live. Here we would like to take a step further and include some of the concept sketches that may be worth further investigation and investment. The first concept is an optics-free THz PC switch (Fig. 7.1 (a)). The form factor and the cost of a time domain THz spectroscopy (TDTS) setup can

be significantly improved with plasmonic antenna arrays [86]. Here you can see three pieces of the setup integrated into one.

This significantly reduces the cost. The efficiency and maintenance can also be improved with guiding the THz beam at the back of the chip with spoof plasmonic technique. This eliminates hours of fine alignment necessary in conventional THz TDTS.

Subwavelength apertures with resonant transmission at THz frequencies can be used to do high resolution THz microscopy. The only problem is a necessity for a high power THz illumination of the sample which is solved by quantum cascade lasers. There is an integrated continuous wave THz photomixer or some other THz detector at the back of the probe shown in the sketch in Fig. 7.1 (b). The sample may be illuminated from the top or bottom depending on its thickness.

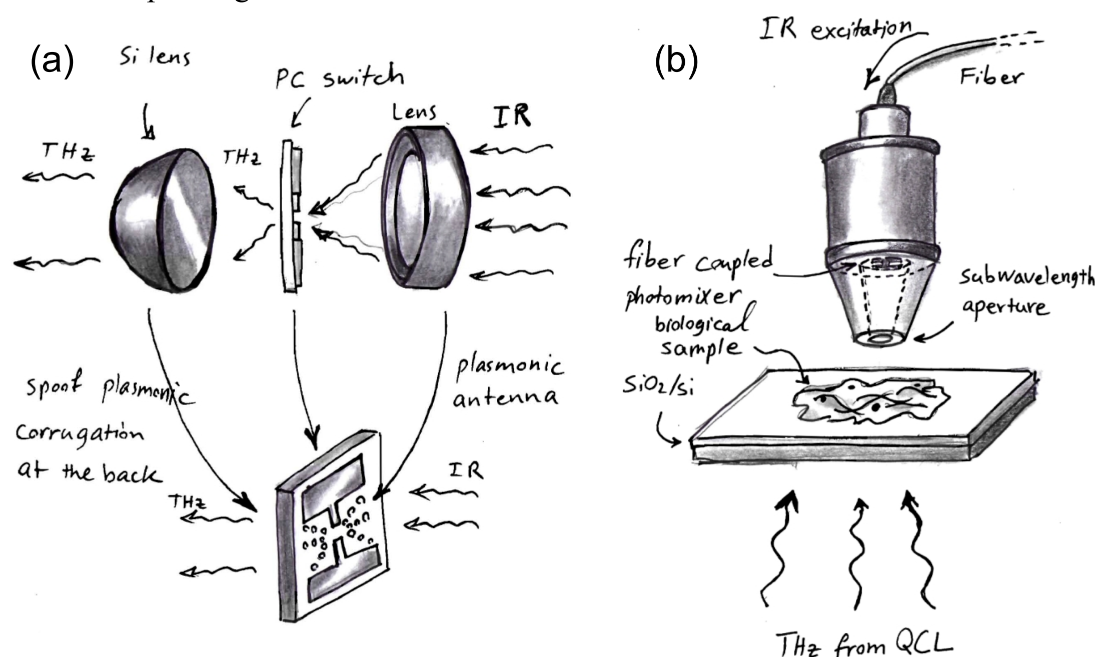

Figure 7.1 (a) Concept sketch of an all in one THz PC switch. (b) Concept sketch of a THz microscopy setup. The probe uses enhanced resonant transmission.

Recently emerging liquid silver ink printing [87] has a good potential for THz waveguides and cables. Figure 7.2 (a) shows a concept slotline waveguide that has been printed on a flexible tape; there are sub-mm holes in the gap of the waveguide to let it interact with the sample. This would be highly promising for in-vivo spectroscopy and probing applications. Another concept (sketch in Fig. 7.2 (b)) is resonant hole arrays and metal grids for THz sensory applications. With longer length of the THz wavelength, the

metal grids [88] and holes can have larger geometry. This allows higher fluid flow and enables THz spectroscopy of different gases and maybe even human breath.

There are many novel concepts for further enhancement in THz technology and engaging this technology in real-life applications. We believe that the realization of these concepts depend on the interest of the researcher community and investment of industrial sections.

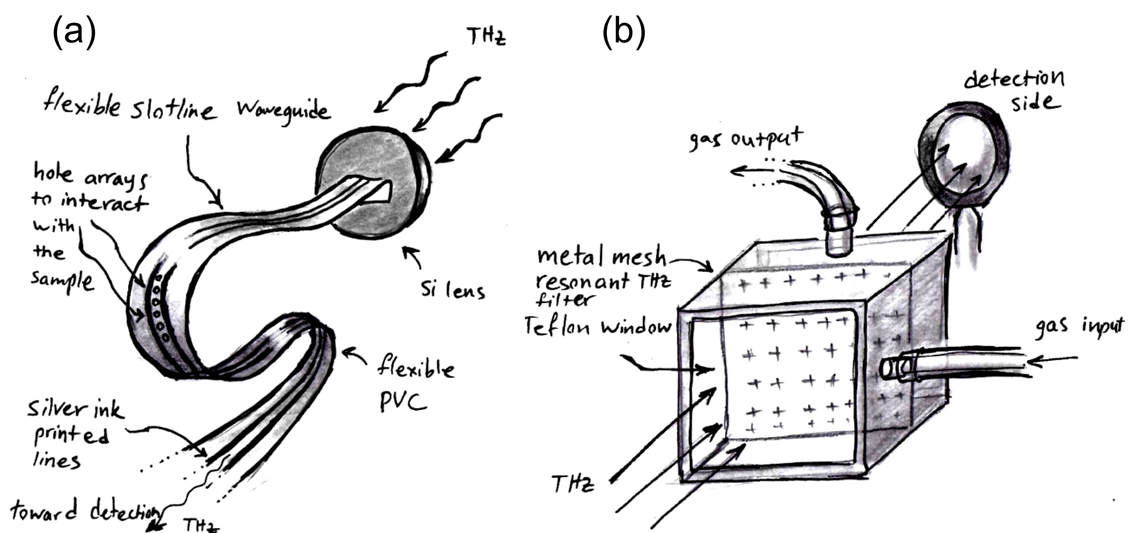

Figure 7.2 (a) Concept sketch of a THz flexible slotline-probe. The gold lines are printed with cheap silver printing technology. (b) A metal mesh that is resonant in THz is used for gas sensing.

Bibliography

1. B. J. Thompson, *Terahertz Spectroscopy: Principles and applications*, CRC Press, pp.125 (2008).
2. D. Dragoman, and M. Dragoman, “Terahertz fields and applications,” Progress in Quantum Electronics Vol. 28, pp.1-66 (2004).
3. Online THz data base: http://thzdb.org/
4. R. M. Woodward, V. P. Wallace, R. J. Pye, B. E. Cole, D. D. Arnone, E. H. Linfield, and M. Pepper, “Terahertz pulse imaging of ex vivo Basal cell carcinoma,” Journal of Investigative Dermatology, Vol. 120, pp.72-78 (2003).
5. V. P. Wallace, A. J. Fitzgerald, S. Shankar, N. Flanagan, R. Pye, J. Cluff, and D. D. Arnone, “Terahertz pulse imaging of Basal cell carcinoma ex vivo and in vivo,” British Journal of Dermatology, Vol. 151, pp.424-432 (2004).
6. P. Parkinson, J. L. Hughes, Q. Gao, H. H. Tan, C. Jagadish, M. B. Johnston, and L. M. Herz, “Transient terahertz conductivity of GaAs nanowires,” Nano Letters, Vol. 7, pp.2162–2165 (2007).
7. G. Ya. Slepyan, M. V. Shuba, and S. A. Maksimenko, “Terahertz conductivity peak in composite materials containing carbon nanotubes: Theory and interpretation of experiment,” Physical Review B, Vol. 81, pp.205423 (2010).
8. D.J. Paul "The progress towards terahertz quantum cascade lasers on silicon substrates" Laser and Photonics Review, Vol. 4, pp.610 (2010).
9. T. Kataoka, K. Kajikawa, J. Kitagawa, Y. Kadoya, and Y. Takemura, “Improved sensitivity of terahertz detection by GaAs photoconductive antennas excited at 1560 nm” Applied Physics Letter, Vol. 97, pp.201110 (2010).
10. K. A. McIntosh, E. R. Brown, K. B. Nichols, O. B. McMahon, W. F. Dinatale, and T. M. Lyszczarz, “Terhahertz measurements of low-temperature-grown GaAs photomixers coupled to resonant-planar antennas,” Applied Physics Letter, Vol. 69, pp. 3632 (1996).
11. H. Lu, R. S. Singh, A. C. Gossard, and E. R. Brown, “Towards a 1550 nm InGaAs Photoconductive Switch,” Optics Letter, Vol. 34, pp.3068-3070 (2009).
12. H. Chen, W. J. Padilla, J. M. O. Zide, S. R. Bank, A. C. Gossard, A. J. Taylor, and R. D. Averitt, “Ultrafast optical switching of terahertz metamaterials fabricated on ErAs/GaAs nanoisland superlattices,” Optics Letter, Vol. 32, pp.1620-1622 (2007).

13. K. L.Vodopyanov, M. M. Fejer, X. Yu, J. S. Harris, Y. S. Lee, W. C. Hurlbut, V. G. Kozlov, D. Bliss, C. Lynch, “Terahertz wave generation in quasi-phase-matched GaAs,” Applied Physics Letter, Vol. 89, pp.141119 (2006).

14. K. L. Vodopyanov, “Optical generation of narrow-band terahertz packets in periodically-inverted electro-optic crystals: conversion efficiency and optimal laser pulse format”, Optics Express, Vol. 14, pp.2263-76 (2006).

15. B. Fischer, M. Hoffmann, H. Helm, G. Modjesch and P. U. Jepsen, “Chemical recognition in terahertz time-domain spectroscopy and imaging,” Semiconductor Science and Technology, Vol. 20, pp.S246, 2005.

16. S. Preu, G. H. Döhler, S. Malzer, L. J. Wang, and A. C. Gossard, “Tunable, continuous-wave Terahertz photomixer sources and applications,” Journal of Applied Physics, Vol. 109, pp.061301 (2011).

17. Industrial THz detectors: http://www.terahertz.co.uk/index.php?option=com_content&view=article&id=236&Itemid=530

18. V. V. Popov, D. M. Ermolaev, K. V. Maremyanin, N. A. Maleev, V. E. Zemlyakov, V. I. Gavrilenko, and S. Yu. Shapoval, “High-responsivity terahertz detection by on-chip InGaAs/GaAs field-effect-transistor array,” Applied Physics Letter, Vol. 98, pp.153504 (2011).

19. D. Stehr, C. M. Morris, C. Schmidt, and M. S. Sherwin, “High-performance fiber-laser-based terahertz spectrometer,” Optics Letter, Vol. 35, pp. 3799-3801 (2010).

20. S. Verghese, K. A. McIntosh, and E. R. Brown “Optical and terahertz power limits in the low temperature-grown GaAs photomixers” Applied Physics Letter, Vol. 71, pp.2743 (1997).

21. K. Ma, R. Urata, A. B. Miller, and J. S. Harris “Low-Temperature growth of GaAs on Si used for ultrafast photoconductive switches,” IEEE Journal of Quantum Electronic, Vol. 40, pp.800-804 (2004).

22. M. Haiml, U. Siegner, F. M. Genoud, U. Keller, M. Luysberg, R. C. Lutz, P. Specht, and E. R. Weber, “Optical nonlinearity in low-temperature-grown GaAs: Microscopic limitations and optimization strategies,” Applied Physics Letter, Vol. 74, pp.3134 (1999).

23. S. Rihani, R. Faulks, H. E. Beere, I. Farrer, M. Evans, D. A. Ritchie, and M. Pepper, “Enhanced terahertz emission from a multilayered low temperature grown GaAs structure,” Applied Physics Letter, Vol. 96, pp.091101, (2010).

24. H. Tanoto, J. H. Teng, Q. Y. Wu, M. Sun, Z. N. Chen, S. A. Maier, B. Wang, C. C. Chum, G. Y. Si, A. J. Danner and S. J. Chua, “Greatly enhanced continuous-

wave terahertz emission by nano-electrodes in a photoconductive photomixer," Nature Photonics, Vol. 6, pp.121-126 (2012).

25. E. R. Brown, F. W. Smith and K. A. McIntosh, "Coherent millimeter-wave generation by heterodyne conversion in low-temperature-grown GaAs photoconductors" Applied Physics Letter, Vol. 73, pp.1480 (1992).

26. Batop optoelectronics: http://www.batop.com/information/PCA_infos.html

27. T. Liu, G. Lin, Y. C. Lee, and S. C. Wang, M. Tani, H. H.Wu, C. L. Panb, "Dark current and trailing-edge suppression in ultrafast photoconductive switches and terahertz spiral antennas fabricated on multi-energy arsenic-ion-implanted GaAs," Journal of Applied Physics, Vol. 98, pp.013711 (2005).

28. L. Duvillaret, F. Garet, J. Roux, and J. Coutaz, "Analytical modeling and optimization of terahertz time-domain spectroscopy experiments using photo switches as antennas," IEEE Journal of Selected Topics in Q. Electronic, Vol. 7, pp. 615-623 (2001).

29. S. Wei, Y. Chenghai, Z. Jun, W. Ke, "Analysis of terahertz radiation under nonlinear mode of photoconductive switches," Proceeding of SPIE, Vol. 6625, pp. 66251L (2008).

30. M. C. Beard, G. M. Turner, and C. A. Schmuttenmaera, "Subpicosecond carrier dynamics in low-temperature grown GaAs as measured by time-resolved terahertz spectroscopy," Journal of Applied Physics, Vol. 90, pp.5915-5923 (2001).

31. M. Haiml, U. Siegner, F. Morier-Genoud, U. Keller, M. Luysberg, P. Specht, E. R. Weber, "Femtosecond response times and high optical nonlinearity in beryllium-doped low-temperature grown GaAs," Applied Physics Letter, Vol. 74, pp.1269-1271 (1999).

32. M. C. Beard, G. M. Turner, and C. A. Schmuttenmaer "Transient photoconductivity in GaAs as measured by time-resolved terahertz spectroscopy" Physical Review B, Vol. 62, pp. 15764-15777 (2000).

33. Toptica Photonics AG, http://www.toptica.com/applications/terahertz_applications/terahertz_applications_spectroscopy.html

34. Menlosystemns: http://www.menlosystems.com/home/products/thz-solutions/tera8-1-thz-antennas-overview.html,m47

35. R. N. Kini, L. Bhusal, A. J. Ptak, R. France, and A. Mascarenhas, "Electron Hall mobility in GaAsBi," Journal Applied Physics, Vol. 106, pp.043705 (2009).

36. G. Pettinari, A. Patanè, A. Polimeni, M. Capizzi, X. Lu, and T. Tiedje, “Bi-induced p-type conductivity in nominally undoped Ga(AsBi),” Applied Physics Letter, Vol. 100, pp.092109 (2012).

37. F. W. Smith, H. Q. Le, V. Diadiuk, M. A. Hollis, A. R. Calawa, S. Gupta, M. Frankel, D. R. Dykaar, G. A. Mourou, and T. Y. Hsiang, “Picosecond GaAs-based photoconductive optoelectronic detectors,” Applied Physics Letter, Vol. 54, pp.890 (1989).

38. M. Tani, S. Matsuura, K. Sakai, and S. Nakashima, “Emission characteristics of photoconductive antennas based on low-temperature-grown GaAs and semi-insulating GaAs,” Applied Optics, Vol. 36, pp. 7853-7859 (1997).

39. Si properties: http://www.ioffe.rssi.ru/SVA/NSM/Semicond/Si/electric.html

40. GaAs properties: http://www.ioffe.ru/SVA/NSM/Semicond/GaAs/electric.html

41. S. Gupta, M. Y. Frankel, J. A. Valdmanis, J. F. Whitaker, and G. A. Mourou, F. W. Smith and A. R. Calawa, “Subpicosecond carrier lifetime in GaAs grown by molecular beam epitaxy at low temperatures,” Applied Physics Letter, Vol. 59, pp. 3276 (1991).

42. B. Cechavicius, R. Adomavicius, A. Koroliov and A. Krotkus, “Thermal annealing effect on photoexcite carrier dynamics in $GaBi_xAs_{1-x}$,” Semiconductor Science and Technology, Vol. 26, pp.085033 (2011).

43. E. H. C. Parker, *The Technology and Physics of Molecular Beam Epitaxy*, Plenum Press, New York (1985).

44. D. A. Beaton, “Electronic States and Transport in GaN_xAs_{1-x} and $GaAs_{1-x}Bi_x$” Ph. D. thesis submitted at UBC, pp.22 (2011).

45. X. Lu, D. A. Beaton, R. B. Lewis, T. Tiedje, and M. B. Whitwick, “Effect of molecular beam epitaxy growth conditions on the Bi content of $GaAs_{1-x}Bi_x$,” Applied Physics Letter, Vol. 92, pp.192110 (2008).

46. V. Pačebutas, K. Bertulis, A. Bičiūnas, and A. Krotkus, “Low-temperature MBE-grown GaBiAs layers for terahertz optoelectronic applications,” Physics Status Solidi C, Vol., pp.2649–2651 (2009).

47. M. M. Shirazi, D. A. Beaton, R. B. Lewis, X. Lu and T. Tiedje, “Surface reconstructions during growth of $GaAs_{1-x}Bi_x$ alloys by molecular beam epitaxy,” Journal of Crystal Growth, Vol. 338, pp. 80-84 (2012).

48. M. C. Beard, J. L. Blackburn, and M. J. Heben, “Photogenerated free carrier dynamics in metal and semiconductor single-walled carbon nanotube films,” Nano Letters,Vol. 8, pp.4238-4242 (2008).

49. H. Terrones and M. Terrones, “Curved nanostructured materials”, New Journal of Physics, Vol. 5, 126.1–126.37 (2003).

50. S. Reich, C. Thomsen, J. Maultzsch, *Carbon nanotubes basic concepts and physical properties*, Wiley (2004).

51. R. Waser, *Nanoelectronics and Information Technology: Advanced electronic materials and novel devices*, Wiley-VCH, chapter 19, pp. 473-496, (2003).

52. A. Javey, J. Guo, M. Paulsson, “High-field quasiballistic transport in short carbon nanotubes,” Physical Review Letter, Vol. 92, pp.1068041-1068044 (2004).

53. L. Shang, L. Ming, S. Tanachutiwat, W. Wang, “Analyzing Mixed Carbon Nanotube Bundles: A current density study,” IEEE Int. Symposium on Circuits and Systems, pp.173-176 (2008).

54. S. Subash and M. H. Chowdhury, “Mixed carbon nanotube bundles for interconnect applications,” International Journal of Electronics, Vol. 96, pp.657-671 (2009).

55. T Dürkop, B. M. Kim and M. S. Fuhrer, “Properties and applications of high-mobility Semiconducting nanotubes,” Journal of Physics: Condensed Material, Vol. 16, pp.553-580 (2008).

56. T. Nakamiya, T. Ueda, T. Ikegami, F. Mitsugi, K. Ebihara and R. Tsuda, “Pulsed laser heating process of multi-walled carbon nanoubes film,” Dimond and Related Material, Vol. 17, pp.1458-1461 (2008).

57. I. Hsu, M. T. Pettes, A. Bushmaker, M. Aykol, L. Shi and S. B. Cronin, “Optical absorption and thermal transport of individual suspended carbon nanotube bundles,” Nano Letters, Vol. 9, pp.590-594 (2009).

58. H. Huang, R. Maruyama, K. Noda, H. Kajiura, and K. Kadono, “Preferential destruction of metallic single-walled carbon nanotubes by laser irradiation,” Journal of Physical Chemistry B, Vol. 110, pp.7316-7320 (2006).

59. H. Sun, X. Shen, S. Cui and N. Xu, “Preparation and absorption properties in near infrared wavelength of carbon nanotubes/Acrylate coatings,” Chinese Journal of Chemical Physics, Vol. 20, pp.784-788 (2007).

60. M. F. Lin, “Optical spectra of single-wall carbon nanotube bundles,” Physical Review B., Vol. 62, pp.13153-13159 (2000).

61. L. Dai, *Carbon nanotechnology*, Elsevier, Academic Press, pp.261 (2006).

62. http://www.photon.t.u-tokyo.ac.jp/~maruyama/kataura/kataura.pdf

63. W. R. Donaldson, “Effect of illumination uniformity on GaAs photoconductive switches,” IEEE Journal of Quantum Electronic, Vol. 30, pp.2866-2875 (1994).

64. S. Verghese, K. A. McIntosh, and E. R. Brown, “Optical and terahertz power limits in the low-temperature-grown GaAs photomixers,” Applied Physics Letter, Vol. 19, pp.2743-2745 (1997).

65. M. Ruff, D. Streb, S. U. Dankowski, S. Tautz, P. Kiesel, B. Knupfer, M. Kneiss, N. Linder, and G. H. Dohlera, U. D. Keil "Polarization dependence of the electroabsorption in low-temperature grown GaAs for above band-gap energies," Applied Physics Letter, Vol. 68, pp.2968-2970 (1996).

66. S. E. Ralph and D. Grischkowsky, "Trap-enhanced electric fields in semi-insulators: The role od electrical and optical carrier injection," Applied Physics Letter, Vol. 59, pp.1972-1974 (1991).

67. E. C. Camus, J. L. Hughes, and M. B. Johnston, "Three-dimensional carrier-dynamics simulation of terahertz emission from photoconductive switches," Phy. Review B **71**, pp.195301 (2005).

68. C. Rulliere, *Femtosecond laser pulses; Principles and experiments*, Springer, pp.202 (2003).

69. S. Preu, G. H. Döhler, S. Malzer, L. J. Wang, and A. C. Gossard, "Tunable, continuous-wave terahertz photomixer sources and applications," J. Applied Physics, Vol. 109, pp.061301 (2011).

70. Y. Chen, S. Williamson, and T. Bock, F. W. Smith and A. R. Calawa, "375 GHz bandwidth photoconductive detector," Applied Physics Letter, Vol. 16, pp.1984-1986 (1991).

71. J. E. Bjarnason and E. R. Brown, "Sensetivity measurement and analysis of an ErAs: GaAs coherent photomixing transceiver," Applied Physics Letter, Vol. 87, pp. 124105 (2005).

72. M. Walther, G. S. Chambers, Z. Liu, M. R. Freeman, and F. A. Hegmann, "Emission and detection of terahertz pulses from a metal-tip antenna," JOSA B, Vol. 22, pp. 2357-2365 (2005).

73. T. W. Ebbesen, H. J. Lezec, H. F. Ghaemi, T. Thio, and P. A. Wolff, "Extraordinary optical transmission through subwavelength hole arrays," Nature, Vol. 391, pp.667-669 (1998).

74. A. W. Bargioni, A. Schwartzberg, M. Cornaglia, A. Ismach, J. J. Urban, Y. Pang, R. Gordon, J. Bokor, M. B. Salmeron, D. F. Ogletree, P. Ashby, S. Cabrini, P. J. Schuck, "Hyperspectral nanoscale imaging on dielectric substrates with coaxial optical antenna scan probes," Nano Letters, Vol. 11, pp.1201-1207 (2011).

75. A. Marimuthu, P. Christopher, and S. Linic, "Design of plasmonic platforms for selective molecular sensing based on surface-enhanced Raman spectroscopy," Journal of Physical Chem. C, Vol. 116, pp.9824-9829 (2012).

76. X. Zhu, J. Zhang, J. Xu, and D. Yu, "Vertical plasmonic resonant nanocavities," Nano Letters, Vol. 11, pp.1117-1121 (2011).

77. A. R. Boccaccini, J. Cho, J. A. Roether, B. J. C. Thomas, E. J. Minay, M. S. P. Shaffer, “Electrophoretic deposition of carbon nanotubes,” Elsevier: Carbon, Vol. 44, pp.3149-3160 (2006).

78. H. Altan, F. Huang, J. F. Federici, A. Lan and H. Grebel “Optical and electronic characteristics of single walled carbon nanotubes and silicon nanoclusters by tetrahertz spectroscopy” Journal of Applied Physics, Vol. 96, pp. 6685-6689 (2004).

79. M. Y. Zavodchikova, A. G. Nasibulin, T. Kulmala, K. Grigoras, A. S. Anisimov, S. Franssila, V. Ermolov, and E. I. Kauppinen, “Novel carbon nanotube network deposition technique for electronic device fabrication,” Physics stat. sol. (b), Vol. 245, pp.2272–2275 (2008).

80. M. Engel, J. P. Small, M. Steiner, M. Freitag, A. A. Green, M. C. Hersam, and P. Avouris, “Thin film nanotube transistors based on self-assembled, aligned, semiconducting carbon nanotube arrays,” ACS Nano, Vol. 2, pp.2445-2452 (2008).

81. B. Y. Lee, K. Heo, A. L. Schmucker, H. J. Jin, J. K. Lim, T. Kim, H. Lee , K. Jeon , Y. D. Suh , C. A. Mirkin, and S. Hong, “Nanotube-bridged wires with sub-10 nm gaps,” Nano Letters, Vol. 12, pp 1879-1884 (2012).

82. H. Pahlevaninezhad, B. Heshmat and T. E. Darcie "Efficient THz slotline waveguides" Optics Express, Vol. 19, pp.B47-B55 (2011).

83. H. Pahlevaninezhad, B. Heshmat, T. E. Darcie, "Advances in THz technology", IEEE Photonics, Vol. 3, pp. 307-310 (2011).

84. H. Pahlevaninezhad, T. E. Darcie, B. Heshmat, "Two-Wire waveguide for terahertz", Optics Express, Vol. 18, pp.7415-7420 (2010).

85. H. Pahlevaninezhad, B. Heshmat, T. E. Darcie, "Logitudal guided wave THz spectroscopy", submitted.

86. R. Blanchard, S. V. Boriskina, P. Genevet, M. A. Kats, J. Tetienne, N. Yu, M. O. Scully, L. D. Negro, and F. Capasso “Multi-wavelength mid-infrared plasmonic antennas with single nanoscale focal point,” Optics Express, Vol. 19, pp. 22113-22124 (2011).

87. B. Y. Ahn, D. J. Lorang, J. A. Lewis, “Transparent conductive grids via direct writing of silver nanoparticle inks,” Nanoscale, Vol. 3, pp.2700-2702 (2011).

88. A. M. Melo, M. A. Kornberg, P. Kaufmann, M. H. Piazzetta, E. C. Bortolucci, M. B. Zakia, O. H. Bauer, A. Poglitsch, and A. M. P. Alves da Silva, “Metal mesh resonant filters for terahertz frequencies,” Applied Optics, Vol. 47, pp.6064-6069 (2008).

89. C. W. Berry, M. R. Hashemi, M. Unlu, and M. Jarrahi, "Significant radiation enhancement in photoconductive terahertz emitters by incorporating plasmonic contact electrodes," Published online at http://arxiv.org/abs/1209.1680, (2012).

90. S. G. Park, K. H. Jin, M. Yi, J. C. Ye, J. Ahn, K. H. Jeong, "Enhancement of terahertz pulse emission by optical nanoantenna," ACS Nano, Vol. 6, pp.2026−2031 (2012).

Appendix A: GaBiAs THz PC switches: substrate optimization and nanoplasmonic gap design

(2012, To be bubmitted)

GaBiAs THz PC Switches: Substrate Optimization and Nanoplasmonic gap design

Barmak Heshmat†, Mostafa Masnadi Shirazi‡, Ryan Lewis‡, Thomas Tiedje†, Reuven Gordon† and Thomas Edward Darcie†*

†*Department of Electrical and Computer Engineering, University of Victoria, V8P 5C2, Victoria, BC Canada*

‡*Department of Electrical and Computer Engineering, University of British Columbia, V6T 1Z4, Vancouver, BC, Canada*
**rgordon@uvic.ca*

Abstract: THz photoconductive switches made on low-temperature-grown GaAs offer hyper THz bandwidth only with low output power. GaBiAs is a more recent material that is shown to be promising for THz photoconductive switching. Unlike LT-GaAs, the optimized growth and annealing condition are yet unknown for GaBiAs. We have optimized GaBiAs material for THz photoconductive switching. Measurements for different annealing temperatures and Bi percentages have lead us to an optimized recipe for GaBiAs-based PC switches. GaBiAs is found to have a significantly higher ratio of photocurrent to dark current (over 2 orders of magnitude higher in some cases) compared to conventional LT-GaAs, which is promising for optical switching applications. We have used this capability along with nanoplasmonic resonant optical transmission to significantly enhance the performance of the device. The results show 68% increase in emitted power and 0.5 THz increase in bandwidth relative to commercial PC swithces.

Keywords: Nanoplasmonics; Terahertz Transmission; GaBiAs; Photoconductive switches.

Photoconductive switches were first demonstrated by Austin et al. in 1979[1] as a mean to switch an electrical path with an optical trigger. The concept gradually became widespread as faster materials enabled switching speeds that could not be realized with conventional electronics. Switches fabricated on Si[1] and later on GaAs enabled switching in the GHz frequency range[2]. Low-temperature grown GaAs (LT-GaAs) substrates increased that into the THz range[3] such that the picosecond surge of electrons to the switch could be used as a source of THz radiation when coupled to a microantenna.

Today THz photoconductive antennas (PCAs) are used widely as THz sources for different applications including imaging and spectroscopy[4, 5]. Along with commercialization of these applications, the demand for more efficient PCAs has increased. Therefore, ongoing research focuses on increasing the output power and bandwidth of these devices. Different materials such as carbon nanotubes[6] and ion-implanted GaAs and quantum-well based substrates[7-9] have been investigated for more efficient THz switches. Mobility and carrier lifetime of the material are two main factors in determining the efficiency of the PCA. Mobility directly increases the amplitude of the radiation and carrier lifetime affects the bandwidth[10].

Recent incorporation of Bi (a group V poor metal) in semiconducting GaAs has been shown to shrink the bandgap and affect the carrier density in GaAs[11, 12]. The resulting GaBiAs has a higher mobility than LT-GaAs[11] and can therefore be used as a more efficient substrate for THz PC switches[13-15]. Incorporation of a high percentage of Bi in GaBiAs is found to be challenging due to the large size of Bismuth molecules. Optimized annealing and growth conditions for THz PC switching have not yet been fully explored[16, 17].

In addition to development of new substrate materials, nanoplasmonics has been found to enhance the performance of PCAs[12]. Nanoplasmonics (i.e. engineering of surface plasmons at the nanometer scale for enhancement of electro-optical devices performance) has been used in various electro-optical devices ranging from subwavelength probes to solar cells[18, 19]. It has been demonstrated that periodic interlaced structures with 100 nm gaps between the electrodes increase the efficiency of a GaAs-based PCA by 40 times[20]. This enhancement occurs due to increased optical coupling through resonant transmission and faster carrier sweep-out in the 100 nm gaps.

This study thoroughly investigates GaBiAs material as a substrate material for a THz emitting PCA. First, optimized growth and annealing conditions are found through emission measurements in a THz heterodyne setup. Next, utilizing nanoplasmonics, we fabricated a resonant nanostructure with 100 nm gaps to further enhance the efficiency of the device. The results of the resonant nanostructure are compared to that of LT-GaAs and a commercial PCA. A 68% improvement in emission and a 0.5 THz increase in

bandwidth is found. The study also provides an insight into the photo-physics of the GaBiAs material.

To measure the THz emission from different PCAs we used a heterodyne THz setup as shown in Fig. 1 (a). The transmitter and receiver PCAs are pumped by a 810 nm Ti-Sapphire laser with 30 fs pulses at 80 MHz repetition rate. A retro-reflector is translated along a precision stage to vary the phase of the generated THz pulse. When the incident THz pulse overlaps with the optical excitation pulse in the THz receiving PCA, a small current is induced in the receiver and measured by a lock-in amplifier.

The conventional design of the micro antenna is a subwavelength dipole with a 5-10 μm gap in the middle. The dipole in the THz emitting PCA is biased such that when the optical excitation pulse hits the gap a sharp current pulse propagates though the dipole arms causing the center-fed microantenna to radiate (Fig. 1 (b)). The gap structure is conventionally chosen as a blank space to let the optical excitation pulse into the substrate. However, due to short carrier lifetime of the photocarriers, only the electrons that are excited in a close proximity with the edge of the electrodes can be collected with the dipole. In this work we have replaced this gap structure with a nanoplasmonic structure shown in Fig. 1 (c). The structure is a periodic set of 600 nm gold strips separated with 100 nm gaps.

In our previous studies[20] we have shown that plasmonic strips with 100 nm gaps and periodicity of 700 nm have resonant enhanced transmission at 830 nm optical excitation when made on GaAs. This has been confirmed both by reflection measurements and FDTD analysis[20]. Neglecting the refractive index difference between GaBiAs and GaAs, we fabricated a similar resonant structure on GaBiAs. The 100 nm gap width induces faster carrier sweep-out time (~1 ps) in GaBiAs and this enhances the peak emission. Considering the saturation velocity for electrons in GaAs (1.3×10^7 cm/s), the 100 nm gap width is just about the distance that is needed to mimic the sub-picosecond carrier lifetime in LT-GaAs by nanoplasmonic structure on GaBiAs.

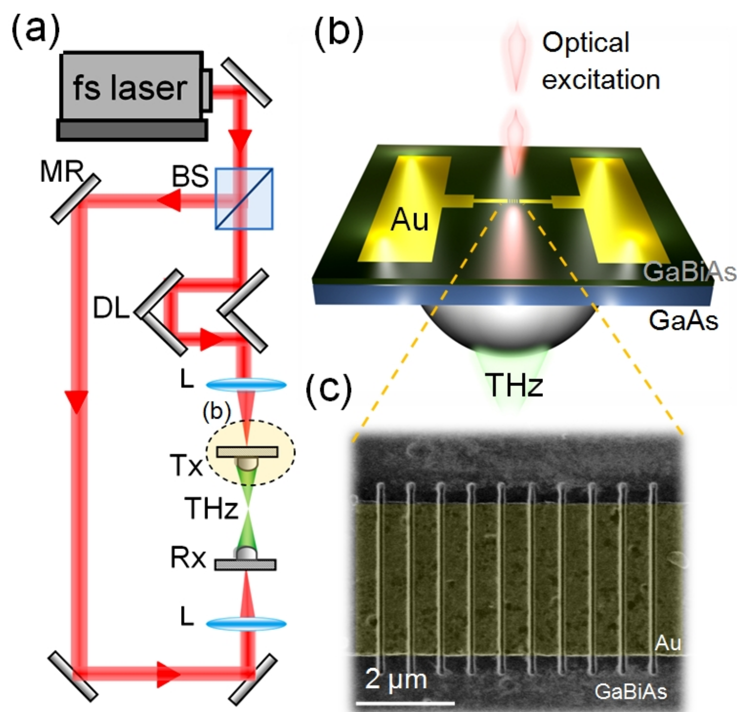

Fig. 1. (a) Schematic of the THz heterodyne setup. Abbreviations used: MR = Mirror, BS = Beam splitter, DL = Delay line, L= Lens, Rx = THz receiving PCA, Tx = THz transmitting PCA, and fs laser = femtosecond Ti-Sapphire pulse laser. The shaded area in the ellipse is enlarged in (b). Silicon lenses are used at the back of the PCAs to focus the THz beam. (b) 3D schematic of the plasmonic THz transmitting PCA. (c) SEM image of the plasmonic strips in the middle of the PCA gap. The gaps are 100 nm and the metallic strips are 600 nm wide, and fabricated on a GaBiAs substrate.

In addition to nanoplasmonic structures, ordinary short dipole structures (20 µm dipole with 5-6 µm center gap, 5 µm width, and 100 nm Au/5 nm Ti thickness) were fabricated on different GaBiAs substrates to find the optimized recipe for the substrate material. A key factor in the electrical efficiency of an optical switch is the ratio between dark and photo current (Iphoto/Idark) or On-Off Current Ratio (OOCR). The photocurrent or "On" current is the total average DC current measured when the infrared light is illuminating the gap and the dark current or "Off" current is the DC current measured when there is no illumination. Fig. 2 (a) shows the measurement results for the OOCR in different GaBiAs samples (orange curve with triangle marks) and LT-GaAs samples (light blue curve with circle marks). It is noticed that for lower temperatures the GaBiAs OOCR is far superior to LT-GaAs. This can be of great significance to THz switching applications where leakage current can either increase the power consumption of the switch or can be considered as a noise inducing factor. The graph clearly shows a decreasing trend and a

minimum at 670°C for the GaBiAs OOCR with increase in the annealing temperature. A minimum is also present in the LT-GaAs curve at around 600°C. The orange and blue shaded areas show that the OOCR decreases for both the LT-GaAs and the GaBiAs with increase in the annealing time. The dark current indirectly affects the performance of the device by pushing the subwavelength gold structures closer to their current breakdown limit. As long as the dark current does not cause device malfunctioning, the emission amplitude is only influenced by the net photocurrent (Iphoto-Idark) and carrier lifetime. The measured net photocurrent is depicted in Fig. 2 (b). In this figure an opposing trend is observed for the LT-GaAs and the GaBiAs materials. While GaBiAs shows a maximum in net photocurrent, the same parameter shows a minimum for LT-GaAs. The results are also compared to a commercial device (BATOP PCA-800 nm) that shows a slightly improved OOCR and net photocurrent compared to our LT-GaAs samples. This is expected due to antireflection coating of the commercial device that enhances the optical coupling efficiency of the gap.

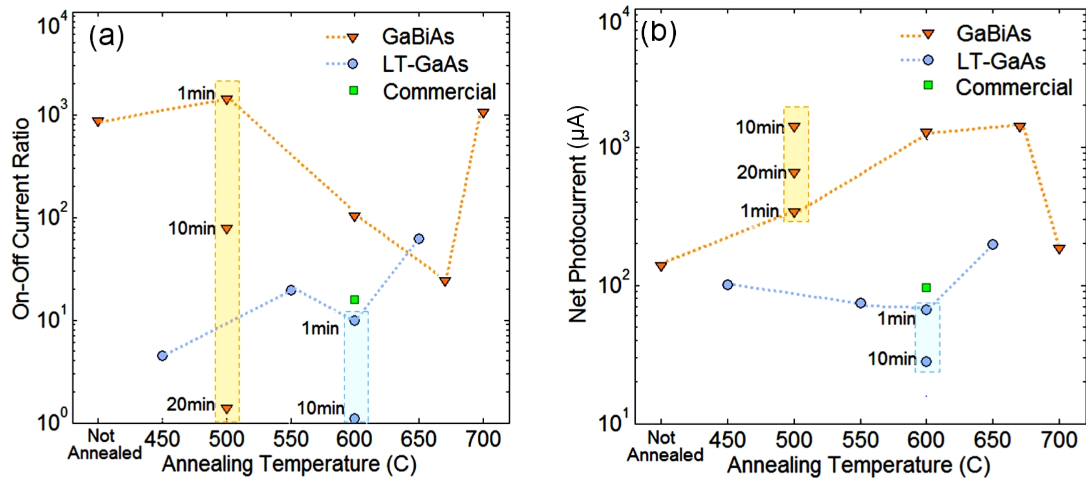

Fig. 2. (a) OOCR for GaBiAs and LT-GaAs versus annealing temperature. The annealing time is investigated in highlighted area. The green square marks show the OOCR for a commercial device. (b) Net photocurrent for different annealing conditions for GaBiAs and LT-GaAs. GaBiAs and LT-GaAs show different behavior with increase in temperature and annealing time. All the measurements are done at 10 V bias voltage and ~17 mW average optical power.

Fig. 2 (b) indicates that the effect of annealing in GaBiAs and LT-GaAs are rather different. While the OOCR is reduced in GaBiAs due to a higher increase in the dark current, the same ratio is reduced in the LT-GaAs due to a relative decrease of the photocurrent. This indicates that a PCA made on the GaBiAs substrate can have a higher

efficiency (more photocurrent for the same optical power and bias voltage) compared to LT-GaAs. However, another factor that should be considered is the carrier lifetime and thus THz emission should be measured to fully validate this assertion.

Fig. 3 shows the peak-to-peak amplitude of the emitted THz pulse measured with the heterodyne setup (Fig. 1 (a)) for PCAs with different substrate materials. As expected, the emission amplitude is notably (3 times) enhanced relative to our LT-GaAs samples. GaBiAs clearly shows a peak at around 670°C annealing temperature. Also, as seen in the red shaded area for 500°C, the annealing time also has a maximum between 10 min and 20 min. This is evident since the sample annealed for 20 min has lower emission than the identical sample annealed for 10 min at the same temperature. The annealing was performed with a rapid thermal annealing machine (RTA). The RTA chamber is evacuated down to 10^{-6} torr and a thermocouple measures the temperature at the sample surface. We also measured the results for GaBiAs with 3.0% and 4.4% Bi. The results showed a slight improvement in emission with increase in Bi percentage.

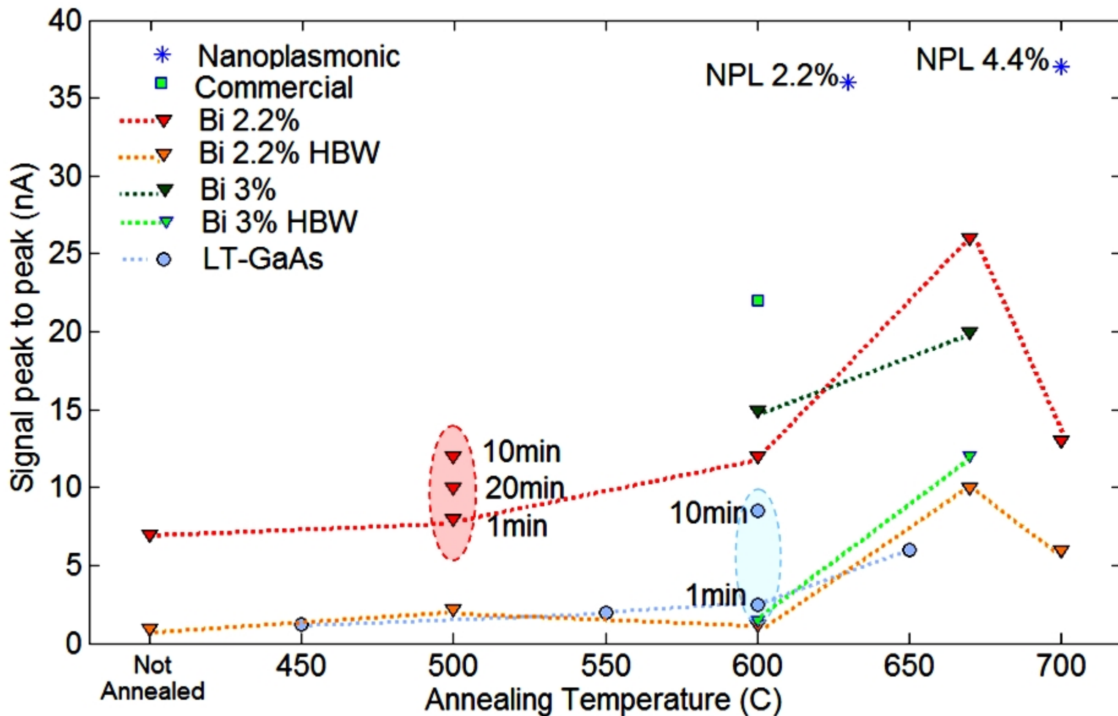

Fig. 3. Measured THz signal for GaBiAs and LT-GaAs samples. The samples are used as THz emitter. The shaded areas show the variation with annealing time. The orange and light green curves show the primary peak that has higher bandwidth. All the conventional dipole samples were biased with 20 V and the nanoplasmonics structures were biased up to device burning point (~15 V).

By recording the temporal profile of our samples (Fig. 4 (a)) we found notable consistent dual emission peaks from GaBiAs samples (red curve in figure 4 (a)). The temporal profile of the emitted THz pulse shows that there is a high frequency peak (with 0.3 ps peak-to-peak time) followed by a lower frequency peak (2.5 ps peak-to-peak). As seen in Fig. 4 (a) the high frequency and low frequency peaks are significantly different in peak-to-peak length (0.3 ps vs. 2.5 ps) compared to the oscillations for LT-GaAs signal (0.6 ps and 1.2 ps). The orange curve and the light green curve in Fig. 3 show the dynamics of the first higher bandwidth (HBW) peak with variation of annealing temperature. At first glance it might be thought that the secondary peak is generated by GaAs beneath the 350 nm GaBiAs layer at the top. However, based on our previous experiments with GaAs PCAs, such high emission peak is very unlikely from underneath GaAs excited with remaining 30% of the excitation power. Moreover, there are some smaller tails following the main pulses that are more likely to be generated by long lifetime carriers in GaAs (Fig. 4 (a)).

This dual emission behavior may be rooted in surface anomalies and GaBi droplets on the GaBiAs samples. Annealing affects these GaBi droplets and the imbedded Ga and Bi defects. Since these defects (which act as carrier recombination hubs) are more present at the surface[16] the average carrier lifetime is shorter on the surface than deeper in the substrate. This suggests that the first high frequency peak is generated from the surface and the wider peak is followed due to longer lifetime carriers generated deeper in the substrate. Another evidence can be the notable effect of Bi percentage in the first sharp peak. It is a well known fact that incorporation of higher Bi percentage increases the number of these droplets and defects at the surface. And therefore the increase in the amplitude of this primary peak in the 3% Bi samples in Fig. 3 can further support this theory. Finally, the dual emission is also consistent with a duo-exponential photocarrier decay rate previously reported for GaBiAs[14]. Unlike LT-GaAs[22-28], the dependencies of carrier lifetime versus growth condition and annealing is rather unexplored for GaBiAs. A few previous studies have noted that the carrier lifetime is measured to be around few picoseconds for samples with over 600°C annealing temperature[14, 15]. However, the dependencies of Bi percentage, growth temperature and annealing time and temperature is rather unknown. One of the challenges for measuring the carrier lifetime in GaBiAs

samples is surface roughness. The notable number of surface defects and droplets causes the typical reflective optical pump-optical probe techniques to be challenging and inaccurate in case of GaBiAs[21].

After identifying the substrate with highest emission peak, we fabricated dipoles with plasmonic strips in the gap to further enhance the amplitude. The measured emission peak-to-peak amplitude is shown with blue asterisks in Fig. 3. As expected, a significant improvement is obtained. In general, we did not notice a significant difference between the results for GaBiAs samples with 2.2% and 4.4% Bi samples with nanoplasmonics structures. This is because the nanoplasmonic structure partially overwrites some of the material properties such as carrier lifetime and optical reflection.

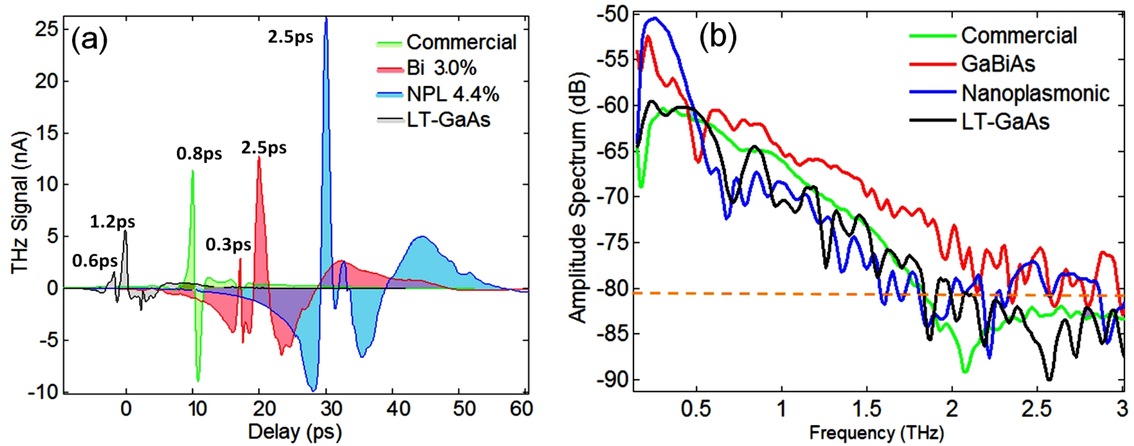

Fig.4 (a) THz pulse emitted from: commercial device (peak to peak 22 nA), GaBiAs with 4.4% Bismuth (peak to peak 20 nA), plasmonic strips on GaBiAs (peak to peak 37 nA), dipole on LT-GaAs (peak to peak 2 nA), and dipole on LT-GaAs (peak to peak 8 nA). The signal is measured in the same condition with a commercial PCA (b) Signal amplitude spectrum ($10\log_{10}|F(\mathrm{I}))|$) in dB. Noise level is about -80 dB.

The temporal profiles of the emitted signals for four distinct samples are shown in Fig. 4 (a). The peak-to-peak duration is shown for significant peaks in each signal. Fig. 4 (b) shows the amplitude spectrum of the detected signal in dB. Compared to the commercial LT-GaAs based PCA, the spectrum of the GaBiAs is notably enhanced in hyper THz range due to the sharp primary peak. The cut-off to the -80 dB noise level is increased by almost 0.5 THz. Additionally, for the nanoplasmonics PCA (blue curve) the spectrum has improved by 10 dB in lower THz range.

The gap structure has capacitance of ~0.02 fF[29] and resistance of ~15 kΩ when illuminated. Therefore, there is roughly a 500 GHz -3 dB RC cut-off induced by the

capacitive effect of the parallel strips. Our LT-GaAs sample also follows the commercial device performance as seen in Fig. 4 (b). The carrier lifetime in LT-GaAs is in the subpicosecond range. Although this has improved the higher frequency performance of the device, it has negatively affected the mobility and amplitude of the emission as seen in Fig. 4 (a).

The performance and compatibility of the plasmonic structure depends on its electrical performance as well. For instance, here we have used parallel strips (Fig. 1 (c)) instead of a nano-interlaced structure[20] to divide the bias voltage between the strips. Such a design along with high OOCR helps to lower the negative effects (additional heating) of dark current that would be otherwise too high for an interlaced structure with a single 100 nm gap. The nanoplasmonic devices with parallel strips were operational up to 15 V of bias voltage. Additionally, the high OOCR in GaBiAs material supports higher bias voltage and deeper modulation in the photoconductivity of the substrate.

The details of the sample growth condition is given in Table. 1. X-ray measurements were used to make sure that the structure has an acceptable crystalline structure. As the third column shows, the thickness of the top layer is significantly reduced by increasing the Bi percentage. This is because it is more difficult to grow a thick uniform crystalline layer with increased Bi concentration. The forth column of the table shows the As_2/Ga Beam Equivalent Pressure (BEP). The layers are fabricated on identical semi-insulating GaAs ([100] and 350 μm thick) substrates.

Table 1. Growth condition in molecular beam epitaxy VG-V80H machine for different substrates.

Sample Type	Growth Temp. (°C)	Thickness (nm)	As_2:Ga BEP
GaBiAs 2.2%	365	350	As_2/Ga BEP= 2.21
GaBiAs 3.0%	360	90	As_2/Ga BEP= 1.14
GaBiAs 4.4%	295	75	As2/Ga BEP: 2.26
LT-GaAs 0.5% excess As	240	900	As2/Ga BEP: 12

The dipoles were fabricated by common photolithography procedures. For the nanoplasmonic structures we fabricated a full gap dipole with photolithography and then sputtered the 100 nm gaps with Focused Ion Beam machine (Hitachi FB-2100).

In summary, we found a superior On-Off current ratio in GaBiAs samples. Based on measurements, the highest THz emission is found at annealing temperatures around 670°C. The highest emission is consistent with highest level of net photocurrent. We then fabricated nanoplasmonic structures on the GaBiAs samples with highest emission peak which increased emission by 68%. Additionally, we found a dual emission behavior in ordinary dipoles on GaBiAs that is likely to result from surface defects and dual photocarrier decay rate of GaBiAs material. The sharp primary peak shows over 2 THz measurable frequency components. Realizing the same concept of nanoplasmonic strips for enhancement in THz emission of 1550 nm-excited InGaAs material can be considered as the future progression of this study.

Acknowledgements

The authors acknowledge support from Natural Sciences and Engineering Research Council (NSERC) Canada.

References

1. D.H. Auston, "Picosecond optoelectronic switching and gating in silicon," Applied Physics Letter, Vol. 26, pp.101-103 (1975).

2. C.H. Lee, "Picosecond Optoelectronic Switching in GaAs," Applied Physics Letter, 30, pp.84-86 (1977).

3. M. Y. Frankel, J. F. Whitaker, G. A. Mourou, F. W. Smith, and A. R. Calawa, "High-voltage picosecond photoconductor switch based on low-temperature-grown GaAs," IEEE Transaction on Electronic Devices, Vol. 37, pp.2493-2498 (1990).

4. N. Horiuchi, Nature Photonics "Terahertz nano-exploration," Vol. 6, pp.82–83 (2012).

5. M. Tonouchi, "Cutting-edge terahertz technology," Nature Photonics, Vol. 1, pp.97-105 (2007).

6. B. Heshmat, H. Pahlevaninezhad, M. C. Beard, C. Papadopoulos and T. E. Darcie, "Single-walled carbon nanotubes as base material for THz photoconductive switching: a theoretical study from input power to output THz emission," Optics Express, Vol. 19, pp.15077-15089 (2011).

7. H. Roehle, R. J. B Dietz, H. J. Hensel, J. Böttcher, H. Künzel, D. Stanze, M. Schell, and B. Sartorius, "Next generation 1.5 μm terahertz antennas: mesa-structuring of InGaAs/InAlAs photoconductive layers," Optics Express, Vol. 18, pp.2296-2301, (2010).

8. K. Bertulis, A. Krotkus, G. Aleksejenko, V. Pačebutas, R. Adomavičius, and G. Molis, "GaBiAs: A material for optoelectronic terahertz devices" Applied Physics Letter, Vol. 88, pp.201112 (2006).

9. H. H. Tan, C. Jagadish, K. Korona, J. Jasinski, M. Kaminska, R. Viselga, S. Marcinkevicius, and A. Krotkus, "Ion-implanted GaAs for subpicosecond optoelectronic applications," IEEE Journal of Sel. Top. in Q. EElectronic, 1996, 2, 66.

10. E. C. Camus, J. L. Hughes, and M. B. Johnston, "Three-dimensional carrier-dynamics simulation of terahertz emission from photoconductive switches," Physical Review B, Vol. 71, pp.195301 (2005).

11. R. N. Kini, L. Bhusal, A. J. Ptak, R. France, and A., J. Mascarenhas, "Electron Hall mobility in GaAsBi," Applied Physics, Vol. 106, pp.043705 (2009).

12. K. Alberi, O. D. Dubon, W. Walukiewicz, K. M. Yu, K. Bertulis, and A. Krotkus, "Valence band anticrossing in $GaBi_xAs_{1-x}$," Applied Physics Letter, Vol. 91, pp.051909 (2007).

13. V. Pačebutas; A. Bičiūnas; S. Balakauskas, A. Krotkus; G. Andriukaitis; D. Lorenc, A. Pugžlys, A. and Baltuška, "Terahertz time-domain-spectroscopy system based on femtosecond Yb:fiber laser and GaBiAs photoconducting components," Applied Physics Letter, Vol. 97, pp.031111 (2010).

14. V. Pačebutas, K. Bertulis, A. Bičiūnas, and A. Krotkus, "Low-temperature MBE-grown GaBiAs layers for terahertz optoelectronic applications," Physics Status Solidi C, Vol. 6, pp.2649–2651 (2009).

15. A. Arlauskas, P. Svidovsky, K. Bertulis, R. Adomavicius, and A. Krotkus, "GaAsBi photoconductive terahertz detector sensitivity at long excitation wavelengths," Journal of Applied Physics Express, Vol. 5, pp.022601 (2012).

16. S. Francoeur, M. J. Seong, and A. Mascarenhas, S. Tixier, M. Adamcyk, and T. Tiedje, "Band gap of $GaAs_{1-x}Bi_x$, $0<x<3.6\%$," Applied Physics Letter, Vol. 82, pp.3874-3876 (2003).

17. B. Cechavicius, R. Adomavicius, A. Koroliov and A. Krotkus, "Thermal annealing effect on photoexcited carrier dynamics in $GaBi_xAs_{1-x}$," Semiconductor Science Technology, Vol. 26, pp085033 (2011).

18. A. W. Bargioni, A. Schwartzberg, M. Cornaglia,A. Ismach, J. J. Urban, Y. Pang, R. Gordon, J. Bokor, M. B. Salmeron, D. F. Ogletree, P. Ashby, S. Cabrini, P. J. Schuck,

"Hyperspectral Nanoscale imaging on dielectric substrates with coaxial optical antenna scan probes," Nano Letterss, Vol. 11, pp.1201-1207 (2011).

19. S. Pillai, K. R. Catchpole, T. Trupke, and M. A. Green "Surface plasmon enhanced silicon solar cells," Journal of Applied Physics, Vol. 101, pp.093105 (2007).

20. B. Heshmat, H. Pahlevaninezhad,Y. Pang, M. Masnadi, R. Lewis, T. Tiedje, R. Gordon and T. E. Darcie, "Nanoplasmonic terahertz photoconductive switch on GaAs", Nano Letters, Article ASAP (2012).

21. V. Pačebutas, K. Bertulis, L. Dapkus, G. Aleksejenko, A. Krotkus, K. M. Yu and W. Walukiewicz, "Characterization of low-temperature molecular-beam-epitaxy grown GaBiAs layers," Semiconductor Science and Technology, Vol. 22, pp.819–823 (2007).

22. R. Yano, Y. Hirayama, S. Miyashita, N. Uesugi, S. Uehara, "Arsenic pressure dependence of carrier lifetime and annealing dynamics for low-temperature grown GaAs studied by pump–probe spectroscopy," Journal of Applied Physics, Vol. 94, pp.3966-3971 (2003).

23. H. S. Loka, S. D Benjamin, and P. W. E. Smith, "Influence of material growth and annealing conditions on recombination processes in low-temperature-grown GaAs," Optics Communication, Vol. 161, pp.232–235 (1999).

24. H. Nemec, A. Pashkin, P. Kuzela, M. Khazan, S. Schnull, and I. Wilke, "Carrier dynamics in low-temperature grown GaAs studied by terahertz emission spectroscopy," Journal of Applied Physics, Vol. 90, pp.1303-1306 (2001).

25. Z. L. Weber, H. J. Cheng, S. Gupta, J. Whitaker, K. Nickolas, F. W. Smith, "Structure and carrier lifetime in LT-GaAs," Journal of Electronic Material, Vol. 22, pp.1465-1469 (1993).

26. A. Krotkus, R. Viselga, K. Bertulis and V. Jasutis, S. Marcinkeviciusa, U. Olin, "Subpicosecond carrier lifetimes in GaAs grown by molecular beam epitaxy at low substrate temperature,"Applied Physics Letter, Vol. 66, pp.1939-1941 (1995).

27. M. Stellmacher, J. Nagle, J. F. Lampin, P. Santoro, J. Vaneecloo, and A. J. Alexandrou, "Dependence of the carrier lifetime on acceptor concentration in GaAs grown at low-temperature under different growth and annealing conditions," Applied Physics, Vol. 88, pp.6026-6031 (2000).

28. E. S. Harmon, M. R. Melloch, J. M. Woodall, D. D. Nolte, N. Otsuka, and C. L. Chang, "Carrier lifetime versus anneal in low temperature growth GaAs," Applied Physics Letter, Vol. 63, pp.2248-2250 (1993).

29. J. B. D Soole, and H. Schumacher, "Transit-time limited frequency response of InGaAs MSM photodetectors," IEEE Transaction on Electronic Devices, Vol. 37, pp.2285-2291 (1990).

ppendix B: Single-walled carbon nanotubes as base material for THz photoconductive switching

(2011, Optics Express, volume 19, pp. 15077)

Reprinted with permission from the Optics Express Journal © Copyright (2012)

Optical Society of America

Single-walled carbon nanotubes as base material for THz photoconductive switching: A Theoretical study from input power to output THz emission

Barmak Heshmat,[1], Hamid Pahlevaninezhad, [1] Mathew Craig Beard, [2] Chris Papadopoulos, [1] Thomas Edward Darcie [1]*

[1]*Department of Electrical and Computer Engineering, University of Victoria, 3800 Finnerty Rd., Victoria, BC,V8P 5C2, Canada*
[2] *Chemical and Materials Research Center, The National Renewable Energy Laboratory, 1617 Cole Blvd., Golden, CO 80401, USA*
**barmak@uvic.ca*

Abstract: This paper studies the relation between photoexcitation of a single-walled carbon nanotube (SWNT) based device, and its THz output power in the context of THz photoconductive (PC) switching and THz photomixing. A detailed approach of calculating output THz power for such a device describes the effect of each parameter on the performance of the THz PC switch and highlights the design dependent achievable limits. A numerical assessment, with typical values for each parameter, shows that --subject to thermal stability of the device-- SWNT based PC switch can improve the output power by almost two orders of magnitudes compared to conventional materials such as LT-GaAs.

1. Introduction

Since the initial success of Auston et al with photoconductive switches (PC switches) in 1983, there has been an increasing demand for terahertz (THz) sources. Many approaches for generation of coherent THz radiation have been proposed so far, each having its own advantages and disadvantages [1, 2]. Among alternatives, THz PC switches have received considerable attention, mostly due to wide frequency tunability range, fabrication simplicity and recent advancement of ultrafast pulse lasers [3-8]. Different types of THz photoconductive switches have been developed in recent decades mostly by the use of fast semiconductor materials such as low temperature grown GaAs (LT-GaAs), LT-InGaAs and more recently GaAsBi. These materials are used as the base material that feeds an antenna structure with the photocurrent (Fig1. (a)) [3-8]. THz PC switches can also work in continuous wave mode (CW mode) as THz photomixers, offering more flexibility in different applications. However, low output power (less than 10μW) for PC

switches and photomixers has been a major challenge, leaving these THz sources as inefficient choices for many applications [4, 7, 8].

Nanomaterials —especially carbon nanotubes (CNT) and graphene— offer a set of exceptional properties that are potentially suitable for more efficient THz PC switches and photomixers [8-10]. This includes both using these materials as high impedance waveguides in the antenna structure and as a high mobility, high absorption, base material in the antenna gap (Fig. 1 (b)) [8-10].

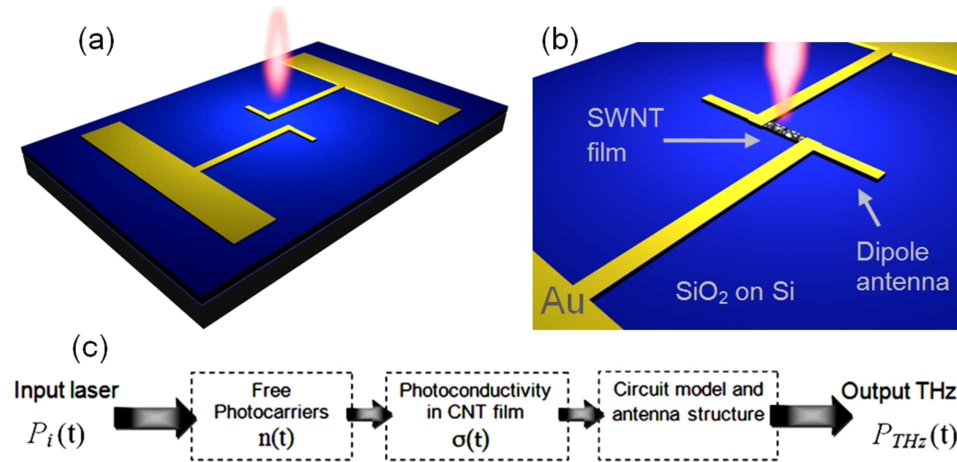

Fig. 1.(a) Illustration of optical excitation of a THz photoconductive switch that has a center fed dipole antenna structure. (b) A PC switch made on a thin SiO_2 oxide layer grown on a Si wafer. The gap is filled with aligned SWNTs and the antenna pattern is fabricated similar to conventional PC switches through common lithography processes (c) Block diagram of different steps of the analysis that links input laser excitation power and output THz emitted power.

In both cases, increase in output power is anticipated, based on primary estimations [8, 10]. However, there has been no design guidance for fabrication of such devices. So the effect of different parameters, such as tube alignment, carrier lifetime, exciton-exciton annihilation rate and contact resistance on the performance of such devices remains questionable. In order to choose a design path, the dynamics of a PC switch based on CNT material should be addressed thoroughly and that is the main focus of this paper.

In this paper, we present a theoretical analysis that links the input optical pump excitation power and the output THz power (Fig. 1 (c)). The first step in the link deals with fast free photocarrier dynamics of the single-walled carbon nanotube (SWNT) films. The second step is to model the photoconductivity based on the photocarrier dynamics from the first step. Finally, the dynamics of the metallic antenna structure and equivalent circuit model are engaged. The purpose is to address the effect of important parameters

and highlight the limits and behaviors of each one on the THz PC switching process. This procedure then can be further modified for any specific desired antenna and gap structure.

2. Conversion of input power to free photocarriers in SWNT film

The connection between input power and free photocarriers in the SWNT film is found in two steps. First, the initial absorbed photon density is calculated and then, the dynamics of the excitons and photocarriers are considered in the film. The initial absorbed photon density is expressed by:

$$n_{abs} \approx \frac{\eta(\nu)\int_0^{T} p_i(t)dt}{h\nu V}, \tag{1}$$

where $p_i(t)$ is the illuminating pulsed-laser power with repetition rate of 1/T. In the denominator, $h\nu$ is the energy of each photon with frequency ν, and V is the volume of the material in which the photons are absorbed. The function $\eta(\nu)$ takes values between 0 and 1, depending on the optical density and quantum efficiency of SWNT film [11, 12]. These parameters depend on CNT types present in the film, alignment of the tubes with the direction of the input light polarization, and filling factor of the CNT bundles. In the case of continuous wave illumination, the integration in Eq. 1 can be reduced to average power per second that will result in average absorbed photon density. Eq. 1 is essentially the ratio of number of incident photons to the volume of the sample times the quantum efficiency. This equation assumes a linear relation between input power amplitude and absorbed photon density at a given frequency, thus slight variations of quantum efficiency with input power amplitude is neglected for simplicity [12, 13]. If a wide, non-uniform frequency spectrum is assumed for input power ($p_i(t) \rightarrow p_i(t,\nu)$), the right hand side of Eq.1 can be integrated over the total frequency range.

The conversion of the input light into photocurrent in the THz spectrum range is related to fast photocarrier dynamics of the SWNT film. This is different from previously measured photocurrents for SWNT films under infrared and visible illumination [14-16]. The latter is mainly considered for solar cell applications and is described by drift-diffusion equations that are proper for lower frequency dynamics [17, 18]. Experimental studies on fast photoconductivity of CNT films have confirmed that given the initial

absorbed photon density n_{abs}, the fast carrier dynamics can be described by a set of joint continuity equations between exciton density function $n_e(t)$ and total photogenerated carrier density $n(t)$ as in Eq.2 [19].

$$\frac{dn_e(t)}{dt} = -\gamma_{EE} n_e^2(t) - \gamma_{CC} n_e(t), \qquad n_e(0) = n_{abs};$$
$$\frac{dn(t)}{dt} = \gamma_{CC} n_e(t) - \gamma_d n(t), \qquad n(0) = 0. \tag{2}$$

In this equation γ_{EE} is exciton-exciton annihilation rate, γ_{CC} is the carrier generation rate by exciton dissociation, and γ_d is the carrier decay rate equal to the reciprocal of the carrier lifetime τ [20]. In Eq. 2, n(t) itself can be written as sum of free (nf(t)) and localized (n(t)-nf(t)) photocarrier densities; however, the equation holds regardless of the nature of the total photocarrier density. In the boundary conditions of Eq. 2 the initial exciton density is equated to the initial absorbed photon density; therefore, it is implicitly assumed that each absorbed photon immediately generates an exciton in the material. Also it is further assumed that excitons don't decay during the period of integration (0 to T) in Eq. 1. It is noteworthy that this mathematical assumption holds in pulsed excitation because p(t) is typically nonzero only for a very short period of time (from 0 to pulse width, which is typically less than 200fs) and the excitons will enter the carrier dynamics (Eq. 2) immediately after the pulse have been absorbed by the material. In other words, for pulsed excitation the exciton decay is ignored in the small period of excitation itself, however, for continuous wave excitation a proper period of integration should be considered in Eq. 1 so that $n_e(0)$ can be fairly equated to nabs in Eq.2. Eq. 2 can be solved explicitly, and the result is in the form of a hypergeometric function ${}_2F_1$;

$$n(t) = \gamma_{CC}^2 \left[\frac{k_2}{\gamma_{CC}^2} - \frac{{}_2F_1\left(1, \frac{\gamma_d}{\gamma_{CC}}, 1 + \frac{\gamma_d}{\gamma_{CC}}, \frac{e^{\gamma_{CC}(t+k_1)}}{\gamma_{EE}}\right)}{\gamma_{EE}\gamma_d} \right], \tag{3}$$

where,

$$k_1 = \frac{\ln(\gamma_{EE} + \gamma_{CC} / n_{abs})}{\gamma_{CC}}, \quad \text{and} \quad k_2 = \frac{\gamma_{CC}^2 \, {}_2F_1\left(1, \frac{\gamma_d}{\gamma_{CC}}, 1 + \frac{\gamma_d}{\gamma_{CC}}, \frac{e^{\gamma_{CC} \times k_1}}{\gamma_{EE}}\right)}{\gamma_{EE}\gamma_d}. \tag{4}$$

Since the conversion of absorbed photons to excitons is assumed to be instantaneous on the femtosecond time scales, the results of Eq. 2 can be considered as an approximation of the pulse response of the material to $n_{abs}\delta(t)$. Therefore, the response to the Gaussian pulse would be roughly (due to presence of nonlinearity between n_{abs} and n(t)) estimated by the convolution of the $n(t)$ with the Gaussian profile of input power (inset graph in Fig. 2 (a)). This estimate matches the previous experimental measurement of photocarrier density both in profile and scale [19].

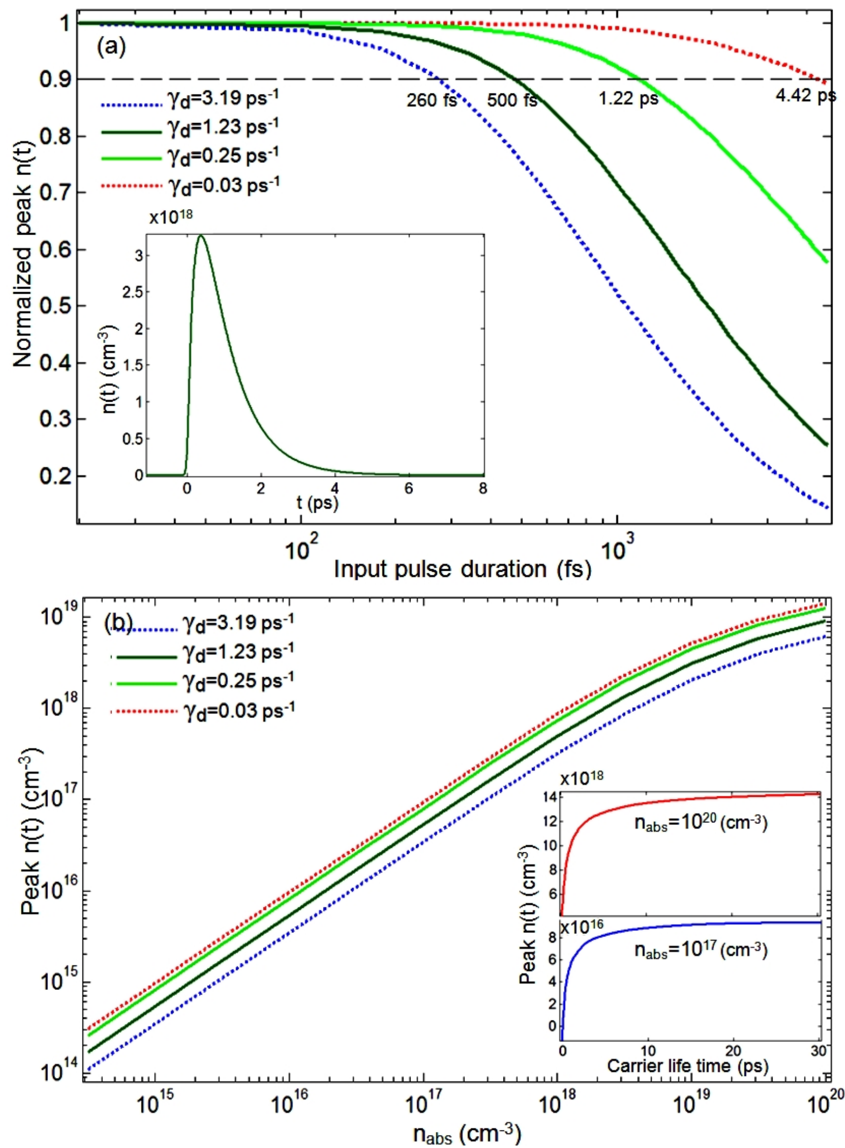

Fig. 2. (a) Peak total photocarrier density as a function of excitation pulse duration and carrier decay rate, γ_d (carrier lifetime, $\tau = 1/\gamma_d$). The inset graph depicts the carrier density as a function of time (optical excitation pulse duration=100fs, $n_{abs}=10^{19}$ cm^{-3} and decay rate=1.23 ps^{-1}). (b) Peak total photocarrier density as a function of n_{abs}. The inset graph shows the behavior of the same function within allowable carrier lifetime of SWNT.

As it will be seen in sections 3 and 4, two key parameters of the carrier density function are its peak value and its pulse width (bandwidth). Both of these parameters are strongly influenced by excitation profile and the other rate parameters involved in Eq.3. A typical set of experimental values, for randomly deposited SWNT films, is mentioned in Table.1 [19- 21].

Table 1 A typical set of experimental values for rate parameters in Eq. 2

Parameter and dimension	γ_{EE} (cm^3.ps^{-1})	γ_{CC} (ps^{-1})	γ_d (ps^{-1})	n_{abs} (cm^{-3})
Typical experimental value range	6.9×10^{-19}	3.4	0.033~3.19	10^{14}~10^{20}

Figure 2 shows the influence of n_{abs} and excitation pulse width on the peak total number of photocarriers.

As it can be seen in Fig.2 (a), the peak photocarrier density curve has a knee after which the peak $n(t)$ falls with exponential behavior. The location of the knee is directly influenced by carrier lifetime. For example, if a reduction to 90% of the maximum $n(t)$ is allowed in a design, based on Fig.2 (a), the maximum of allowable input pulse width is increased from 0.26 ps to 4.42 ps with a decrease of carrier decay rate from 3.19 ps^{-1} to 0.03 ps^{-1}. Care must be taken when using this graph in its lower limits, as the physics of the material excitation can change for pulse width less than 20fs range. The curves in Fig.2 (a) are likely to roll off on the left hand side as well [22, 23]. Also, the saturation of peak $n(t)$ in higher absorbed carrier densities is captured with Eq. 3 and 4, as shown in Fig. 2 (b). This is consistent with the experimental measurement of photocarriers reported in [19]. The inset graph in Fig. 2 (b) reveals that the variation of carrier lifetime has an exponential dependence for values less than 3 ps. The peak photocarrier density, however, enters a saturation region immediately after this value, and thus further increase of carrier lifetime will no longer have a significant contribution.

It should be further emphasized that unlike the case of CW THz photomixing where a short carrier lifetime (less than 2 ps) is vital to deepen the THz photoconductivity modulation of the material in the gap, short carrier lifetime is not a necessity for THz PC switching. This is due to the pulsed nature of THz PC switching and the fact that the pulses are well distanced in time relative to carrier lifetime. In THz PC switching the THz

components of the microantenna feed current are generated mainly by the initial sharp rise in the photocarrier density as seen in the inset graph of Fig 2. (a). Consequently, the smoother roll-off of photocarrier density that is affected by the carrier lifetime does not induce THz components in the current. In THz PC switching the carrier lifetime affects the peak photocarrier density as seen in the inset graph of Fig. 2 (b) and the peak photocarrier density can affect the output THz power as it will be explained in the rest of this study.

3. Photocarriers conversion to photoconductivity in SWCNT film

The calculation of photoconductivity of a SWNT film is a challenging problem. It can be viewed from a diverse range of perspectives, varying from non-equilibrium ab initio simulations [24] and consideration of Luttinger liquid behavior for individual CNTs [25] to use of an equivalent drude model for the entire sample [26]. Other than free photocarrier density that was calculated in the previous section, there are a considerable number of other parameters that can affect the photoconductivity of SWNT film. In order to focus this study, we will determine the anticipated range based on modified Drude-Smith (DS) model. Different fabrication conditions are considered, ranging from the idealistic fabrication condition of perfectly aligned, perfectly purified to totally random and partially purified cases. The DS model has given fair results for the study of ultrafast conductivity of varieties of nanomaterials [19, 27, 28]. In general the photoconductivity can be calculated via the Drude-Smith model as [27]

$$\sigma_{photo}(\omega) = \frac{\mu n_f e}{(1 - i\omega\tau_s)}\left(1 - \frac{\xi}{1 - i\omega\tau_s}\right) + i\frac{\mu(n - n_f)e\omega}{\tau_s(\omega^2 - \omega_l^2 - i\omega\gamma_l)}. \quad (5)$$

In this equation μ is the mobility of the material, nf is the free photocarrier density, e is the electron charge, ω is the frequency of the voltage applied to the material, ω_l is the Lorentzian frequency, γ_l is the Lorentzian momentum rate, τ_s is the average carrier scattering time, and ξ is a constant between 0 and 1 that indicates the photocarrier localization level. The second Lorentzian term is introduced for generality. This term is for localized carrier density that typically constitutes a small fraction of total photocarrier density ($n-n_f<0.3n$). The proportion of localized to free photocarriers can be obtained

through Time-Resolved THz Spectroscopy (TRTS) and does not play a significant role in Eq. 2. However, this proportion can affect the photoconductivity as explained by DS formula in Eq. 5 [19]. For the chopping frequency range of THz heterodyne systems (ω typically less than 1MHz for the bias voltage of the emitter) the second term is negligible and can be ignored. This term, however, can play an important role in the receiver PC switch, where the THz received field also contributes to THz modulation of conductance and photoconductance. As mentioned previously in section 2, n and n_f are both functions of time (inset graph of Fig. 2 (a)). Consequently, $\sigma_{photo}(\omega)$ is also a function of time. The time variable, t, is omitted from Eq. 5 for simplicity. It is this temporal variation of photocarrier density that contains THz components and thus modulates the antenna feed current with THz components through DC or low-frequency bias voltage applied to the gap of THz emitting PC switch.

The previously reported value ranges and dimensions of these parameters are given in Table 2. These values are experimentally justified in previous studies [19, 29-31].

Table 2. Previously reported values for Drude Smith modeling of CNT films

Parameter and dimension	μ ($m^2.v^{-1}s^{-1}$)	τ_S (ps)	ζ	ω_l (THz)	γ_l (ps^{-1})
Experimentally justified, reported value range	10^{-2}~10	10^{-2}~5	0.5~1	20~80	0.2~20

For the case of a perfectly aligned, perfectly purified CNT film, values of mobility, localization constant, and percentage of free photocarriers are chosen within the range from Table 2 so that the conductivity is maximized. In a real case, however, parameters such as carrier lifetime, carrier mobility, electrical coupling and alignment with the applied field, etc., can be different for each CNT in the film. Therefore, a Monte Carlo (MC) integration method should be used for a more realistic result [32]. This integration is based on Eq. 5 and is presented in Eq. 6 for q^{th} iteration of calculation.

$$\sigma_{photo_q}(\omega) = \sum_{j=1}^{J}\sum_{k=1}^{K}\frac{\mu_{jk}n_{fjk}e}{(1-im\omega\mu_{jk}/e)}\left(1-\frac{\xi}{1-im\omega\mu_{jk}/e}\right). \tag{6}$$

In Eq. 6 m is the average effective mass of electrons.

The MC integration is performed by iteratively generating the initial distribution of the photocarriers. This distribution is based on a 3D probability density function with a 2D Gaussian (normal) distribution cross section and an exponential distribution along the radiation axis. This represents an illumination with Gaussian beam, and a material with Beer-Lambert absorption behavior [33]. In each iteration, the simulation bins the carriers into J×K cells along the gap (Fig. 3 (a)), applies randomly generated parameters to each cell, and does an overall summation. The outcomes of Q iterations are then averaged to give the final result.

There have been many different reports on mobility of CNTs in semiconducting SWNT samples [24, 30, 31]. Based on Eq. 5, it is found that the conductivity is approximately linearly affected by the mobility at lower frequencies (f<1MHz). Here the mobility itself is assumed to be affected by alignment of CNTs with the applied field and the local carrier density of the bin ρ_{jk} as below [30]:

$$\mu_{jk} = (0.1 + 0.9u_1)\left(1 - \frac{0.99\rho_{jk}}{\rho_{\max}}\right)\cos(15^\circ \times u_2). \tag{7}$$

In Eq.7, u1 and u2 are two independent random variables, sampled from a uniform distribution between zero and one, and mobility has units of $\mathrm{m^2/Vs}$. ρ_{max} is the maximum local carrier density in the total volume. Also, the average effective mass is affected by local carrier density ($m_{jk}^{-1} \approx (18 - 5\rho_{jk})m_e^{-1}$) as reported in [30]. An angular deviation of almost 15º is consistent with our observation under scanning electron microscope (SEM) (Fig. 3 (b)). This alignment is realizable via the slip-stick method [34]. Alignment is assumed to affect the mobility so that the conductance can be approximated with simple classical formulation without concerns of CNTs directional conductance [35] (section 4).

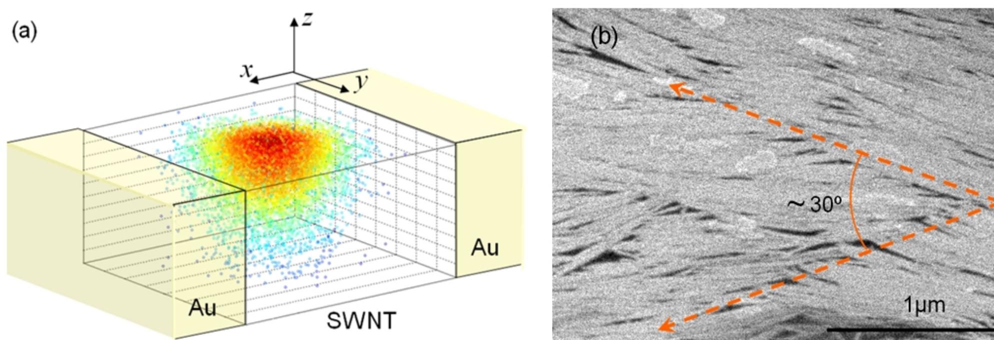

Fig. 3. (a) An illustration of binning process in MC calculation of conductivity in a partially aligned SWNT film. Each cell is a rectangular cuboid extending along the gap. (b) SEM image of a typical dip and slip deposition method results for s-SWNTs on a SiO_2 substrate.

Figure 4 depicts the peak photoconductance, so each point is the peak of a time varying photoconductance that has the same temporal profile as n(t) in the inset graph of Fig. 2 (a).

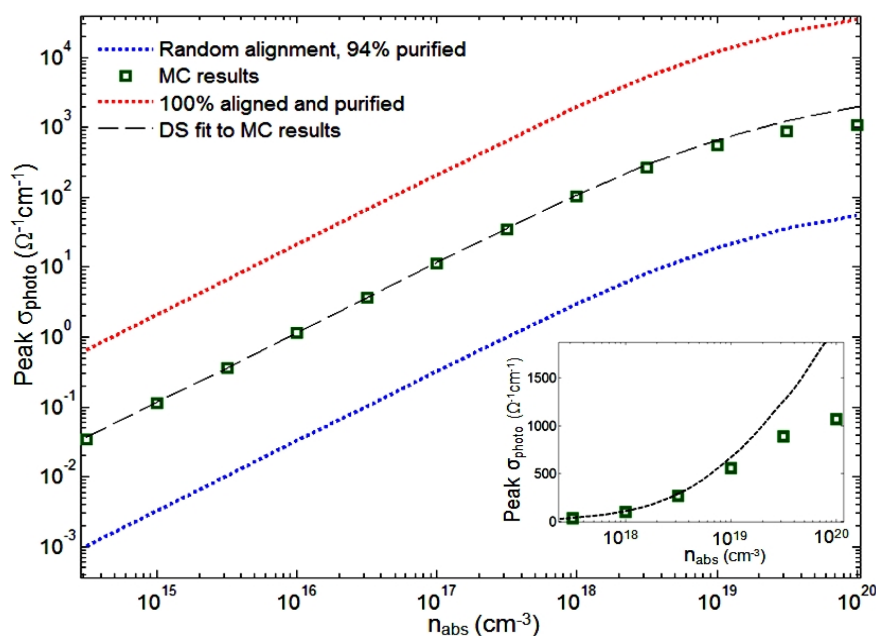

Fig. 4. Photoconductivity for three cases of: perfectly aligned and purified, partially aligned and purified, and randomly deposited and partially purified s-SWNT.

The lower limit (blue dotted line) is based on the random alignment and experimental verification in [19]. The higher limit shown with dotted red line is based on the experimental semiconductor SWNT mobility measurement of 10 m^2/Vs reported in [30, 31]. The MC integration result agrees closely with the DS model with mobility of 0.55 m^2/Vs for lower carrier concentrations. The inset graph in Fig. 4 shows a close-up of the extra photoconductivity saturation effect due to mobility reduction with carrier density increase. This saturation is only due to phonon scattering effects, although further defects can also cause such behavior [30].

4. Modeling the photoconductance effect on output power

For both PC switches and THz photomixers the last step of the analysis that connects the input power to the output THz power is the photoconductance, which appears in the equivalent circuit model (Fig. 5).

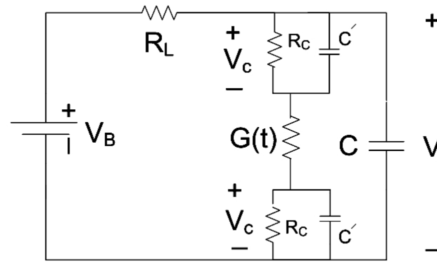

Fig. 5. Schematic of the circuit model for the PC switch with s-SWNT in the gap. V_B is the DC bias voltage, R_L is the antenna resistance, V_c is the contact voltage , R_c and c´ are contact resistance and capacitance, and C is the capacitance of the gap.

Unlike two previous steps, this step is not affected by the physics of the material, but it is rather affected by the design of the electrodes and fabrication of the antenna itself. The effects of antenna structure and contact fabrication are some widely studied topics both in PC switches and in CNT film research [36-39]. We address the dynamics, rather than proposing an optimized design by focusing on parameters that affect and the output power. The design of the gap can affect the conductance; assuming the gap has dimensions of x, y, z depicted in Fig. 3 (a), then the conductance can be calculated by classical definition of conductance $G(t) = (\sigma_{dark} + \sigma_{photo}(t))yz/x$. This is the average conductance in the gap, since the misalignment and directional conductivity of CNTs [35] have already been considered in calculation of photoconductance.

Based on the equivalent circuit model in Fig. 5, the voltage V across both the time varying conductance G(t) and the contacts is given by the solution to the following set of coupled, first-order inhomogeneous linear differential equations;

$$\begin{aligned} &\frac{dV}{dt} + \frac{(1+R_L G(t))}{R_L C}V - \frac{V_B + 2R_L G(t)V_C}{R_L C} = 0, \text{ wtih } \quad V(0) = \frac{(2R_C + G^{-1}(0))V_B}{2R_C + G^{-1}(0) + R_L}, \\ &\frac{dV_C}{dt} + \left(\frac{1+2R_C G(t)}{c' R_C}\right)V_C - \frac{G(t)}{c'}V = 0, \text{with } \; V_C(0) = \frac{R_C V_B}{2R_C + G^{-1}(0) + R_L}. \end{aligned} \quad (8)$$

The parameters in this formula are explained in Fig. 5. Unlike THz photomixers, where two lasers are beating together and the circuit model can be simplified into steady state sinusoidal form [6, 7], for a PC switch such simplification is not possible. Contact

resistances cannot be ignored as in LT-GaAs model [7]. Contact resistance values can vary significantly, depending on the electrode material and fabrication method; this is a widely studied topic for CNTs in a gap [38, 39]. It is very likely that in higher frequencies a shunt capacitance dominates the contact behavior. This capacitance models the portion of CNTs that do not reach the contact and thus couple capacitively [38-40]. Considering the hypergeometric behavior embedded in conductivity and thus conductance, the value of V(t) cannot be expressed explicitly. Here, we have used the numerical Euler method with 10 fs step sizes to estimate V(t).

The output THz power can be calculated directly from the voltage V(t) and the Kirchoff voltage law in the main loop of the circuit as:

$$P_{THz}(t) = \frac{(V_B - V(t))^2 - (V_B - V(0))^2}{R_L}. \quad (9)$$

Since carrier density is a linear function of input power as shown in Eq. 1, the analytic link between input power and output THz power, illustrated in Fig. 1 (c), is completed at this point.

As an example, consider a design with typical gap dimensions of x=5 μm, y=5 μm and z=100 nm; a common set of values for the parameters in Eq. 8 and Eq.1 are assumed as follow: V_B=36 V [7, 38, 39], R_L≈30 Ω [6, 7], C≈ 10 fF [6, 7], c′≈ 100 fF [40], R_c≈20 kΩ [40, 41], G_0≈2.5 $\mu\Omega^{-1}$ [41], $\eta(\nu) = \eta$=0.1 [12], pulse duration of 70 fs, repetition rate=76MHz, and the illumination wavelength of 1030 nm. Using these values (some estimated relative to gap dimensions) and the photoconductivity values of Fig. 4, the THz output power can be calculated as a function of excitation power. In this calculation, n_{abs} is converted to average power with means of Eq.1 and consideration of repetition rate of the excitation laser. As can be seen in Fig. 6, the average output power for CNT is higher than GaBiAs PC switches [42], LT-GaAs PC switches and LT-GaAs photomixers [42-44]. Previous work reports a few microwatts of output THz power for GaBiAs, hundreds of nanowatts for LT-GaAs PC switches and tens of nanowatts for LT-GaAs photomixers, biased with the same voltage (36V) and excited with incident power of 10 to 30 mW. At 20mW of input power, the MC results for CNT's THz output power show 66 fold improvement relative to GaBiAs and 95 fold increase relative to LT-GaAs PC switches. Due to lower efficiency in continuous wave photomixing, the average output power for

the LT-GaAs photomixer hardly shows up on the scale; it is lower than the CNT output power by almost 3 to 4 orders of magnitude [44].

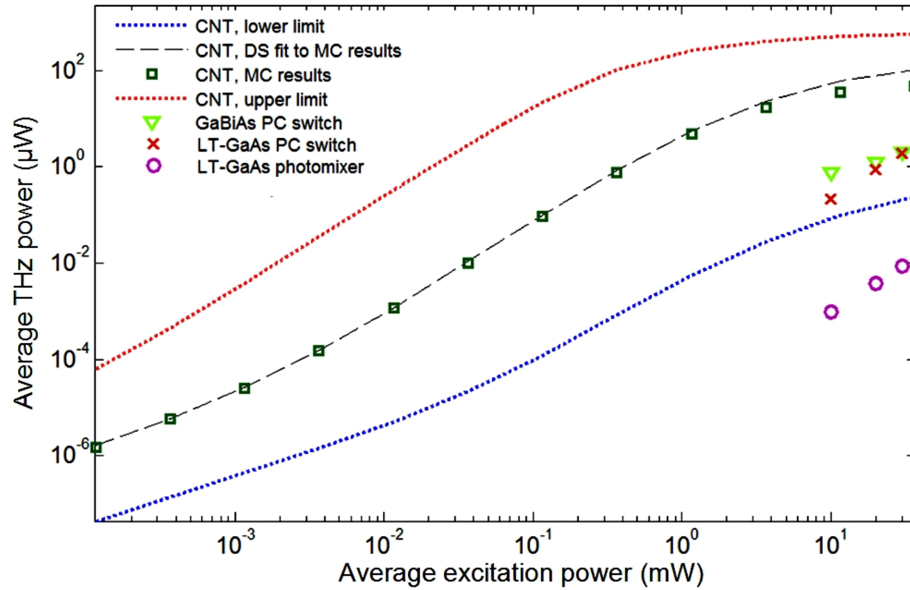

Fig. 6. Emitted average THz power vs average input excitation power. CNT curves are based on the conductivity values in Fig. 4. The GaBiAs PC switch and GaAs based photomixer output powers are inserted in 10, 20 and 30 mW of excitation power for comparison [42-44].

Figure 6 reveals that GaBiAs and LT-GaAs PC switches perform better than randomly aligned and partially purified CNTs; the case that we have chosen as lower limit condition (blue dotted line in Fig.6). Improvement in alignment and purification boosts the CNT THz power to around 103μW, calculated based on MC results for photoconductivity; the output power is then limited by the saturation effect induced by high carrier density and circuit dynamics at around 561μW in 36.6mW of input power. Fig. 6 shows that curves for higher conductivity are distorted by circuit dynamics, and as a result the power reaches saturation for lower carrier densities compared to the conductivity in Fig. 4. This is the direct result of the nonlinear relation between these two parameters. Although SWNT films are well known for high thermal conductance [45], it must be considered that the experimental validation of this increase in THz power is also subject to the thermal stability of the device.

This specific example shows the emitted THz power range for the full spectrum of the pulse. Further dynamics of the output power relative to different parameters, however, can only be found by sweeping each parameter in the solution of Eq. 8. This is necessary, since each parameter can affect both power level and bandwidth. Via this method, it is

found that the peak power changes approximately quadratically with V_B. This is consistent with previous models for fast semiconductor cases [6, 7]. Also, the dynamics of the output power with variation of each parameter in Eq. 8 is presented in Fig. 7.

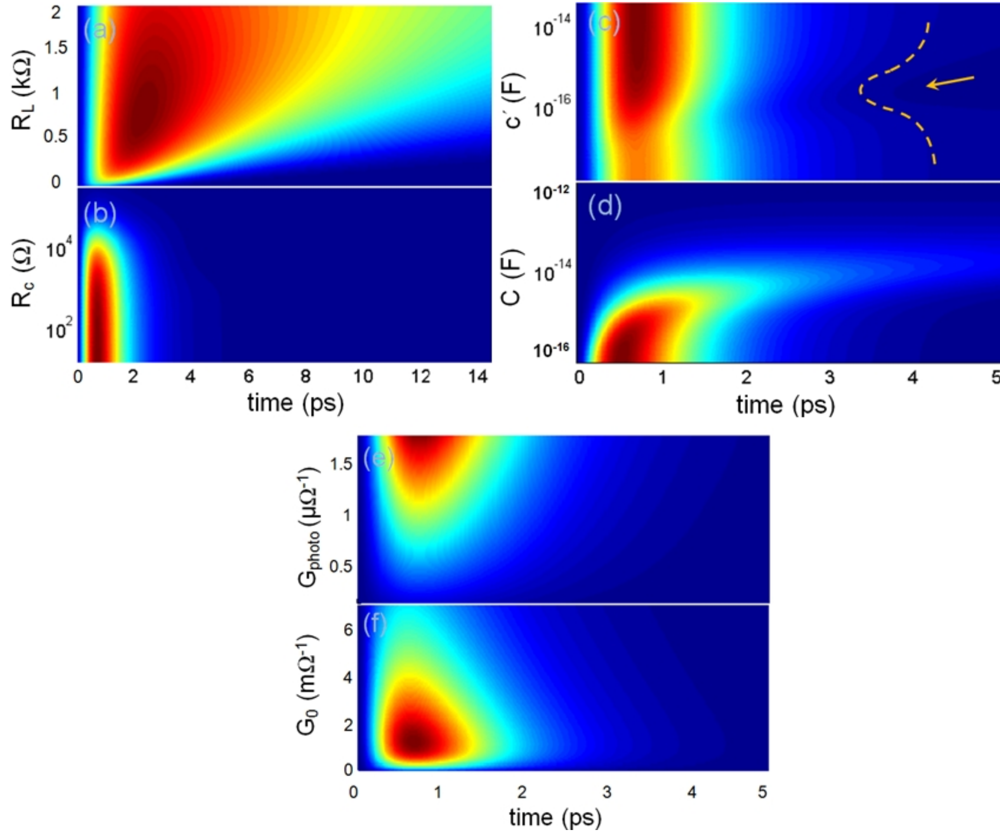

Fig. 7. The dynamics of output THz power with: (a) antenna resistance, R_L (b) CNT to metal plate contance resistance, R_c (c) contance capacitace, c´ (d) gap capacitance, C (e) photoconductance, G_{photo} (f) dark conductance, G_0 .

Based on Fig. 7 (a), P_{THz} has a maximum in certain value of R_L. Increasing R_L widens the pulse and thus reduces the bandwidth. This suggests that increase of R_L might be desired up to a certain limit (here 500Ω) with trade off for bandwidth of the emitted THz pulse. Fig. 7 (b) shows the exponential decrease of power with increase in contact resistance. This exponential decrease is the result of voltage drop on the contacts, and also, it depends on the relative value of contact capacitance and G_0. The dependence of P_{THz} on contact capacitance can be of interest for cases in which a capacitive coupling mechanism is unavoidable due to difficulties in fabrication of low resistance contacts [38-41]. This can be the case when the gap is wider than the average length of CNTs in the film. It is found that with variation of contact capacitance, the power changes between

two constant values with an exponential transition (Fig. 7 (c)). These two lower level and higher level powers are reached when c' impedance is considered a short circuit or open circuit compared to R_c. Additionally, it is seen that the higher value of c' decreases the bandwidth; this is highlighted with dashed orange line in Fig.7 (c). Such increase of the pulse bandwidth is expected based on circuit theory, and the low-pass behavior of a capacitive contact. The gap capacitance C can also play a similar role. It is seen that by increasing the gap capacitance, the bandwidth and amplitude of the output THz power is dramatically reduced (Fig. 7 (d)). This can be a significant factor in the design of the PC switch structure, since $C = \varepsilon_{film} yz / x$, where ε_{film} is the average permittivity of the CNT film placed in the gap.

The photoconductance (G_{photo}) and dark conductance (G_0) are also affected by the geometry of the gap. The variation of these two parameters also affects the terahertz power. As can be seen in Fig. 7 (e) and (f), the power has a non-monotonic behavior with variations of G_0, while it increases exponentially with initial increase in G_{photo} and then saturates at higher values. The variation of G_{photo} in its typical $\mu\Omega^{-1}$ range is too small to have a significant effect on the output pulse bandwidth.

Finally, it is worthwhile to mention that the circuit dynamics presented here can also be applied to the photomixing case in which G(t) is changed in Eq. 8 with a sinusoidal function of time.

6. Conclusion

Based on exceptional properties of SWNTs such as high mobility (up to 10 $m^2.v^{-1}s^{-1}$) [29-31], high thermal conductance [45], and high absorption in infrared region [33], SWNTs were previously proposed as an attractive material for efficient THz PC switching and photomixing [10, 46]. Through this study, we established a theoretical link between the input excitation power on a PC switch made by a SWNT film as semiconducting material and its output THz power. We addressed the effect of each parameter. Based on the fast photocarrier dynamics of the SWNT nanomaterial, it was found that the photocarrier density temporal profile can be expressed as a hypergeometric function. The effect of key parameters such as mobility, carrier lifetime, pulse width, and exciton-exciton annihilation rate were explicitly addressed in this function. The upper and lower limits of

the photoconductivity were calculated, based on the Drude-Smith theory, and were compared with the average expected value, determined using Monte Carlo integration. Finally, the dependence of the emitted THz power with variation of different PC switch design parameters such as: contact impedance, dark resistance, and antenna resistance was explored. We found that higher mobility in highly purified and aligned SWNTs can increase the THz power. The power may also be increased by other desired parameters such as smaller contact resistance and smaller gap capacitance for the microantenna. Based on a numerical example with typical values for different parameters and assumption of thermal stability of the device, approximately 2 orders of magnitude increase in CNT THz power are anticipated compared to conventional GaBiAs and LT-GaAs based PC switches.

References and links

1. D. Auston, P. Smith, "Generation and detection of millimeter waves by picosecond photoconductivity," Applied Physics Letter, Vol. 43, pp.631 (1983).

2. T. D. Dragoman and M. Dragoman, "Terahertz fields and applications," Progress in Quantum Electronics, Vol. 28, pp.1-66 (2004).

3. S. Ono, H. Murakami, A. Quema, G. Diwab, N. Sarukura, R. Nagasaka , Y. Ichikawa, H. Ogino, E. Ohshima, A. Yoshikawa, and T. Fukuda, "Generation of terahertz radiation using zinc oxide as photoconductive material excited by ultraviolet pulses ," Applied Physics Letter, Vol. 87, 261112 (2005).

4. V. Pačebutas, A. Bičiūnas, S. Balakauskas, A. Krotkus, G. Andriukaitis, D. Lorenc, A. Pugžlys, and A. Baltuška, "Terahertz time-domain-spectroscopy system based on femtosecond Yb:fiber laser and GaBiAs photoconducting components," Applied Physics Letter, Vol. 97, pp.031111 (2010).

5. J, F. Ohara, J. M. Zide, A. C. Gossard, A. J. Taylor, and R. D. Averitt, "Enhanced terahertz detection via ErAs:GaAs nanoisland superlattices," Applied Physics Letter, Vol. 88, pp.251119 (2006).

6. J. Y. Suen, W. Li, Z. D. Taylor, and E. R. Brown, "Characterization and modeling of a terahertz photoconductive switch," Applied Physics Letter, Vol. 96, pp.141103 (2010).

7. E. R. Brown, F. W. Smith, and K. A. McIntosh, "Coherent millimeter-wave generation by heterodyne conversion in low-temperature-grown GaAs photoconductors," Journal of Applied Physics, Vol. 73, pp.1480 (1993).

8. M. J. Hagmann, "Possibility of generating terahertz radiation by photomixing with clusters of carbon nanotubes," Journal of Vacuum Science and Technology B, Vol. 26, pp.794 (2008).

9. V. Ryzhii, A. A. Dubinov, T. Otsuji, V. Mitin, and M. S. Shur, "Terahertz lasers based on optically pumped multiple graphene structures with slot-line and dielectric waveguides," Journal of Applied Physics, Vol. 107, pp.054505 (2010).

10. B. Heshmat, H. Pahlevaninezhad, T. E. Darcie, C. Papadopoulos, "Evaluation of carbon nanotubes for THz photomixing," *International Radar Conf*erence, (IEEE 2010), pp. 1176 – 1179.

11. M. E. Itkis, F. Borondics, A. Yu, R. C. Haddon "Bolometric infrared photporesponse of suspended single-walled carbon nanotube film," Science, Vol. 312, pp.413-416 (2006).

12. D. A. Stewart and F. Leonard "Energy conversion efficiency in nanotube optoelectronics," Nano Letters, Vol. 5, pp.219-222 (2005).

13. M. Freitag, Y. Martin, J. A. Misewich, R. Martel, and P. Avouris "Photoconductivity of single carbon nanotubes," Nano Letters, Vol. 3, pp.1067-1071 (2003).

14. A. Fujiwara, Y. Matsuoka, Y. Matsuoka, H. Suematsu, N. Ogawa, K. Miyano, H. Kataura, Y. Maniwa, S. Suzuki and Y. Achiba "Photoconductivity of single-wall carbon nanotube films," Elsevier Carbon, Vol. 42, pp.919-922 (2004).

15. X. Qiu, M. Freitag, V. Perebeinos, and P. Avouris, "Photoconductivity Spectra of Single-Carbon Nanotubes: Implications on the Nature of Their Excited States," Nano Letters, Vol. 5, pp.749-752 (2005).

16. A. Serra, D. Manno, E. Filippo, A. Tepore, M. L.Terranova, S. Orlanducci, and M. Rossi "Photoconductivity of packed homotype bundles formed by aligned single-walled carbon nanotubes," Nano Letters, Vol. 8, pp.968-971 (2008).

17. S. Lu and B. Panchapakesan, "Photoconductivity in single wall carbon nanotube sheets," IOP Nanotechnology, Vol. 17, pp.1843–1850 (2006).

18. S. Chuang, *Physics of optoelectronic devices*, (J. Wiley, 1995), Chap. 2.

19. M. C. Beard, J. L. Blackburn, and M. J. Heben, "Photogenerated free carrier dynamics in metal and semiconductor single-walled carbon nanotube films", Nano Letters, Vol. 8, pp.4238–4242 (2008).

20. S. Reich, M. Dworzak, A. Hoffmann, C. Thomsen, and M. S. Strano, "Excited-state carrier lifetime in single-walled carbon nanotubes", Physical Review B 71, 033402 (2005).

21. Y. Zhong Ma, L. Valkunas, S. L. Dexheimer, S. M. Bachilo, and G. R. Fleming, “Femtosecond spectroscopy of optical excitations in single-walled carbon nanotubes: evidence for exciton-exciton annihilation,” Physical Review Letter, Vol. 94, pp.157402 (2005).

22. E. C. Camus, J. L. Hughes, and M. B. Johnston, “Three-dimensional carrier-dynamics simulation of terahertz emission from photoconductive switches,” Physical Review B, Vol. 71, pp.195301 (2005).

23. A. Gambetta, G. Galzerano, A. G. Rozhin, A. C. Ferrari, R. Ramponi, P. Laporta, and M. Marangoni, “Sub-100 fs two-color pump-probe spectroscopy of single wall carbon nanotubes with a 100 MHz Er-fiber laser system,” Optics Express, Vol. 16, pp.11727-11734 (2008).

24. T. Hertel, R. Fasel, G. Moos, “Charge-carrier dynamics in single-wall carbon nanotube bundles: a time-domain study,” Applied Physics and Material Science Proceeding, Vol. 75, pp.449-465 (2002).

25. M. Bockrath, D. H. Cobden, J. Lu, A. G. Rinzler, R. E. Smalley, L. Balents and P. L. McEuen, “Luttinger-liquid behavior in carbon nanotubes,” Nature, Vol. 397, pp.598-601 (1999).

26. T. Durkop, B. M. Kim and M. S. Fuhrer, “Properties and applications of high-mobility semiconducting nanotubes,” Journal of Physics: Condensed Matter, Vol. 16, pp.R553–R580 (2004).

27. N. V. Smith, “Classical generalization of the drude formula for the optical conductivity,” Physical Review B, Vol. 64, pp.155106 (2001).

28. P. Parkinson, J. L. Hughes, Q. Gao, H. H. Tan, C. Jagadish, M.B. Johnston, and L. M. Herz, “Transient terahertz conductivity of GaAs nanowires,” Nano Letters, Vol. 7, pp.2162–2165 (2007).

29. M. Tsai, C. Yu, C. Yang, N. Tai, T. Perng, C. Tu, Z. Khan, Y. Liao, and C. Chi, “Electrical transport properties of individual disordered multiwalled carbon nanotubes,” Applied Physics Letter, Vol. 89, pp.192115 (2009).

30. V. Perebeinos, J. Tersoff, and P. Avouris, “Mobility in semiconducting carbon nanotubes at finite carrier density,” Nano Letters, Vol. 6, pp.205–208 (2006).

31. T. Durkop, S. A. Getty, E. Cobas, and M. S. Fuhrer, “Extraordinary mobility in semiconducting carbon nanotubes,” Nano Letters, Vol. 4, pp.35-39 (2004).

32. A. Behnam and A. Ural, “Computational study of geometry-dependent resistivity scaling in single-walled carbon nanotube films,” Physical Review B, Vol. 75, pp.125432 (2007).

33. S. Haque, C. Marinelli, F. Udrea and W.I. Milne, "Absorption characteristics of single wall carbon nanotubes," *NSTI Nanotechnolog Conference*, (NSTI 2006), pp.134-137.

34. M. Engel, J. P. Small, M. Steiner, M. Freitag, A. Green, M. C. Hersam, and P. Avouris, "Thin film nanotube transistors based on self-assembled, aligned, semiconducting carbon nanotube arrays", ACS Nano, Vol. 2, pp.2445–2452 (2008).

35. J. Hone, M. C. Llaguno, N. M. Nemes, A. T. Johnson, J. E. Fischer, D. A. Walters, M. J. Casavant, J. Schmidt, and R. E. Smalley, "Electrical and thermal transport properties of magnetically aligned single wall carbon nanotube films," Applied Physics Letter, Vol. 77, pp.666-669 (2000).

36. S. Verghese, K. A. McIntosh, and E. R. Brown, "Highly tunable fiber-coupled photomixers with coherent terahertz output power", IEEE Transaction Microwave Theory and Technology, Vol. 45, pp.1301–1309 (1997).

37. S. Duffy, S. Verghese, K. A. McIntosh, A. Jackson, A. C. Gossard, and S. Matsuura, "Accurate modeling of dual dipole and slot elements used with photomixers for coherent terahertz output power", IEEE Transaction Microwave Theory and Technology, Vol. 49, pp.1032–1038 (2001).

38. Y. C. Tsenga and J. Bokor, "Characterization of the junction capacitance of metal-semiconductor carbon nanotube Schottky contacts," Applied Physics Letter, Vol. 96, pp.013103 (2010).

39. S. H. Hana, S. H. Leea, J. H. Hura, J. Janga, Y. B. Parkb, G. Irvinb and P. Drzaicb, "Contact resistance between Au and solution-processed CNT," Elsevier Solid-State Electronic, Vol. 54, pp.586–589 (2010) .

40. M. G. Kang, J. H. Lim, S. H. Hong, D. J. Lee, S. W. Hwang, D. Whang, J. S. Hwang, and D. Ahn, "Microwave characterization of a single wall carbon nanotube bundle," Jap. Journal of Applied Physics, Vol. 47, pp.4965-4968 (2008).

41. Z. Yao, C. L. Kane, and C. Dekker, "High-field electrical transport in single-wall carbon nanotubes," Physical Review Letter, Vol. 84, pp.2941-2944 (2000).

42. V. Pacebutas, A. Biciūnas, S. Balakauskas, A. Krotkus, G. Andriukaitis, D. Lorenc, A. Pugzlys, and A. Baltuska, "Terahertz time-domain-spectroscopy system based on femtosecond Yb:fiber laser and GaBiAs photoconducting components," Applied Physics Letter, Vol. 97, pp.031111 (2010).

43. M. Tani, S. Matsuura, K. Sakai, and S. Nakashima, "Emission characteristics of photoconductive antennas based on low-temperature-grown GaAs and semi-insulating GaAs," Applied Optics, Vol. 36, pp.7853-7859 (1997).

44. P. Kordos, M. Marso, and M. Mikulics, “Performance optimization of GaAs-based photomixers as sources of THz radiation,” Applied Physics A, Vol. 87, pp.563–567 (2007).

45. K. Kordás, G. Tóth, P. Moilanen, M. Kumpumäki, J. Vähäkangas, A. Uusimäki, R. Vajtai, and P. M. Ajayan, “Chip cooling with integrated carbon nanotube microfin architectures ,” Applied Physics Letter, Vol. 90, pp.123105 (2007).

46. H. Pahlevaninezhad, B. Heshmat, and T. E. Darcie, "Advances in THz technology" IEEE Photonics Journal, Vol. 3, pp.307-310 (2011).

Appendix C: Carbon nanotube based photoconductive switches for THz detection: An assessment of capabilities and limitations

(2012, IEEE Photonics Journal, volume 4, pp.970)

Reprinted with permission from the IEEE Photonics Journal © Copyright (2012)

Institute of Electrical and Electronics Engineers.

Carbon nanotube based photoconductive switches for THz detection: An assessment of capabilities and limitations

B.Heshmat, H.Pahlevaninezhad, T.E.Darcie, Fellow, IEEE

Department of Electrical and Computer Engineering, University of Victoria, Victoria, BC V8P 5C2, Canada

Abstract: Carbon nanotubes possess appealing properties for THz applications. This work investigates the contribution of these properties in the context of THz PC switches as THz detectors. The analysis engages the received THz electric field, the optical excitation, and the photocarrier dynamics of the carbon nanotube material through Drude-Smith theory and equivalent circuit model. Through this analysis the effect of each parameter in the detected current can be investigated. Based on a realistic numerical assessment and comparison with our measurements for a conventional LT-GaAs PC switch, it is found that improvement in detected current is theoretically achievable, depending on the relative value of the imaginary photoconductivity of the CNT film. This is a parameter that can be varied through chemical treatment of the film. We found that, unlike the case of PC switches as THz emitting devices where a higher mobility is desired for higher output THz power, the detected current in the THz receiving PC switch is a nonmonotonic function of the mobility in the SWNT film. The capabilities and limitations revealed in this study set guidelines for fabrication and optimization of more efficient carbon nanotube-based THz receiving PC switches. The study also addresses the fabrication process and challenges.

Index Terms: Terahertz, Photoconductive switch, Photomixers, Carbon nanotubes.

1. Introduction

Terahertz (THz) photoconductive switches (PC switches) are optically excited, fast semiconductor switches that can both emit and detect THz radiation [1]. These devices are composed of microantenna structures (typically made with gold), that are fabricated on fast semiconducting materials such as low temperature grown GaAs (LT-GaAs), InGaAs and GaBiAs [1-3] (Fig. 1 (a)). Low output power at the transmission side and

low detected current at the receiver side have limited the applications of these devices since their invention [1, 4].

Exceptional properties of single-wall carbon nanotubes (SWNT), such as high mobility, high optical density, high heat conductance and band gap tunability, have been applied successfully for fabrication of more sensitive infrared and terahertz detectors [5-11]. These properties have raised a noticeable research interest in carbon nanotube-based THz and IR detection and sensing. Bolometric [7-9], diodic [10], and direct excitation mechanisms [11] have been considered for CNT-based THz detection. Improvement in detection is especially desired and pursued in THz range, where the generated radiation powers are typically in the nanowatts range [1].

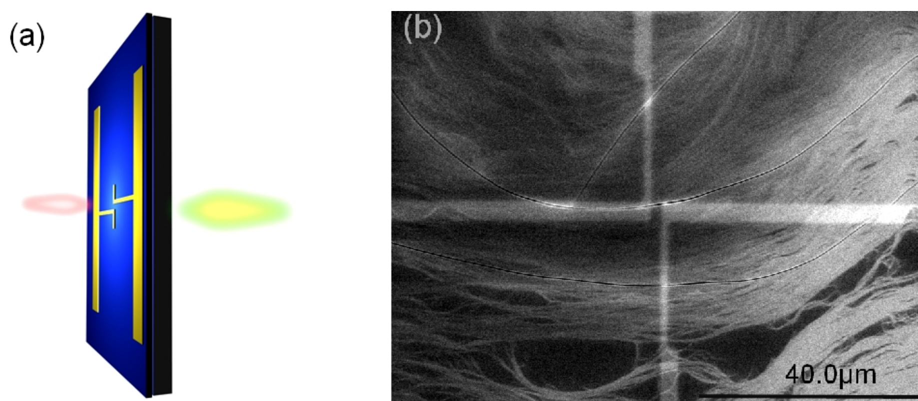

Fig. 1. (a) Photoconductive switch is excited with an optical pulse on the left to detect the incoming THz pulse from the right. (b) Scanning electron microscope image of a carbon nanotubes deposited on the gap of a center fed antenna. The image is taken at 30kV to reveal the gold antenna structure beneath the CNT film. The substrate is a thin film SiO_2 on float zone Si and the antenna pattern is made through common lithographic processes.

Recent studies have predicted higher power THz emission when using CNTs in a PC switch device [12-14] (Fig. 1 (b)). These studies have been focused on higher output power when the PC switch is used as THz transmitter [12, 13]. However, it is not known if a CNT-based PC switch has the same superior potential for THz detection at the THz receiving side of a THz heterodyne detection system. Previous work on PC switches made with conventional materials has shown significant difference in design concerns for a THz photomixer when it is used as THz receiver compared to when it is used as THz transmitter [15]. The dynamics of the substrate material in THz-receiving PC switches have not been explored in a systematic theoretical approach even in case of bulk

materials. As it will be explained further in this study, the material that is proper for the transmitter is not necessarily the best choice for the receiver.

In this work, we present a theory that predicts and explains the CNTs' capabilities and limitations as THz detectors in the context of a THz receiver PC switch. We apply a recently introduced concept on CNT-based THz-emitting pc switches [12] to develop a model for predicting the dynamics and performance of CNT-based THz-receiving PC switches. The theory relates input optical and THz radiations to the detected DC current as depicted in Fig. 2. As it can be seen in this figure, with the knowledge of the free photocarrier concentration in the SWNT film, its photoconductivity can be calculated. In the next step, the photoconductivity is converted into photoconductance with consideration of gap geometry. The received THz field induces voltage across the same gap, and thus these two parameters affect the detected current through the circuit model of the antenna structure. Based on this approach the effect of each parameter is then investigated and the potential and limitations are highlighted through numerical evaluations. Finally, the fabrication challenges and procedures are investigated in the last section.

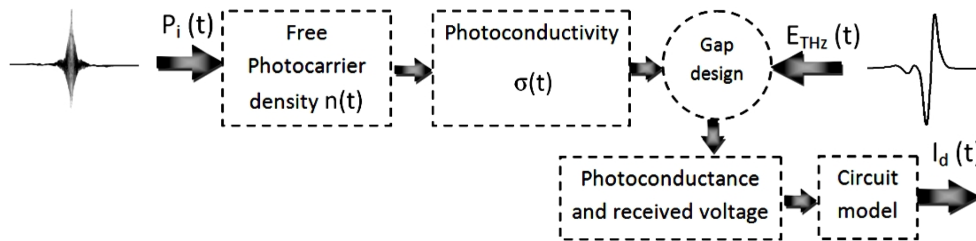

Fig. 2. Block diagram of the analysis that connects input optical and THz power to detected current in the THz receiver PC switch or photomixer.

2. Calculation of free photocarrier density

Calculation of free photocarrier density for a THz-receiving PC switch is similar to that of a THz-emitting PC switch. Both devices are excited optically in a heterodyne configuration. We will cover this step briefly to preserve the continuity of the theory. In order to calculate the total photocarrier density, the input optical excitation power is converted into the initial absorbed photon density. For an optical pulse with power of $p_i(t,v)$ the initial absorbed photon density can be estimated by integrating the number of absorbed photons over frequency and time; that is

$$n_{abs} = \int_{\nu_0 - 0.5\Delta\nu}^{\nu_0 + 0.5\Delta\nu} \int_0^{\mathrm{T}} \frac{\eta(\nu) p_i(t,\nu) dt}{h\nu V} d\nu \approx \frac{\eta(\nu_0)\int_0^T p_i(t,\nu_0) dt}{h\nu_0 V}. \quad (1)$$

In this estimation the pulse bandwidth, $\Delta\nu$, is considered negligible compared to the center frequency of the radiation ν_0. At the denominator, V is the volume of the sample and $h\nu$ is the energy of each photon with frequency ν. $\eta(\nu)$ is quantum efficiency of the material, which is directly dependent on the chirality of individual CNTs and purification level of the sample [16]. As it is revealed by Eq. 1 the absorbed photon density (n_{abs}) has a linear relation with input optical power level and thus the rest of the analysis can be expressed in terms of n_{abs} for simplicity. This is preferred since the function $\eta(\nu)$ is highly sample dependent and is usually measured in practice [16]. Due to exponential decay rate in power for a pulsed excitation, the integration limit T can be replaced by pulse width while inducing a negligible inaccuracy in the result of the integration.

Not all of absorbed photons can contribute to the fast photoconductivity of the material, and thus carrier dynamics of the SWNT film should be considered to find the total number of photocarriers. Previous studies on the THz photoconductivity of SWNT films show that a set of rate equations with the following solution can be used to express and predict the photoconductivity of the material [17].

$$n(t) = k_2 - \frac{\gamma_{CC}^2 \, {}_2F_1\left(1, \frac{\gamma_d}{\gamma_{CC}}, 1 + \frac{\gamma_d}{\gamma_{CC}}, \frac{e^{\gamma_{CC}(t+k_1)}}{\gamma_{EE}}\right)}{\gamma_{EE}\gamma_d}, \quad (2)$$

where,

$$k_1 = \frac{\ln\left(\gamma_{EE} + \gamma_{CC} / n_{abs}\right)}{\gamma_{CC}}, \quad \text{and} \quad k_2 = \frac{\gamma_{CC}^2 \, {}_2F_1\left(1, \frac{\gamma_d}{\gamma_{CC}}, 1 + \frac{\gamma_d}{\gamma_{CC}}, \frac{e^{\gamma_{CC} \times k_1}}{\gamma_{EE}}\right)}{\gamma_{EE}\gamma_d}.$$

Eq. 2 relates the total photocarrier density n to the initial absorbed photon density n_{abs}. In this equation, ${}_2F_1$ is a hypergeometric function, γ_{CC} is the carrier generation rate by exciton dissociation, γ_{EE} is exciton-exciton annihilation rate, and γ_d is equal to the reciprocal of the carrier lifetime τ and is called carrier decay rate. To obtain Eq. 2, it is implicitly assumed that each absorbed photon generates an exciton on the femtosecond timescale and excitons do not decay in the short duration of the excitation itself. With

typical set of values for these parameters [17-19] (γ_{CC}=3.4 ps^{-1}, γ_{EE}=6.9×10^{-19} exciton^{-1}cm^{-3}ps^{-1}, 0.033 <γ_d<3.19 ps^{-1}) the following dynamics is found for the total photocarrier density (Fig. 3 (a)).

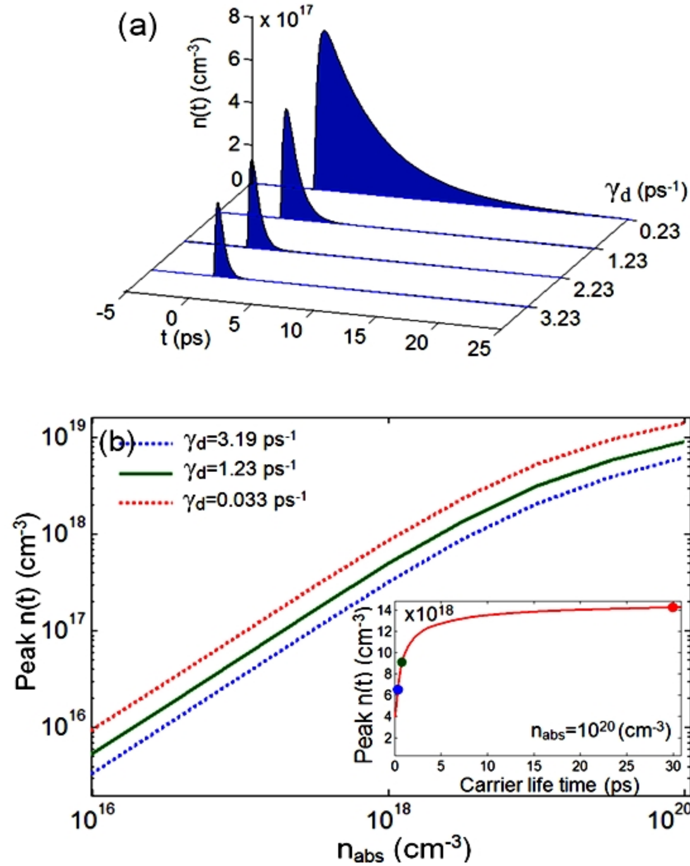

Fig. 3. (a) Total photocarrier density as a function of time at four different carrier decay rates
(b) Peak photocarrier density as a function of absorbed photon density; the inset graph shows the variation of peak n(t) with changes in carrier lifetime.

Here a typical 100fs Gaussian excitation pulse is assumed for generation of initial n_{abs}. As it is seen in Fig.3 (b), the peak value of $n(t)$ slowly saturates with increase in absorbed photon density; this behavior agrees with previous measurements [17]. The total photocarrier density also saturates with the increase in carrier lifetime. This happens rather rapidly after $\tau \approx 4$ ps, as seen in the inset graph of Fig. 3 (b).

These dynamics play a definitive role in the design of the CNT film that is to be used in the gap of a PC switch. Based on Fig. 3, the carrier lifetime and input optical pulse can dramatically affect the number of photocarriers present in a given instance. This directly

affects the photoconductivity of the sample that is involved in detecting the THz signal. The total carrier density $n(t)$ is itself the summation of free photocarrier density $n_f(t)$ and localized carrier density $n_b(t)=n(t)-n_f(t)$. As we will see in the following section these two parts have a linear relation with the fast photoconductivity of the CNT film.

3. SWNT film's photoconductivity dynamics

There are several accurate models for calculation of photoconductivity in individual SWNTs [20-23]. To study the photoconductivity of simple small scale systems ab initio simulation [21] and Luttinger-liquid theory [22] can be used. However, for the case of a PC switch two important factors must be considered: first, the antenna gap is filled with millions of carbon nanotubes typically bundled into bundles of 50 to 100nm width (Fig. 1 (b)); second, the photoconductivity of concern in this study is the fast photoconductivity in THz range and thus its dynamics are rather different from the low frequency range photoconductivity that is obtained by drift diffusion equations. The drift diffusion dynamics are commonly used in solar energy conversion applications [24, 25]. These two factors leave Drude-based models as a more proper choice compared to ab initio, density functional theory based models. The Drude-Smith (DS) model has been used with fair results in case of different 1D materials [17, 26, 27]. The Drude-Smith formulation for photoconductivity that is given as:

$$\sigma_{photo}(\omega,t)=\frac{\tau_s n_f(t)e^2}{m^*(1-i\omega\tau_s)}\left(1-\frac{\xi}{1-i\omega\tau_s}\right)+i\frac{n_b(t)e^2\omega}{m^*(\omega^2-\omega_l^2-i\omega\gamma_l)}, \tag{3}$$

has a linear relation with temporal profile of free photocarrier density $n_f(t)$ and localized photocarrier density $n_b(t)$. The other parameters in Eq.3 are: effective mass (m^*), applied field frequency (ω), photocarrier localization factor ($0<\zeta<1$), average carrier scattering time (τ_s), Lorentzian term frequency (ω_l), and Lorentzian momentum rate (γ_l). The total photocarrier density that was obtained in previous section is equal to the sum of n_f and n_b (for SWNT films $|n_b|<n_f$). n_b is negative when the optical excitation bleaches the previously available localized carriers into free photocarriers and it is positive when the excitation generates some new localized carriers. The ratio between localized and free photocarriers is usually found through time resolved terahertz spectroscopy measurements (TRTS) and curve fitting process [17, 28].

In contrast to a THz-emitting PC switch, where the bias is either a DC bias or a low-frequency chopped bias, for the receiver PC switch the bias voltage is directly induced on the antenna by the received THz electric field. Therefore, the THz dynamics of the DS model cannot be neglected as in THz-emitting PC switch. The antenna design and performance thus must be considered in the primary steps of the theory in case of the receiver, while in case of the transmitter the antenna design is a secondary concern that is considered mostly for obtaining desired directivity and radiation pattern. Figure 4 shows the photoconductivity of a semiconducting SWNT film. As it is seen and also previously measured [17], both the imaginary and the real part of the photoconductivity can significantly change over the THz region. THz induced bias adds a new twist to our model – the CNT bundles cannot be simplified as an ohmic high mobility photoconductance anymore, and the frequency dependent inductive and/or capacitive behavior of the CNT film itself should be considered both in DS model and circuit analysis. Considering the wide range of variations in the reported values for the parameters in Eq. 3 ($0.01<\mu<10$ m^{2}v^{-1}s^{-1}, $0.01<\tau_s<5$ ps, $0.6<\xi<0.9$, $20<\omega_l<80$THz and $0.2<\gamma_l<20$ ps^{-1}) [27, 29, 30] it is necessary to address the dynamics of the photoconductivity with variation of these parameters. In THz frequency range, the photoconductivity is not highly sensitive to the variations of γ_l and ξ. ω_l is the parameter that tunes the peak frequency as seen in the inset graphs of Fig. 4. (The values used for figure 4 are as follow: μ=0.0155 m^{2}v^{-1}s^{-1}, τ_s=0.088ps, ξ=0.83, ω_l=23THz, γ_l=2.5 ps^{-1}, $m^*=m_e$, $\max(|n_b(t)|)=2.1\times10^{18}$ cm^{-3} and $\max(n_f(t))=4\times10^{18}$ cm^{-3}).

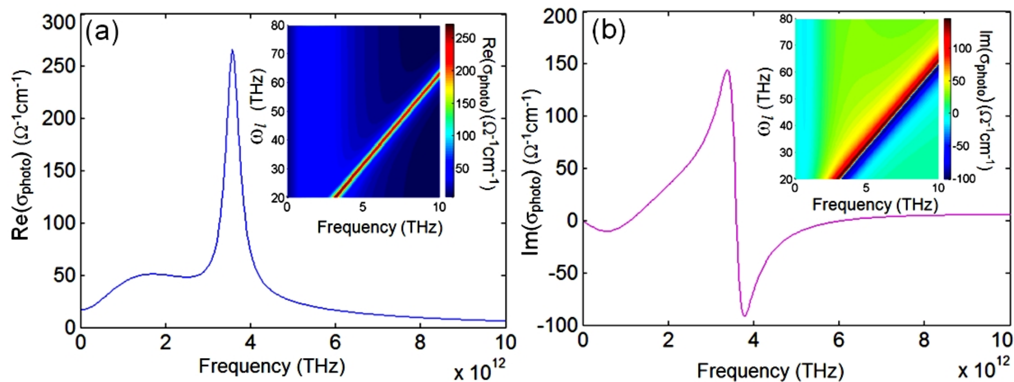

Fig. 4. (a) Real part of photoconductivity in the SWNT film. The inset graph shows further dynamics of the parameter versus Lorentzian frequency. (b) Imaginary part of the photoconductivity in SWNT film. The inset graph shows the 2D color graph of the photoconductivity with variation of ω_l and bias frequency.

Based on previous measurements [17], this frequency can increase with increasing the percentage of metallic CNTs in the film. Therefore, in case of a CNT-based THz-receiving PC switch, the semiconducting percentage or purification level of the film should be chosen so that the photoconductivity is optimized with regard to the receiving antenna circuit. This is rather unexpected and significantly different from the case of transmitter, where higher mobility and proper carrier lifetime are the major concerns. It is also in contrast to the common trend in bulk-material PC switches where the transmitter and receiver are both made from the same substrate. Mobility implicitly affects the photoconductivity in Eq. 3 since $\mu = e\tau_S / m^*$ [31]. It might be assumed that the higher mobility results in a higher photoconductivity. However, that is not always the case in the THz frequency range.

The relative effect of the mobility in photoconductivity depends on the physical nature of the factor that varies the mobility; if the mobility is increased with a constant average scattering time due to reduction in effective mass [31], then the photoconductivity increases as same as mobility with a reciprocal of the effective mass (dotted lines in Fig. 5). However, if the mobility is increased only because of increase in average carrier scattering time, then the photoconductivity might even be reduced in the THz range (solid lines in Fig. 5). Such reverse relation is more pronounced in the real part of the photoconductivity since the imaginary part in THz frequency ranges varies slightly with changes of τ_S (Eq. 3). It is noteworthy that in theory the average carrier scattering time itself is a function of effective mass, temperature and conduction band shifts near the Fermi surface, so for tuning the carrier scattering time, temperature and chirality of the SWNT can be varied [32].

Fig. 5 shows that the increase in mobility does not necessary provide higher photoconductance for this application, and thus for the highest level of photoconductivity the mobility should be increased only due to decrease in effective mass. Since the absorption of the pulse laser directly affects the number of excited photocarriers (Eq. 1) and consequently the photoconductance (Eq. 3), the diameter distribution in the SWNT film should be chosen so that the absorption is maximized. The CNT diameters have a Gaussian distribution that relates to the range of chiralities available in the sample [33]. For a given excitation wavelength the diameter range of the semiconducting chiralities

are preferred since samples with higher level of semiconducting CNTs generally tend to show lower Lorentzian frequencies [17]. As shown in the inset graphs of Fig. 4, a lower Lorentzian frequency (ω_l) shifts the photoconductivity peak closer to 1THz. An approximation for the diameter range can be found through Kataura plots [34] that relate the CNT diameter to its absorption peaks and chirality. It is difficult to purify a large sample to a specific chirality; however, metallic or semiconducting enrichment of a sample can be performed to a fair level [35, 35].

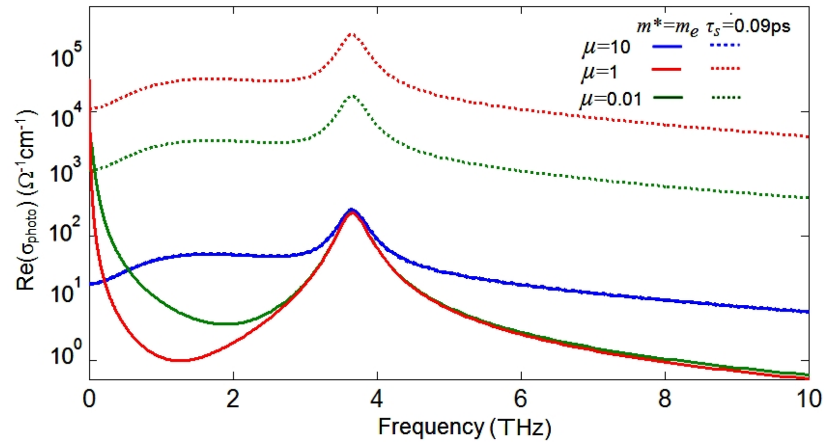

Fig. 5. Real part of photoconductivity for different mobility values when the mobility changes with fixed effective mass (solid line curves), and when it changes with fixed average carrier scattering time (dotted line curves).

4. Receiver circuit model and detected current dynamics

For the circuit model, photoconductivity and conductivity of the SWNT film should be converted to photoconductance and conductance. For bulk material the simple classical definition of conductance holds; that is:

$$G(t,\omega) = (\sigma_{dark}(\omega) + \sigma_{photo}(t,\omega))yz/x, \tag{4}$$

where yz is the area of the cross section of the film, x is the gap length and $\sigma_{dark}(\omega)$ is the frequency dependent conductivity of the film. This model is accurate for bulk material; however, for SWNT films, the directional conductance, and randomness in the CNT types can cause inaccuracy [37]. The anisotropic conductance of CNTs raises concern regarding the alignment of the CNTs in the CNT film with the received THz filed across the gap. SWNTs can be fairly aligned with the gap structure via slip-stick deposition method (Fig1. (b)) [38]. For calculating the conductance of the film in the antenna gap we assumed that misalignments with the electric field are negligible (less than 15º). Since

there are CNTs with different types and lengths in the SWNT film, the statistical distribution for each parameter should be considered in calculating the average conductance. Monte Carlo integrations can be used to obtain a more accurate result for the conductance. In this study we will use the highest and the lowest measured reported values so that the average results are covered within the calculated range.

Based on significant variations of the imaginary parts of CNT conductance and photoconductance at THz frequencies, both negative and positive values of the imaginary part should be considered. The circuit model is depicted in Fig. 6. In this circuit the SWNT film conductance and photoconductance are shown with a resistive element ($G_r(t)$) and an imaginary time varying capacitive or inductive element ($G_i(t)$). The other elements are: antenna impedance R_L, contact shunt capacitance C_c, contact resistance R_c and gap capacitance C. Also, other variables are depicted in Fig. 6. The gap capacitance, C, is created by two antenna electrodes facing each other (Fig. 1). Also, in this model an ohmic behavior is assumed for CNT film-metal contacts [39]. As it is depicted in Fig. 6, the circuit model is significantly different from bulk material THz photomixers [2]. When CNTs are used as base material in the gap, the imaginary part cannot be ignored. Additionally, the contact resistance is a significant point of concern when dealing with SWNTs in the gap [39]; the contact resistance is usually noticeable for CNT to metal contacts and such resistance cannot be neglected as same as LT-GaAs PC switches and photomixers [2]. On the other hand, as it will be further explained in section 5, there is a good chance that many of the CNTs couple capacitively with the electrodes and thus a contact capacitance should be used in the model. The study of the electrical behavior of CNT-metal contacts is an ongoing field of research [39, 40] and further details regarding the contacts are out of the scope of this study. Compared to a THz transmitter, the THz receiver has a different circuit model based on the different functionality of the two devices. While in a THz-emitting PC switch the circuit model is to calculate the output THz power, the detected DC current is the parameter of interest in case of the receiver. As mentioned previously, the THz field received in the receiver biases the gap material (in this case CNTs), and therefore, the THz model of the material enters the circuit analysis.

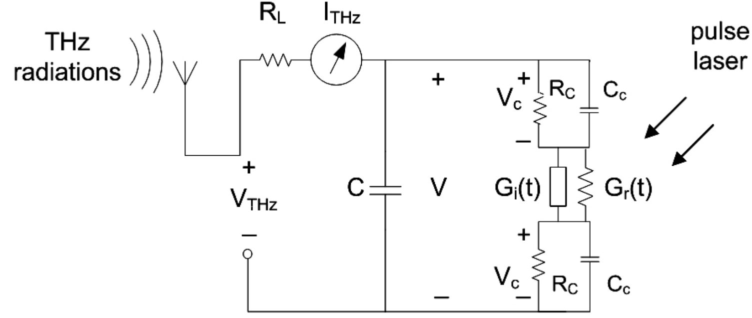

Fig. 6. Schematic view of the circuit model for the SWNT-based THz PC switch as a THz receiver. The received THz radiation generates V_{THz} on the antenna and at the same time the pulse laser is generating photocarriers in the gap.

By applying Kirchhoff's current laws to this circuit, a set of coupled inhomogeneous differential equations are obtained. These equations can vary based on the sign of $G_i(t)$; if $G_i(t)$ is positive the equivalent element is capacitive with capacitance $C_g(t) = G_i(t)/\omega$; in this case Eq. 5 holds.

$$\begin{aligned} C\frac{dV}{dt} + G_r(t)(V - 2V_c) + C_g(t)\frac{d(V - 2V_c)}{dt} &= \frac{V_{THz} - V}{R_L}, \text{ wtih} \frac{dV(0)}{dt} = V(0) = 0, \\ C_c\frac{dV_c}{dt} + \frac{V_c}{R_c} &= G_r(t)(V - 2V_c) + C_g(t)\frac{d(V - 2V_c)}{dt}, \text{with} \frac{dV_c(0)}{dt} = V_c(0) = 0. \end{aligned} \tag{5}$$

If $G_i(t)$ is negative, the equivalent element is inductive with inductance $L_g(t) = 1/(\omega G_i(t))$ and Eq. 6 holds. And finally, if $G_i(t)$ is insignificant, Eq. 5 merges with Eq. 6 when $C_g(t)$ is replaced with zero in Eq. 5 and $L_g(t)$ is replaced with infinity in Eq. 6.

$$\begin{aligned} C\frac{dV}{dt} + G_r(t)(V - 2V_c) + \frac{1}{L_g(t)}\int_0^t (V - 2V_c)dt &= \frac{V_{THz} - V}{R_L}, \text{ wtih } \frac{dV(0)}{dt} = V(0) = 0, \\ C_c\frac{dV_c}{dt} + \frac{V_c}{R_c} &= G_r(t)(V - 2V_c) + \frac{1}{L_g(t)}\int_0^t (V - 2V_c)dt, \text{ with } \frac{dV_c(0)}{dt} = V_c(0) = 0. \end{aligned} \tag{6}$$

In Eq. 5 and Eq.6 all voltages are function of time and received THz frequency, since $G_r(t)$ and $G_i(t)$ are function of time and received E-field frequency ω; t and ω are dropped only for simplicity.

Unlike photomixers made with bulk materials such as LT-GaAs and GaBiAs where the differential equations can be simplified due to single frequency operation and negligibility of contact resistances [2-4], further simplification is not possible for case of

SWNT films. The time varying voltage, V(t) cannot be expressed explicitly. This is due to hypergeometric nature of the photoconductivity functions (Eq. 2 and 3).

The case of pulsed mode is assumed in this study to keep the equations general; the results for this case can be simplified to continuous wave (CW) mode for the THz photomixing, if the relative CW photoconductance is substituted. Finally, the average detected current in the SWNT-based THz PC switch is calculated as:

$$I_{dc} = \frac{1}{T}\int_0^T I_{THz}(t)dt = \frac{1}{T}\int_0^T \frac{V_{THz}(t) - V(t)}{R_L}dt, \qquad (7)$$

In this equation, T is the period obtained from repetition rate of the pulse laser as in Eq.1. At this point the desired link between input optical pulse, received THz signal and detected current is obtained (Fig. 2). I_{dc} is a constant DC current that is usually detected by a lock-in amplifier; however, since in practice $V_{THz}(t)$ can have a temporal phase difference with incoming optical excitation pulse, the detected current is usually monitored (sampled) with variations of delay in the received THz signal. This is usually done with varying the length of the light path for some hundreds of micrometers [1-4]. In this case $V_{THz}(t)$ and I_{dc} in Eq. 7 can be replaced with $V_{THz}(t\text{-}d)$ and $I_{dc}(d)$, where d is the delay between the received THz field and input optical pulse.

In order to evaluate the presented theory, we measured the THz electric field for 100nW radiation generated by a LT-GaAs PC switch (Fig. 7 (a)). Considering a typical PC switch design with a dipole antenna structure (x=y=5µm and z=100nm). This field can be converted to a voltage that is induced in the antenna (Fig. 7 (a)). By substitution of common values for SWNT film, dipole antenna, and pulse excitation parameters in Eq. 6 and 7, (R_L≈30Ω [2-4], C≈ 7fF [2, 41], Cc≈ 100fF [42], Rc≈20kΩ [41, 42], $G_{r\ (dark)}$ = -$G_{i\ (dark)}$ ≈2mΩ^{-1}, peak $G_{r\ (photo)}$ =-10 peak $G_{i\ (photo)}$ ≈640µΩ^{-1},$G_{i\ (photo)}$ ≈0 [17, 41, 42], $\eta(v) = \eta$ =0.1 [16], received THz power=100nW, optical pulse duration=100fs, excitation wavelength=830nm, and repetition rate=100MHz) the current can be calculated as shown in Fig. 7 (b). Here, we have used the numerical Euler method with 10 fs step sizes to estimate $V(t)$. $V(t)$ is then substituted in the current integral in Eq. 7. V_{THz} was also calculated using the measured field and antenna theory, for an effective length of 10µm [43].

Figure 7 (c) shows the complete range of results for the numerical example. As can be seen in the inset graph, the decrease in effective mass does not linearly affect the detected current. This is the direct result of the presence of inductive behavior for the SWNTs photoconductance. The increase in mobility both increases the imaginary part and the real part of conductance and photoconductance and as a result the total effect turns out to be a decrease in detected current level for higher mobility values (lower effective masses). We find that the negative imaginary part significantly damps the detected signal. This is because the negative imaginary part has a reciprocal relation with the equivalent inductance and therefore for larger imaginary parts smaller inductance is in parallel with the resistive photoconductance that generates the current (Fig. 6).

The dotted blue line in Fig 7(c) shows the peak detected current versus optical excitation power for a SWNT sample with negative imaginary dark conductance $G_{i\,(\mathrm{dark})}$ (abbreviated as G_{id} in the figure) equal to the value of the real dark conductance $G_{r\,(\mathrm{dark})}$ (abbreviated as G_{rd} in the figure). As can be seen, the curve slightly loses its slope for higher powers due to carrier density saturation that was found in Fig. 3 (b). The negative imaginary part of the dark conductance can be significantly reduced depending on sample preparation and frequency of the incoming THz E-field [17]. If $G_{i\,(\mathrm{dark})}$ is reduced to one tenth of the real dark conductance ($G_{r\,(\mathrm{dark})}$) the dark green curve is found. The light green curve in Fig. 7 (c) is found if the imaginary part is equated to zero. As it can be seen, no noticeable improvement can be achieved relative to the dark green curve. With increase in mobility (decrease in m_e) the dark red (triangle marked) curve is found. It is found that even if the negative imaginary dark conductance is set to zero, the peak detected current still reaches an early saturation region in higher optical powers due to negative imaginary part of the photoconductance itself. This is the direct result of reciprocal relation between imaginary part of $\sigma_{(\mathrm{photo})}$ and m_e that was considered in DS model. Finally the dashed red curve is the highest limit of the peak detected current; it is obtained only if both imaginary parts of dark and photoconductance are set to zero and the mobility is raised in the sample close to its intrinsic value of 10 $m^2v^{-1}s^{-1}$. Therefore, in summary the results of this typical SWNT-based PC switch as a THz receiver can be categorized into three regions (Fig. 7 (c)):

Green region: this region is obtainable with no necessity for high mobility or very low negative imaginary part. The detected currents are likely to be around 100pA to 10nA. This partially covers the current range reported in some earlier studies for conventional PC switches [44, 45].

Yellow region: this region, that is between the light green curve and dark marked red curve, is found only if the dark imaginary conductance is tuned to zero and if the mobility is increased to 1 $m^2v^{-1}s^{-1}$. We find that further increase of mobility does not help to extend this region to higher current levels because of the simultaneous increase in imaginary photoconductance. As it can be seen, our measurements for LT-GaAs PC switch falls in this region that is extended from 10nA to around 100nA. In order to access the current levels in this region the alignment and semiconducting purification of the SWNTs in the film should be considered to improve the mobility and efficiency. Also the decrease in imaginary part might be realizable through some chemical treatments to the film [17]. The results show an order of magnitude increase in higher limit of this range relative to measured currents for LT-GaAs PC switch.

Red region: In order to realize the range of currents detected in this region (100nA to 10μA), the imaginary part of both photoconductance and conductance should be tuned to zero. And the sample needs to possess mobility levels close to previously measured intrinsic mobility of SWNTs [29, 30]. Fabrication challenges are very significant for operating in this region, since high mobility and zero imaginary conductivity are needed simultaneously. However, the region clearly marks the highest current level that is obtainable in theory.

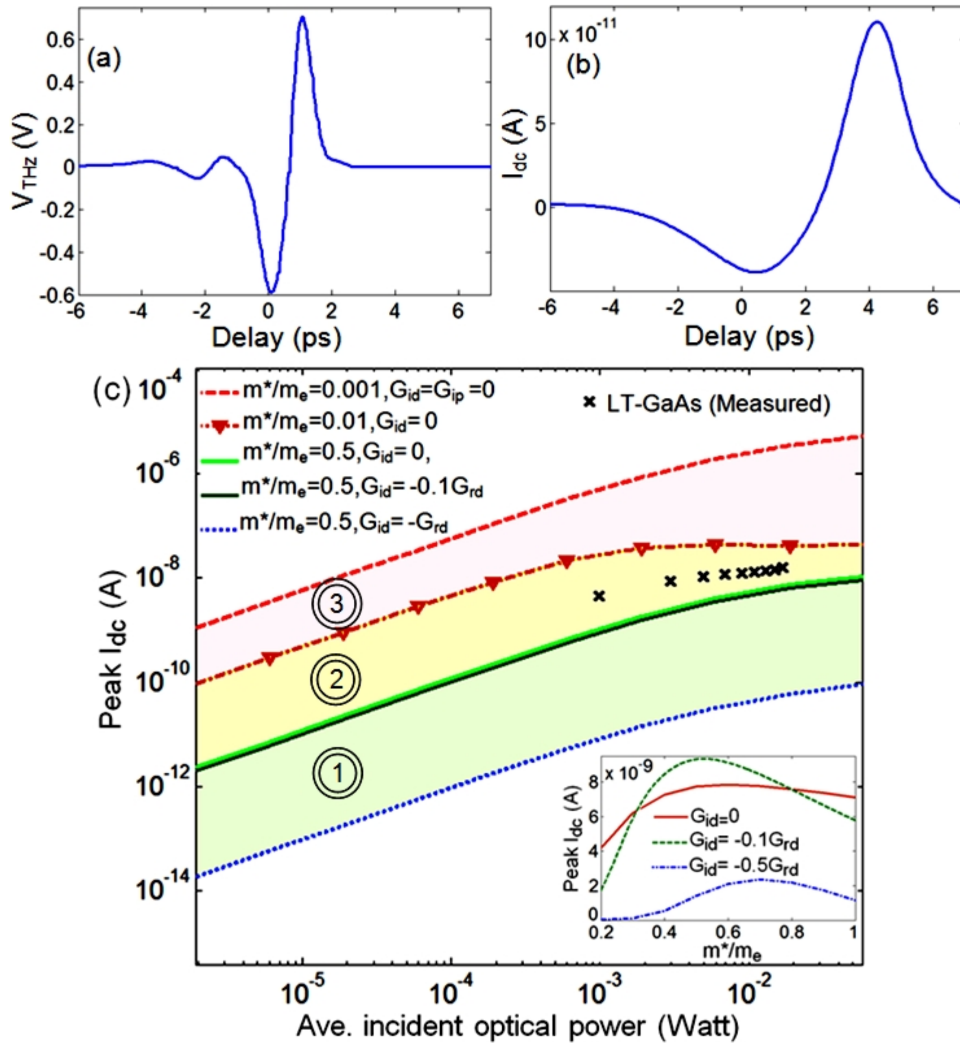

Fig. 7. (a) Received THz field that is converted to the voltage on the dipole microantenna. (b) A sample of calculated detected current with $G_{i\,(dark)}$=-$G_{r\,(dark)}$. (c) The estimated peak detected currents with different values for mobility and imaginary photoconductivity. Based on different assumptions 3 regions are found. The inset graph shows the peak detected current variations with change in the effective mass.

In order to understand the dynamics of the circuit model, it is important to investigate the effect of each parameter. The parameters that are considered in the circuit model can be varied in practice with change in the gap design and antenna design [1-4]. Figure 8 shows the behavior of peak detected current with variation of different PC switch parameters.

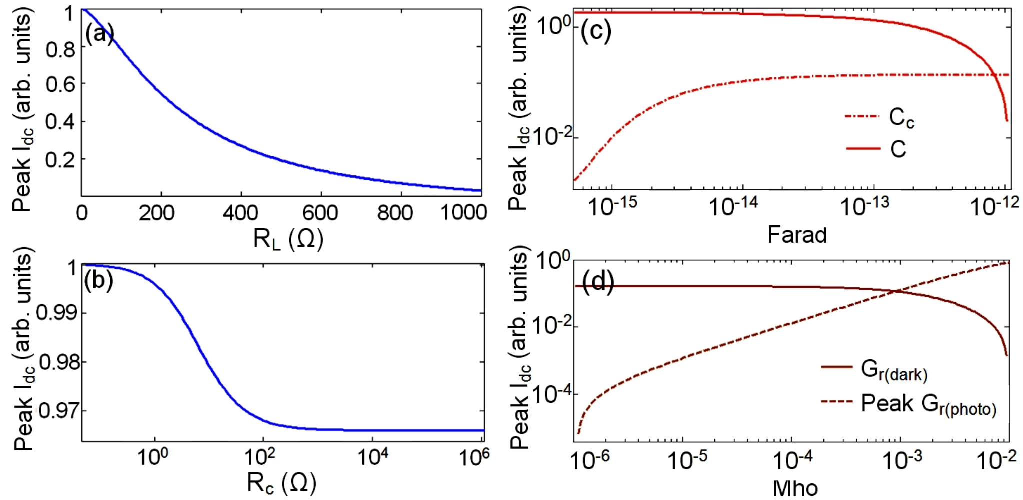

Fig. 8. (a) Peak detected DC current in the receiver PC switch versus: (a) antenna resistance, (b) CNT-metal contact resistance, (c) contact capacitance C_c and gap capacitance C, (d) real dark conductance G_r (dark) and peak of the real photoconductance G_r (photo).

Fig. 8 (a) shows that the reduction in antenna resistance is desirable in the receiver. This is in contrast with a THz emitting PC switch where higher antenna resistance is needed for higher power THz radiation. Such contrast stems from the difference in the functionality of the PC switch as a receiver. Unlike the THz transmitting PC switch where the current needs to be converted to radiated power through a microantenna, the DC current needs to be received by the lock-in amplifier in the receiver and thus higher voltage drop on the antenna resistance is not necessarily desired (Eq. 7) [15]. The increase in contact resistance (Fig. 8 (b)) can reduce the detected current. For contact resistances higher than 1kΩ, the reduction is not visible due to domination of the capacitive coupling of the SWNTs with the metallic electrodes. It is found that increase in contact capacitance increases the detected current up to a certain level. However, the gap capacitance should be kept small in order to avoid the SWNTs in the gap from being short circuited in higher frequencies by the parallel gap capacitance (Fig. 8 (c)). Fig. 8 (d) shows that in contrast to higher values of real photoconductance, that is desired, the peak detected current is significantly reduced by increase in dark conductance for values higher than $10m\Omega^{-1}$. This further explains the nonmonotonic behavior of the detected current with increase in mobility that was observed in the inset graph of Fig. 7 (c).

Two other parameters of significance are the imaginary dark conductance and the carrier lifetime in the SWNTs. Figure 9 investigates these two parameters in detail. It is found that the negative imaginary part not only affects the amplitude but also distorts the

detected pulse shape. This can have a vital role for spectroscopy applications where a clean pulse needs to be detected [46]. It should be further emphasized that distortion in the pulse shape is similarly seen in other new material for PC switching. Since typically both transmitter and receiver are made from same material it might be wrongly concluded that the transmitter is emitting a distorted pulse and thus care must be taken for interpretation of the detected pulse shapes in the THz heterodyne setups. As the DS model predicts, the imaginary part might also become positive for some frequencies [47]. Such a case is addressed in Fig. 9 (b). As it is seen in this figure, the increase in positive imaginary part of conductance has a slighter effect on the pulse shape—the positive imaginary part must be more than an order of magnitude higher than the real part for the pulse shape to be notably distorted.

Figure 9 (c) shows the change in the absolute value of the detected current peak for positive and negative values of the dark imaginary conductance. Based on Fig. 9 (c), for the negative values of imaginary part the peak is reduced exponentially. This reduction is also followed by some oscillations around zero. Because of the oscillations the sign of the detected current also changes and thus (as seen in the absolute value plot in Fig. 9 (b)) there are multiple values that the detected current crosses zero. This can be expected from significant phase variations that is induced in $V(t)$ due to exponential increase in the inductive element ($L_g(t)$) as the negative $G_i(t)$ value is reduced toward zero. On the right side of the graph the capacitive element $C_g(t)$ has a linear relation with positive values of $G_i(t)$,therefore, the peak is also reduced linearly with the increase in positive $G_i(t)$.

As expected, the carrier lifetime plays a significant role in the receiver bandwidth. This is demonstrated in Fig. 9 (c). It must be further emphasized that such an effect is rather different in the transmitter where the THz field is generated due to sudden rise of photocarrier density. In the receiver the rise time of the photocarrier density captures one side of the pulse where the fall time captures the other half with opposite sign. This agrees with previous experimental observations for SI-GaAs based THz receiving PC switch [48]. Furthermore, as it is depicted in Fig. 9 (c) the smaller carrier decay rate (larger carrier lifetime) corresponds to lower bandwidth. It has been shown that the carrier density peak has a direct relation with excitation pulse width and γ_d parameter [12]. The longer the excitation pulse is, the lower the carrier density peak would be (the

total pulse power is kept constant). For carrier density peak, this has a similar effect to having a higher value for γ_d parameter. And therefore, assessing the dynamics of this γ_d parameter in detection bandwidth (as investigated in Fig. 9 (d)) is similar to that of excitation pulse width. Based on integration in Eq. 7, the field is integrated as long as there are carriers available. Therefore, the detection bandwidth is set by the maximum of carrier lifetime and optical pulse duration. At an ideal theoretical scenario (infinitesimal carrier lifetime and infinitesimal excitation pulse width) the carrier density profile of $n(t) = \delta(t)$ is achieved. In this case, the THz pulse shape is fully replicated in the detected current (Fig. 9 (d)). Certainly, a shorter carrier lifetime should be accompanied by a larger peak carrier density (higher optical pulse intensity) to preserve the same output signal level after the integration in Eq. 7.

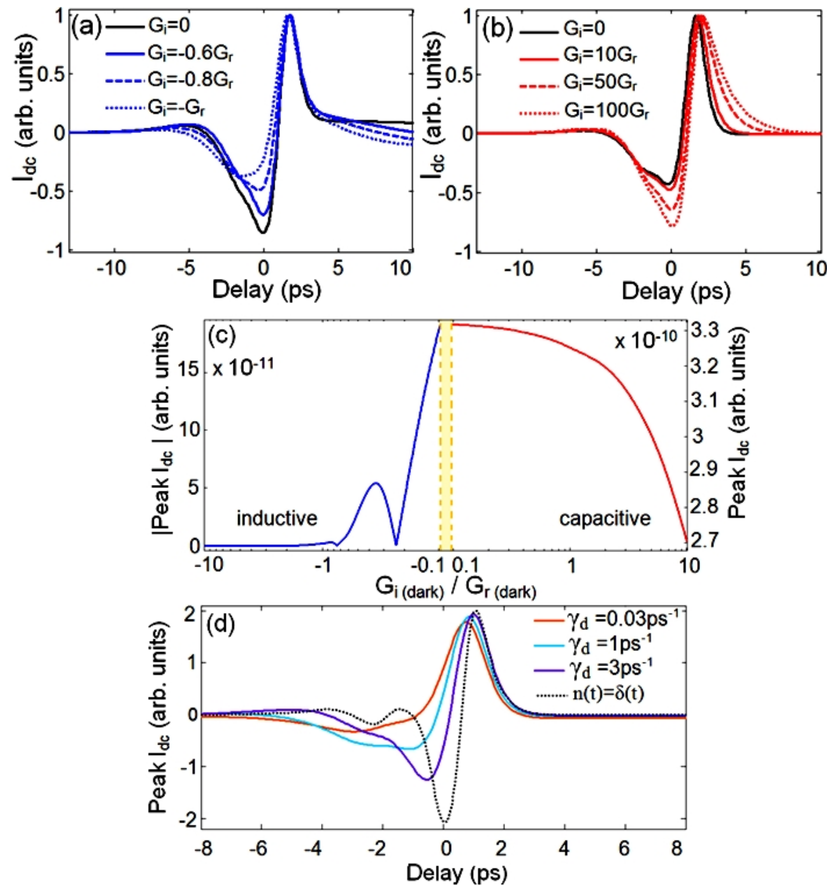

Fig. 9. (a) Temporal profile of the detected current for different negative imaginary values of dark conductance in SWNT film. (b) Temporal profile of the detected current for different positive values of imaginary dark conductance. (c) Variation of peak detected current in the receiver PC switch versus variations of the imaginary photoconductance of the SWNT film in the gap. (d) The effect of carrier lifetime on the temporal profile of the detected current in the receiver PC switch.

Finally, it should be mentioned that the results obtained in this section are subject to thermal stability of the device. Fortunately, carbon nanotubes possess high thermal conduction properties [49] and thus the thermal breakdown might not be considered as a primary limiting factor. Also, in this study we investigated the detected current in the receiver as this is a convenient fundamental parameter in the THz PC switch detection systems and thus can be used for comparison purposes [1-4]. This parameter can be converted to other detection criterions such as responsivity (Watts/A) that are more common in other optical detectors. The Systematic Drude-Smith-Circuit method (SDSC) used in this study can be applied to other new DS nanomaterials for photomixing and PC switching purposes. A proper example of such materials might be semiconducting nanowires such as GaAs and InAlAs nanowires [26, 50].

5. Fabrication

Fabrication is one of the main challenges for application of carbon nanotubes in photonic devices. There are several factors that simplify the fabrication of CNT-based photomixers over other CNT-based devices: a) The CNT-based PC switch works with a large number of CNTs in the gap. Surely the efficiency and quality of the device depends on the alignment of individual CNTs and their contact qualities, but as the theory predicts both in case of a transmission [12] and in case of reception, a partially aligned CNT film with an average length longer than that of gap should work. This facilitates device fabrication compared to other CNT-based devices that might work with a specific number of structured CNTs in a gap; b) THz photomixers are two-electrode micro structures, thus unlike transistors a simple bulk Si/SiO_2 or SiO_2 wafer can be used as the substrate. c) The structure allows several verification procedures for primary certification of the fabrication quality (these will be explained further in this section).

Despite the above simplifying factors, there are several fabrication challenges: a) Small gap size. Depending on the CNT fabrication procedure it can be challenging to fabricate semiconducting CNTs longer than 1μm. Therefore, since gap size of 1μm or less is desired, high precision photolithography or focused ion beam milling is preferred compared to easier, low resolution lithography techniques. b) Break down and quality uncertainty. The randomness of CNT type and position in the gap can be a fabrication

challenge as some of the CNTs might experience optical or electrical breakdown, depending on the local electric field and illumination intensity. c) Other common THz PC switch draw backs. This is one of the major challenges. Heterodyne THz setups consist of two PC switches and are hard to align and also low in THz power level. Therefore, for testing a new CNT based device one should utilize both a very sensitive THz receiver and a high power THz transmitter, which is itself the main challenge of the THz field. This precludes the option of step by step improvement in fabrication of the device, due to lack of step by step feedback, and therefore, the first working device needs to perform almost as well as commercially available photomixers.

The fabrication quality can be verified through several methods. SEM imaging of the gap is fairly accurate but time consuming and partially damaging to the sample (Fig. 1(b)). Raman spectroscopy is a faster and more convenient tool for verifying the CNT deposition quality. However, the problem with Raman is its lower spatial resolution. Figure 10 shows the Raman measurement results for one of our preliminary samples. Fig. 10 (a) shows the 2D color map of the Raman signal measured on a structure similar to one shown in Fig 1 (b).

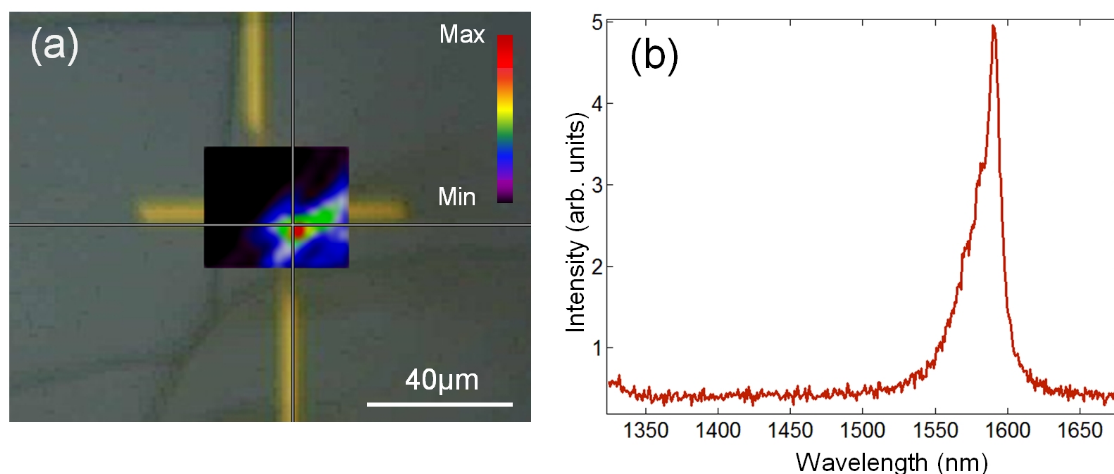

Fig. 10. (a) Raman 2D map of a sample with CNT bundles deposited via slip-stick method. The CNTs are aggregated on one of the electrodes. (b) The Raman Spectra measured for the same sample. The peak certifies high semiconducting CNT percentage on the surface of the sample.

The color map is superimposed on the image of the structure captured with the optical microscope. As it can be seen the CNTs are not deposited at the right spot for this sample, since the peak signal is detected at the bottom right rather than middle of the gap.

However, the semiconducting G-band peak is detected at 1590nm which indicates the dominant presence of semiconducting CNTs in the deposited film (Fig. 10 (b)). The photocurrent, dark current, and the THz output or THz detected signal are the last verification criteria.

6. Discussion

Although, DS formula provides a simple and relatively accurate model for THz conductivity of CNT films, it must be pointed that there is a significant amount of ongoing research on explaining the fundamental physics of the THz conductivity of the CNT films. In most studies [51, 52] a THz conductivity peak (TCP) is noticed (this peak is also present in Fig. 5) and the accuracy of the conductivity models varies in different studies. The accuracy of the DS model can be as well subject to different fabrication parameters such as film filling factor, field alignment, and metallic-semiconducting percentage of CNTs [17, 51, 52]. Also another issue with accuracy of the DS model can be other simultaneous electron scattering phenomena that could occur in the film but are not covered with DS terms [53].

Based on our analysis, an order of magnitude improvement in the detected current can be obtained only if the negative imaginary part of dark conductance is negligible and the mobility is around 1 $m^2v^{-1}s^{-1}$. Achieving higher improvement (operating in red region at Fig. 7 (c)) is possible in theory but rather difficult in practice. The operation in this region might be considered rather idealistic with current fabrication limitations. Tube-tube interactions tend to reduce the mobility of the CNT films. And therefore, there is an ongoing research on fabrication of better aligned, straight CNT bridges [54].

Finally, not all the imaginary values that were used to feed the circuit analysis are measured for ordinary DS SWNT films; however, it is necessary to consider the full allowable theoretical range so that the ultimate limitations in performance can be predicted by the theory. This can be used as a guideline for practical and fabrication directions. For instance, it is shown [17] that the SWNT films THz conductivity can significantly change based on chemical treatment of the film. Additionally, based on conventional circuit theory, the improper imaginary part of the DS conductivity of the

material in the gap can be compensated or even tuned through electrode design (antenna design) in the PC switch [55].

7. Conclusion

Through this study a theoretical analysis was established for assessment of capabilities and limitations of CNT-based THz PC switches used as THz receivers. The analysis uses the incoming THz field, optical excitation parameters, and fast photocarrier dynamics in SWNT films to estimate the detected current through an equivalent circuit model that depends on the design of the microantenna. Such approach allows the effect of each parameter to be investigated and predicted in the detected current. Based on the Drude-Smith model it was found that the high mobility in SWNT material does not necessary contribute to higher detected current. The high mobility in SWNT film can only improve the detected current if the mobility is increased due to decrease in effective mass and if the imaginary part of SWNT THz conductance is smaller than the real part ($|G_i|<0.1G_r$). Based on a numerical example with typical values for all parameters and comparison with our measurements for a LT-GaAs PC switch, it was shown that the detected current level for a CNT-based PC switch should cover the range of currents that are detected in conventional LT-GaAs PC switches.

Finally, the effect of parameters such as contact resistance, gap capacitance, and carrier lifetime were addressed in detail along with experimental fabrication challenges and procedures. Based on this theory, the effect of carrier lifetime on the bandwidth of the THz receiver and detected pulse shape was also addressed.

Acknowledgements

The authors thank Dr. Chris Papadopoulos, Dr. Jinye Zhang, Dr. Rueven Gordon for their technical assistance and kind support with the experimental parts of this work. Also we thank Dr. Matthew Craig Beard for his noticeable guidance. The authors further acknowledge support from Natural Sciences and Engineering Research Council (NSERC) Canada.

References

[1]T. D. Dragoman and M. Dragoman, “Terahertz fields and applications,” Progress in Quantum Electronics , Vol. 28, pp.1-66, (2003).

[2]E. R. Brown, F. W. Smith, and K. A. McIntosh, “Coherent millimeter-wave generation by heterodyne conversion in low-temperature-grown GaAs photoconductors,” Journal of Applied Physics, Vol. 73, pp.1480, (1993).

[3]V. Pačebutas, A. Bičiūnas, S. Balakauskas, A. Krotkus, G. Andriukaitis, D. Lorenc, A. Pugžlys, and A. Baltuška, “Terahertz time-domain-spectroscopy system based on femtosecond Yb:fiber laser and GaBiAs photoconducting components,” Applied Physics Letter, Vol. 97, pp. 031111 (2010).

[4]D. Auston, P. Smith, “Generation and detection of millimeter waves by picosecond photoconductivity,” Applied Physics Letter, Vol. 43, pp. 631 (1983).

[5]S. Haque, C. Marinelli, F. Udrea and W.I. Milne, “Absorption characteristics of single wall carbon nanotubes,” NSTI Nanotech. Conference, Anaheim California USA, 2006, pp.134-137.

[6]Z. Jiangbo, X. Ning, C. Hongzhi, L. King, L. Guangyong, U.C. Wejinya, “Design, Manufacturing, and Testing of Single-Carbon-Nanotube-Based Infrared Sensors,” IEEE Transaction on Nano., Vol. 8, pp. 245 (2009).

[7]R. Lu, Z. Li, G. Xu, and J. Z. Wu, “Suspending single-wall carbon nanotube thin film infrared bolometers on microchannels,” Applied Physics Letter, Vol. 94, pp. 163110 (2009).

[8]K. S. Yngvesso, “Very wide bandwidth hot electron bolometer heterodyne detectors based on single-walled carbon nanotubes,” Applied Physics Letter, Vol. 87, pp. 043503 (2005).

[9]M. E. Itkis, F. Borondics, A. Yu, R. C. Haddon “Bolometric infrared photoresponse of suspended single-walled carbon nanotube film,” Science, Vol. 312, pp.413-416 (2006).

[10] K. Fu, R. Zannoni, C. Chan, S. H. Adams, J. Nicholson, E. Polizzi, and K. S. Yngvesson, “Terahertz detection in single wall carbon nanotubes,” Applied Physics Letter, Vol. 92, pp. 033105 (2008).

[11] S. Watanabe, N. Minami, and R. Shimano, “Intense terahertz pulse induced exciton generation in carbon nanotubes,” Optics Express Vol. 19, pp.1528 (2011).

[12] B. Heshmat, H. Pahlevaninezhad, M. C. Beard,C. Papadopoulos and T.E. Darcie, "Single wall carbon nanotubes as base material for THz PC switching: A Theoretical study from input power to output THz emission," Optics Express, Vol. 19, pp.15077 (2011).

[13] H. Pahlevaninezhad, B. Heshmat, T. E. Darcie, "Advances in THz technology", IEEE Photonics Journal, Vol. 3, pp. 307-310 (2011).

[14] M. J. Hagmann, "Possibility of generating terahertz radiation by photomixing with clusters of carbon nanotubes," Journal of Vaccum Science and Technology B, Vol. 26, pp. 794 (2008).

[15] I. S. Gregory, M. J. Evans, H. Page, S. Malik, I. Farrer, and H. E. Beere, "Analysis of photomixer receivers for continuous-wave terahertz radiation," Applied Physics Letter, Vol. 91, pp.154103 (2007).

[16] D. A. Stewart and F. Leonard "Energy conversion efficiency in nanotube optoelectronics," Nano Letters, Vol. 5, pp.219-222, (2005).

[17] M. C. Beard, J. L. Blackburn, and M. J. Heben, "Photogenerated free carrier dynamics in metal and semiconductor single-walled carbon nanotube films", Nano Letters, Vol. 8, pp.4238–4242 (2008).

[18] S. Reich, M. Dworzak, A. Hoffmann, C. Thomsen, and M. S. Strano, "Excited-state carrier lifetime in single-walled carbon nanotubes", Physical Review B, Vol. 71, pp. 033402 (2005).

[19] Y. Zhong Ma, L. Valkunas, S. L. Dexheimer, S. M. Bachilo, and G. R. Fleming, "Femtosecond spectroscopy of optical excitations in single-walled carbon nanotubes: evidence for exciton-exciton annihilation," Physical Review Letter, Vol. 94, pp. 157402 (2005).

[20] E. C. Camus, J. L. Hughes, and M. B. Johnston, "Three-dimensional carrier-dynamics simulation of terahertz emission from photoconductive switches," Physical Review B, Vol. 71, pp. 195301 (2005).

[21] T. Hertel, R. Fasel, G. Moos, "Charge-carrier dynamics in single-wall carbon nanotube bundles: a time-domain study," Applied Physics A Material Science and Proceeding, Vol. 75, pp. 449-465 (2002).

[22] M. Bockrath, D. H. Cobden, J. Lu, A. G. Rinzler, R. E. Smalley, L. Balents and P. L. McEuen, "Luttinger-liquid behavior in carbon nanotubes," Nature, Vol. 397, pp. 598-601 (1999).

[23] N. V. Smith, "Classical generalization of the Drude formula for the optical conductivity," Physical Review B, Vol. 64, pp. 155106 (2001).

[24] S. Lu and B. Panchapakesan, "Photoconductivity in single wall carbon nanotube sheets," IOP Nanotechnology., Vol. 17, pp.1843-1850 (2006).

[25] A. Serra, D. Manno, E. Filippo, A. Tepore, M. L.Terranova, S. Orlanducci, and M. Rossi "Photoconductivity of packed homotype bundles formed by aligned single-walled carbon nanotubes," Nano Letters, Vol. 8, pp. 968-971 (2008).

[26] P. Parkinson, J. L. Hughes, Q. Gao, H. H. Tan, C. Jagadish, M.B. Johnston, and L. M. Herz, “Transient terahertz conductivity of GaAs nanowires,” Nano Letters, Vol. 7, pp. 2162–2165 (2007).

[27] M. Tsai, C. Yu, C. Yang, N. Tai, T. Perng, C. Tu, Z. Khan, Y. Liao, and C. Chi, “Electrical transport properties of individual disordered multiwalled carbon nanotubes,” Applied Physics Letter, Vol. 89, pp.192115 (2009).

[28] G. M. Turner, M. C. Beard, and C. A. Schmuttenmaer, “Carrier localization and cooling in dye-sensitized nanocrystalline titanium dioxide,” Journal of Physics Chemistry B, Vol. 106, pp. 11716 (2002).

[29] V. Perebeinos, J. Tersoff, and P. Avouris, “Mobility in semiconducting carbon nanotubes at finite carrier density,” Nano Letters, Vol. 6, pp. 205–208 (2006).

[30] T. Durkop, S. A. Getty, E. Cobas, and M. S. Fuhrer, “Extraordinary mobility in semiconducting carbon nanotubes,” Nano Letters, Vol. 4, pp. 35-39, (2004).

[31] J. M. Marulanda and A. Srivastava, “Carrier density and effective mass calculations in carbon nanotubes,” Physics Stat. Sol., Vol. 245, pp. 2558-2562 (2008).

[32] B. Xu, Y. D. Xia, J. Yin, X. G. Wan, K. Jiang, A. D. Li, D. Wu, and Z. G. Liu, “The effect of acoustic phonon scattering on the carrier mobility in the semiconducting zigzag single wall carbon nanotubes,” Applied Physics Letter Vol. 96, pp.183108 (2010).

[33] C. L. Cheung, A. Kurtz, H. Park, and C. M. Liebe, “Diameter-controlled synthesis of carbon nanotubes,” J. Physics Chem. B, Vol. 106, pp. 2429-2433 (2002).

[34] H. Kataura, Y. Kumazawa, Y. Maniwa, I. Umezu, S. Suzuki, Y. Ohtsuka and Y. Achiba, “Optical properties of single-wall carbon nanotubes,” Synthetic Metals, Vol. 103, pp. 2555-2558 (1999).

[35] R. Saito, G. Dresselhaus, and M. S. Dresselhaus, Physical properties of carbon nanotubes, Imperial College Press, 1998, pp. 73-89.

[36] H. Dai, “Carbon nanotubes: synthesis, integration, and properties,” Acc. Chem. Res., Vol. 35, pp.1035-1044 (2002).

[37] J. Hone, M. C. Llaguno, N. M. Nemes, A. T. Johnson, J. E. Fischer, D. A. Walters, M. J. Casavant, J. Schmidt, and R. E. Smalley, “Electrical and thermal transport properties of magnetically aligned single wall carbon nanotube films,” Applied Physics Letter, Vol. 77, pp.666-669 (2000).

[38] M. Engel, J. P. Small, M. Steiner, M. Freitag, A. Green, M. C. Hersam, and P. Avouris, “Thin film nanotube transistors based on self-assembled, aligned, semiconducting carbon nanotube arrays,” ACS Nano, Vol. 2, pp.2445–2452 (2008).

[39] S. H. Hana, S. H. Leea, J. H. Hura, J. Janga, Y. B. Parkb, G. Irvinb and P. Drzaicb, “Contact resistance between Au and solution-processed CNT,” Elsevier Solid-State Electronic, Vol. 54, pp.586-589 (2010).

[40] Y. C. Tsenga and J. Bokor, “Characterization of the junction capacitance of metal-semiconductor carbon nanotube Schottky contacts,” Applied Physics Letter, Vol. 96, pp. 013103 (2010).

[41] J. Y. Suen, W. Li, Z. D. Taylor, and E. R. Brown, “Characterization and modeling of a terahertz photoconductive switch,” Applied Physics Letter, Vol. 96, pp. 141103 (2010).

[42] M. G. Kang, J. H. Lim, S. H. Hong, D. J. Lee, S. W. Hwang, D. Whang, J. S. Hwang, and D. Ahn, “Microwave characterization of a single wall carbon nanotube bundle,” Japenese Journal of Applied Physics, Vol. 47, pp.4965-4968 (2008).

[43] Z. Yao, C. L. Kane, and C. Dekker, “High-field electrical transport in single-wall carbon nanotubes,” Physical Review Letter, Vol. 84, pp. 2941-2944 (2000).

[44] E.F. Plinski, “Terahertz photomixer,” Technical Science OptoElectronic, Vol. 58, pp.463-470 (2010).

[45] M. V. Exter and D. R. Grischkowsky, “Characterization of an optoelectronic terahertz beam system,” IEEE Transaction on Microwave theory and Tech., Vol. 38, pp. 1684-1691,(1990).

[46] S. L. Dexheimer, Terahertz spectroscopy; principles and applications, CRC Press, 2008, pp. 269.299.

[47] T. Jeona, K. Kim, C. Kang, I. Maeng, J. Son, K. H. An, J. Y. Lee, and Y. H. Lee “Optical and electrical properties of preferentially anisotropic single-walled carbon-nanotube films in terahertz region,” J. Applied Physics, Vol. 95, pp. 5736 (2004).

[48] F. G. Sun, G. A. Wagoner, and X.-C. Zhang, “Measurement of free-space terahertz pulses via long-lifetime photoconductors,” Applied Physics Letter Vol. 67, pp.1656-1658 (1995).

[49] S. Berber, Y. K. Kwon, and D. Tomanek, “Unusually high thermal conductivity of carbon nanotubes,” Physical Review Letter, Vol. 84, pp.4613-4616 (2000).

[50] M. S. Vitiello, D. Coquillat, L. Viti, D. Ercolani, F. Teppe, A. Pitanti, F.Beltram, L. Sorba, W. Knap, and A. Tredicucci, “Room-temperature terahertz detectors based on semiconductor nanowire field-effect transistors,” Nano Letters, Vol. 12, pp 96–101 (2012).

[51] A. Ugawa, A. G. Rinzler, and D. B. Tanner, “Far-infrared gaps in single-wall carbon nanotubes,” Physical Review B, Vol. 60, pp. R11305 (1999).

[52]G. Ya. Slepyan, M. V. Shuba, and S. A. Maksimenko, "Terahertz conductivity peak in composite materials containing carbon nanotubes: Theory and interpretation of experiment," Physical Review B, Vol. 81, pp. 205423, 2010.

[53] J. B. Baxter and C. A. Schmuttenmaer, "Conductivity of ZnO nanowires, nanoparticles, and thin films using time-resolved terahertz spectroscopy," J. Physics Chem. B, Vol. 110, pp. 25229-25239 (2006).

[54] B. Y. Lee, K. Heo, A. L. Schmucker, H. J. Jin, J. K. Lim, T. Kim, H. Lee, K. Jeon, Y. D. Suh, C. A. Mirkin, and S. Hong, "Nanotube-Bridged Wires with Sub-10 nm Gaps," Nano Letters, Vol. 12, pp. 1879-1884 (2012).

[55] M. I. Kazim, P. U. Jepsen, V. Krozer, "Design of THz antennas for a continuous-wave interdigitated electrode photomixer," European Conference on Antennas and Propagation (EuCAP), Berlin, Germany, 2009, pp. 1640-1644.

Appendix D: Optical efficiency enhancement methods for terahertz receiving photoconductive switches

(2012, submitted)

Optical efficiency enhancement methods for terahertz receiving photoconductive switches

Barmak Heshmat,[1,*] *Hamid Pahlevaninezhad*[1] *Thomas Edward Darcie*[1]

[1]*Department of Electrical and Computer Engineering, University of Victoria, 3800 Finnerty Rd., Victoria, BC,V8P 5C2, Canada*

**barmak@uvic.ca*

Abstract: We improve the efficiency of THz receiving photoconductive switches by improving the conversion of the optical pump to signal current. This is achieved by both optimizing the incident excitation beam polarization and spatial profile. Due to boundary conditions of the electric field at the electrode edge, a nanometer-sized polarization-dependent shadow is created in the substrate at the electrode edge, where most picosecond lifetime photocarriers are collected. This edge effect is further harnessed by elongating the excitation beam next to the stripline electrode. The effects of excitation beam polarization and spatial profile were experimented with InGaAs/InAlAs quantum-well-based photoconductive switch. In both cases notable enhancement in the signal is observed—30% with polarization optimization and up to 100% with beam elongation. Both techniques preserve the pulse quality and are applicable with readily available optical elements.

1. Introduction

There are various methods for detecting radiation within the terahertz (THz) frequency range [1]. Among these methods, the heterodyne time-domain-terahertz-spectrometer (TDTS) using a pair of THz photoconductive switches (PC switches) offers many advantages over other methods that have led to its popularity (Fig.1 (a)). PC switches are affordable, compact, compatible with common femtosecond pulse and continuous wave lasers, and operate both as THz transmitters and THz receivers at room temperature. Despite these advantages, low efficiency has limited the realization of many potential applications [2]. Increasing the efficiency of a THz PC switch in converting the optical pump to THz radiation (at the transmitter) or to low frequency signal current (at the receiver) has a significant positive effect on all THz applications, motivating substantial research into increasing the efficiency of these devices.

Efficiency can be improved by three different directions: material enhancement, antenna design optimization, and optical excitation efficiency enhancement. Material studies have been successful at the price of reduced bandwidth or excessive fabrication complexity [2-4]. Nanomaterials and quantum engineering have been applied to tune the properties of substrate materials in photoconductive switches. Due to band gap tunability, multi-quantum-well (MQW) based semiconducting substrates are increasingly used to fabricate more efficient PC switches for desired excitation wavelengths [6] (Fig.1 (b)).

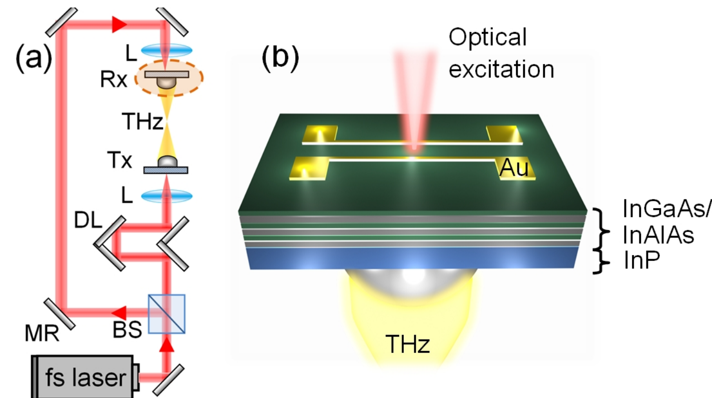

Figure1. (a) Schematic of a TDTS setup. In this setup, the pulsed laser beam is split into two beams; one excites the transmitter and the other excites the detector. The path of the excitation beam for THz transmitting PC switch is varied via a delay line so that the THz pulse and the optical pulse arrive in phase at the detector side. This phase is then varied finely to obtain the temporal profile of the detected THz pulse. (b) Schematic view of the optical excitation of a MQW based stripline PC switch. The stripline (25 µm gap and 2 mm length) is fabricated on a substrate that is composed of 100 layers of InGaAs/InAlAs (20 nm each layer). These are grown on the InP wafer. A silicon lens is attached to the other side of the wafer to focus the incident THz radiation.

Antenna designs have been improved with conventional resonant dipoles and log-periodic toothed structures as the body of the antenna. Additionally, the tip-to-tip nanogaps and interlaced structures in the gap of the antenna have been found to increase the efficiency [7, 8]. The optical excitation efficiency has also been improved by antenna arrays, and integrated microlenses [7-9]. However, the optical excitation can also be enhanced externally

In this study we explore two practical techniques that can notably improve the signal level detected in the receiving stripline PC switches. Both techniques preserve the detection bandwidth and are applicable with readily available optical elements. We first explain and study the causes of previously reported polarization dependence efficiency of

THz PC switches [10]. The obtained insight is then used to enhance the excitation beam profile experimentally.

2. Subwavelength effects of polarization variation

2. 1. Theory

There are numerous theories that describe THz emission in photoconductive switches. However, THz detection via PC switches is less explored [11]. THz PC switches on both sides require similar optical excitation; a gating femtosecond pulse that excites carriers. The photocarriers are then modulated through the THz pulse that impinges on the receiver structure. Carrier dynamics and photo-physics of the substrate material enter the calculations and then the performance of the device is predicted through proper circuit model for the considered antenna design [2, 11]. The polarization of the incident optical pulse should enter at the first step of the PC switching mechanism where the photocarriers are excited via the ultrafast optical pulse. However, the effect of polarization is not directly expressed even in most rigorous Monte-Carlo carrier simulations [12]. This is because the effect of polarization is usually hidden in other parameters that are related to both substrate material and electrode design. Eq. 1 shows the relation between the incident optical pulse and the excited photocarrier density n_{abs}:

$$n_{abs} \approx \frac{\eta(\nu_0)\int_0^T p_i(t,\nu_0)dt}{h\nu_0 V}, \tag{1}$$

where ν_0 is the center frequency of the radiation, $p_i(t,\nu_0)$ is the power at time t and frequency ν_0 , V is the part of sample volume engaged actively in the phenomena, $h\nu$ is the incident photon energy, and $\eta(\nu)$ is the quantum efficiency of the material. Eq. 1 reveals that an increase in quantum efficiency can directly compensate a low-level incident optical power in the linear regime. The effect of polarization is implicit in the quantum efficiency. It is difficult to come up with an exact formulation for quantum efficiency in a PC switch, as it depends on numerous simultaneous mechanisms (Eq. 2). However, there are several major factors that can be addressed.

$$\eta \approx \eta_i \eta_e \eta_t \eta_a \,. \tag{2}$$

In Eq. 2, η_i is the internal quantum efficiency or number of electron-hole pairs generated per photon absorbed. η_e is the excitation sweep out efficiency, that is the portion of

carrier contributing to the generated photocurrent. This coefficient is a function of carrier lifetime, substrate defects, and also relative illuminated spot location on the gap. η_t is the substrate transmissivity that depends on the reflection of the beam from the substrate and electrodes. This is a function of refractive index of the substrate and the surrounding medium and also the electrode design. η_a is the absorption efficiency that depends on the wavelength, the intensity of the incident beam, and the thickness of the absorbing layer.

The excitation polarization can directly affect η_a and η_t. However, as we will see, η_e will also be indirectly affected. The coefficient η_a depends on polarization since the absorption coefficient is polarization dependent for some substrates such as MQW structures [13]. The dependence of η_t on polarization is rather implicit. In the case of an ordinary coplanar stripline structure (Fig. 1), numerical simulations are necessary to investigate the effect of polarization on light coupling. Fig. 2 shows the FDTD results as a 2D profile of the optical power for a pulsed plane wave (800 nm to 830 nm bandwidth) illuminating the electrode structure on an InP substrate. This figure shows the cross section of one of the electrodes where the beam is focused (Fig.2 (a), (b)). The optical power distribution is polarization dependent in the substrate as clearly shown in Fig. 2 (c)-(e). We used the Lumerical FDTD solutions software; the mesh accuracy is 2 nm by 2 nm, and perfectly-matched-layer (PML) boundary conditions are used. Johnson-Christy [14] and Palik values [15] are used for permittivity in gold and InP material respectively.

Fig. 2 (c) shows the optical power profile for TE mode, where the E-field is aligned with the x-axis and is thus perpendicular to the electrode edges. Since the tangential component of the electric field is zero on the surface of the electrode, the field is intensified at the edge and thus higher power is penetrating the substrate. This is an important contribution; due to short carrier lifetime in PC switches most of the viable carriers are collected right at the edge of the electrode. These are the ultrafast carriers that are collected by the electrodes and can contribute to the detected current. For our sample of InGaAs/InAlAs the carrier lifetime is approximately 1.5ps [15] and the saturation velocity is $V_s = 0.75 \times 10^7$ cm/s [16], which results in a 112.5nm active distance from the electrodes. This is the average distance of survival for the photocarriers considering an exponential distribution for the carrier lifetime [11]. When the structure is excited with

TM polarization there is a submicrometer-sized shadow close to the electrode edge (Fig. 2 (d)). This is also visible in the differential graph that shows the difference in the optical power level of TE and TM polarizations (Fig. 2 (e)). The electrode edge is at x = 400nm and y = 0, and thus the number of viable ultrafast photocarriers increases in TE mode. As seen in Fig. 2 (c) and (d) the E-field above the electrode is asymmetrically perturbed due to presence of gold electrodes.

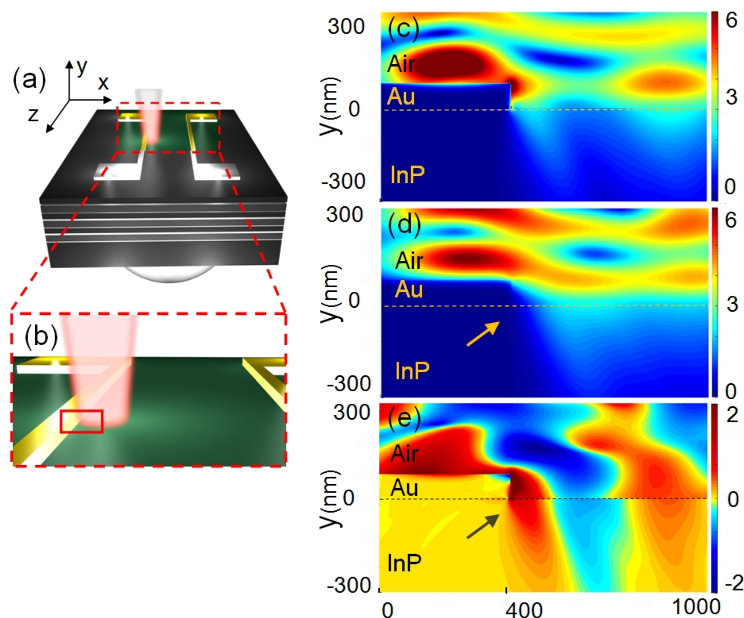

Figure 2. (a) Schematic view for the optical excitation of a PC switch. The area inside the dashed rectangle is enlarged in Fig. 2 (b). (b) The red rectangle at the electrode edge shows the boundaries of the FDTD simulation region. (c) FDTD results for optical power profile for TE mode (E-field aligned with x axis) (d) TM mode (E-field perpendicular to the xy plane) (e) Differential optical power profile (TE-TM).

It worth noting that quantum efficiency in a PC switch is rather different from the same parameter in photodetectors. Unlike most photodetectors, PC switches do not generate any current or voltage as a result of the optical excitation since there is no bipolar structure embedded into these devices. In PC switches, the conductivity is modulated and therefore an external bias is always needed for these modulations to be detected electronically. In the transmitter, the bias is applied via an external DC power supply and in the receiver the bias is emerged through the imposed THz waves on the antenna structure.

2. 2. Experiment

To measure the effect of excitation beam polarization on the detected THz signal, a half-wave plate crystal was inserted in the optical excitation path of the THz receiving PC switch (Fig.1 (a)). The half-wave plate was rotated via a fine precision automated rotational stage and the signal level was recorded for each point (10000 points in 360º). The results are presented in Fig. 3. The polar plot perimeter is the angle θ between the axis of the half-wave plate crystal and the primary incident polarization.

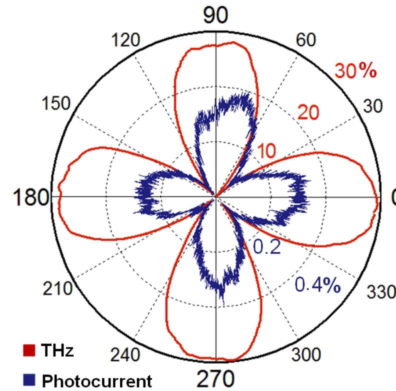

Figure 3. Measured THz signal with an InGaAs/AlGaAs MQW-based PC switch. The perimeter is the angle between the half-wave plate crystal axis and the incident beam polarization. The diameter is percentage of the photocurrent relative increase for blue curve and percentage of signal level relative increase for red graph.

The signal level (red graph) increases by 30 percent by changing the polarization from a TM mode at $\theta = 45°$ to a TE mode at $\theta = 90°$. This increase is relative to the minimum detected signal level at the TM polarization. The half-wave plate is rotated 360 degrees and since the relative polarization rotation is 2θ, TM and TE modes are realized 4 times with 360 degree rotation of the wave plate. The detection bandwidth remains unchanged in both modes. The blue graph shows the percentage of total photocurrent increase with polarization rotation when 10V voltage is directly applied to the stripline and the photocurrent is measured with a multi-meter. The increase is relative to the minimum photocurrent level at the TM polarization. The amount of changes is significantly less than that obtained for the signal level. This further clarifies that the improvement in the THz detection efficiency is due to an increase in local ultrafast carrier collection rather than the material absorption.

3. Excitation spot profile

As discussed in Section 2, the active distance from the electrodes is typically less than 200nm, which is much smaller than common practical illumination spot diameters (in the range of 5-15μm). The spot size is limited by the Abbes diffraction limit, and additionally, the material itself is optically saturated for smaller spot sizes (higher illumination intensities) [17]. Therefore, there is a good potential for increasing efficiency by elongation of the beam at the electrode edges. An elongated beam can reduce the intensity and also increase the length of the illuminated active area at the electrode edges. The reduction in the intensity through beam elongation allows more of the excitation beam to be absorbed within the linear absorption regime. In other words, spot elongation lowers the intensity level thus reducing the chance of absorption saturation [17]. Optical spot elongation can also reduce excessive localized heating that can result in thermal breakdown. This is especially more appealing for wide metallic structures such as striplines and nano-antenna arrays [5, 7, 8].

3.1. Theory

In order to elongate the beam, a configuration shown in Fig. 4 can be used. The beam is focused with an aspherical lens (L1) on to the substrate. A cylindrical lens (L2) reduces the vertical focal length and thus the beam becomes elongated in the y-direction.

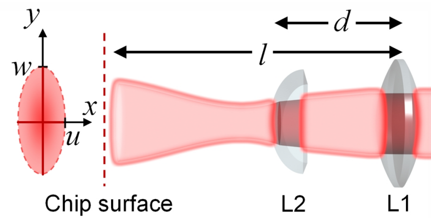

Figure4. Compound cylindrical-convex lens configuration. The optical spot is elongated on the surface of the chip since the vertical focal length is shorter than the horizontal focal length. *w* and *u* are vertical and horizontal beam radius.

Gaussian beam theory and ray optics can be used to calculate the vertical (w) and horizontal (u) beam radii (see supportive information A). The parameter of interest is the effect of beam elongation on total photocurrent (I_{total}). Based on the 2D Gaussian profile of the beam, the exponential carrier decay profile, and nonlinear absorption coefficient in InGaAs/InAlAs, the photocurrent available to the electrodes is found by Eq. 3. (see supportive information B)

$$I_{photo}(u,w) \propto g(u) \times \left(1 - e^{-\alpha(u,w)z}\right) erf\left(\frac{\sqrt{2}y_0}{w}\right), \tag{3}$$

where y_0 is the beam radius of the THz field focused on the THz receiving PC switch, z is the active region depth in the substrate, $g(u)$ is a function of u, and α is the intensity dependent absorption coefficient of the substrate. Based on Eq. 3, one can estimate the photocurrent level with variations in optical beam spot size. Eq. 3 covers the necessary dynamics between THz spot size, optical intensity, absorption coefficient, photocurrent, and optical spot size. This will be further utilized and discussed in the following sections.

3.2. Results

In order to measure the effect of optical spot elongation, the plano-convex spherical lens preceding the THz receiving PC switch (Fig. 1 (a)) was replaced by a spherical lens and a cylindrical lens in series (Fig. 4). By moving the cylindrical lens along the beam axis the excitation spot vertical radii was elongated from 100μm to more than 700μm while the horizontal radius (u) was kept constant at 11 μm on the PC switch substrate. The average optical power of the 80fs laser pulse was kept constant at 20mW (80MHz repetition rate, wavelength of 830nm). The total current, dark current, and detected signal level were measured for each step as shown in Fig. 5. Fig. 5 (a) shows a peak in the detected total current (red square markers). The theory (black curve) also follows the measurement results; however, there is an overshoot in the measured data due to thermal effect that is not considered in the theory. This is evident from the dark current data and the fact that $I_{total}=I_{dark}+I_{photo}$. Each point on the I_{dark} curve is recorded right after blocking the beam, before the substrate cools down (blue triangles). Fig. 5 (b) shows the measured signal level in the lock-in amplifier. The efficiency of the receiver has a peak when the beam is elongated to an elliptical spot with 137μm vertical radius. The result for a circular beam diameter of 5.2 μm is also indicated in the graph for comparison. The inset graph of Fig. 5 (b) shows a sample of the temporal profile of the measured THz pulse. It is found that signal level reduces for w >150μm. For this range (100< w <150μm), the signal level for the elongated spot is almost double of that of the circular spot. Our measurements (Fig. 5 (b)) show that further elongation of the spot vertical radii will at some point (in this experiment around 500μm) bring the detected signal level even lower than the conventional excitation with circular profile (red dashed curve in Fig. 5 (b)). This is because the 100nm wide active region that was introduced earlier has a limited length as well. The length of the active region is proportional to the THz spot size that

biases the receiver stripline electrodes (Eq. 3). With common hemispherical silicon lenses the THz spot radii of 500-600μm is achievable [17].

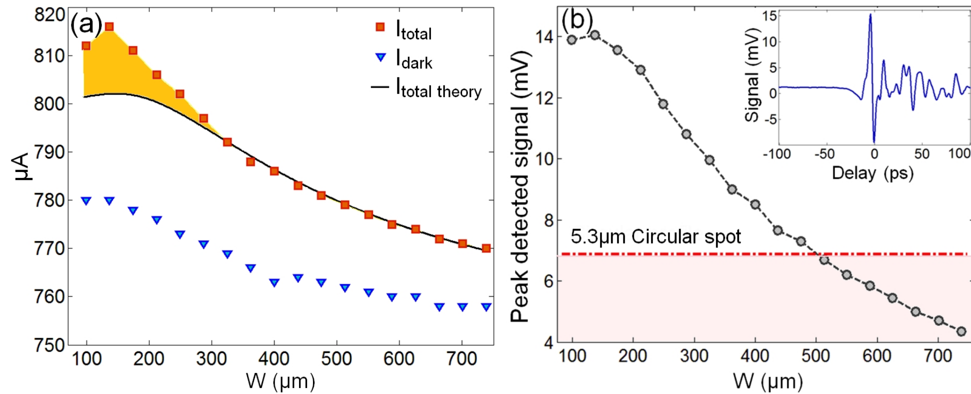

Figure 5. (a) Measured total current and dark current at 10V DC bias and 20mW optical power. The colored area shows the difference between black curve obtained from the theory and experimental data. (b) Measured signal level at the receiver for elongated profile. The red dashed line shows the signal level for a 5.3μm circular spot size and the inset graph is the temporal profile of the pulse.

4. Discussion

There are limitations for enhancement with polarization optimization. We found that polarization effect is less significant for PC switches with dipole antenna structures. That is because the tips of 5 μm dipole are usually rounded due to precision limitations of photolithography. Therefore, the contrast between the TE and the TM polarization field effects on the curved edge of the electrodes are not pronounced as much as those of a straight edge in the stripline structure [10]. The limitations for elongated beam should also be addressed. As seen in Fig. (5), the signal is improved although the width of the elongated beam (u) is larger than the width of the circular beam. This is a notable improvement, however, one can speculate that a significantly better result would have been obtained if the elongated beam could have been further squeezed next to the electrode edge. This might be achievable with significant investment in excitation optics. There are two limiting factors for realization of a perfectly narrowed (u≈100nm and w≈137μm) beam right next to the electrodes solely with external optics. The first limiting factor is practical. A compound lens, as in Fig. 4, requires a larger focal length for the first convex lens due to space limitation enforced by presence of the second cylindrical lens. The longer focal length induces a larger beam spot width compared to a single spherical lens with a shorter focal length. The second factor is the diffraction limit. These factors can be both eliminated if the PC switch is totally redesigned to guide the light

right into the active region. That is beyond the scope of this study and will be explored in future works.

5. Conclusion

Polarization variation and beam elongation are found to be two practical solutions for enhancement of the performance of the THz receiving PC switch. This was studied experimentally on a PC switch made on an InGaAs/InAlAs QW structure. It was found that optimizing the polarization improves the performance by 30% due to subwavelength edge effect close to the electrode. The elongated beam is found to boost the performance of the device by 100%. There are two factors that contribute to this latter enhancement: larger active region illumination for elongated spot, and lower optical intensity that reduces the chance of substrate optical saturation. The results of this study are applicable to different types of wide structures such as coplanar striplines, slot lines [8] and specially nanoantenna arrays, where the field is intensely localized at the electrode edges [5].

References and links

1. T. D. Dragoman and M. Dragoman, "Terahertz fields and applications," Progress in Quantum Electronics, Vol. 28, pp.1-66 (2004).

2. B. Heshmat, H. Pahlevaninezhad, M. C. Beard, C. Papadopoulos and T.E. Darcie, "Single wall carbon nanotubes as base material for THz photomixing: A Theoretical study from input power to output THz emission," Optics Express, Vol. 19, pp.15077-15089 (2011).

3. J. F. Scott, H. J. Fan, S. Kawasaki, J. Banys, M. Ivanov, A. Krotkus, J. Macutkevic, R. Blinc, V. V. Laguta, P. Cevc, J. S. Liu and A. L. Kholkin, "Terahertz emission from tubular Pb(Zr,Ti)O3 nanostructures," Nano Letters, Vol. 8, pp.4404–4409 (2008).

4. M. S. Vitiello, D. Coquillat, L. Viti, D. Ercolani, F. Teppe, A. Pitanti, F. Beltram, L. Sorba, W. Knap, and A.Tredicucci, "Room-temperature terahertz detectors based on semiconductor nanowire field-effect transistors," Nano Letters, Vol. 12 , pp.96–101 (2012).

5. H. Tanoto, J. H. Teng, Q. Y. Wu, M. Sun, Z. N. Chen, S. A. Maier, B. Wang, C. C. Chum, G. Y. Si, A. J. Danner, and S. J. Chua, "Greatly enhanced continuous-wave terahertz emission by nano-electrodes in a photoconductive photomixer" Nature Photon., Vol. 6, pp.121-126 (2012).

6. H. Roehle, R. J. B. Dietz, H. J. Hensel, J. Böttcher, H. Künzel, D. Stanze, M. Schell, and B. Sartorius, "Next generation 1.5 μm terahertz antennas:mesa-structuring of InGaAs/InAlAs photoconductive layers" Optics Express, Vol. 18, pp.2296-2301 (2010).

7. E. C. Camus, J. L. Hughes, and M.B. Johnston, M. D. Fraser, H. H. Tan, and C. Jagadish, “Polarisation-sensitive terahertz detection by multicontact photoconductive receivers,” Optics Express, Vol. 86, pp.254102 (2005).

8. H. Pahlevaninezhad, B. Heshmat and T. E. Darcie "Efficient THz slotline waveguides" Optics Express, Vol. 19, pp.B47-B55 (2011)

9. G. Matthäus, S. Nolte, R. Hohmuth, M. Voitsch, W. Richter, B. Pradarutti, S. Riehemann, G. Notni, and A.Tünnermann, “Microlens coupled interdigital photoconductive switch,” Applied Physics Letter, Vol. 93, pp.091110 (2008).

10. P. G. Huggard, C. J. Shaw, J. A. Cluff, and S. R. Andrews, “Polarization-dependent efficiency of photoconducting THz transmitters and receivers,” Applied Physics Letter, Vol.72, pp.2069 (1998).

11. E. R. Brown, F. W. Smith, and K. A. McIntosh, “Coherent millimeter-wave generation by heterodyne conversion in low-temperature-grown GaAs photoconductors,” Journal of Applied Physics, Vol.73, pp.1480 (1993).

12. E. C. Camus, J. L. Hughes, and M. B. Johnston, “Three-dimensional carrier-dynamics simulation of terahertz emission from photoconductive switches,” Physical Review B, Vol. 71, pp.195301 (2005).

13. K. G. Ravikumar, T. Aizawa, and R. Yamauchi, “Polarization-Independent Field-Induced Absorption-Coefficient Variation Spectrum in an InGaAs/InP Tensile-Strained Quantum Well,” IEEE Photonics Technology Letter, Vol. 5, pp.310-312 (1993).

14. E. R. Brown, D. C. Driscoll, and A. C. Gossard, “State-of-the-art in 1.55 µm ultrafast InGaAs photoconductors, and the use of signal-processing techniques to extract the photocarrier lifetime,” Semicond. Science Technol. Vol. 20, pp.S199–S204 (2005).

15. T. Windhorn, L. W. Cook, and G. E. Stillman, “The electron velocity-field characteristic for n-InGaAs at 300K,” IEEE Ele. Devices Letter, Vol. 3, pp.18-20 (1982).

16. J. S. Weiner, D. B. Pearson, D. A. B. Miller, D. S. Chemla, D. Sivco, and A. Y. Cho, “Nonlinear spectroscopy of InGaAs/InAlAs multiple quantum well structures,” Applied Physics Letter, Vol. 49, pp.531 (1986).

17. F. Formanek, M. Brun, T. Umetsu, S. Omori, and A. Yasuda, “Aspheric silicon lenses for THz photoconductive antennas,” Applied Physics Letter, Vol. 94, pp.021113 (2009).

Supprotive information

Part A

Based on ray optics, the vertical focal length f_v and horizontal focal length f_h of the compound lens L1-L2 are given in Eq. 4.

$$\frac{1}{f_v} \approx \frac{1}{f_{L1}} + \frac{1}{f_{L2}} - \frac{d}{f_{L1} f_{L2}}, \qquad (4)$$
$$f_h \approx f_{L1} - (1.33 \times L2\, thickness)$$

where f_{L1} and f_{L2} are the focal length of the aspherical lens and cylindrical lens. The spot size at the beam waist is estimated as $u = \lambda f_h / \pi w_0$ where w_0 is the Gaussian beam radius before L1. Since the vertical focus is not on the substrate, the elongated beam vertical radius w is estimated through simple trigonometric relation as follows:

$$w = (l - f_v)\frac{w_0}{f_v}. \qquad (5)$$

The practical values measured for our experiment were: $f_{L1} = 12$ cm, $f_{L2} = 4.5$ cm, $w_0 = 2$ mm, *L2* thickness = 4 mm, $l = 11.8$ cm. 9 cm < d < 10.1 cm, $\lambda = 830$ nm.

Part B

The detected photocurrent is proportional to the portion of the optical beam covered by the active region. Considering a Gaussian profile for the beam, an exponential carrier decay rate and a Beer Lambert absorption, the photocurrent is found as in Eq. 6.

$$I_{photo} \propto I_0\left(1 - e^{-\alpha z}\right)\int_{-y0}^{y_0}\int_{-x_0}^{\infty} e^{-2\frac{(x-x_0)^2}{u^2} - 2\frac{y^2}{w^2}} e^{-\frac{x}{\tau V_{sat}}} dxdy, \qquad (6)$$

where the absorption coefficient is itself a nonlinear function of the illumination intensity and it is estimated as $\alpha \approx -2.1 \times 10^3 \times \log(P_0 / \pi w u) + 11 \times 10^3$ cm^{-1} for the optical intensity $I_0 > 1$ kW/cm^2 [16]. P_0 is the average optical power. Since the integral in Eq. 6 is separable, the integral on *x* results in a function of u ($g(u)$) and the result in Eq. 3 is obtained.

Appendix E: Tuning plasmonic resonances of an annular aperture in metal plate

(2011, Optics Express, volume 19, pp.5912)

Reprinted with permission from the Optics Express Journal © Copyright (2012) Optical Society of America

Tuning plasmonic resonances of an annular aperture in metal plate

Barmak Heshmat, Dan Li, Thomas E. Darcie, Reuven Gordon[*]
Department of Electrical and Computer Engineering, University of Victoria
3800 Finnerty Rd., Victoria, BC,V8P 5C2, Canada

Abstract: We present theory to describe the plasmonic resonances of a subwavelength annular aperture in a real metal plate. The theory provides the reflection, including the amplitude and phase, of radially polarized surface plasmon waves from the end faces of the aperture with a significant departure from the perfect electric conductor case due to plasmonic effects. Oscillations in the reflection amplitude and phase are observed. These oscillations arise from transverse resonances and depend on the geometry of the annulus. The theory is applied to the design of various aperture structures operating at the same resonance wavelength, and it is confirmed by comprehensive electromagnetic simulations. The results are contrasted to the perfect electric conductor case and they will be of significant interest to emerging applications in metamaterials, plasmonic sensors, and near-field optics.

1. Introduction

Coaxial waveguides are used extensively at the microwave frequencies because they support a propagating TEM mode for infinitesimal dimensions. For visible and infrared frequencies, the situation changes and there has been considerable effort to understand the influence of surface plasmons within cylindrical coaxial waveguides and geometries [1-10]. The cylindrical surface plasmon (CSP) can extend the cut-off of the waveguide modes for narrow gaps between the metal sides. The Bessel field profile of the CSP can have rapid decay in metal and free space, with sharp localization at metal boundaries. In this regard, phenomena such as extraordinary optical transmission requires consideration of the localized resonances associated with the CSP, which have shown to play an important role, both theoretically and experimentally [4, 11-16]. The properties of CSPs have been of interest to a wide range of applications including; nonlinear optics [4,5],

metamaterials [17,18], THz waveguiding [19], subwavelength and near-field optics [3,20-25], and band-pass filters [26,27].

While past works focused on the propagation of light within the aperture structure, the reflection properties at the end-face are critical to determining both the wavelength and quality of Fabry-Perot resonant transmission from the CSP. The phase of reflection associated with the end-faces of a coaxial aperture affect the Fabry-Perot resonances seen at the microwave frequencies [28]. Recently, a theory to account for those resonant shifts for the perfect electric conductor (PEC) case was presented [29]. In the real metal case, the phase and amplitude of reflection are quantitatively different from the PEC case because of plasmonic effects. In this work, we quantify the differences in the phase and amplitude of the reflection coefficient, which clearly demonstrate that the PEC case cannot be used (not even approximately) to model the real metal case. The difference arises from the new physics associated with surface plasmons: in particular, changes in the propagation constant, finite penetration of the field into the metal region, changes in the sign of the normal electric field component at the boundary, and the sharply peaked field profile. Therefore, care should be taken to include the real metal response.

It is common in the literature to first consider the PEC case as simplified theory that accounts for the geometric optical physics, and later to develop a more detailed theory to account for the plasmonic influence. For example, the progression of study on the single slit problem has followed that trend. An early work to account for the phase and amplitude of reflection for a single slit in a metal concentrated on the PEC case, showing significant geometric influence on the phase of reflection [30]. Following that work, the effects associated with the finite conductance of the metal were shown to dominate the resonances in the microwave regime [31]. For real metals in the visible-IR regime, later theories revealed the plasmonic influences on the reflection properties [32] and the ability to generate surface plasmons at the slit [33]. In each of those works, new physics was uncovered when accounting for the real response of the metal.

In this paper, we present an analytic theory that accurately describes the reflection of the radial CSP mode within a coaxial geometry. The theory provides the reflection amplitude and phase of radially polarized surface plasmon waves from the end faces of an annular aperture in a plate made of a real material. Based on this theory, it is demonstrated that

transverse resonances produce oscillations in the dependence of reflection amplitude and phase on the aperture geometry, which is of direct relevance to the wavelength and quality of the plasmonic resonances. The theoretical approach is also used to tune apertures to a specific resonant transmission peak, as confirmed by comprehensive finite-difference time-domain (FDTD) simulations.

2. Theory of end-face reflection from an annular aperture in a metal plate

The theoretical approach is based upon the single-mode-matching method, where a single mode within the waveguide region is matched to a continuum of radiation and evanescent modes to obtain the reflection properties. With the reflection coefficient and the mode's propagation constant, the wavelength and quality of the localized resonances can be obtained using Fabry-Perot theory. This method is accurate for subwavelength systems where the single-mode approximation represents the field distribution well. It has been applied successfully to the reflection from an annulus in a perfect electric conductor [29] and a number of other systems including subwavelength slits [30, 32], and surface plasmons at a step-edge [34, 35].

Fig. 1 shows a schematic of the geometry under consideration. An annular aperture in a metal film is coaxial with the *z*-axis within the cylindrical coordinate system (ρ,φ,z), and the end-face of the metal terminates at $z=0$. Considering only the lowest-order mode (CSP) [36], the field at $z=0^-$ can be expressed as:

$$E_\rho(\rho,\varphi,z=0^-)\approx\begin{cases}E_\rho^{(1)}=(1+r)\dfrac{-j\beta}{p_1}A_1 I_1(p_1\rho) & \text{if}\quad \rho<a\\ E_\rho^{(2)}=(1+r)\dfrac{-j\beta}{p_2}[A_2 I_1(p_2\rho)-A_3K_1(p_2\rho)] & \text{if}\ a<\rho<b\\ E_\rho^{(3)}=(1+r)\dfrac{j\beta}{p_3}A_4K_1(p_3\rho) & \text{if}\quad \rho>b\end{cases} \tag{1}$$

$$H_\varphi(\rho,\varphi,z=0^-)\approx\begin{cases}H_\varphi^{(1)}=(1-r)\dfrac{j\omega\varepsilon_1}{p_1}A_1 I_1(p_1\rho) & \text{if}\quad \rho<a\\ H_\varphi^{(2)}=(1-r)\dfrac{j\omega\varepsilon_2}{p_2}[A_2 I_1(p_2\rho)-A_3K_1(p_2\rho)] & \text{if}\ a<\rho<b\\ H_\varphi^{(3)}=(1-r)\dfrac{-j\omega\varepsilon_3}{p_3}A_4K_1(p_3\rho) & \text{if}\quad \rho>b\end{cases} \tag{2}$$

Where I_n and K_n are the modified Bessel function of the first and the second kind of order n and $p_i = \sqrt{\beta^2 - \omega^2 \mu_0 \varepsilon_i}$ is the transverse decay constant (i.e., the product of j and the transverse wave-vector), with $i = 1,2,3,4$. Also, μ_0 is the permeability of free space, ε_i is the permittivity of each region, r is the reflection coefficient and $A_i, i = 1,2,3,4$ are coefficients of the field amplitude. Assuming an arbitrary value for one of these coefficients, the other three are found by matching the boundary conditions [36].

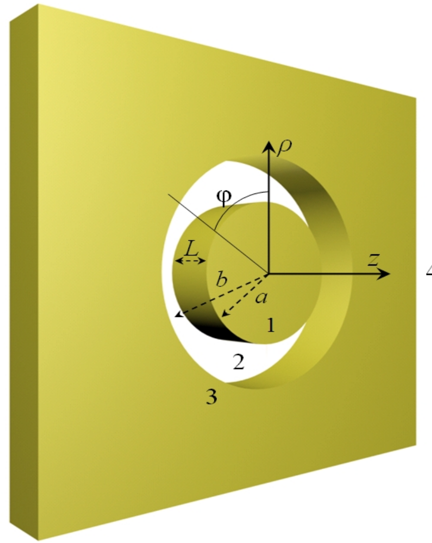

Fig. 1. Schematic view of an annular aperture in a metal film. The regions 1, 2, 3 and 4 have relative permittivity constants of ε_1, ε_2, ε_3 and ε_4 .

The propagation constant β for the fields in this structure can be found via dispersion relation:

$$AB - CD = 0 \tag{3}$$

where

$$\begin{aligned} A &= \frac{I_0(p_2a)}{I_0(p_1a)} - \frac{\varepsilon_2 p_1}{\varepsilon_1 p_2}\frac{I_1(p_2a)}{I_1(p_1a)}, \quad & B &= \frac{\varepsilon_2 p_3}{\varepsilon_3 p_2}\frac{K_1(p_2b)}{K_1(p_1b)} - \frac{K_0(p_2b)}{K_0(p_1b)}, \\ C &= \frac{K_0(p_2a)}{I_0(p_1a)} + \frac{\varepsilon_2 p_1}{\varepsilon_1 p_2}\frac{K_1(p_2a)}{I_1(p_1a)}, \quad & D &= -\frac{\varepsilon_2 p_3}{\varepsilon_3 p_2}\frac{I_1(p_2b)}{K_1(p_3b)} - \frac{I_0(p_2b)}{K_0(p_3b)}. \end{aligned} \tag{4}$$

Here the propagation constant β is a function of the wavelength, the corresponding permittivity of the materials and the geometry of structure, a and b.

For $z = 0^+$, the electric and magnetic fields are expanded in terms of a continuum of modes with the same symmetry as the CSP:

$$E_\rho(\rho,\varphi,z=0^+) = \int_0^\infty t(k)\frac{\sqrt{\omega^2\mu_0\varepsilon_4 - k^2}}{\omega\varepsilon_4} J_1(k\rho)dk \tag{5}$$

$$H_\varphi(\rho,\varphi,z=0^+) = \int_0^\infty t(k)J_1(k\rho)dk. \tag{6}$$

In these equations, $t(k)$ is a coefficient that represents the modes on the transmission side, and $J_1(k\rho)$ is the first order Bessel function of the first kind that describes the mode shape. When $z>0$ has a different dielectric than in the gap, merely $\varepsilon_4 \neq \varepsilon_2$ (in Eq. 5).

The transverse electric and magnetic fields are matched at $z=0$, and the mode orthogonality relations are used to determine r. Eq. 1 is equated to Eq. 5 and both sides are multiplied by $J_1(k\rho)\rho$ and integrated over ρ from 0 to ∞. Considering the orthogonality of the Bessel functions, this integration gives:

$$t(k) = (1+r)\frac{\omega k\beta\varepsilon_4}{\sqrt{\omega^2\mu_0\varepsilon_4 - k^2}}\left[D_1(k) + D_2(k) + D_3(k) + D_4(k)\right] \tag{7}$$

with the different regions giving four separate terms:

$$D_1(k) = \frac{-jA_1}{p_1(p_1^2+k^2)} a\left(p_1 J_1(ka) I_2(p_1 a) + kJ_2(ka) I_1(p_1 a)\right) \tag{8}$$

$$D_2(k) = \frac{-jA_2}{p_2(p_2^2+k^2)}\left[b\left(p_2 J_1(kb) I_2(p_2 b) + kJ_2(kb) I_1(p_2 b)\right) - a\left(p_2 J_1(ka) I_2(p_2 a) + kJ_2(ka) I_1(p_1 a)\right)\right] \tag{9}$$

$$D_3(k) = \frac{jA_3}{p_2(p_2^2+k^2)}\left[b\left(kJ_2(kb) K_1(p_2 b) - p_2 J_1(kb) K_2(p_2 b)\right) - a\left(kJ_2(ka) K_1(p_2 a) - p_2 J_1(ka) K_2(p_2 a)\right)\right] \tag{10}$$

$$D_4(k) = \frac{-jA_4}{p_3(p_3^2+k^2)} b\left(kJ_2(kb) K_1(p_3 b) - p_3 J_1(ka) K_2(p_3 b)\right) \tag{11}$$

Next, Eq. 2 and 6 are equated, and both sides are multiplied by $\rho E_\rho(\rho,\varphi,z=0^-)/(1+r)$ and again integrated over ρ from 0 to ∞. This gives the reflection coefficient:

$$r = \frac{1-G}{1+G} \tag{12}$$

with:

$$G = \frac{\int_0^{\infty} \frac{k\beta\varepsilon_4}{\sqrt{\omega^2\mu_0\varepsilon_4 - k^2}} \left[D_1(k) + D_2(k) + D_3(k) + D_4(k)\right]^2 dk}{\frac{\varepsilon_1 A_1^2}{p_1^2}\int_0^a I_1^2(p_1\rho)\rho d\rho + \frac{\varepsilon_2}{p_2^2}\int_a^b [A_2 I_1(p_2\rho) - A_3 K_1(p_2\rho)]^2 \rho d\rho - \frac{\varepsilon_3 A_4^2}{p_3^2}\int_b^{\infty} K_1^2(p_3\rho)\rho d\rho} \quad (13)$$

In contrast to the PEC case, which involves only a single simple integral [29], the derivation and final formulation is considerably more elaborate. This is necessary, however, to capture the plasmonic dispersion and the finite penetration of the field into the metal. Nevertheless, the integrals in Eq. 13 converge and G can be calculated as a complex number to give the reflectivity $(|r^2|)$ and reflection phase (φ).

The solution in Eqs. 12 and 13 represent the main result of this work. It captures the amplitude and phase of reflection of the lowest order mode at the interface to free space (or uniform dielectric). This incorporates both the physical effects of mode-shape mismatch and impedance mismatch that lead to the reflection coefficient. The theory is limited to the subwavelength regime. For larger slit widths, where higher order radial modes are allowed to propagate, the theory will give inaccurate results and full numerical simulations will typically be required to capture the scattering of such a system. Furthermore, for large radii, higher order azimuthal modes may be allowed. This does not necessarily mean that the theory presented will not be invalid – so long as the rotational symmetry of the zeroth order mode is preserved, the theory presented here is valid for larger radii. The theory assumes that the plasmon mode is supported, as defined by the existence of solutions to Eq. 3.

3. Behavior of reflection coefficient

Having developed a theoretical expression for reflection, we proceed to evaluate the reflection amplitude and phase of various structures. Fig. 2 shows the calculated amplitude and phase at the end-face of an annular aperture in PEC case and real gold. The calculation is done for wavelength of 632.8 nm and a relative permittivity of -11.694+1.225i in real case [37], with the dielectric medium having relative permittivity of 1. Two main features can be seen from this figure: that the amplitude and phase

experience an offset when changing the slit width of the annulus (b-a), and that there are oscillations with variation in the annulus radius.

The changes with slit width result from variations in coupling to the free space (or uniform dielectric) modes. Narrower slits have larger reflection amplitudes because of increased impedance mismatch and mode-shape mismatch (between the CSP mode in the slit and the continuum of propagating modes in the uniform dielectric) as the width is decreased. It is well known for gap plasmons that decreasing the distance between two metals can increase the propagation constant of the mode in the gap, and the same is true for the CSP here [1]. Furthermore, the narrower gap confines the electromagnetic energy to a subwavelength region.

The oscillatory behavior with changes in the annulus radius arises from transverse resonances. Such transverse resonances are not present for a single linear slit, but do arise for double slits, where the electromagnetic energy is scattered resonantly between the slits [38]. For the annulus here, the scattering occurs transversely between opposite sides. For a more mathematical description of this phenomenon, it is instructive to consider Eq. 13, for which the integrand diverges when $k^2 = \omega^2 \mu_0 \varepsilon_4$. The integrand at this value of the wave-vector will play an important role in the value of r, and the oscillation arises from the oscillatory nature of the J Bessel functions with variations in the radius. It should be noted as well that the integrals in denominator have monotonic behavior with changes of radius because of the presence of modified Bessel functions.

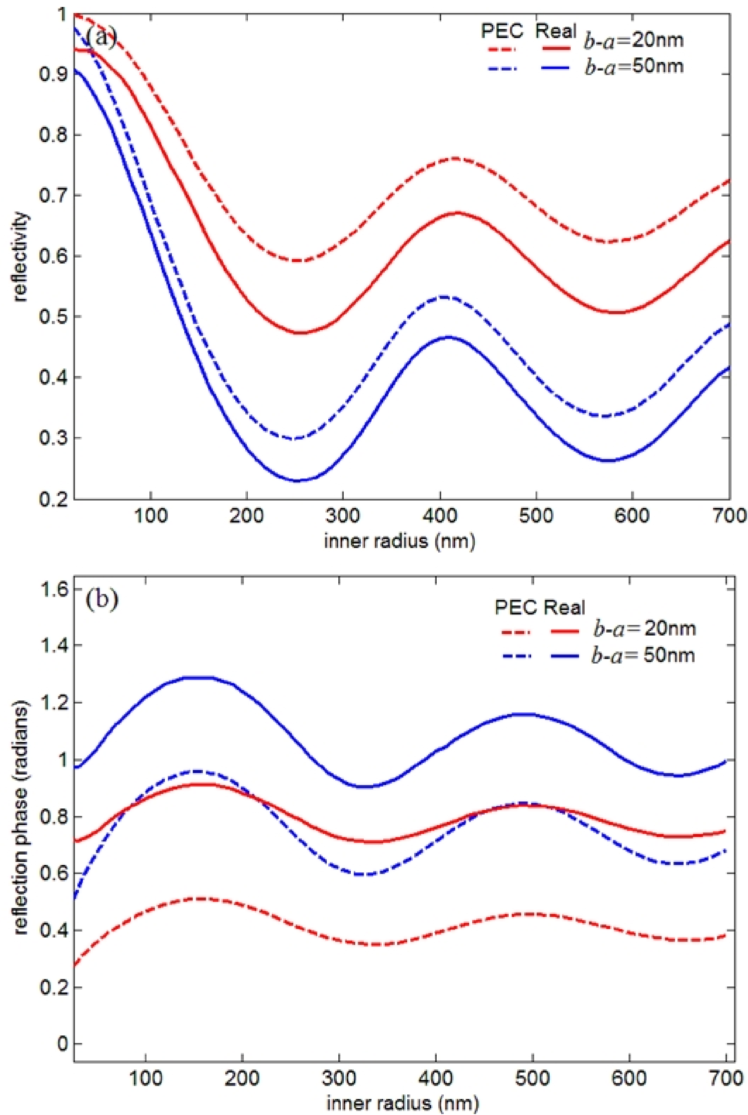

Fig. 2. Evaluation of the theoretical reflection expression (Eq. 12) for annular apertures in gold plate at 632.8 nm free-space wavelength. The results are contrasted with PEC case, using dashed lines. (a) The reflectivity and (b) the phase of reflection as function of inner radius, *a*, for slit widths (*b-a*) of 20 nm and 50 nm.

Fig. 2 shows considerable differences between PEC case and real metal case. This difference increases further if the wavelength is closer to the plasmon resonance. At the wavelength of 500 nm, the reflectivity is noticeably different, as shown in Fig 3. The differences in the locations of the extrema in PEC and real metal case are also due to plasmonic effects. These differences increase from less than 20 nm in Fig. 2 to 40 nm in Fig. 3 by change of excitation wavelength from 632.8 nm to 500 nm.

For the wavelengths and geometries considered here, the reflection is larger for the PEC case; but this is not generally true. For instance, in case of a single slit, which can be

considered as an annular aperture with the inner radius of infinity, higher reflectivity has been found in PEC compared to real metal case [32]. Close to zero outer radius (for finite inner radius), the PEC case approaches unity reflection because the field is confined to extreme subwavelength dimensions and therefore the mode-shape mismatch with free-space becomes infinite. For the real metal case, however, there is finite extension of the electric field into the metal, even for infinitesimal dimensions, and so the reflection amplitude remains below unity.

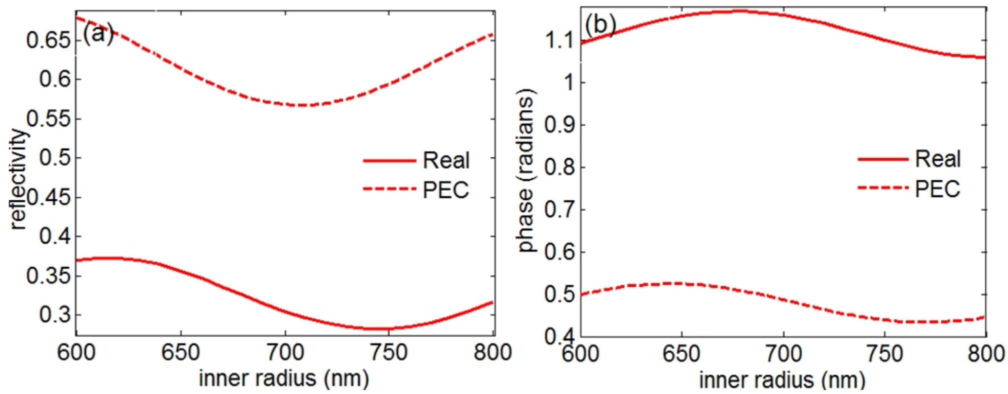

Fig. 3. Comparison between reflection for the PEC case and the real metal case, both for annular aperture with slit size of 20 nm illuminated with 500 nm wavelength light. (a) Reflectivity and (b) phase.

The phase of reflection is quantitatively different between the real metal and PEC cases, more than double in the graphs shown in Fig. 2 and 3. In the verbiage of microwave engineering, the increase in the phase of reflection can be thought of as coming from a more inductive termination waveguide. This is consistent with the interpretation that real metals can be thought of as inductive elements in the plasmonic regime [39]. As will be discussed in the next section, the resonant thickness of the metal plates will be considerably less for the real metal case than predicted by the PEC case, even after accounting for the differences in the propagation constant within the aperture.

4. Fabry-Perot resonances

For a finite metal plate of thickness l, the CSP propagating inside the annular aperture will experience reflection at both end-faces. Fabry-Perot resonances arise from multiple reflections between the end-faces, depending on the phase of reflection, φ :

$$l = \frac{m\pi - \varphi}{\beta}, \tag{14}$$

where m is the integer order of the Fabry-Perot resonance and β is found from Eq. 3.

Based on the results of Fig. 2 and Eq. 14, we designed several annular aperture geometries to all have a Fabry-Perot resonance at the same wavelength of 632.8 nm. The geometric parameters of each design were then simulated by FDTD (Lumerical Solutions Inc.). The metal plate spanned from $z = 0$ to $z = l$ nm, with l the thickness of the plate. A parametric dispersion model was used with gold permittivity set to -11.694+1.225i at 632.8 nm [35] (that software uses a proprietary multi-coefficient model for extrapolating the permittivity in different wavelengths fitting the experimental data). A z-polarized broadband dipole source was located at $z = 100$ nm. The perfect matched layer (PML) boundary conditions were used for the computational domain, and the symmetric boundaries were adopted at x and y axis. A 1 nm mesh was set at both ends of the annular aperture and the mesh resolution was set to smaller than 2 nm inside the annulus. The convergence was ensured with variations of the simulation region size and simulation time.

Fig. 4 shows the results of the FDTD simulations for the various designs. Each case clearly shows a peak in the transmission through the aperture near the specified wavelength of 632.8 nm. The variations in the peak-widths and heights are expected from variations in the reflection amplitude and the propagation loss for the different geometries.

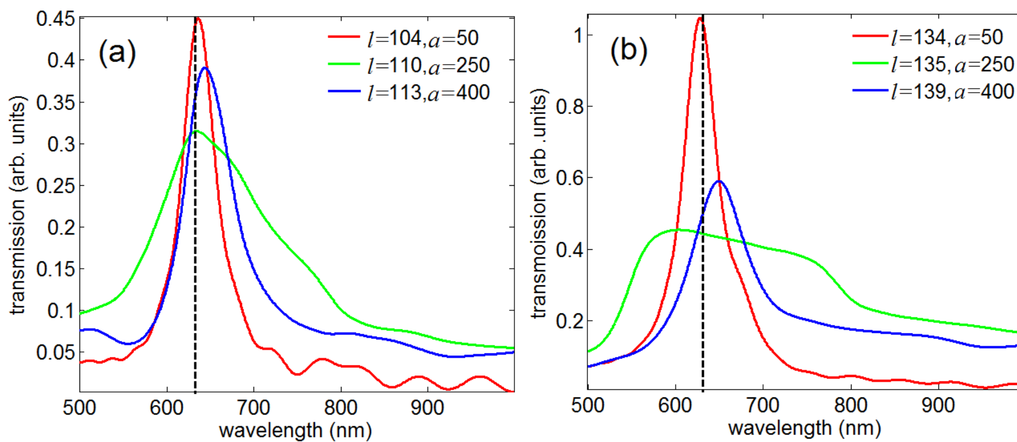

Fig. 4. (a) Transmission in arbitrary units for (b-a) value of 20 nm. Each curve relates to a different structure as specified in the legend and the dashed line is at 632.8 nm. In this figure a is the inner radius and l is the thickness of the plate (b) The (b-a) value is changed to 50 nm.

As it can be seen, by comparing Fig. 4 (a) and (b), the quality of the frequency profile of the resonance not only changes with a but also with slit size (b-a). This is a direct effect of propagation constant and reflection amplitude being functions of a and b as stated in Eqs. 3, 4 and 12, and shown in Fig. 2. For example, the reflection amplitude for the red curve at inner radius of 50 nm is higher than reflection of green curve at inner radius of 250 nm (Fig. 2(a)), and this correlates with the higher quality resonance seen in Fig. 4(a). It can be inferred from Fig. 4(b) that change of slit size (b-a) causes the relative value of peaks to be influenced. This is because the reflectivity in this case follows 50 nm curve in Fig. 2 (a), and therefore the variations in reflection amplitude are more significant.

The good agreement of the resonances seen in the comprehensive electromagnetic simulations with the specified wavelength (632.8 nm) shows the predictive capability of the theory presented, which will be useful in future designs of apertures in metal films. Table 1 shows the wavelength at which the peaks arise from several additional simulations, all very close to 632.8 nm. Also, it is further evident from this Table that the propagation constant inside the annulus obtained from finite-difference mode solver simulations match the calculated values of Eq. 3. This is because the effective refractive index$(\beta\lambda/2\pi)$ obtained from the finite difference method agrees to that found by the calculation within 0.004 on average, showing that the simulations accurately capture the analytic CSP dispersion.

Table 1. The effective refractive indexes and peak wavelength for geometries in Fig. 4, for annular

a (nm)	b (nm)	l (nm)	n (analytic)	n (finite difference)	FP peak (nm)
50	100	124.23	1.7020	1.7067	634.03
50	100	310.12	1.7020	1.7038	636.20
50	100	496.02	1.7020	1.7004	638.73
250	300	135.38	1.5308	1.5600	611.85
250	300	342.06	1.5308	1.5407	629.39
250	300	548.75	1.5308	1.5361	634.39
400	450	139.04	1.5308	1.5202	649.23
400	450	345.72	1.5308	1.5243	643.42
400	450	552.41	1.5308	1.5262	640.96
50	70	104.42	2.3063	2.3029	639.83
50	70	241.61	2.3063	2.3029	639.83
50	70	378.80	2.3063	2.3046	639.10
250	270	110.81	2.1250	2.1403	638.00
250	270	259.71	2.1250	2.1354	640.56
250	270	408.60	2.1250	2.1334	641.66
400	420	113.44	2.1150	2.1177	647.56
400	420	263.04	2.1150	2.1204	645.89
400	420	416.64	2.1150	2.1177	647.56

aperture structures in gold designed to have peak at 632.8 nm.

It is important to note that the geometric values presented in Table 1 are not the result of any optimization, but rather, they are found directly from the analytic theory presented

in Section 2. With knowledge of a and b, l is derived directly from the theory. To obtain sharper resonances, the reflectivity should be increased (for example, by choosing maxima in Fig. 2(a)), and the material loss should be minimized. Therefore, it is worthwhile to consider the relative contribution of the reflection loss and the propagation loss on the Fabry-Perot resonances. The reflection loss for one round-trip can be written as $(1-|r|^2)^2$, which describes how efficiently the energy escapes from the cavity. The propagation loss is given by $1-\exp(-4\,\mathrm{Im}\{\beta\}l)$, where Im is the imaginary part. The propagation loss describes how the energy is lost to the metal absorption. As an example, for the case of the 20 nm slit width red curve in Fig. 4(a), the round trip reflection loss is 0.005 and the propagation loss is 0.28. For the green curve in Fig. 4(a), the round trip reflection loss is 0.28 and the propagation loss is 0.23. Therefore, in the first example, the propagation loss dominates, but for the second example, where the reflection is reduced, the loss from imperfect reflection is larger. Clearly, the proper design of such apertures can have a large impact on the relative contributions to resonant energy transmission and to the loss through material absorption.

Figure 5 illustrates the changes of resonance wavelength with change of thickness. As can be seen, the resonance wavelength for the same order increases with thickness, and once again, good agreement is seen between our analytic method and FDTD simulations.

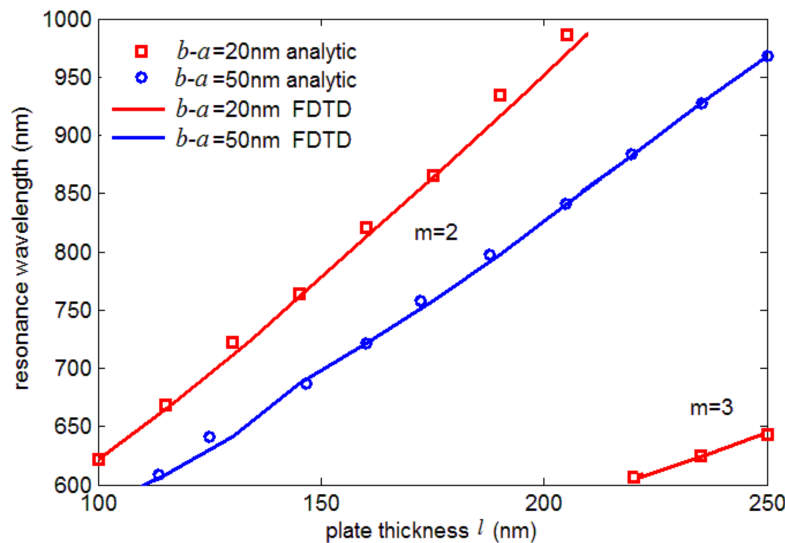

Fig. 5. Variations of resonance wavelength with plate thickness l. The annular aperture inner radius is kept fixed at a=50 nm.

As the effect of inner and outer radius of the annular aperture was fully captured in reflection phase and amplitude, the effect of plate thickness l is important in tuning the plasmonic resonances in such an aperture as well. This is attainable both with the Eq. 12 and 14 and with the FDTD approach. The analytic approach, however, can directly give the resonance thickness simply by substitution of phase in Eq. 14. Unlike FDTD in which the thickness of the structure needs to be known prior to the simulation, the analytic approach can predict the thickness with a choice of a wavelength. This can serve as a prefabrication design guide for an intended wavelength of resonance. Care should be taken when extrapolating the curves in Fig. 5 to thinner plate thicknesses, and to shorter wavelengths. For shorter wavelengths, the CSP mode may not be supported (as prescribed by the existence of solutions to Eq. 3). Furthermore, if the plate is too thin, transmission by higher order modes may start to contribute significantly, and the theory presented here will no longer be valid, as described at the end of Section 2. Here, we have considered only gold, however, the theory may be equally applied to other metals for wavelengths that support the CSP.

Fig. 6 shows the distribution of the intensity of the electric-field in cross section of the annular aperture, when on resonance and when off resonance. For the on-resonance case, there is a nearly symmetric field distribution in the aperture (as expected from the Fabry-Perot resonance) and significant electric field intensity transmits through the aperture to the other side of the gold plate. For the off-resonance case, the electromagnetic energy does not build up within the aperture and significantly less transmission is observed.

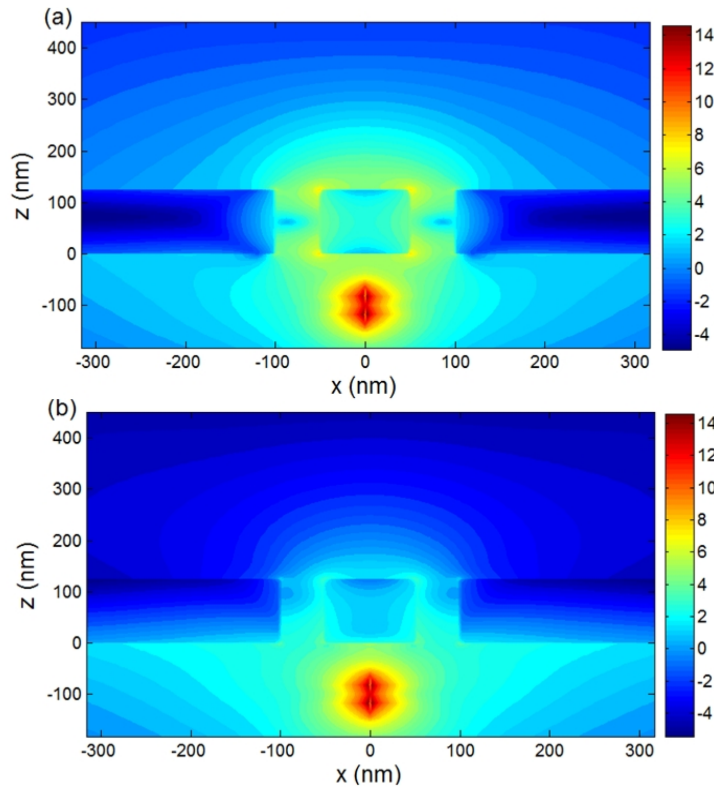

Fig. 6. 2D electric field intensity plot in logarithmic scale (base 10) calculated by FDTD showing cross section of the annular aperture with a=50 nm, b=100 nm and l=124 nm. (a) On resonance at the wavelength 632.8 nm. (b) Off resonance at 500 nm wavelength.

5. Conclusion

We presented a theory for the end-face reflection of an annular aperture in a real metal. This theory is useful for determining the localized surface plasmon resonances associated with an annular aperture in a metal plate. Comparison with comprehensive FDTD simulations showed the good predictive design capability of the analytical approach and the results were contrasted with PEC case. The results presented in this work are relevant to annular apertures for use in metamaterials applications [17, 18], near-field optics [21], sensors [22-25], and band-pass filters [26,27]. In particular, metamaterials based on annular structures rely on the plasmonic metal response to obtain interesting new physics, such as negative refractive index [17,18]. However, in those works the important influence of the reflection remains elusive. This work provides a better understanding of the reflection properties in real metals for the annular geometry. For near-field optics applications, annular aperture resonances can boost the performance, for example, as found in a recent work involving near-field hyperspectral Raman imaging [40].

Knowledge of the influence of real metals is necessary to design near-field probes with the desired resonance wavelengths.

References and links

1. L. Novotny and C. Hafner, “Light propagation in a cylindrical waveguide with a complex, metallic, dielectric function,” Physical Review E, Vol. 50, pp.4094–4106 (1994).

2. T. W. Ebbesen, H. J. Lezec, H. F. Ghaemi, T. Thio, and P.A. Wolf, “Extraordinary optical transmission through subwavelength hole arrays,” Nature, Vol. 39, pp.667-669 (1998).

3. M. Walther, M. R. Freeman, and F. A. Hegmann, “Metal-wire terahertz time-domain spectroscopy,” Applied Physics Letter, Vol. 87, pp.261107 (2005).

4. F. I. Baida, A. Belkhir and D. Van Labeke, “Subwavelength metallic coaxial waveguides in the optical range: Role of the plasmonic modes,” Physical Review B, Vol. 74, pp.205419 (2006).

5. Y. Poujet, J. Salvi, and F.I. Baida, “90% Extraordinary optical transmission in the visible range through annular aperture metallic arrays,” Optics Letter, Vol. 32, pp.2942-2944 (2007).

6. Reuven Gordon, “Reflection of cylindrical surface waves,” Optics Express, Vol. 17, pp.18621-18629 (2009).

7. P. B. Catrysse and S. Fan, “Understanding the dispersion of coaxial plasmonic structures through a connection with the planar metal-insulator-metal geometry,” Applied Physics Letter, Vol.94, pp.231111 (2009).

8. J. Wang, W. Zhou and E. Li, “Enhancing the light transmission of plasmonic metamaterials through polygonal aperture arrays,” Optics Express, Vol. 17, pp.20349-20354, (2009).

9. F. I. Baida, Y. Poujet, J. Salvi, D. V. Labeke and B. Guizal, “Extraordinary transmission beyond the cut-off through sub-k annular aperture arrays,” Journal of Optics Communication, Vol. 282, pp.1463–1466 (2009).

10. P. Banzer, J. Kindler, S. Quabis, U. Peschel, and G. Leuchs,” Extraordinary transmission through a single coaxial aperture in a thin metal film,” Optics Express, Vol. 18, pp.10896-10904 (2010).

11. H. Caglayan, I. Bulu, and E. Ozbay, “Extraordinary grating-coupled microwave transmission through a subwavelength annular aperture,” Optics Express, Vol. 13, pp.1666-1671 (2005).

12. J. Zhang, S. Zhang, D. Li, A. Neumann, C. Hains, A. Frauenglass, and S. R. Brueck, “Infrared transmission resonances in double-layered, complementary-structure metallic gratings,” Optics Express, Vol. 15, pp.8737-8744 (2007).

13. W. Fan, S. Zhang, B. Minhas, K. J. Malloy, and S. R. J. Brueck, “Enhanced infrared transmission through subwavelength coaxial metallic arrays,” Physical Review Letter, Vol. 94, pp.033902 (2005).

14. S. M. Orbons and A. Roberts, “Resonance and extraordinary transmission in annular aperture arrays,” Optics Express, Vol. 14, pp.12623-12628 (2006).

15. S. M. Orbons, M. I. Haftel, C. Schlockermann, D. Freeman, M. Milicevic, T. J. Davis, B. Luther-Davies, D. N. Jamieson, and A. Roberts, “Dual resonance mechanisms facilitating enhanced optical transmission in coaxial waveguide arrays,” Optics Letter, Vol. 33, pp.821-823 (2008).

16. S. M. Orbons, A. Roberts, D. Jamieson, M. I. Haftel, C. Schlockermann, D. Freeman, B. Luther-Davies, “Extraordinary optical transmission with coaxial apertures,” Applied Physics Letter, Vol. 90, pp.251107 (2007).

17. S. P. Burgos, R. Waele, A. Polman, and H. A. Atwater, “A single-layer wide-angle negative-index metamaterial at visible frequencies,” Nature Materials, Vol. 9, pp.407-412 (2010).

18. R. Waele, S. P. Burgos, and A. Polman,” Negative refractive index in coaxial plasmon waveguides,” Optics Express, Vol. 18, pp.12770-12778 (2010).

19. Q. Cao and J. Jahns, “Azimuthally polarized surface plasmons as effective terahertz waveguides,” Optics Express, Vol. 13, pp.511–518 (2005).

20. Y. Poujet, M. Roussey, J. Salvi, F.I. Baida, D. Van Labeke, A. Perentes, C. Santschi and P. Hoffmann, “Super-transmission of light through subwavelength annular aperture arrays in metallic films: Spectral analysis and near-field optical images in the visible range,” Photonics and Nanostructures, Vol. 4, pp.47–53 (2006).

21. B. Hecht, B. Sick and U. P. Wild, “Scanning near-field optical microscopy with aperture probes: Fundamentals and applications,” Journal of Chemistry Physics, Vol. 112, pp.7761–7774 (2000).

22. A. G. Brolo, R. Gordon, B. Leathem, K. Kavanagh, “ Surface plasmon sensor based on the enhanced light transmission through arrays of nanoholes in gold films,” Langmuir, Vol. 20, pp.4813–4815 (2004).

23. H. V. Chu, Y. Liu, Y. Huang and Y. Zhao, “A high sensitive fiber SERS probe based on silver nanorod arrays,” Optics Express, Vol. 15, pp.12230–12239 (2007).

24. R. Gordon, D. Sinton, K. L. Kavanagh and A. G. Brolo, ” A new generation of sensors based on extraordinary optical transmission,” Accounts of Chemistry Research, Vol. 41, pp.1049–1057 (2008).

25. K. A. Tetz, L. Pang and Y. Fainman, “High-resolution surface plasmon resonance sensor based on linewidth-optimized nanohole array transmittance,” Optics Letter, Vol. 31, pp.1528–1530 (2006).

26. P. A. Krug, D. H. Dawes, R. C. McPhedran, W. Wright, J. C. Macfarlane and L. B. Whitbourn, “Annular-slot arrays as far-infrared bandpass-filters,” Optics Letter, Vol. 14, pp.931-933 (1989).

27. A. Roberts and R. C. McPhedran, “Bandpass grids with annular apertures,” IEEE Trans Antennas Propagation, Vol. 36, pp.607-611 (1988).

28. M. J. Lockyear, A. P. Hibbins, J. R. Sambles and C. R. Lawrence, “Microwave transmission through a single subwavelength annular aperture in a metal plate,” Phy. Review Letter, Vol. 94, pp.1939021-1939024 (2005).

29. D. Li and R. Gordon, “Electromagnetic transmission resonances for a single annular aperture in a metal plate,” Physical Review A, Vol. 82, pp.041801 (2010).

30. Y. Takakura, “Optical resonance in a narrow slit in a thick metallic screen,” Physical Review Letter, Vol. 86, pp.5601–5603 (2001).

31. J. R. Suckling, A. P. Hibbins, M. J. Lockyear, T. W. Preist, J. R. Sambles, and C. R. Lawrence, “Finite conductance governs the resonance transmission of thin metal slits at microwave frequencies,” Physical Review Letter, Vol. 92, pp.147401 (2004).

32. R. Gordon, "Light in a subwavelength slit in a metal: propagation and reflection," Physical Review B, Vol. 73, pp.153405 (2006).

33. P. Lalanne, J. P. Hugonin, and J. C. Rodier, "Theory of surface plasmon generation at nanoslit apertures," Physical Review Letter, Vol. 95, pp.263902 (2005).

34. R. Gordon, "Vectorial method for calculating the fresnel reflection of surface plasmon polaritons," Physical Review B, Vol. 74, pp.153417 (2006).

35. R. Kolesov, B. Grotz, G. Balasubramanian, R. J. Stöhr, A. A. L. Nicolet, P. R. Hemmer, F. Jelezko and J. Wrachtrup, "Wave–particle duality of single surface plasmon polaritons," Nature Physics, Vol. 5, pp.470-474 (2009).

36. C. Yeh, F. I. Shimabukuro, *The Essence of Dielectric Waveguides*, (Springer, 2007), Chap. 5.

37. P. B. Johnson and R. W. Christy, "Optical constants of the noble metals," Physical Review B, Vol. 6, pp.4370–4379 (1972).

38. R Gordon, "Near-field interference in a subwavelength double slit in a perfect conductor," Journal of Optics A, Vol. 8, pp.L1 (2006).

39. N. Engheta, "Circuits with light at nanoscales: optical nanocircuits inspired by metamaterials," Science, Vol. 317, pp. 1698-1702 (2007).

40. A. Weber-Bargioni, A. Schwartzberg, M. Cornaglia, A. Ismach, J. J. Urban, Y. Pang, R. Gordon, J. Bokor, M. B. Salmeron, D. F. Ogletree, P. Ashby, S. Cabrini, and P. J. Schuck, "Hyperspectral nanoscale imaging on dielectric substrates with coaxial optical antenna scan probes," Nano Letters, Vol. 11, pp.1201–1207 (2011).

Appendix F: Nanoplasmonic Terahertz Photoconductive Switch on GaAs

(2012, Nanolettrer,ASAP)

Reprinted with permission from the Nano Letterss Journal © Copyright (2012) American Chemical Society.

Nanoplasmonic Terahertz Photoconductive Switch on GaAs

Barmak Heshmat[†], Hamid Pahlevaninezhad[†], Yuanje Pang[†], Mostafa Masnadi Shirazi[‡],

Ryan Lewis[‡], Thomas Tiedje[†], Reuven Gordon[†] and Thomas Edward Darcie[†]*

[†]*Department of Electrical and Computer Engineering, University of Victoria, V8P 5C2, Victoria, BC Canada*

‡*Department of Electrical and Computer Engineering, University of British Columbia, V6T 1Z4, Vancouver, BC, Canada*

Abstract: Low-temperature (LT) grown GaAs has a subpicosecond carrier response time that makes it favorable for terahertz photoconductive (PC) switching. However, this is obtained at the price of lower mobility and lower thermal conductivity than GaAs. Here we demonstrate subpicosecond carrier sweep-out and over an order of magnitude higher sensitivity in detection from a GaAs-based PC switch by using a nanoplasmonic structure. As compared to a conventional GaAs PC switch, we observe 40 times the peak-to-peak response from the nanoplasmonic structure on GaAs. The response is double that of a commercial, antireflection coated LT-GaAs PC switch.

Research in terahertz (THz) imaging [1-3] and spectroscopy [4-8] has advanced significantly in the past decade, fueled particularly by advances in the output power of THz sources and the efficiency of THz detectors [9-11]. Photoconductive (PC) switching offers advantages over other methods of THz generation and detection [11]. In particular, PC switches are compact and low cost, they operate at room temperature, and they can function both as emitters and receivers of THz waves. These PC switches are center-fed microantennas, usually fabricated on a short carrier-lifetime semiconducting material, such as low-temperature (LT) grown GaAs [12] The feed current of the microantenna is provided by the short-lifetime photocarriers that are generated through optical excitation of the center gap of the antenna.

Research efforts have focused on improving the efficiency of PC switches for THz applications [13-15]. From the material perspective, low-mobility LT-GaAs replaced high-mobility GaAs due to shorter carrier lifetime more than a decade ago [11]. This allowed higher bandwidth operation and deeper carrier density modulation that was vital to access the hyper-THz (>1 THz) range and higher sensitivity. However, this was

achieved at the price of lower mobility. Since the efficiency is directly dependent on mobility [12, 15], numerous studies have been conducted to compensate for the low mobility in LT-GaAs using more complex materials such as GaAsBi and ion-implanted GaAs [16, 17]. Recent work has focused on nanomaterials, such as semiconducting ErAs/GaAs nanoisland superlattices[18], quantum wells [19], carbon nanotubes [15], and metamaterials [20].

Separately, from the antenna perspective there has been an effort to use interlaced structures [12, 21] and nanostructures in the gap of the antenna to improve the efficiency. The size of the center gap of the antenna was conventionally defined by the optical excitation spot size and thermal conduction of the substrate. Conventional designs tend to converge to gap size of 4–6 μm. Recently, a submicrometer-sized gap was proposed and successfully implemented in the form of tip-to-tip nanogaps and nanoantenna [13, 22, 23]. Tip-to-tip nanogaps [22] provide high electric bias-field intensity in continuous-wave THz emission, but due to their small scale they have low optical coupling efficiency. Interlaced structures on LT-GaAs, with gaps of a few micrometers, provide more efficient carrier collection at the price of lower optical coupling and higher undesired dark current in THz emitting PC switches [12, 21].

Nanoplasmonics (i.e., the nanostructuring of metals to achieve an enhanced optical response due to interaction of metal surface plasmons with the incident light) has been used to improve the performance of detectors [24, 25], light emitters [26, 27], imaging systems [28-31], nanoantennas [32, 33] and waveguides [34-39]. A key capability of nanoplasmonics is efficient coupling of light into subwavelength structures [40-47]. The optical electric-field affects the surface plasmons of the metal nanostructures; if the metallic nanostructure has proper geometry, the induced effects can constructively resonate with the surface plasmons in a desired fashion. Such resonances are tuned to notably affect the transmission or reflection of subwavelength metallic apertures [48-55].

Here we demonstrate a nanoplasmonic PC switch that efficiently couples light into 100 nm gaps. These small gaps enable fast carrier sweep out from a GaAs substrate for efficient THz detection. We compare the performance of this nanoplasmonic PC switch with a conventional PC switch structure on GaAs and LT-GaAs and with a commercial

LT-GaAs antireflection coated device. Peak-to-peak response enhancements of 40×, 10×, and 2× are found, respectively.

A schematic of a contemporary THz heterodyne setup is shown in Figure 1a. In this setup, the phase of the THz pulse is varied with variations of the length of the optical excitation pulse path using a delay line. The THz pulse is focused by a silicon lens through the back side of the chip. The receiver is connected to a lock-in amplifier that detects the current signal. Conventional designs for THz receiving PC switches are 10–200 μm dipoles with 5–10 μm center gaps fabricated on LT-GaAs substrates. In our experiment, this center gap is replaced with a nanoplasmonic interlaced structure with 100 nm gaps (Figure 1b,c).

We used semi-insulating GaAs wafer ([100] orientation, 350 μm thickness, ~1.3 × 10^8 ohm·cm resistivity and ~5500 $cm^2/V \cdot s$ mobility). The carrier lifetime exceeds 200 ps for bulk GaAs substrates, as confirmed by reflective pump–probe measurements. For the first step of fabrication, a closed-gap structure is fabricated by photolithography (95 nm Au with a 5 nm Cr adhesive layer). The closed gap is then sputtered using a focused ion beam machine (Hitachi FB-2100 Focused Ion Beam system). The interlaced structure is connected to gold electrodes which are connected to larger gold pads. The gold pads facilitate biasing and measurement of the signal from the structure (Figure 1b).

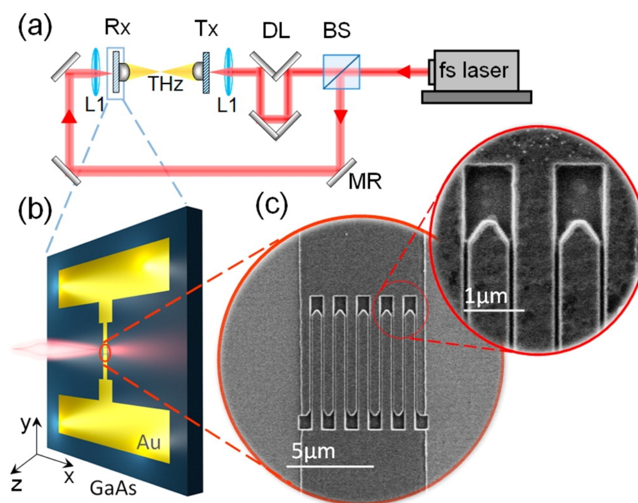

Figure 1. (a) Schematic of the THz detection setup. Abbreviations used: MR = mirror, BS = beam splitter, DL = delay line, L = lens, Rx = THz receiving PC switch, Tx = THz transmitting PC switch, and fs laser = femtosecond Ti–sapphire pulse laser. (b) 3D model of the plasmonic THz receiving PC switch. (c) SEM image of the interlaced structure. The gaps are 100 nm and the metallic fingers are 600 nm wide each. The inset shows further details of the structure.

To compare the performance of the interlaced structure, we also fabricated a conventional 20 μm dipole with 5 μm center gap on the same GaAs substrate. Additionally, we fabricated the same dipole structure on an LT-GaAs substrate (1 μm LT-GaAs grown at 250 °C, in situ MBE annealing at 600 °C for 60 s, 0.5% excess As). A commercial LT-GaAs PC switch (BATOP PCA-800 nm) was used as the THz transmitter. The signal is first measured with another similar commercial PC switch at the receiver side (10 μm dipole with 5 μm center gap with back-mounted silicon lens and substrate antireflection coating). There is a difference in the size of the commercial dipole (10 μm) and our fabricated dipole (20 μm). However, since the THz wave wavelength is 330 μm, both dipoles can be treated as a “short dipole”.

In order to correctly illuminate the center gap, the receiver is biased first to maximize the photocurrent measured in the THz receiving PC switch. After optical alignment the receiver is connected to the lock-in amplifier and the silicon lens at the back of the receiver (Figure 1a) is aligned for maximum signal. Results for the commercial receiver are shown in green in Figure 2a. The pulse has sharp subpicosecond features that translate into hyper-THz frequency components in the frequency domain (Figure 2b). The receiver PC switch is then replaced with our PC switches and the results are measured again. For each measurement the silicon lens is aligned to obtain the maximum signal. As is seen in Figure 2b, the ordinary dipole on GaAs has lower bandwidth. The positive and negative peaks of the detected pulse depend on the photocarrier rise time and fall time respectively [56]. The rise time in GaAs is similar to that of LT-GaAs, and therefore, the GaAs PC switch can detect the positive side of the THz pulse. However, due to long photocarrier fall time, the negative peak of the pulse is not captured completely and the results are relatively low in frequency and amplitude. Short photocarrier fall time in LT-GaAs enables the PC switch to capture both positive and negative peaks and this enhances the bandwidth and sensitivity of the device as seen in Figure 2 (blue curve). The commercial device shows better performance compared to our conventional (not nanoplasmonic) dipole on LT-GaAs due to antireflection coating which enhances the

optical coupling of its gap by roughly 30%.

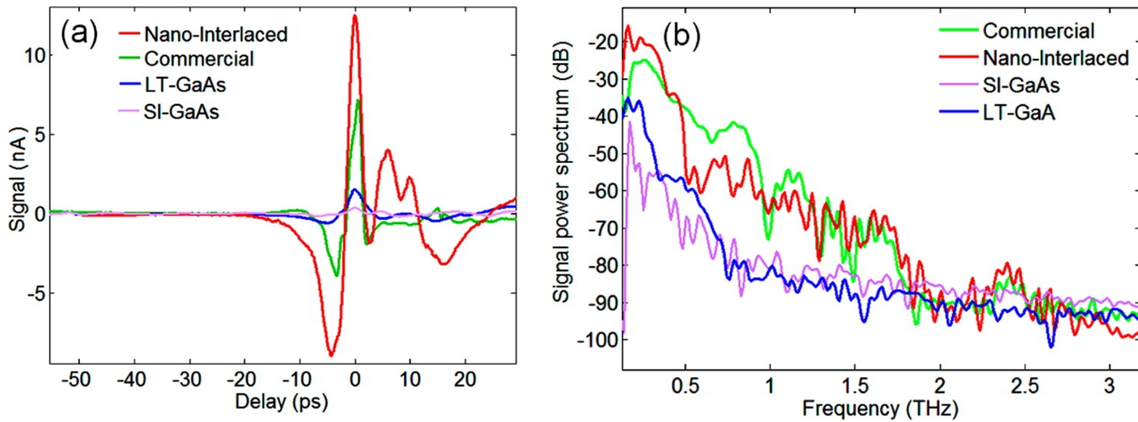

Figure 2. (a) Same THz pulse measured with: plasmonic interlaced structure on GaAs (peak to peak 20.5 nA), commercial PC switch (peak to peak 10 nA), dipole on LT-GaAs (peak to peak 2 nA), and dipole on GaAs (peak to peak 0.5 nA). (b) Signal power spectrum (20 log10 (|F(I)|) + cte) in dB. Noise level is −80 dB.

The nanoplasmonic PC switch shows superior performance compared to the other devices. As seen in Figure 2, the detected signal in the plasmonic PC switch is double that of commercial device on LT-GaAs, 1 order of magnitude higher than our LT-GaAs PC switch, and around 40 times more than that of ordinary 20 μm dipole on GaAs.

There are two mechanisms that result in the enhanced response for GaAs. Higher detection bandwidth is obtained due to short carrier sweep-out time which causes deeper photocarrier density modulations. There is an active region adjacent to each electrode that defines the number of photocarriers that are collected. This active region is equivalent to the photocarrier lifetime multiplied by saturation velocity.

For LT-GaAs with approximately 0.8 ps carrier lifetime and 1.3 × 107 cm/s electron saturation velocity [57] the active distance from the electrodes is around 100 nm. This implies that photocarriers that are generated further than 100 nm from the edge of the electrodes are on average more likely to recombine before reaching the electrodes. On the other hand, for GaAs with more than 200 ps carrier lifetime, the photocarriers are yet present long after the THz field is gone. This results in reduced bandwidth and blurring of the sharp peaks in the detected signal. The carrier transit time across the 100 nm gap between the fingers in the interlaced structure is much shorter than their original lifetime. On the basis of GaAs electron saturation velocity, the 100 nm gap size is just about the right size to artificially mimic the 0.8 ps carrier lifetime of the LT-GaAs.

The nanoplasmonic resonances in the slits lead to high total optical transmission that increases the efficiency. The 100 nm gap size also increases the THz field intensity across the gap and this increases the detected current. Secondary peaks appear approximately 6 ps after the main peak in the detected signal, corresponding to the roundtrip time of the THz wave internal reflections inside the 350 μm thick GaAs wafer. The longer tail in the detected signal is in part caused by longer lifetime photocarriers that are excited deeper than 200 nm into the substrate. Due to longer distance from the gold electrodes, these photocarriers (a small fraction of around 10%) are swept out later than the carriers at the surface.

To design and study an interlaced structure that is resonant with the incident beam, we used FDTD simulations (FDTD Lumerical software, mesh accuracy 1 nm ×1 nm) and searched for the resonant transmission peak with finger and gap width variations. In the simulations, the periodicity was swept from 300 nm to 1000 nm in 100 nm steps, the gap width was swept from 50 to 200 nm in 50 nm steps, and the thickness was swept from 50 to 200 nm in 50 nm steps. On the basis of this analysis, the best dimensions were chosen as determined by maximal electric field loss in the semiconductor. Figure 3a shows the 2D E-field profile of a single finger, in a periodic structure with period of 700 nm which results in 100 nm gaps between the fingers (Figure 1c). Here z is the vertical coordinate to the substrate; x is the transverse coordinate of the periodic structure perpendicular to the axis of the slits as shown in Figure 1b.

When the optical pulse illuminates the structure from the top, as shown in Figure 3a, the optical E-field excites the surface plasmons of the gold electrode surface. The structure periodicity and geometry are chosen in such a way to trigger the resonant enhanced transmission from the Au–air region of the structure [58]. This significantly enhances the optical transmission through the 100 nm gap based on gap plasmons behavior for a metallic slit [59]. The fringed decaying E-field that is present due to edge effects and high curvature of the structure is then absorbed and attenuated in the substrate based on the exponential Beer–Lambert profile.

As seen in Figure 3b, the structure shows a peak in the substrate E-field loss at excitation wavelength of 830 nm. E-field loss is the difference between the optical transmissions at the substrate surface ($z = 0$ nm) and depth of 200 nm. Here, 830 nm is

the center wavelength of the excitation pulse generated by the Ti–sapphire femtosecond laser (pulse width =80 fs and 80 MHz repetition rate). The electric field loss in 200 nm depth of substrate (z axis) is used as a criterion of transmission in each frequency.

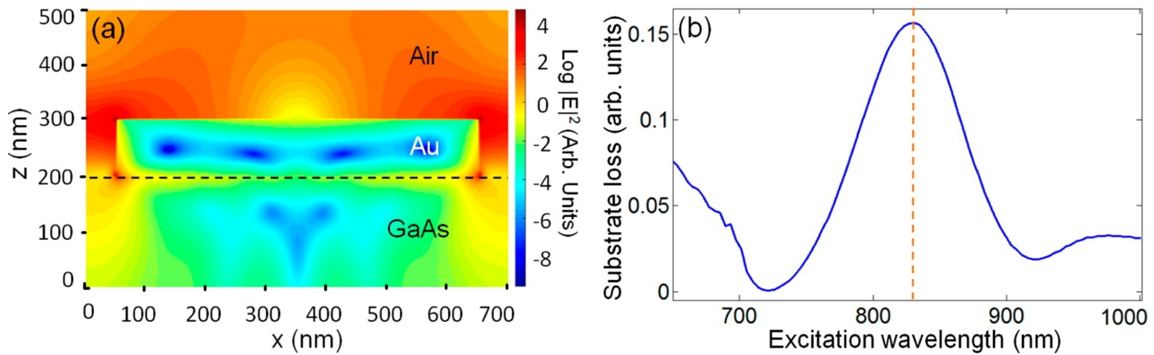

Figure 3. FDTD simulation results. (a) 2D E-field profile (log10 (|E|2) scale) of a single finger cross section. The structure is repeated with 700 nm periodicity for 10 periods in the gap (Figure 1c). (b) Electric field loss spectrum in 200 nm depth of the substrate.

The reason for calculating the loss to a depth of 200 nm was to focus on the fast photocarriers swept out by the THz field that decays as the square of the depth. We have estimated that a depth of 200 nm accounts for 90% of the photocarriers swept out within less than 2 ps, and therefore, the depth to 200 nm is used to ensure that this surface layer dynamics is accurately captured. Palik permittivity values were used for GaAs [60] and Johnson and Christy values were used for gold [61].

To confirm the presence of nanoplasmonic resonances, we measured the reflection of the interlaced structure for two different optical excitation polarizations (R; the reflection when the polarization is perpendicular to the slits and R; the reflection when the E-field polarization is parallel with the slits). We then compared the results with FDTD simulation results. Based on the simulations the ratio R/R was found to be 2.6. This ratio was measured to be 2.1 for our fabricated interlaced structure. The measured polarization dependent transmission indicates a resonant transmission. As seen in Figure 4, the measured reflection shows reasonable agreement with the simulation results. The mismatch between the theory and measurement can be due to surface roughness that is induced by the FIB process. The roughness in the gold surface can induce scattering that weakens the effect [62]. It is likely that there is some level of Ga contamination from the

FIB process that would influence both the optical properties and the electrical properties of the samples measured. While not seeing pronounced changes in the conductivity and reflectivity during routine measurements, we have not characterized the influence of contamination fully. Based on previous experimental reports [63], however, for thickness of damaged layers in GaAs (maximum of 40 nm depth for 30 keV and 1000 pA) the Ga ion contamination depth with our milling settings (40 keV, and 57 pA, at 22K zoom with 1 μs dwell time for each milling point) should be less than 10 nm.

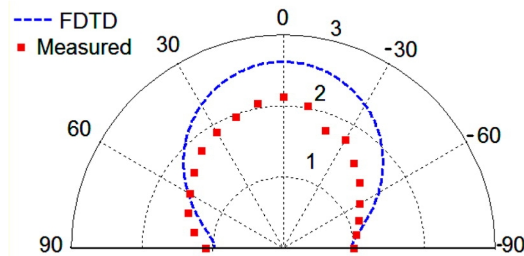

Figure 4. Polar plot of the reflection ratio. The dotted blue line is based on the FDTD result, and the red squared dots are the measured results.

Unlike the THz transmitting PC switch, where the gap is biased by the DC voltage supply, the THz receiving PC switch is biased by the received THz waves. The 100 nm gaps between the fingers can lead to a significant dark current in the THz emitting PC switch, which can burn the device. The fingers for each of the dipole electrodes are electrically parallel and thus the dark current for each gap is added. Consequently, using the same interlaced nanoplasmonic structure as a THz emitter will likely give lower maximum powers. A better solution for the transmitter is to divide the DC bias between the fingers, using a series electrical configuration. This is possible with having parallel strips (or rods) in the gap instead of interlaced electrodes [64, 65]. While dark current is not a notable concern for THz receiving PC switches, capacitance of the narrow gap can set an upper limit for detection bandwidth. Increasing the number of fingers or reducing the gap size intensifies this undesired capacitive effect. For our design with 10 periods, the capacitive time constant is estimated to be less than 180 fs. This induces a −3 dB point at 550 GHz. Considering the generated THz pulse spectrum, this can explain the relative decrease in detection enhancement for frequencies higher than 550 GHz (red curve in Figure 2b). Such capacitive bandwidth limitation may be further improved by engineering the THz impedance of the dipole. This requires more complex design relative to common single dipole structures [22].

On the fabrication side, the molecular beam epitaxy (MBE) process to grow LT-GaAs is not necessary as simple as using GaAs wafers. Also the high resolution photolithography that might be needed for 4–5 μm center gap dipoles can be replaced with lower resolution photolithography processes. However, the nanostructure itself needs to be fabricated via focused ion beam machines. The fabrication is not as challenging as many multilayered nanostructure fabrications; the continuous zigzag like pattern can be milled in one run. One might consider direct e-beam writing as another fabrication approach that is free from Ga contamination.

The interlaced nanoplasmonic THz-receiving PC switch shows superior performance relative to its LT-GaAs and GaAs peers. The device uses the plasmonic resonances of the interlaced structure to efficiently couple the excitation pulse into narrow 100 nm gaps. These gaps sweep out the generated photocarriers in the subpicosecond time range allowing comparable bandwidth operation on otherwise long carrier lifetime GaAs. Future work includes using higher resistance substrates to improve the output power level in the THz transmitting PC switches for both 810 and 1550 nm optical pumping.

Acknowledgements

The authors acknowledge support from Natural Sciences and Engineering Research Council (NSERC) Canada.

References

1. A. J. Huber, F. Keilmann, J; Wittborn, J. Aizpurua, and R. Hillenbrand, “Terahertz near-field nanoscopy of mobile carriers in single semiconductor nanodevices,” Nano Letters, Vol. 11, pp.3770 (2008).

2. V. Krishnakumar, and R. Nagalakshmi, “Terahertz generation in 3-Nitroaniline single crystals,” Nano Letters, Vol. 8, pp.3882–3884 (2008).

3. W. M. Lee, and Q. Hu, “Real-time, continuous-wave terahertz imaging by use of a microbolometer focal-plane array,” Optics Letter, Vol. 30, pp.2563 (2005).

4. M. C. Beard, G. M. Turner, and C. A. Schmuttenmaer, “Terahertz Spectroscopy,” Journal of Physics Chemistry B, Vol. 106, pp.7146–7159 (2002).

5. S. Vitiello, D. Coquillat, L. Viti, D. Ercolani, F. Teppe, A. Pitanti, F. Beltram, L. Sorba, W. Knap, and A. Tredicucci, “Room-temperature terahertz detectors based on

semiconductor nanowire field-effect transistors," Nano Letters, Vol. 12, pp.96–101 (2012).

6. N. Horiuchi, "Terahertz nano-exploration," Nature Photonics, Vol. 6, pp.82–83 (2012).

7. P. K. Mandal, and V. Chikan, "Plasmon−phonon coupling in charged n-type CdSe quantum dots: a THz time-domain spectroscopic study," Nano Letters, Vol. 7, pp.2521–2528 (2007).

8. M. Tonouchi, "Cutting-edge terahertz technology," Nature Photonics, Vol. 1, pp.97 (2007).

9. Q. Hu, "Quantum warming," Nature Photonics, Vol. 3, pp.64 (2009).

10. N. Yu, Q. Wang, F. Capasso, "Beam engineering of quantum cascade lasers," Laser and Photonics Review, Vol. 6, pp.24 (2012).

11. T. D. Dragoman, M. Dragoman, "Terahertz fields and applications," Progress in Quntum Electronic, Vol. 28, pp.1-66 (2004).

12. E. R. Brown, F. W. Smith, K. A. McIntosh, "Coherent millimeter-wave generation by heterodyne conversion in low-temperature-grown GaAs photoconductors," Journal of Applied Physics, Vol. 73, pp.1480 (1993).

13. S. Park, K. Jin, M. Yi, C. J. Ye, J. Ahn, and K. Jeong, "Enhancement of terahertz pulse emission by optical nanoantenna," Nano Letters, Vol. 6, pp.2026–2031 (2012).

14. N. Large, M. Abb, J. Aizpurua, and O. Muskens, "Photoconductively loaded plasmonic nanoantenna as building block for ultracompact optical switches," Nano Letters, Vol. 10 , pp.1741–1746 (2010).

15. B. Heshmat, H. Pahlevaninezhad, M. C. Beard, C. Papadopoulos, and T. E. Darcie, "Single-walled carbon nanotubes as base material for THz photoconductive switching: a theoretical study from input power to output THz emission," Optics Express, Vol. 19, pp.15077-15089 (2011).

16. K. Bertulis, A. Krotkus, G. Aleksejenko, V. Pačebutas, R. Adomavičius, and G. Molis, "GaBiAs: A material for optoelectronic terahertz devices,"Applied Physics Letter, Vol. 88, pp.201112 (2006).

17. H. H. Tan, C. Jagadish, K. Korona, J. Jasinski, M. Kaminska, R. Viselga, S. Marcinkevicius, and A. Krotkus, "Ion-implanted GaAs for subpicosecond optoelectronic applications," IEEE Journal of Selected Topics in Quntum Electronics, Vol. 2, pp.66 (1996).

18. H. T. Chen, W. J. Padilla, J. M. Zide, S. R. Bank, A. C. Gossard, A. J. Taylor, and R. D. Averitt, "Ultrafast optical switching of terahertz metamaterials fabricated on ErAs/GaAs nanoisland superlattices," Optics Letter, Vol. 32, pp.1620 (2007).

19. H. Roehle, R. J. B. Dietz, H. J. Hensel, J. Böttcher, H. Künzel, D. Stanze, M. Schell, and B. Sartorius, "Next generation 1.5 µm terahertz antennas: mesa-structuring of InGaAs/InAlAs photoconductive layers," Optics Express, Vol. 18, pp.2296-2301 (2010).

20. A. Alu, and N. Engheta, "Enhanced directivity from subwavelength infrared/optical nano-antennas loaded with plasmonic materials or metamaterials," IEEE Transaction on Antenna and Propagation, Vol. 55, pp.3027-3039 (2007).

21. Y. Chen, S. Williamson, T. Brock, F. W. Smith, and A. R. Calawa, "375-GHz-bandwidth photoconductive detector," Applied Physics Letter, Vol. 59, pp.1984 (1991).

22. H. Tanoto, J. H. Teng, Q. Y. Wu, Sun, M. Chen, Z. N. Maier, S. A. Wang, B. Chum, C. C. Si, G. Y. Danner, A. J. and Chua, S. J., "Greatly enhanced continuous-wave terahertz emission by nano-electrodes in a photoconductive photomixer," Nature Photonics, Vol. 6, pp.121–126 (2012).

23. H. R. Park, Y. Bahk, K. Ahn, Q. Park, D. S. Kim, L. Moreno, F. J. Vidal, and J. B. Abad, "Controlling terahertz radiation with nanoscale metal barriers embedded in nano slot antennas," ACS Nano, Vol. 5, pp.8340 (2011).

24. C. Chang, Y. D. Sharma, Y. Kim, J. A. Bur, R. V. Shenoi, S. Krishna, D. Huang, and S. Lin, "A surface plasmon enhanced infrared photodetector based on InAs quantum dots," Nano Letters, Vol. 10, pp.1704–1709 (2010).

25. C. E. Hofmann, F. J. G. Abajo, and H. A. Atwater, "Enhancing the radiative rate in III−V semiconductor plasmonic core−shell nanowire resonators," Nano Letters, Vol. 11, pp.372–376 (2011).

26. P. Fan, U. Chettiar, L. Cao, F. Afshinmanesh, N. Engheta, , and M. Brongersma, "An invisible metal–semiconductor photodetector," Nature Photonics, Vol. 6, pp.380-385 (2012).

27. T. Zhai, X. Zhang, Z. Pang, X. Su, H. Liu, S. Feng, and L. Wang, "Random laser based on waveguided plasmonic gain channels," Nano Letters, Vol. 11, pp.4295–4298 (2011).

28. A. Weber-Bargioni, A. Schwartzberg, M. Cornaglia, A. Ismach, J. J. Urban, Y. Pang, R. Gordon, J. Bokor, M. B. Salmeron, D. F. Ogletree, P. Ashby, S. Cabrini, P. J Schuck, "Hyperspectral nanoscale imaging on dielectric substrates with coaxial optical antenna scan probes," Nano Letters, Vol. 11, pp.1201 (2011).

29. T. K. Shimizu, R. A. Pala, J. D. Fabbri, M. L. Brongersma, and N. A. Melosh, “Probing molecular junctions using surface plasmon resonance spectroscopy,” Nano Letters, Vol. 6, pp.2797-803 (2006).

30. Z. Yu, J. S. White, E. S. Barnard, M. L. Brongersma, and S. Fan, “Planar lenses based on nanoscale slit arrays in a metallic film,” Nano Letters, Vol. 9, pp.235–238 (2009).

31. K. Diest, J. Dionne, M. Spain, and H. Atwater, “Tunable color filters based on metal-insulator-metal resonators,” Nano Letters, Vol. 9, pp.2579 (2009).

32. P. Ginzburg, A. Nevet, N. Berkovitch, A. Normatov, G. M. Lerman, A. Yanai, U. Levy, and M. Orenstein, “Plasmonic resonance effects for tandem receiving-transmitting nanoantennas,” Nano Letters, Vol. 11, pp.220-224 (2001).

33. T. R. Lin, S. W. Chang, S. L. Chuang, Z. Zhang, P. J. Schuck, “Coating effect on optical resonance of plasmonic nanobowtie antenna,” Applied Physics Letter, Vol. 97, pp.063106 (2010).

34. G. Lerman, A. Yanai, and U. Levy, “Demonstration of nanofocusing by the use of plasmonic lens illuminated with radially polarized light,” Nano Letters, Vol. 9, pp.2139-2143 (2009).

35. P. Berini, R.Charbonneau, and N. Lahoud, “Long-range surface plasmons on ultrathin membranes,” Nano Letters, Vol. 7, pp.1376–1380 (2007).

36. Y. Fang, Z. Li, Y. Huang, S. Zhang, P. Nordlander, N. J. Halas, and H. Xu, “Branched silver nanowires as controllable plasmon routers,” Nano Letters, Vol. 10, pp.1950–1954 (2010).

37. R. Oulton, V. Sorger, D. A. Genov, D. F. P. Pile, X. Zhang, “A hybrid plasmonic waveguide for subwavelength confinement and long-range propagation,” Nature Photonics, Vol. 2, pp.496 (2008).

38. V. J. Sorger, Z. Ye, R. F. Oulton, Y. Wang, G. Bartal, X. Yin, and X. Zhang, “Experimental demonstration of low-loss optical waveguiding at deep sub-wavelength scales,” Nature Communiction, Vol. 2, pp.331 (2011).

39. T. Tanemura, K. C. Balram, D. Ly-Gagnon, P. Wahl, J. S. White, M. Brongersma, and. D. A. B. Miller, “Multiple-wavelength focusing of surface plasmons with a nonperiodic nanoslit coupler,” Nano Letters, Vol. 11, pp.2693–2698 (2011).

40. U. K. Chettiar, R. F. Garcia, S. Maier, and N. Engheta, “Enhancement of radiation from dielectric waveguides using resonant plasmonic coreshells,” Optics Express, Vol. 10, pp.16104-16112 (2012).

41. B-Y. Hsieh, M. Jarrahi, "Analysis of periodic metallic nano-slits for efficient interaction of terahertz and optical waves at nano-scale dimensions," Journal of Applied Physics, Vol. 109, pp.084326 (2011).

42. P. Genevet, J. Tetienne, E. Gatzogiannis, R. Blanchard, M. A. Kats, M. Scully, and F. Capasso, "Large enhancement of nonlinear optical phenomena by plasmonic nanocavity gratings," Nano Letters, Vol. 10, pp.4880–4883 (2010).

43. M. W. Knight, N. K. Grady, R. Bardhan, F. Hao, P. Nordlander, and N. J. Halas, "Nanoparticle-mediated coupling of light into a nanowire," Nano Letters, Vol. 7, pp.2346–2350 (2007).

44. N. K. Grady, M. W. Knight, R. Bardhan, and N. J. Halas, "Optically-driven collapse of a plasmonic nanogap self-monitored by optical frequency mixing," Nano Letters, Vol. 10, pp.1522–1528 (2010).

45. S. Xiang, A. Nahata, "Coherent detection of multiband terahertz radiation using a surface plasmon-polariton based photoconductive antenna," IEEE Transaction on Terahertz Science and Technology, Vol. 1, pp.412-415 (2011).

46. T. Matsui, A. Agrawal, A. Nahata, and Z. V. Vardeny, "Transmission resonances through aperiodic arrays of subwavelength apertures," Nature, Vol. 446, pp.517-520 (2007).

47. T. D. Nguyen, Z. V. Vardeny, and A. Nahata, "Concentration of terahertz radiation through a conically tapered aperture," Optics Express, Vol. 18, pp.25441-25448 (2010).

48. T. Sondergaard, S. I. Bozhevolnyi, S. M. Novikov, J. Beermann, E. Devaux, T. W. Ebbesen, "Extraordinary optical transmission enhanced by nanofocusing," Nano Letters, Vol. 10, pp.3123−3128 (2010).

49. T. W. Ebbesen, H. J. Lezec, H. F. Ghaemi, T. Thio, P. A. Wolff, "Extraordinary optical transmission through sub-wavelength hole arrays," Nature, Vol. 391, pp.667−669 (1998).

50. P. Nagpal, N. C. Lindquist, S. H. Oh, D. J. Norris, "Ultrasmooth patterned metals for plasmonics and metamaterials," Science, Vol. 325, pp.594−597 (2009).

51. M. A. Seo, H. R. Park, S. M. Koo, D. J. Park, J. H. Kang, O. K. Suwal, S. S. Choi, P. C. M. Planken, G. S. Park, N. K. Park, Q. H. Park, D. S. Kim, "Terahertz field enhancement by a metallic nano slit operating beyond the skin-depth limit," Nature Photonics, Vol. 3, pp.152−156 (2009).

52. A. Novitsky, M. Zalkovskij, R. Malureanu, P. Jepsen, A. V. Lavrinenko, "Optical waveguide mode control by nanoslit-enhanced terahertz field," Optics Letter, Vol. 15, pp.3903−5 (2012).

53. D. S. Bulgarevich, M. Watanabe, M. Shiwa, "Single sub-wavelength aperture with greatly enhanced transmission," New Journal of Physics, Vol.14, pp.0530001 (2012).

54. M. Seo, J. Kyoung, H. Park, S. Koo, H. Kim, H. Bernien, B. J. Kim, J. H. Choe, Y. H. Ahn, H. Kim, N. Park, Q. Park, K. Ahn, D. S. Kim, "Active terahertz nanoantennas based on VO2 phase transition," Nano Letter, Vol. 10, pp.2064−2068 (2010).

55. H. R. Park, Y. M. Park, H. S. Kim, J. S. Kyoung, M. A. Seo, D. J. Park, Y. H. Ahn, K. J. Ahn, D. S. Kim, "Terahertz nanoresonators: giant field enhancement and ultrabroadband performance," Applied Physics Letter, Vol. 96, pp.121106 (2010).

56. F. G. Sun, G. A. Wagoner, X. C. Zhang, "Measurement of free-space terahertz pulses via long-lifetime photoconductors," Applied Physics Letter, Vol. 67, pp.1656−1658 (1995).

57. Y. M. Hsin, W. B. Tang, H. T. Hsu, "Temperature dependence of electron saturation velocity in GaAs measured in InGaP/GaAs HBT using DC and AC approaches," Solid-State Electronics, Vol. 49, pp.295−300 (2003).

58. G. D. Aguanno, N. Mattiucci, M. J. Bloemer, D. Ceglia, M. A. Vincenti, A. Alu, "Transmission resonances in plasmonic metallic gratings," JOSA B, Vol. 28, pp.253−264 (2011).

59. Q. Min, R. Gordon, "Surface plasmon microcavity for resonant transmission through a slit in a gold film," Optics Express, Vol. 16, pp.9708−9713 (2008).

60. E. D. Palik, Handbook of optical constants of solids Academic: San Diego, CA, 1985.

61. P. B. Johnson, R. W. Christy, "Optical constants of the noble metals," Physical Review B, Vol. 6, pp.4370−4379 (1972).

62. W. Cai, M. L. Brongersma, "Plasmonics gets transformed," Nature Nanotechnology, Vol. 5, pp.485−486 (2010).

63. S. Rubanov, P. R. Munroe, "Damage in III-V compounds during focused ion beam milling," Microscopy Microanalysis, Vol. 11, pp.446−455 (2005).

64. C. W. Berry, M. R. Hashemi, M. Unlu, and M. Jarrahi, "Significant radiation enhancement in photoconductive terahertz emitters by incorporating plasmonic contact electrodes," Published online at http://arxiv.org/abs/1209.1680, (2012).

65. S. G. Park, K. H. Jin, M. Yi, J. C. Ye, J. Ahn, K. H. Jeong, "Enhancement of terahertz pulse emission by optical nanoantenna," ACS Nano, Vol. 6, pp.2026−2031 (2012).